Universidade de São Paulo
Instituto de Física

O Potencial Nuclear em Sistemas de Íons Pesados

Luiz Carlos Chamon

Tese de livre-docência apresentada ao
Instituto de Física da Universidade de São Paulo

SÃO PAULO
1999

Para a razão maior de minha existência,
meus filhos Fabrício e Regina.

RESUMO

Neste trabalho, apresentamos um modelo teórico e um método experimental para a determinação do potencial nuclear em sistemas de íons pesados. A interação foi construída considerando os efeitos da não-localidade de Pauli, advinda do caráter de identidade dos núcleons que constituem a matéria nuclear. O modelo têm sido aplicado com sucesso na análise de dados experimentais de espalhamentos elástico e inelástico para vários sistemas e em uma ampla região de energia. O método experimental é baseado na análise de dados de espalhamento elástico em energias subcoulombianas e já foi aplicado na obtenção do potencial nuclear para os sistemas $^{16}O + {}^{58,60,62,64}Ni$, ^{88}Sr, $^{90,92}Zr$, ^{92}Mo.

ÍNDICE

I - INTRODUÇÃO

Um tratamento exato para uma colisão entre núcleos pesados envolve a resolução de um problema de muitos corpos (núcleons) extremamente complexo. Assim, a descrição desse processo se faz de maneira aproximada, utilizando um potencial médio de interação entre os íons e algum modelo para os canais de reação. Dessa forma, o estudo do potencial médio entre núcleos em colisão (potencial íon-íon) é um dos problemas fundamentais na área de Reações Nucleares entre Íons Pesados. Ainda devido ao número de graus de liberdade envolvido neste tipo de colisão, existe grande dificuldade na determinação experimental do respectivo potencial. Neste trabalho será apresentado um método experimental para a determinação da parte nuclear do potencial íon-íon (potencial nuclear), através de medidas de espalhamento elástico em energias subcoulombianas, e também um modelo teórico para esse campo médio, que incorpora os efeitos da não-localidade intrínseca da interação, devido à identidade das partículas que constituem a matéria nuclear.

Em energias próximas da barreira coulombiana, o espalhamento elástico entre núcleos pesados é o processo dominante em termos da seção de choque, o que faz com que este seja uma importante fonte de informação a respeito do mecanismo de reação. Um dos modelos mais utilizados para a análise de dados experimentais de espalhamento elástico é o Modelo Ótico. Nesse modelo, os graus de liberdade internos dos íons são considerados congelados e o potencial de interação, denominado potencial ótico, torna-se complexo, sendo que o potencial nuclear está representado na parte real, e a parte imaginária simula a absorção de fluxo devida aos diversos canais de reação. É bastante conhecido [Sa74] que o ajuste de dados experimentais de

espalhamento elástico, em energias pouco acima da barreira coulombiana, só consegue determinar o potencial ótico numa pequena região de distâncias de interação, em torno de um ponto conhecido como raio de absorção forte. Como será discutido adiante, a origem desta ambigüidade na determinação do potencial está na forte absorção característica de sistemas entre núcleos pesados, representada pela parte imaginária do potencial. Por simular um processo muito complexo de absorção de fluxo do canal elástico, esta parte imaginária carrega parâmetros que podem variar amplamente no ajuste de dados experimentais.

Dados de espalhamento inelástico e de reações com transferência de núcleons são analisados através de cálculos tipo DWBA ou Canais Acoplados; sendo que, em geral, em ambos são utilizados potenciais óticos. Portanto, também resultam ambigüidades com relação à determinação da parte nuclear do potencial íon-íon através da análise deste tipo de dados experimentais.

No caso da fusão nuclear é possível mostrar [Wo73] que, para energias acima da barreira, a seção de choque de fusão depende apenas de dois parâmetros: o raio da barreira e o valor do potencial no raio da barreira. Assim, os dados de fusão somente determinam o potencial em um único ponto, de maneira análoga ao que acontece com o espalhamento elástico. Para energias abaixo da barreira existem importantes contribuições para a fusão devido ao acoplamento com outros canais de reação [Be85], tornando novamente difícil a obtenção do potencial nuclear.

Alguns autores têm mostrado a necessidade de uma análise conjunta e consistente entre os diversos canais de reação. Alguns trabalhos envolvem a análise simultânea do espalhamento elástico e da fusão com potenciais óticos [Ud89, Ho89, Ch92]. Cálculos mais elaborados, do tipo canais acoplados [Ta65], em princípio poderiam levar em conta todos os canais de reação,

tornando desnecessária a utilização da parte imaginária do potencial ótico. Na prática, porém, a solução completa do conjunto de todos os canais de reação acoplados é de dificuldade equivalente à resolução exata para o problema de colisão entre muitos corpos (núcleons). Assim, na maioria das aplicações tais cálculos são realizados com apenas alguns canais acoplados, sendo que ainda mantém uma parte imaginária do potencial para simular os efeitos de canais de reação que não entraram explicitamente nos acoplamentos. Quando um número muito grande de canais acoplados é considerado, a solução numérica das muitas equações diferenciais torna o resultado dos cálculos impreciso, prevendo corretamente o comportamento dos dados experimentais do ponto de vista qualitativo, mas deixando a desejar no que diz respeito ao ajuste quantitativo (veja exemplo na referência Th85).

Em resumo, a determinação da parte nuclear do potencial íon-íon, através da análise de dados experimentais em energias próximas (acima) da barreira coulombiana, é sujeita a ambigüidades devido à grande complexidade dos muitos canais de reação envolvidos neste tipo de colisão. Nos últimos anos têm sido obtidos, também, dados experimentais de espalhamento elástico em altas energias (até centenas de *MeV/núcleon*). Em alguns casos, tais dados permitem a extração do potencial com menor grau de ambigüidade [Br97]. As análises têm mostrado que a intensidade do potencial nuclear decresce com o aumento da energia de bombardeio. Vários modelos teóricos têm sido propostos para descrever essa variação [Ko82, Ko84, Kh93, Kh94, Kh95a, Kh95b]. No entanto, a consistência desses modelos na análise conjunta de dados de alta e baixa energia ainda não é clara, devido à já comentada ambigüidade na extração do potencial através de experimentos em energias próximas da barreira coulombiana.

O plano de pesquisa que tenho desenvolvido nos últimos anos no Laboratório Pelletron do IFUSP, está baseado, em parte, num programa de obtenção de dados experimentais em energias subcoulombianas, que permite extrair o potencial nuclear entre íons pesados de forma muito menos ambígüa do que vinha sendo feito anteriormente. Para energias de alguns *MeV* abaixo da barreira coulombiana, quase todos os canais de reação têm seções de choque desprezíveis. Assim, nessa região de baixas energias, a complexidade do tratamento teórico advinda dos canais de reação é muito diminuída em comparação com regiões de energia acima da barreira. Isto permite que o potencial de interação entre íons pesados seja extraído sem ambigüidade da análise de dados experimentais de espalhamento elástico (e, eventualmente, dos poucos canais de reação relevantes). Para essas energias, o potencial nuclear pode ser considerado como uma pequena perturbação do potencial coulombiano, e a seção de choque de espalhamento elástico é muito próxima da seção de choque de Rutherford. Assim, os dados experimentais devem ser obtidos com grande precisão, de maneira a extrair o potencial nuclear com boa definição. Até o momento, esse método já foi aplicado com sucesso no estudo do potencial íon-íon para os sistemas ^{16}O + $^{58,60,62,64}Ni$, ^{88}Sr, $^{90,92}Zr$, ^{92}Mo [Ch95, Ch96, Al99].

Também tenho trabalhado no desenvolvimento de um modelo teórico para a interação entre íons pesados. Esse modelo [Ri97, Ch97, Ch98, Ga98] leva em consideração a natureza fermiônica da matéria nuclear, que implica numa não-localidade da interação, denominada não-localidade de Pauli. Esse tipo de interação não-local já havia sido empregado em 1962 por Perey e Buck [Pe62], na descrição do processo de espalhamento elástico para sistemas nêutron-núcleo. A interação que propomos para sistemas núcleo-núcleo altera o já conhecido potencial local *Double-Folding* [Sa79], levando-se em

consideração os efeitos da não-localidade de Pauli. O modelo tem sido bem sucedido na descrição de dados experimentais de espalhamento elástico e inelástico, para diversos sistemas e numa vasta região de energia [Ch97, Ch98].

O método experimental que desenvolvemos para a determinação do potencial íon-íon e o modelo teórico de interação não-local são complementares no estudo do potencial nuclear em colisões entre íons pesados. O potencial *Folding* é baseado numa convolução das densidades nucleares com a interação núcleon-núcleon. Assim, efeitos da estrutura dos núcleos sobre as densidades se refletem no potencial nuclear. Esses efeitos podem ser estudados através da comparação de cálculos teóricos, oriundos de nosso modelo, com resultados obtidos utilizando o método experimental acima citado. Este trabalho de Livre Docência trata desse método experimental e do modelo teórico, sendo baseado em grande parte em resenha de sete artigos que temos publicado nos últimos anos. No próximo capítulo, será exposto um breve resumo, com enfoque crítico, do Modelo Ótico. O modelo teórico sobre interações não-locais será abordado no capítulo III. O método para determinação experimental do potencial íon-íon será objeto do capítulo IV. O último capítulo será dedicado a um resumo e às principais conclusões. Cópias das sete referências: Ch95, Ch96, Al99, Ri97, Ch97, Ch98 e Ga98, que serviram de base para o presente trabalho, encontram-se em anexo no final do texto. Devo salientar que nem sempre a notação e a nomenclatura utilizadas neste trabalho correspondem às adotadas nos artigos.

II – O MODELO ÓTICO

Ao tratar o espalhamento elástico entre íons pesados com interações não-locais, deve-se resolver a seguinte equação integro-diferencial [Ch97]:

$$-\frac{\hbar^2}{2\mu}\vec{\nabla}^2\Psi(\vec{R})+\int U(\vec{R},\vec{R}')\Psi(\vec{R}')\,d\vec{R}'=E\,\Psi(\vec{R}), \qquad \text{(II.1)}$$

onde $\Psi(\vec{R})$ é a função de onda que descreve o espalhamento elástico do sistema núcleo-núcleo. Por considerações físicas [Pe80], a interação efetiva entre os núcleos deve ser simétrica, $U(\vec{R},\vec{R}')=U(\vec{R}',\vec{R})$. Essa interação pode ser escrita, em uma forma esquemática, como:

$$U(\vec{R},\vec{R}')=V(\vec{R},\vec{R}')+\sum_i V_i(\vec{R})\,G_i^+(\vec{R},\vec{R}';E)\,V_i(\vec{R}'). \qquad \text{(II.2)}$$

O primeiro termo, $V(\vec{R},\vec{R}')$, que denominamos interação íon-íon, representa o valor esperado do operador de interação, o qual contém, basicamente, a força efetiva média núcleon-núcleon. A não-localidade neste termo é devida à natureza de identidade fermiônica dos núcleons que constituem a matéria nuclear. No que segue, denominamos esse tipo de não-localidade como "de Pauli". O segundo termo, chamado termo de Feshbach, contém as contribuições oriundas dos canais de reação e de excitações virtuais para estados intermediários (canais inelásticos, de transferência de núcleons, etc.). A correspondente não-localidade, denominada "de Feshbach", provém de polarizações devido à propagação nos canais intermediários. Isto fica estabelecido pela função de Green $G_i^+(\vec{R},\vec{R}';E)$, a qual contém uma explícita dependência em energia.

Ao confrontar teoria e experiência, normalmente se utiliza o Modelo Ótico com um potencial local. Para esse fim, definimos o potencial local-

equivalente através da equação: $U(\vec{R},E)\Psi(\vec{R}) \equiv \int U(\vec{R},\vec{R}')\Psi(\vec{R}')\,d\vec{R}'$. (II.3)

O potencial local-equivalente ao termo de Feshbach é denominado potencial de polarização.

Neste capítulo iremos considerar 2 casos. No primeiro, iremos desprezar a não-localidade de Pauli e tratar a não-localidade de Feshbach utilizando um potencial de polarização médio parametrizado. Esse tipo de abordagem corresponde ao Modelo Ótico em sua forma mais simples. Em seguida, continuaremos desprezando a não-localidade de Pauli, mas iremos tratar explicitamente o acoplamento do canal elástico com alguns canais de reação, através do formalismo de cálculos de canais acoplados. Então, será mostrado como obter o correspondente potencial de polarização. No próximo capítulo iremos discutir o caso em que são considerados os efeitos da não-localidade de Pauli.

II.1 - O Modelo Ótico em sua Forma Mais Simples

Uma aproximação largamente utilizada consiste em desprezar a não localidade de Pauli, e considerar que a interação íon-íon é local, central, e independente da energia, podendo ser escrita como a soma do potencial nuclear, $V_N(R)$, com o potencial coulombiano, $V_C(R)$. O termo de Feshbach é tratado através de um potencial de polarização médio, local, central, complexo e dependente da energia, $V_{Pol}(R,E)+iW(R,E)$. Nestas condições, a interação entre os núcleos em colisão é dada por: $U(R,E)=V_C(R)+V_{Ot}(R,E)$, (II.4)

onde o termo $V_{Ot}(R,E)=V(R,E)+iW(R,E)$ é denominado potencial ótico, e $V(R,E)=V_N(R)+V_{Pol}(R,E)$ é a parte real do potencial ótico.

Devido ao caráter central da interação, com a usual expansão em ondas parciais,

$$\Psi(\vec{R}) = \sum_{\ell} i^{\ell}\,(2\ell+1)\frac{u_{\ell}(R)}{kR}P_{\ell}[\cos(\Theta)], \qquad \text{(II.5)}$$

a equação (II.1) pode ser escrita na forma do conjunto de equações:

$$-\frac{\hbar^2}{2\mu}\left[\frac{d^2}{dR^2}-\frac{\ell(\ell+1)}{R^2}\right]u_{\ell}(R)+\left[E-U(R,E)\right]u_{\ell}(R)=0. \qquad \text{(II.6)}$$

Foi demonstrado [Fe58, Fe62] que a variação com a energia das partes real e imaginária do potencial de polarização deve obedecer a uma relação, conhecida como relação de dispersão: $V_{Pol}(R,E)=\frac{P}{\pi}\int_{-\infty}^{+\infty}\frac{W(R,E')}{E'-E}dE'$, (II.7)

onde P significa o valor principal da integral [Sa91]. Essa relação é análoga à de Kramers-Kronig da Ótica. Ela emerge naturalmente de uma teoria completamente microscópica na interação núcleon-núcleon [Ma82, Ma85]. É possível mostrar [Sa91] que a relação de dispersão é uma expressão da causalidade (nesse contexto, causalidade significa que a onda espalhada não pode deixar o alvo antes da chegada da onda incidente).

Curiosamente, na maioria das aplicações o potencial (energia potencial) coulombiano entre dois núcleos de raios R_1 e R_2, e números atômicos Z_1 e Z_2, tem sido considerado aproximadamente igual ao potencial entre uma carga Z_1e, puntiforme, e uma esfera uniformemente carregada de raio R_1+R_2 e carga total Z_2e. No entanto, essa aproximação não é apropriada nos casos de espalhamento em altas energias, para os quais regiões de distâncias de interação bastante internas (ao raio da barreira) são testadas. Nesses casos, temos utilizado [Ch97, Ch98] o potencial entre duas esferas uniformemente carregadas, para o qual já foi encontrada uma expressão analítica a mais de duas décadas [De75].

A seção de choque de reação está relacionada com a parte imaginária do potencial ótico através da expressão: $\sigma_R = -\frac{2\mu}{\hbar k}\langle \Psi | W | \Psi \rangle$. (II.8)

Na maioria das aplicações, essa parte imaginária tem sido considerada com forma do tipo Woods-Saxon (expressão II.9) ou da respectiva derivada. Esse procedimento é adotado pela suposição de que o potencial deveria ter aproximadamente a mesma forma da distribuição de matéria nuclear. É importante ressaltar que, apesar de útil devido à simplicidade, tal procedimento não está justificado, pois essa parte do potencial ótico tem como função a simulação de um processo de absorção de fluxo bastante complexo, e nada implica que o respectivo potencial local-equivalente tenha uma forma tão simples. Por exemplo, já foi demonstrado [Lo77, Ba79] que o processo de excitações inelásticas coulombianas tem um correspondente potencial de polarização imaginário, de longo alcance, que não pode ser corretamente representado utilizando uma forma do tipo Woods-Saxon.

$$W(R,E) = \frac{-W_0(E)}{1+\exp\left[\frac{R-R_I(E)}{a_I(E)}\right]} \qquad \text{(II.9)}$$

Ao utilizar o Modelo Ótico, o procedimento normalmente adotado na análise de dados de espalhamento elástico entre íons pesados é manter alguns parâmetros livres no potencial ótico, de maneira a ajustar a distribuição angular experimental. Algumas vezes adota-se uma forma Woods-Saxon também para a parte real do potencial ótico. Tem sido observada [Sa74] a seguinte característica relativa a esses procedimentos. Para regiões de energia próximas da barreira coulombiana, diferentes "famílias" de potenciais óticos, isto é, diferentes valores dos parâmetros livres em $V(R,E)$ e $W(R,E)$, produzem ajustes de dados experimentais muito semelhantes. Os parâmetros

estão de tal forma correlacionados, que as diferentes famílias correspondentes à parte real do potencial ótico, $V(R, E)$, cruzam-se (têm a mesma intensidade) somente num ponto conhecido como raio de absorção forte. Ou seja, as previsões de seção de choque teóricas só são sensíveis ao potencial ótico em uma pequena região de distâncias de interação, em torno do raio de absorção forte. Essa característica está ligada ao curto alcance da força nuclear e à correspondente absorção forte nos sistemas de íons pesados [Br97]. Isto é, "contato" entre os núcleos leva quase inevitavelmente a eventos não elásticos e a perda de fluxo do canal elástico; consequentemente, o espalhamento elástico é dominado pelas condições da "região superficial" de distâncias de interação. Além disso, também tem sido observado para diversos sistemas que as intensidades das partes real e imaginária do potencial ótico variam fortemente com a energia, numa estreita região em torno da barreira coulombiana. Esse comportamento, conhecido como anomalia de limiar, tem sido atribuído à relação de dispersão (para uma discussão completa da anomalia de limiar veja o artigo de revisão da referência Sa91).

Em resumo, a determinação da parte real do potencial ótico, através da análise de dados de espalhamento elástico em energias em torno da barreira coulombiana, é sujeita a muitas ambigüidades, com exceção de distâncias de interação muito próximas do raio de absorção forte. Mesmo para essas distâncias, existe uma forte variação do potencial ótico com a energia. Ainda mais, a parte real do potencial ótico é composta da soma do potencial nuclear com a parte real do potencial de polarização; sendo que sobre essa última contribuição as análises de dados com o Modelo Ótico fornecem pouca informação. Assim sendo, fica evidente a grande dificuldade na determinação do potencial nuclear, através da análise de dados experimentais de espalhamento elástico em energias próximas (acima) da barreira coulombiana.

II.2 - Cálculos de Canais Acoplados

O formalismo de cálculos de canais acoplados é utilizado quando é desejável considerar com mais exatidão as contribuições de alguns específicos canais de reação para o potencial de polarização. Como exemplo deste tipo de cálculo, nesta seção apresentaremos o caso do acoplamento de um estado excitado 2^+ (espalhamento inelástico) com um estado fundamental 0^+. Uma discussão detalhada e geral (quaisquer spins dos núcleos alvo e projétil), que inclui o acoplamento de canais de transferência, pode ser encontrada na referência Th88.

O conjunto de equações diferenciais acopladas que se obtém ao realizar a expansão da função de onda em ondas parciais é [Bu63]:

$$[T_J - U(R,E) + E]\, u_J^{0J}(R) = V_{0J:2J}(R)\, u_J^{2J}(R) + V_{0J:2J-2}(R)\, u_J^{2J-2}(R) + V_{0J:2J+2}(R)\, u_J^{2J+2}(R), \quad \text{(II.10)}$$

$$[T_J - U(R,E) - V_{2J:2J}(R) + E']\, u_J^{2J}(R) = V_{2J:0J}(R)\, u_J^{0J}(R) + V_{2J:2J-2}(R)\, u_J^{2J-2}(R) + V_{2J:2J+2}(R)\, u_J^{2J+2}(R), \quad \text{(II.11)}$$

$$[T_{J-2} - U(R,E) - V_{2J-2:2J-2}(R) + E']\, u_J^{2J-2}(R) = V_{2J-2:0J}(R)\, u_J^{0J}(R) + V_{2J-2:2J}(R)\, u_J^{2J}(R), \quad \text{(II.12)}$$

$$[T_{J+2} - U(R,E) - V_{2J+2:2J+2}(R) + E']\, u_J^{2J+2}(R) = V_{2J+2:0J}(R)\, u_J^{0J}(R) + V_{2J+2:2J}(R)\, u_J^{2J}(R), \quad \text{(II.13)}$$

onde $J =$ momento angular total, $T_J = \dfrac{\hbar^2}{2\mu}\left(\dfrac{d^2}{dR^2} - \dfrac{J(J+1)}{R^2}\right)$,

$u_J^{0J} =$ função de onda referente ao estado fundamental,
$u_J^{2J}, u_J^{2J-2}, u_J^{2J+2} =$ funções de onda referentes ao estado excitado,
$E' = E - \varepsilon$, $\varepsilon =$ energia de excitação do estado 2^+.

Os potenciais de acoplamento (termos do tipo $V_{0J:2J}$) são obtidos a partir de algum modelo que descreva o núcleo. Os mais utilizados são o rotacional e o vibracional (vide Bu63, Ta65 e Th88).

O potencial de polarização correspondente ao estado 2^+ é obtido por:

$$V_{Pol}^{J}(R,E)+iW_{Pol}^{J}(R,E)=\frac{V_{0J:2J}(R)\,u_J^{2J}(R)+V_{0J:2J-2}(R)\,u_J^{2J-2}(R)+V_{0J:2J+2}(R)\,u_J^{2J+2}(R)}{u_J^{0J}(R)}. \quad \text{(II.14)}$$

Através da estrutura dessa equação, pode-se verificar que o potencial de polarização depende do momento angular, da energia, e é complexo (pois envolve as funções de onda). Essa última característica é esperada, tendo em vista a absorção de fluxo do canal elástico pelo canal 2^+. Utilizando o potencial de polarização, a equação II.10 para o canal elástico pode ser escrita como:

$$-\frac{\hbar^2}{2\mu}\left[\frac{d^2}{dR^2}-\frac{J(J+1)}{R^2}\right]u_J^{0J}(R)+\left[E-U(R,E)-V_{Pol}^{J}(R,E)-iW_{Pol}^{J}(R,E)\right]u_J^{0J}(R)=0, \quad \text{(II.15)}$$

e fica evidente como o potencial de polarização insere-se no potencial ótico.

Na referência Th89, é sugerido um potencial de polarização médio que elimina a dependência com o momento angular. Aplicado ao caso que estamos discutindo, esse potencial médio seria obtido de:

$$\overline{V}_{Pol}(R,E)+i\overline{W}_{Pol}(R,E)=\frac{\sum_J w_J(R)\left[V_{Pol}^{J}(R,E)+iW_{Pol}^{J}(R,E)\right]}{\sum_J w_J(R)}, \quad \text{(II.16)}$$

com $w_J(R)=a_J\left|u_J^{0J}(R)\right|^2$, $a_J=(2J+1)\left[1-\left|S_J\right|^2\right]$ e $S_J=$elemento da matriz **S** correspondente ao canal elástico. Essa média elimina eventuais pólos do potencial de polarização, atribuindo peso zero a pontos em que $u_J^{0J}(R)=0$. Os coeficientes a_J são diretamente proporcionais às correspondentes seções de choque parciais de reação. Apesar de produzir uma boa aproximação, esse potencial de polarização médio não reproduz exatamente a "verdadeira" (proveniente de cálculos de canais acoplados) função de onda do canal elástico.

II.3 – Um Modelo Local para o Potencial Nuclear

Vários modelos têm sido propostos para a parte nuclear do potencial íon-íon. Nesta seção, vamos apresentar o potencial *Double-Folding*, pois este serviu de base para o nosso modelo de interação não-local que será discutido no próximo capítulo.

O potencial *Folding* é construído [Sa79] a partir de uma convolução da interação núcleon-núcleon com as densidades de matéria dos núcleos em colisão (figura II.1 e equação II.17).

$$V_{Fold}(R) = \iint \rho_1(r_1)\, v_0(\vec{R} - \vec{r}_1 + \vec{r}_2)\, \rho_2(r_2)\, d\vec{r}_1\, d\vec{r}_2 \qquad \text{(II.17)}$$

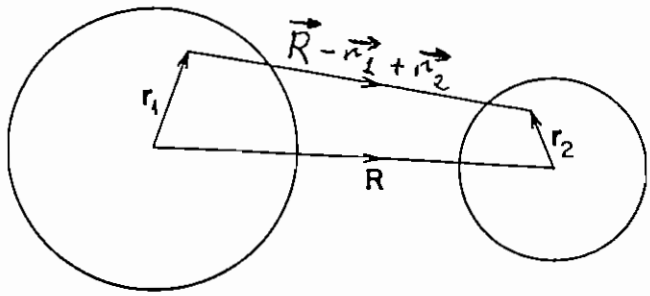

Figura II.1 – Esquema da construção do potencial *Double-Folding*. Os vetores $\vec{r}_1$ e $\vec{r}_2$ representam a posição de dois núcleons nos núcleos em colisão. O vetor $\vec{R}$ liga os centros de massa dos núcleos alvo e projétil.

Na equação II.17, $v_0(\vec{r})$ é a interação efetiva entre dois núcleons. Para tal interação, uma grande variedade de modelos têm sido propostos, mas aqueles conhecidos por M3Y (Reid e Paris) são representativos de interações "realísticas", e são, também, os mais utilizados. Em nossos trabalhos, temos usado a interação efetiva M3Y-Reid (equação II.18). Nessa equação, os dois primeiros termos são responsáveis pela parte direta da interação núcleon-

núcleon, enquanto o último simula efeitos não-locais de troca entre núcleons do projétil e alvo (não-localidade de Pauli), na aproximação de alcance nulo (o alcance da não-localidade será discutido no próximo capítulo). A magnitude de J_{00} foi determinada empiricamente, através do ajuste de dados experimentais de espalhamento de prótons em diversos núcleos, e para várias energias (até 80 *MeV*). Foi obtida a seguinte leve dependência com a energia do próton: $J_{00} \approx -276[1-0.005E]$ $(MeV\ fm^3)$. Outros detalhes acerca da interação M3Y podem ser encontrados na referência Be77.

$$v_0(\vec{r}) = 7999\frac{e^{-4r}}{4r} - 2134\frac{e^{-2.5r}}{2.5r} + J_{00}\delta(\vec{r}) \qquad \text{(II.18)}$$

No contexto do Modelo Ótico, o potencial *Folding* tem sido usado com bastante sucesso [Sa79], em análises de dados experimentais de espalhamento elástico para energias em torno da barreira coulombiana. Nessas análises, a parte real do potencial ótico tem sido assumida igual ao potencial *Folding* (que está associado ao potencial nuclear), multiplicado por um fator de normalização (que pode variar com a energia), de forma a simular os efeitos da polarização. O fator de normalização tem sido obtido próximo da unidade [Sa79], que é um indicativo da propriedade desse procedimento. Entretanto, como passaremos a discutir, o potencial *Folding* nessa versão original de Satchler e Love [Sa79], não obteve o mesmo sucesso na descrição de dados experimentais em mais altas energias.

O fenômeno do espalhamento arco-íris foi amplamente discutido em recente artigo de revisão [Br97]. Foi enfatizado que o potencial nuclear pode ser extraído sem ambigüidades, através de medidas de espalhamento elástico em energias intermediárias (várias dezenas de *MeV/núcleon*). Para ajustar os dados experimentais, o fator de normalização multiplicativo do potencial

Folding apresenta grande variação com a energia, em alguns casos tornando-se bastante menor que um. Isso foi inicialmente observado para sistemas com partículas alpha, onde um fator de normalização de aproximadamente ½ foi encontrado para energias em torno de 35 *MeV/núcleon*. Posteriormente, resultado semelhante foi obtido para vários sistemas de íons pesados. Esse fator (bastante menor que 1) não pôde ser associado aos efeitos do potencial de polarização, pois estimativas teóricas [Ma77] para essas energias mostraram que, além de apresentar intensidade muito pequena em comparação ao potencial *Folding*, a correspondente parte real do potencial de polarização é atrativa (não repulsiva como seria necessário).

Por outro lado, para explicar a saturação da matéria nuclear, já havia sido proposto [Be71] que a interação efetiva entre dois núcleons deveria depender da densidade do meio. Saturação requer que a atração enfraqueça a medida que a densidade aumenta. Assim, surgiram vários modelos para a interação nuclear entre íons pesados (denominados interações dependentes da densidade), baseados no potencial *Folding*, em que a interação efetiva núcleon-núcleon é considerada dependente da densidade. A primeira versão [Ko82, Ko84] assume a interação M3Y-Reid (equação II.18) multiplicada pelo fator:

$$f(\rho, E_N) = C(E_N)\left[1 + \alpha(E_N)\, e^{-\beta(E_N)\rho}\right], \qquad \text{(II.19)}$$

com $\rho = \rho_1(r_1) + \rho_2(r_2)$, e $E_N = E/A =$ energia de bombardeio por núcleon do projétil. Os parâmetros C, α e β, dependentes da energia, foram escolhidos de forma a fazer com que a integral de volume da interação se ajustasse, tão bem quanto possível, aos resultados de cálculos tipo Brueckner, de Jeukenne et al. [Je77], para o espalhamento de um núcleon pela matéria nuclear. Uma dificuldade com a equação II.19, é que densidades grosseiramente duas vezes maior do que a da matéria nuclear "normal" são encontradas quando ocorre

grande superposição dos dois íons. Vários modelos mais "realísticos" têm sido propostos [por exemplo: Kh93, Kh94, Kh95a, Kh95b]. Um aspecto interessante dessas interações é que diferentes modelos para a função $f(\rho, E_n)$, fornecem diferentes valores para a incompressibilidade da matéria nuclear [Kh94, Kh95a, Kh95b]. Na matéria nuclear, a energia de ligação por núcleon, B, deve ter um mínimo para a densidade de saturação $\rho_0 \approx 0.17\ fm^{-3}$. A curvatura de $B(\rho)$ está conectada com a incompressibilidade por: $K = 9\rho_0^2(\partial^2 B/\partial\rho^2)\big|_{\rho=\rho_0}$. Assim, alguns autores acreditam poder extrair informações acerca dessa importante quantidade, através da análise de dados de espalhamento elástico entre íons pesados em energias intermediárias [Kh95a]. Tais análises são realizadas com alguns parâmetros livres na função $f(\rho, E_n)$, utilizados no ajuste dos dados experimentais. Aparentemente, o modelo que fornece melhores ajustes, conhecido como DDM3Y1, implicaria numa incompressibilidade de K=270 MeV [Kh95a], que é compatível com o valor obtido a partir de dados de ressonâncias gigantes isoescalares [Yo99]. Entretanto, para obter resultados satisfatórios na análise dos dados, foi necessário introduzir uma dependência adicional em energia [Kh93]. Dessa forma, consideramos que uma denominação mais apropriada para essas interações seria: "interações dependentes da densidade e da energia". Essa dependência "extra" em energia, e o modo "um pouco arbitrário" pelo qual são assumidas as diferentes formas para a dependência de densidade da função $f(\rho, E_n)$, são os pontos mais criticados desses modelos. É necessário comentar que uma descrição alternativa da variação do potencial nuclear com a energia, como aquela apresentada no próximo capítulo, põe em dúvida os resultados para a incompressibilidade da matéria nuclear obtidos com as interações dependentes da densidade (e energia).

III - UMA DESCRIÇÃO NÃO-LOCAL DA INTERAÇÃO NÚCLEO-NÚCLEO

Como discutido nos capítulos anteriores, dados experimentais de espalhamento elástico, obtidos em energias intermediárias, têm removido as ambigüidades na determinação do potencial nuclear. Foi observado que os potenciais fenomenológicos introduzidos para descrever os dados são significativamente dependentes da energia. Alguns modelos teóricos foram construídos para descrever essa dependência através de potenciais de campo médio realísticos. Atualmente, os mais bem sucedidos parecem ser os potenciais dependentes da densidade. Entretanto, para descrever os dados, tais potenciais ainda necessitam de um fator de normalização, o qual é bastante dependente do sistema e ainda apresenta alguma variação com a energia.

Neste capítulo, será mostrado que a dependência do potencial nuclear com a energia é devida, principalmente, à natureza intrinsecamente não-local da interação, devido à identidade fermiônica das partículas que constituem a matéria nuclear. Essa não-localidade de Pauli foi inicialmente introduzida no contexto do espalhamento núcleon-núcleo [Pe62]. Também já foi utilizada para descrever o comportamento (variação com a energia) de potenciais fenomenológicos em sistemas com partículas alpha [Ja74]. Nós generalizamos o modelo para descrever os espalhamentos elástico e inelástico em sistemas de íons pesados. Cópias dos artigos de nossa autoria em que esse modelo é apresentado [referências: Ri97, Ch97, Ch98 e Ga98] estão anexas no final do texto.

III.1 – O Modelo de Interação Não-Local

A não-localidade de Pauli está associada à identidade das partículas (núcleons) envolvidas na colisão. Um núcleon "pertencente" ao núcleo projétil pode trocar de posição com outro núcleon "do" núcleo alvo. Essa troca está associada à uma interação, $V(\vec{R},\vec{R}')$, que é função dos vetores $\vec{R}$ e $\vec{R}'$, os quais conectam os centros de massa dos dois núcleos antes e depois da troca, respectivamente (vide figura III.1).

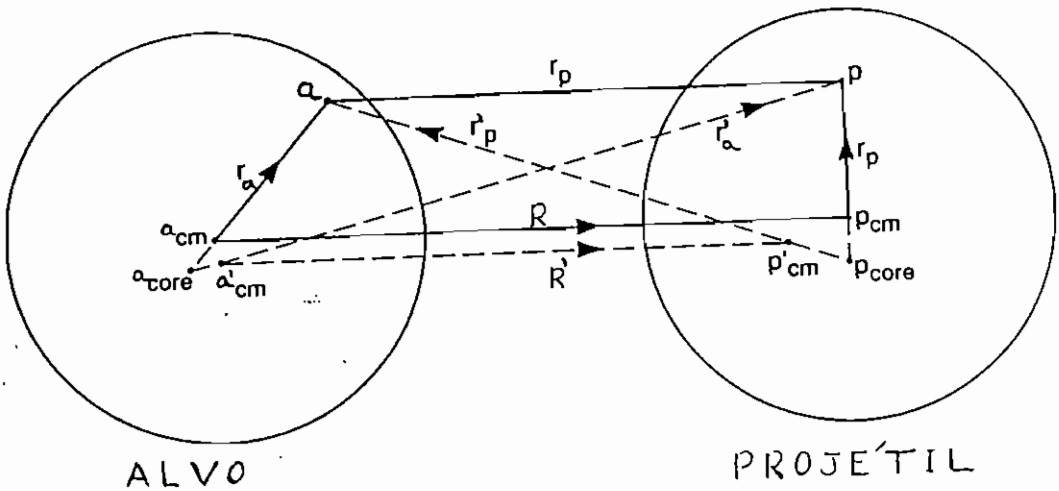

Figura III.1 – Ilustração do sistema de coordenadas utilizado. Um núcleon do alvo (a), de coordenada $\vec{r}_a$, troca de posição com um núcleon do projetil (p), de coordenada $\vec{r}_p$; sendo que passam a ser representados pelas coordenadas $\vec{r}_a'$ e $\vec{r}_p'$, respectivamente. Os centros de massa dos núcleos alvo (a_{CM}) e projétil (p_{CM}) são movidos conforme indicado.

Motivados pela Física do problema, adotamos a seguinte forma para a interação efetiva entre os núcleos: $U(\vec{R},\vec{R}') = V(\vec{R},\vec{R}') + i\delta(\vec{R}-\vec{R}')W(R',E)$. (III.1) Como trataremos do espalhamento em energias bem acima da barreira, o potencial de polarização (considerado local) foi representado apenas pela parte imaginária (que simula absorção), sendo desprezada a parte real. Vamos

separar, na interação íon-íon, a contribuição nuclear (não-local) da coulombiana (local), como segue: $V(\vec{R},\vec{R}') = V_{Nuc}(\vec{R},\vec{R}') + \delta(\vec{R}-\vec{R}')V_C(R')$. (III.2) Para a contribuição nuclear em sistemas de íons pesados, assumimos o *ansatz* de Frahn-Lemmer [Fr57], o qual já havia sido utilizado por Perey-Buck [Pe62] na descrição do espalhamento nêutron-núcleo,

$$V_{Nuc}(\vec{R},\vec{R}') = V_{NL}\left(\frac{R+R'}{2}\right)\frac{1}{\pi^{3/2}b^3}e^{-\left(\frac{|\vec{R}-\vec{R}'|}{b}\right)}. \qquad \text{(III.3)}$$

Nessa equação, b é o alcance da não-localidade de Pauli. No limite em que b tende a zero (alcance nulo), a equação integro-diferencial (II.1) se reduz à usual equação diferencial de Schröedinger. Esse *ansatz* foi justificado no contexto do espalhamento núcleon-núcleo por um tratamento teórico microscópico [Ba83]. Para sistemas de íons pesados, o uso dessa forma gaussiana simples foi justificada por Jackson e Johnson [Ja74], através de um cálculo *Single-Folding* partindo da interação núcleon-núcleo. Também mostraram que o alcance da não-localidade para sistemas de íons pesados, b, está vinculado ao alcance para sistemas núcleon-núcleo, b_0, pela expressão: $b \approx b_0 \frac{m_0}{\mu}$, onde μ é a massa reduzida do sistema de íons pesados e m_0 é a massa do núcleon. O valor $b_0 = 0.85\ fm$ foi obtido através da análise de uma extensa sistemática de dados de espalhamento elástico para sistemas nêutron-núcleo [Pe62].

Como estamos considerando potenciais centrais, podemos expandir a função de onda segundo a expressão II.5, e o termo $V_{Nuc}(\vec{R},\vec{R}')$ de acordo com:

$$V_{Nuc}(\vec{R},\vec{R}') = \sum_L \frac{2L+1}{4\pi RR'} V_L(R,R')\, P_L[\cos(\phi)], \qquad \text{(III.4)}$$

onde $V_L(R,R') = V_{NL}\left(\frac{R+R'}{2}\right)\frac{1}{b\sqrt{\pi}}\left\{Q_L\left(\frac{2RR'}{b^2}\right)e^{-\left(\frac{R-R'}{b}\right)^2} (-)^{L+1} Q_L\left(-\frac{2RR'}{b^2}\right)e^{-\left(\frac{R+R'}{b}\right)^2}\right\}$, (III.5)

$Q_L(z)$ são polinômios em $1/z$ [Pe62], e ϕ é o ângulo entre $\vec{R}$ e $\vec{R}'$. Assim, a equação integro-diferencial (II.1) pode ser escrita na forma do conjunto de equações:

$$-\frac{\hbar^2}{2\mu}\left[\frac{d^2}{dR^2}-\frac{\ell(\ell+1)}{R^2}\right]u_\ell(R)+[E-V_C(R)-iW(R,E)]u_\ell(R)=\int_0^\infty V_\ell(R,R')\,u_\ell(R')\,dR'. \quad \text{(III.6)}$$

Através da estrutura da equação III.6, é fácil verificar que o potencial local-equivalente ao termo $V_{Nuc}(\vec{R},\vec{R}')$ é dependente do momento angular e da energia, e obtido por: $V_{EQ}(R,E;\ell)=\frac{1}{u_\ell(R)}\int_0^\infty V_\ell(R,R')\,u_\ell(R')\,dR'$. (III.7)

Propomos que o potencial não-local, $V_{NL}\left(\frac{R+R'}{2}\right)$, tem a seguinte forma:

$$V_{NL}(\varepsilon)=V_{Fold}(R=\varepsilon), \quad \text{(III.8)}$$

na qual $V_{Fold}(R)$ é o potencial *Double-Folding* "padrão" [Sa79], obtido conforme a equação II.17. Para a interação núcleon-núcleon usamos a interação efetiva M3Y-Reid (equação II.18). Em nosso modelo, desconsideramos a variação em energia de J_{00} (cujo valor é assumido igual a -262 $MeV\ fm^3$), proveniente da aproximação de alcance nulo, pois acreditamos que quase toda a dependência em energia do potencial nuclear advém do parâmetro b, o alcance da não-localidade de Pauli.

Passaremos, agora, a apresentar os resultados obtidos com nosso modelo na análise de dados experimentais de espalhamento elástico. Com a finalidade de testar quão geral é o modelo, analisamos distribuições angulares para sistemas com alcances de não-localidade bem diferentes: ^{12}C + ^{208}Pb (b=0.075 fm), ^{12}C+^{12}C (b=0.14 fm), α + ^{58}Ni (b=0.23 fm), α + ^{12}C (b=0.28 fm).

Para os dois primeiros sistemas, os dados foram obtidos numa vasta região de energia ($1 \leq {}^{E_{Lab}}/_{A_{Proj}} \leq 200\, MeV / nucleon$); enquanto os dois últimos são típicos representantes de casos de espalhamento arco-íris, que deram origem aos estudos que levaram ao desenvolvimento dos potenciais dependentes da densidade. Nos cálculos do potencial *Folding*, utilizamos densidades de matéria "realísticas" provenientes de cálculos tipo *Shell-Model* (obtidos nas referências Sa79, Fa85 e Ch96). Os únicos parâmetros deixados livres no ajuste de dados foram aqueles vinculados à parte imaginária do potencial, $W(R,E)$, cuja forma foi assumida como sendo do tipo Woods-Saxon. As previsões teóricas para as seções de choque de espalhamento elástico foram obtidas resolvendo o conjunto de equações de ondas parciais III.6, no qual foi considerado nosso modelo para o potencial não-local (equações III.5 e III.8). A resolução numérica desse conjunto de equações foi realizada através de um processo iterativo.

Os ajustes das distribuições angulares são apresentados nas figuras III.2 e III.3. O acordo entre cálculos teóricos e dados experimentais é impressionante. Além disso, os valores resultantes para as seções de choque de reação são compatíveis com dados experimentais (e outros cálculos de Modelo Ótico) obtidos nas referências [Sm73, Go74, St79, Tr80, Bo82, Bu84, Sa86, Ho88 e Br97]. De nosso conhecimento, esses resultados correspondem à uma primeira tentativa realizada para reproduzir com tamanha precisão, dados de espalhamento elástico para essa variedade de sistemas, em tal vasta região de energia, utilizando uma interação nuclear real independente da energia e sem nenhum parâmetro livre (os únicos parâmetros livres estão na parte imaginária do potencial). É importante observar que o fator de normalização,

utilizado com potenciais dependentes da densidade, está totalmente ausente de nossas análises.

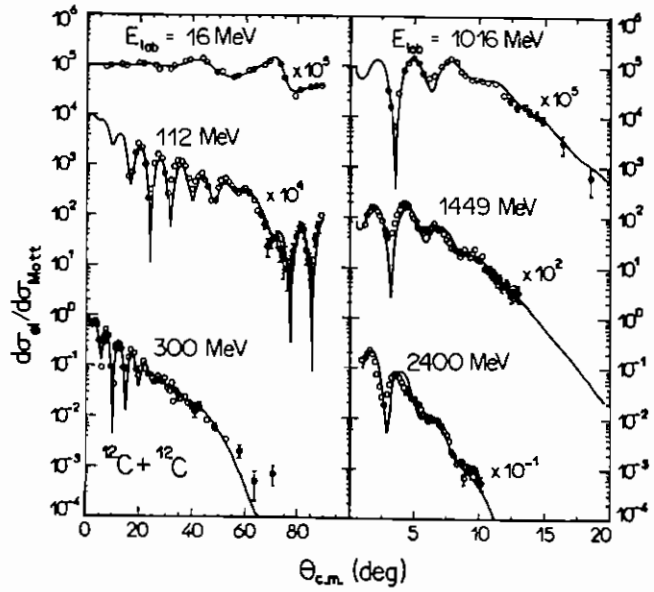

Figura III.2 – Distribuições angulares de espalhamento elástico para o sistema ^{12}C + ^{12}C, para várias energias de bombardeio (como indicado). Os dados experimentais foram extraídos das referências St79, Tr80, Bo82, Bu84 e Ho88. As linhas cheias correspondem aos cálculos para seção de choque utilizando o modelo de interação não-local.

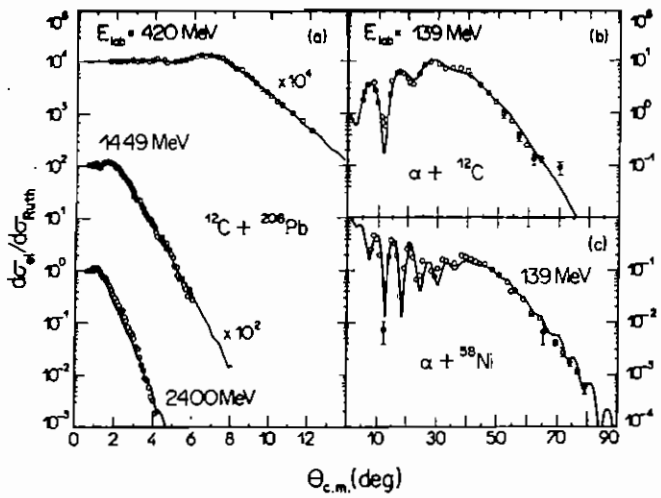

Figura III.3 – O mesmo da figura III.2, para os sistemas ^{12}C + ^{208}Pb e α + ^{12}C, ^{58}Ni. Os dados experimentais foram extraídos das referências Sm73, Go74, Sa86 e Ho88.

III.2 – O Potencial Local-Equivalente

Para íons bastante pesados, a resolução numérica das equações íntegro-diferenciais (III.6) é de difícil convergência para os altos valores de momento angular envolvidos. Assim, é desejável desenvolver um método para obter o potencial local-equivalente (PLE), com a finalidade de calcular as seções de choque solucionando a equação diferencial de Schröedinger usual (local). No início dos anos 60, foi mostrado para sistemas nêutron-núcleo [Pe62] que o PLE é apenas fracamente dependente do momento angular, e foi fornecida uma relação aproximada para obter esse potencial. Nós generalizamos [Ri97, Ch97] aquela expressão para o caso de íons pesados, incluindo o potencial coulombiano, como segue:

$$V_{EQ}(R, E; \ell) \approx V_N(R, E) = V_{Fold}(R)\, e^{-\gamma[E - V_C(R) - V_N(R,E)]}, \qquad \text{(III.9)}$$

onde $\gamma = \frac{\mu b^2}{2\hbar^2}$. Essa equação pode ser resolvida para $V_N(R, E)$ utilizando um método iterativo (o método converge para $|\gamma V_N(R, E)| < 1$).

Para sistemas de íons pesados γ é pequeno, por exemplo: para o sistema ^{12}C + ^{12}C, temos $\gamma = 0.0014\, MeV^{-1}$. Assim, para energias não muito altas podemos expandir a expressão III.9 em:

$$V_N(R, E) \approx V_{Fold}(R)\,(1 - \gamma\, E) = V_{Fold}(R)\,(1 - \beta\, E_N), \qquad \text{(III.10)}$$

onde E_N é a energia de bombardeio por núcleon do projétil ($E_{Lab} / A_{\text{Proj}}$); e $\beta = \frac{m_0 b_0}{2\hbar^2} = 0.0086\, MeV^{-1}$ é uma constante independente do sistema. Esse comportamento linear da intensidade do potencial nuclear com a energia já

havia sido observado para sistemas alpha-núcleo [Ja74], e o valor de γ extraído das análises de dados experimentais concorda com aquele obtido com nossa expressão teórica, $\gamma = \frac{\mu b^2}{2\hbar^2}$ (com $b \approx b_0 \frac{m_0}{\mu}$ e $b_0 = 0.85\,fm$).

Como comentado anteriormente, potenciais nucleares fenomenológicos podem ser extraídos sem ambigüidade da análise de dados de espalhamento elástico em energias intermediárias. Este fato permite que se realize um teste mais profundo da expressão III.9 (conforme discutimos na referência Ri97). De acordo com essa expressão (III.9), o $Log(|V_N(R,E)|)$ deveria apresentar um comportamento linear como função de $[E - V_N(R,E)]$, e o respectivo coeficiente angular estaria vinculado ao parâmetro b. Assim, estudamos os sistemas ^{12}C + ^{12}C e ^{16}O + ^{12}C, para os quais foram obtidos dados de espalhamento elástico em uma região de energia bastante ampla ($10 \leq E_{Lab} / A_{\text{Proj}} \leq 200\,MeV/nucleon$). Para esses sistemas em energias intermediárias, a região de distâncias de interação que é testada (em que a intensidade dos potenciais fenomenológicos é extraída sem ambigüidade) está em torno de $R = 4\,fm$ [Ho88, Ri97]. A figura III.4 mostra que a dependência com a energia dos potenciais fenomenológicos (extraídos da análise de dados) é concordante com a expressão III.9 (dentro de 10% de precisão). Os valores extraídos de b (0.14 fm para ^{12}C + ^{12}C e 0.11 fm para ^{16}O + ^{12}C) concordam de forma bastante razoável com a previsão teórica $b \approx b_0 \frac{m_0}{\mu}$ (0.14 fm para ^{12}C + ^{12}C e 0.13 fm para ^{16}O + ^{12}C).

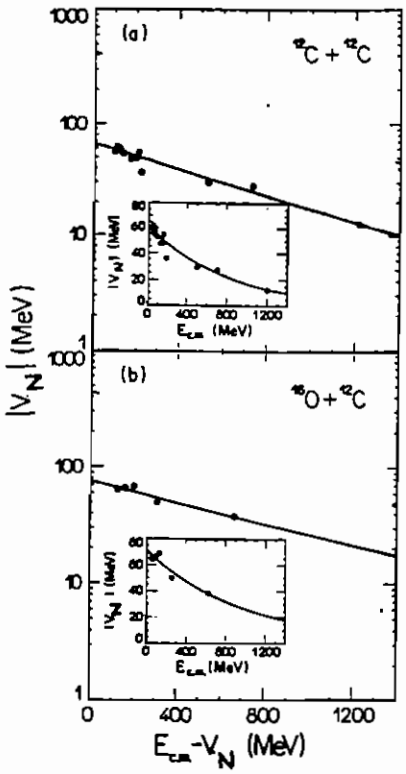

Figura III.4 – Dependência com a energia de potenciais nucleares fenomenológicos em $R = 4\,fm$, extraídos da análise de dados experimentais de espalhamento elástico para os sistemas: a) $^{12}C + ^{12}C$ e b) $^{16}O + ^{12}C$. As linhas cheias representam um ajuste linear, em que foram obtidos os valores dos respectivos parâmetros de alcance da não-localidade de Pauli (b).

Uma melhor aproximação da expressão III.9, válida inclusive para altas energias, é obtida por [Ch97]:

$$V_N(R,E) = \frac{1-\sqrt{1-4\gamma V_{Fold}(R)\, e^{-\gamma[E-V_C(R)]}}}{2\gamma}. \qquad \text{(III.11)}$$

Denominamos o potencial obtido através dessa expressão de interação NLM3Y [Ch98]. No limite de alcance nulo ($b \to 0$), o potencial NLM3Y se reduz ao potencial *Folding*, $V_N(R,E) = V_{Fold}(R)$. Com a utilização dessa aproximação para o potencial local equivalente, o problema da resolução das equações íntegro-diferenciais (III.6) se reduz à resolução das equações diferenciais (locais) de Schröedinger em ondas parciais:

$$-\frac{\hbar^2}{2\mu}\left[\frac{d^2}{dR^2}-\frac{\ell(\ell+1)}{R^2}\right]u_\ell(R)+\left[E-V_C(R)-V_N(R,E)-iW(R,E)\right]u_\ell(R)=0 \qquad \text{(III.12)}$$

Nós calculamos o potencial local-equivalente exato (segundo a equação III.7), resolvendo o conjunto de equações íntegro-diferenciais (III.6) para os sistemas ^{12}C + ^{12}C, ^{208}Pb e α +^{12}C, ^{58}Ni (nas energias correspondentes às figuras III.2 e III.3). O resultado nos convenceu de que a dependência desse potencial com a energia é realmente fraca. Os valores de intensidade obtidos para a parte imaginária são muito pequenos em comparação com os correspondentes valores da parte real. Também, as intensidades da parte real do potencial local-equivalente concordam com a expressão III.11 (interação NLM3Y), dentro de aproximadamente 3%, para todo valor de R (com exceção de regiões muito internas, $R \approx 0$). Ainda mais, as distribuições angulares de espalhamento elástico obtidas com a resolução da equação de Schröedinger local (III.12) utilizando o potencial NLM3Y, apresentam valores de seção de choque muito próximos daqueles obtidos através da resolução exata do conjunto de equações íntegro-diferenciais (III.6). Nesse sentido, consideramos que a utilização do potencial NLM3Y (expressão III.11) simula com precisão satisfatória os efeitos da não-localidade de Pauli em sistemas de íons pesados.

A figura III.5 mostra o potencial NLM3Y (linhas cheias) para o sistema ^{12}C + ^{12}C em três energias e, também, o respectivo potencial *Double-Folding* (linha tracejada). Para a mais alta energia (2400 *MeV*), as intensidades dos potenciais NLM3Y e *Folding* diferem de aproximadamente 1 ordem de grandeza; enquanto que para a energia mais baixa (112 *MeV*), e grandes distâncias de interação ($R \geq 4\ fm$), tais intensidades são aproximadamente iguais. É importante observar que, para sistemas de íons pesados em energias em torno da barreira coulombiana, $E \approx V_C(R_B)$, e distâncias de interação próximas ao raio da barreira, $R \approx R_B$, a expressão III.11 implica que $V_N(R, E) \approx V_{Fold}(R)$. Isso fica claro considerando que, para essas distâncias, o

potencial *Folding* têm ordem de grandeza de $1\,MeV$ e, portanto, $|\gamma V_{Fold}(R \approx R_B)| << 1$. Nessa região de baixas energias, o espalhamento é determinado pelo potencial em distâncias de interação próximas ao raio da barreira. Então, o efeito da não-localidade de Pauli é desprezível para energias próximas da barreira coulombiana, e considerar a parte real do potencial ótico igual ao potencial *Folding* deveria produzir um bom ajuste de dados experimentais. Isso deveria ser válido nos casos em que a parte real do potencial de polarização puder ser desprezada (observe que essa condição foi imposta no início desse capítulo, através da expressão III.1). Essas considerações serão utilizadas no próximo capítulo, em que apresentaremos um método experimental para determinação do potencial nuclear entre íons pesados, através da análise de dados experimentais de espalhamento elástico em energias subcoulombianas.

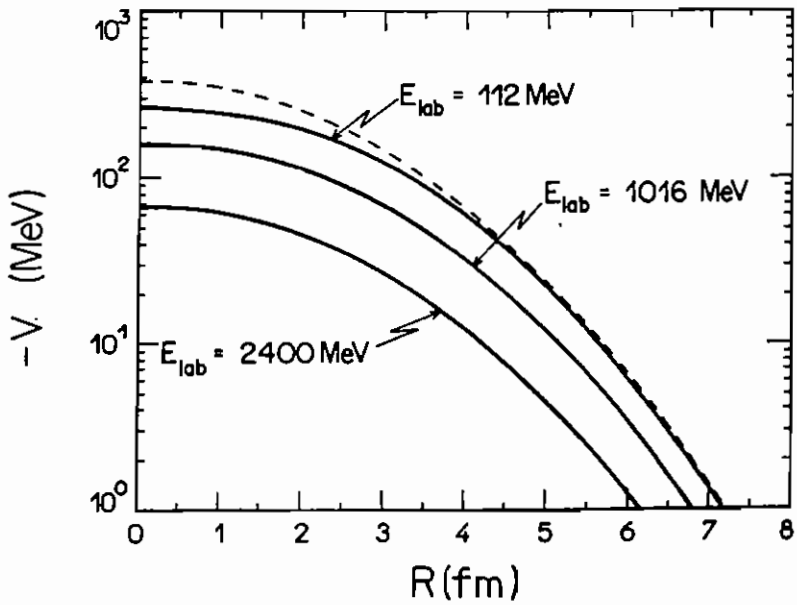

Figura III.5 – O potencial NLM3Y (linhas sólidas) para o sistema $^{12}C + ^{12}C$ em três energias de bombardeio. A linha tracejada corresponde ao potencial *Double-Folding*.

III.3 – A Parte Imaginária do Potencial Ótico

Para testar nosso modelo mais profundamente, buscamos determinar a parte absortiva do potencial sem a utilização de parâmetros livres para o ajuste de dados. Um modelo para essa parte imaginária do potencial de polarização, conhecido como teoria de espalhamento múltiplo de Glauber [Gl70], foi desenvolvido para energias suficientemente altas, em que são satisfeitas as seguintes condições: i) a energia cinética da partícula incidente excede grandemente a magnitude do potencial, e ii) o comprimento de onda da partícula é muito menor que um comprimento característico do potencial (esse comprimento é da ordem de magnitude da difusividade do potencial, ou seja, aproximadamente 0.5 *fm*). Nestas condições, pode ser considerado que toda a absorção de fluxo do canal elástico provém de processos elementares de espalhamento núcleon-núcleon, os quais ocorrem na superposição das densidades dos núcleos em colisão. Isto corresponde a desconsiderar processos de reação em que são envolvidos mais de dois núcleons, tais como excitações coletivas dos núcleos. Nesta aproximação, os únicos ingredientes necessários nos cálculos são as seções de choque de espalhamento núcleon-núcleon, e as densidades de matéria dos núcleos alvo (ρ_T) e projétil (ρ_P). O potencial imaginário é calculado (vide figura III.6) por [Ho88, Hu91]:

$$W(R,E) = -\frac{\hbar v}{2}\bar{\sigma}_{NN}(E_N)\int \rho_P(|\vec{R}-\vec{r}_T|)\,\rho_T(r_T)\,d\vec{r}_T\,, \qquad \text{(III.13)}$$

onde v é a velocidade relativa entre os dois núcleos, e $\bar{\sigma}_{NN}$ é a seção de choque total média para espalhamento núcleon-núcleon, obtida das seções de choque experimentais dos sistemas próton-próton e próton-nêutron, na energia E_N (igual à energia de bombardeio do sistema íon-íon dividida pelo número de núcleons do projetil). Sobre esse cálculo devem ser levadas em conta duas

importantes correções, devido aos efeitos do "Bloqueio de Pauli" e do "Movimento de Fermi". O procedimento para realizar tais correções está amplamente discutido na referência Ho88.

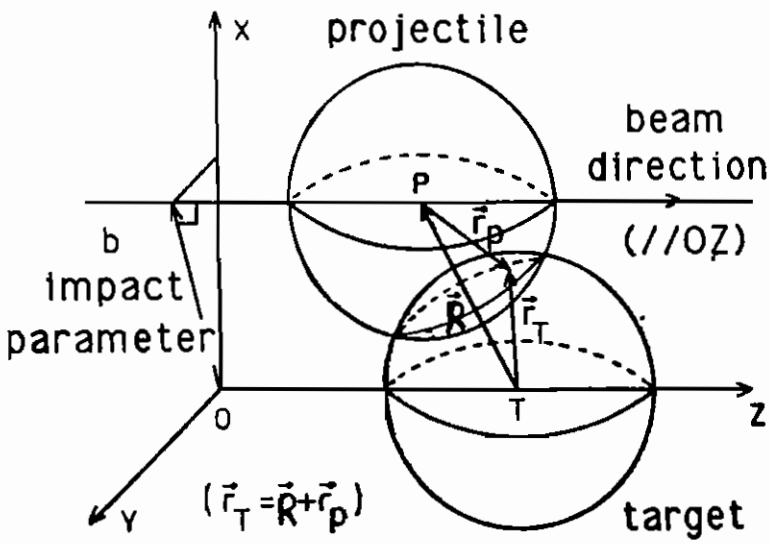

Figura III.6 – Vista esquemática dos núcleos alvo e projétil em colisão, e definição das coordenadas para o cálculo da parte imaginária do potencial de polarização (extraída da referência Ho88).

Nesta seção também iremos mostrar análises de dados de espalhamento inelástico. As análises foram realizadas através de cálculos DWBA, com o seguinte fator de forma para o potencial de acoplamento:

$$F(R) = \delta \left(\frac{\partial V_N(R,E)}{\partial R} + i \frac{\partial W(R,E)}{\partial R} \right), \qquad \text{(III.14)}$$

onde δ é o comprimento de deformação do estado excitado. Como a região de energia analisada é bastante alta, nós desprezamos a excitação coulombiana. Na equação III.14, $V_N(R,E)$ foi tomado como sendo o potencial NLM3Y, e $W(R,E)$ corresponde ao potencial imaginário sem parâmetros livres discutido acima.

A figura III.7 apresenta dados de espalhamentos elástico e inelástico (estado 2^+, com energia de excitação de 4.4 MeV) para o sistema $^{12}C + ^{12}C$. As linhas cheias correspondem às previsões (não mais ajustes, pois não existem parâmetros livres no cálculo) de seções de choque, em que, para compor o potencial ótico, foram utilizados o potencial real NLM3Y e o já discutido potencial imaginário sem parâmetros livres. O valor do comprimento de deformação do estado excitado foi obtido da referência Ho88. Para as duas energias mais baixas, a concordância entre valores teóricos e experimentais é extraordinária (considerando não haver parâmetros livres). Para a energia mais alta (2400 *MeV*), as previsões teóricas reproduzem a magnitude dos dados, porém apresentam um comportamento oscilatório mais pronunciado. Acreditamos que efeitos relativísticos, não incluídos no modelo, poderiam ser responsáveis por essa discrepância, pois para essa energia a velocidade relativa entre os íons é aproximadamente 65% da velocidade da luz.

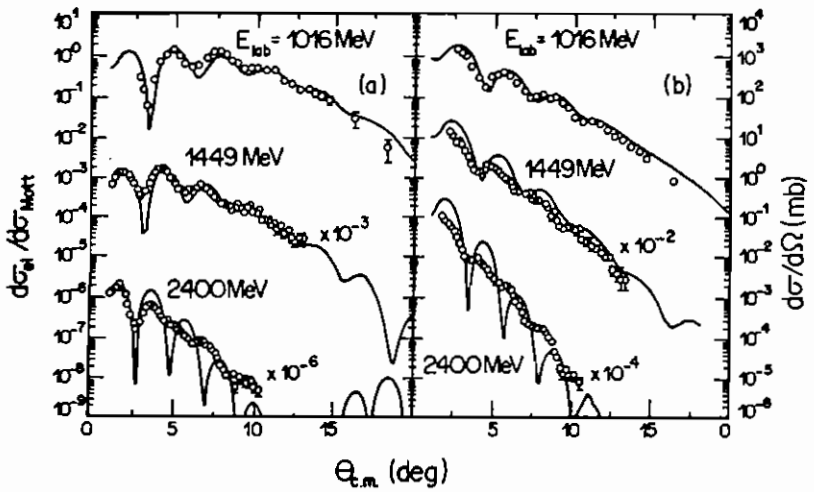

Figura III.7 – Seções de choque diferenciais de espalhamento elástico (a) e inelástico (b) para o sistema $^{12}C + ^{12}C$ nas energias indicadas. As linhas cheias são previsões obtidas com o potencial NLM3Y, sem a utilização de nenhum parâmetro livre para o ajuste dos dados. Os dados foram extraídos das referências Ho88 e Bu84.

Realizamos [Ch98] cálculos semelhantes também para o sistema $^{11}Li + ^{12}C$, de forma a testarmos nosso modelo para núcleos exóticos. Devido à pouca resolução em energia do feixe (núcleo exótico), para esse sistema foram obtidos [Ko92] dados de espalhamento quase-elástico (inclui o espalhamento elástico e os espalhamentos inelásticos para os estados excitados 2^+ e 3^- do núcleo ^{12}C), na energia de 637 *MeV*. A figura III.8 mostra uma comparação entre dados experimentais e previsões teóricas (linha cheia). Nossos resultados são muito semelhantes aos obtidos [Kh95] com a interação dependente da densidade (e energia), em que foram utilizados três parâmetros livres para ajuste de dados na parte imaginária do potencial ótico. Assim, consideramos nosso resultado bastante razoável, sendo que há espaço para aperfeiçoamentos considerando termos de ordem mais alta na teoria de múltiplo espalhamento em $W(R,E)$, posto que os nêutrons de valência do ^{11}Li são fracamente ligados. Também é possível que os dados experimentais incluam seções de choque de outros processos de reação [Ko98], que não foram incluídos em nossos cálculos.

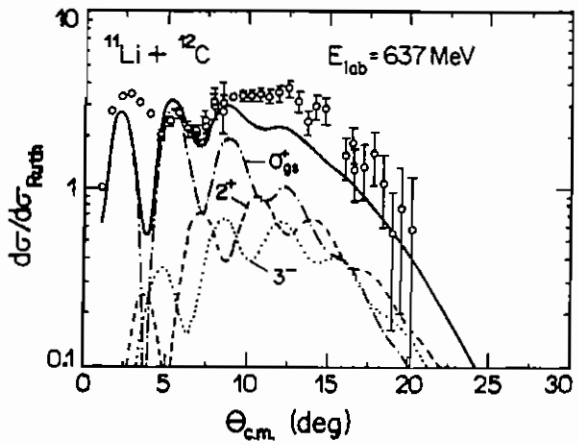

Figura III.8 – Seções de choque de espalhamento quase-elástico para o sistema $^{11}Li + ^{12}C$. A linha cheia corresponde à soma das previsões teóricas, utilizando o potencial NLM3Y, para as seções de choque de espalhamento elástico e inelástico. As demais linhas correspondem às seções de choque para cada canal, como indicado.

Concluímos este capítulo enfatizando que nossas análises têm demonstrado a grande importância de levar em consideração a não-localidade de Pauli na descrição da interação núcleo-núcleo. O potencial NLM3Y parece adequado como aproximação para essa interação, tendo em vista sua simplicidade de obtenção (expressão III.11) e facilidade de utilização (resolvendo a equação diferencial de Schröedinger), bem como a boa precisão dos resultados (seções de choque) obtidos com seu uso.

IV - UM MÉTODO EXPERIMENTAL PARA A DETERMINAÇÃO DO POTENCIAL NUCLEAR

Como discutido nos capítulos anteriores, a determinação do potencial nuclear entre íons pesados, através da análise de dados experimentais em energias em torno (acima) da barreira coulombiana, é sujeita a muitas ambigüidades, devido à grande complexidade do tratamento teórico dos muitos canais de reação. Neste capítulo, será apresentado um método que permite extrair o potencial nuclear de forma muito menos ambígua. Para energias de alguns *MeV* abaixo da barreira coulombiana, quase todos os canais de reação têm seções de choque desprezíveis. Assim, nessa região de energia, a complexidade do tratamento teórico advinda dos canais de reação é muito diminuída em comparação com regiões de energia acima da barreira. Isto permite que o potencial de interação entre íons pesados seja extraído da análise de dados de espalhamento elástico (e, eventualmente, dos poucos canais de reação relevantes) em energias subcoulombianas. Cópias dos artigos de nossa autoria, em que esse método foi aplicado (referências Ch95, Ch96 e Al99), estão anexas no final do texto.

IV.1 – Os Dados Experimentais e os Canais de Reação Relevantes

Os sistemas $^{16}O + ^{58, 60, 62, 64}Ni$ foram os primeiros em que foram obtidos os respectivos potenciais nucleares através do método que estamos discutindo. Em seguida, também foram estudados os sistemas $^{16}O + ^{88}Sr$, $^{90,92}Zr$, ^{92}Mo. Para todos esses sistemas, em energias subcoulombianas, além do canal elástico somente um canal de reação tem seção de choque relevante: o espalhamento inelástico para o primeiro estado excitado (2_1^+) do alvo. Os

dados experimentais foram obtidos no Laboratório Pelletron do IFUSP, utilizando um conjunto de nove detectores de barreira de superfície, com espaçamento angular de 5° para cada par. Os alvos eram constituídos de uma camada de aproximadamente 30 μg/cm^2 do alvo correspondente (níquel, estrôncio, zircônio ou molibdênio), sobre a qual foi aplicada uma camada de 50 μg/cm^2 de ouro (^{197}Au) com o objetivo de normalização dos dados (nas energias estudadas, a seção de choque de espalhamento elástico de oxigênio em ouro é praticamente idêntica à seção de choque de Rutherford). Para sistemas com núcleos alvo de níquel, os dados foram obtidos na região de energia $34 \leq E_{Lab} \leq 38\,MeV$; para os demais sistemas a região estudada foi $43 \leq E_{Lab} \leq 49\,MeV$. Para ambos conjuntos de sistemas, a região de energia de bombardeio corresponde a uma faixa de 4 até 8 *MeV* abaixo da respectiva barreira de fusão (tais barreiras foram obtidas das referências: Bo92, Be93 e Si97). A resolução em energia dos espectros foi de aproximadamente 200 *keV*, que possibilitou uma completa separação entre os picos correspondentes aos canais elástico e inelástico (figura IV.1). O pequeno "fundo" de espalhamento presente nos espectros foi subtraído da taxa de contagem dos picos.

Na região de energia em que os dados foram obtidos, as seções de choque diferenciais de espalhamento inelástico (para o estado 2_1^+ do alvo) têm ordem de magnitude de 1% das correspondentes seções de choque de espalhamento elástico, e as respectivas seções de choque integradas variam entre 5 e 50 *mb*. Não foi encontrada, nos espectros, nenhuma evidência de outros processos de espalhamento inelástico com seções de choque próximas daquelas para o estado 2_1^+. Também os processos de transferência de núcleons e fusão nuclear [An73, Bo92, Be93, Si97, Ro97] têm seções de choque muito inferiores daquelas de espalhamento para o primeiro estado excitado do alvo.

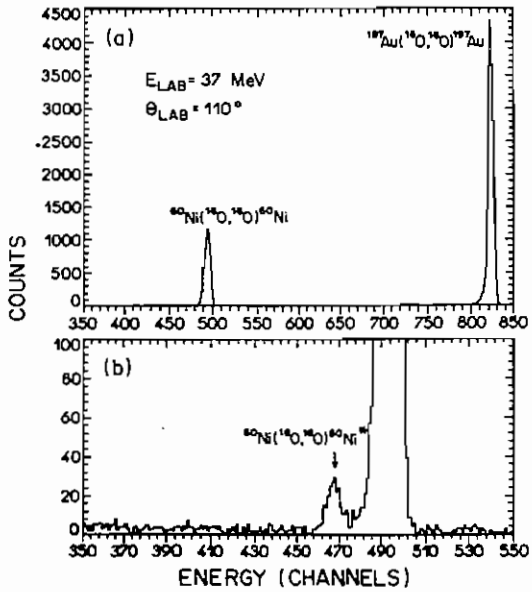

Figura IV.1 – a) Espectro de energia característico das experiências. Os picos correspondem aos processos de espalhamento elástico para os sistemas $^{16}O + ^{60}Ni$, ^{197}Au, como indicado. b) Expansão de ambos os eixos na região do pico de espalhamento elástico do sistema $^{16}O + ^{60}Ni$. A flecha indica o pico correspondente à excitação inelástica para o estado 2_1^+ ($E^* = 1.33$ *MeV*) do níquel.

IV.2 – Os Cálculos de Canais Acoplados

Os potenciais nucleares foram obtidos através da análise de canais acoplados dos dados de espalhamento elástico e inelástico (estado 2_1^+). Os núcleos alvos foram assumidos esfericamente simétricos, mas suscetíveis a vibrações em torno de suas formas esféricas (modelo vibracional) [Ta65, Th88]. Para o raio coulombiano dos núcleos, assumimos a expressão $R_C = r_C\, A^{1/3}$, com $r_C = 1.06\, fm$, proveniente de uma extensa sistemática de experimentos de espalhamento de elétrons [DJ74]. Para os sistemas $^{16}O + ^{58,60,62,64}Ni$, as amplitudes de acoplamento coulombiano (β_C) e nuclear (β_N) foram variadas de forma a ajustar os dados experimentais. Os valores

obtidos encontram-se na tabela IV.1. Os valores deduzidos (equação IV.1) para B(E2) são compatíveis com aqueles encontrados na referência Ra87, os quais são resultantes de uma compilação de dados obtidos usando técnicas diversas, em um grande número de experiências. Os valores obtidos para os comprimentos de deformação coulombiano ($\delta_C = \beta_C R_C$) são próximos dos correspondentes valores nucleares, que é um indicativo da consistência de nossos resultados. Para os sistemas ^{16}O + ^{88}Sr, $^{90,92}Zr$, ^{92}Mo, os dados de espalhamento inelástico estão um pouco "contaminados" devido à subtração do "fundo" dos espectros. Assim sendo, para esses sistemas assumimos os valores das amplitudes de acoplamento das referências Ra87, Es89, Lu95. Outros detalhes acerca do cálculo de canais acoplados que realizamos podem ser encontrados nas referências Ch95, Ch96 e Al99.

$$B(E\lambda)\uparrow = \frac{(2J_{final}+1)}{(2J_{inicial}+1)} B(E\lambda)\downarrow = \frac{2J_{final}+1}{(2J_{inicial}+1)(2\lambda+1)} \left(\frac{3eZ}{4\pi} \beta_C R_C^{\lambda} \right)^2 \qquad \text{(IV.1)}$$

Tabela IV.1 – As amplitudes de acoplamento coulombiano (β_C) e nuclear (β_N), e os correspondentes comprimentos de deformação (δ_C e δ_N), obtidos através da análise de canais acoplados dos dados experimentais. Também estão incluídos os valores deduzidos para B(E2), em unidades $e^2 fm^4$.

Núcleo	β_C	β_N	B(E2)	δ_C (*fm*)	δ_N (*fm*)
^{58}Ni	0.233 ± 0.006	0.22 ± 0.03	688 ± 34	0.96 ± 0.03	0.90 ± 0.12
^{60}Ni	0.265 ± 0.010	0.26 ± 0.03	931 ± 70	1.10 ± 0.04	1.08 ± 0.12
^{62}Ni	0.247 ± 0.010	0.17 ± 0.03	845 ± 68	1.04 ± 0.04	0.71 ± 0.13
^{64}Ni	0.218 ± 0.008	0.19 ± 0.03	686 ± 50	0.87 ± 0.03	0.76 ± 0.12

IV.3 – A Extração dos Potenciais Através da Análise dos Dados

Os potenciais óticos foram extraídos das análises de dados para regiões de distâncias de interação superficiais, que para os sistemas estudados significam $R \approx 11\,fm$. Nos cálculos de canais acoplados, foi levada em conta explicitamente toda a absorção de fluxo do canal elástico pelo único canal de reação com seção de choque relevante. Assim sendo, para a parte imaginária do potencial ótico utilizamos uma forma Woods-Saxon (equação II.9), com parâmetros tais que qualquer absorção superficial adicional é desprezível. Utilizamos: $R_I = 0.8\,(A_P^{1/3} + A_A^{1/3})\,fm$ (A_P e A_A são os números de massa do projétil e alvo), $a_I = 0.2\,fm$ e $W_0 = 30\,MeV$. Na região de distâncias de interação maiores que 9 *fm*, a intensidade desse potencial imaginário é menor que 1 *eV*. Entretanto, fica garantida qualquer pequena absorção interna (relacionada com a fusão nuclear). É importante ressaltar que as previsões de seção de choque dos cálculos de canais acoplados são insensíveis a variações dos parâmetros da parte imaginária do potencial ótico (desde que observada a condição de ausência de absorção superficial). Desejo enfatizar que a escolha desses parâmetros não é arbitrária, mas determinada pelas "condições de contorno" do problema em questão.

Também assumimos uma forma tipo Woods-Saxon (equação IV.1) para a parte real do potencial ótico. Para a região de distâncias de interação superficial ($R \approx 11\,fm$), as previsões do potencial *Double-Folding* indicam que o potencial nuclear tem uma forma muito semelhante à uma exponencial. Assim sendo, assumimos o parâmetro R_0 igual à soma dos raios coulombianos dos núcleos alvo e projétil. Para todos os sistemas estudados temos $R_0 << 11\,fm$, que implica na requerida forma exponencial do potencial na

região superficial. Nossas análises têm indicado que mudanças nos valores adotados para R_0 não alteram os resultados que iremos discutir a seguir.

$$V(R) = \frac{-V_0}{1 + \exp\left[\frac{R - R_0}{a}\right]} \qquad \text{(IV.1)}$$

Para cada sistema e cada energia de bombardeio, utilizamos o seguinte procedimento no ajuste das respectivas distribuições angulares (elástico e inelástico). Atribuímos diversos valores para a difusividade (a) e, para cada um desses valores, obtivemos a profundidade do potencial (V_0) através do ajuste dos dados experimentais. Encontramos uma "família" de potenciais que produzem ajustes igualmente bons (mesmos chi-quadrados). Os potenciais cruzam-se em um particular raio (R_S), como ilustrado na figura IV.1a para o sistema ^{16}O + ^{60}Ni em diversas energias. Nas análises de dados em energias acima da barreira, esse ponto é denominado "raio de absorção forte". Devido à pequena absorção envolvida nas energias subcoulombianas, neste trabalho iremos referir à R_S como "raio de sensibilidade". Estimamos a barra de erro da intensidade do potencial no raio de sensibilidade, variando V_0 em torno do seu melhor valor (que fornece o menor chi-quadrado), e considerando variações de uma unidade no valor do chi-quadrado. Para ilustrar a sensibilidade desse procedimento, a figura IV.2 mostra como tais ajustes, indicados por linhas tracejadas, desviam-se dos dados experimentais.

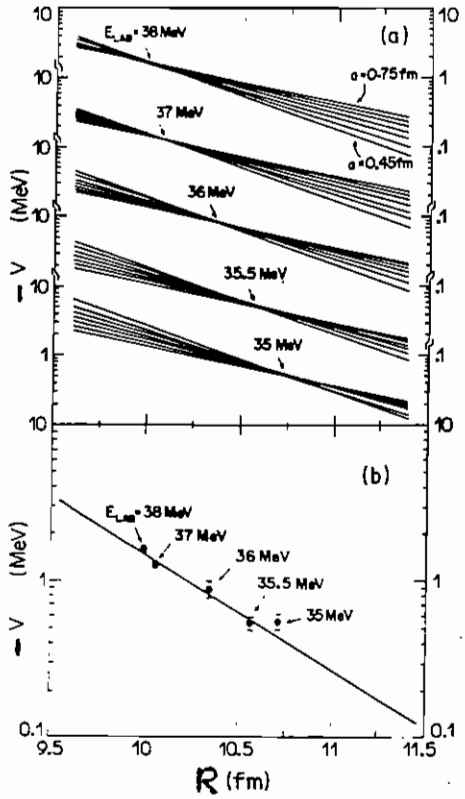

Figura IV.1 – a) A parte real do potencial ótico na região superficial de distâncias de interação, obtida através do ajuste de dados experimentais para diferentes valores de difusividade. Para cada energia os potenciais cruzam no raio de sensibilidade. b) Os pontos representam a intensidade da parte real do potencial ótico no raio de sensibilidade. A linha corresponde à uma exponencial com difusividade de 0.58 *fm*.

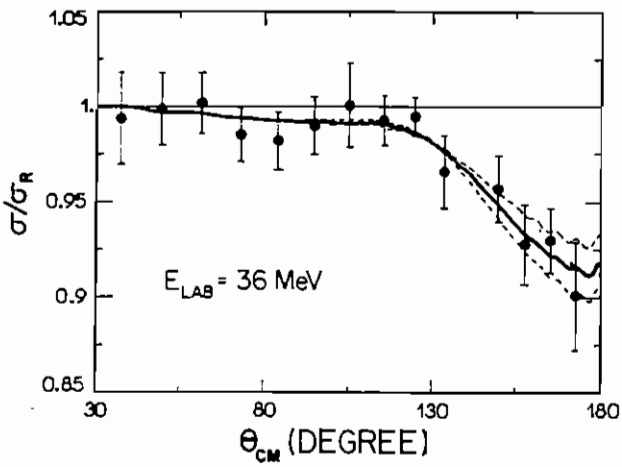

Figura IV.2 – Distribuição angular de espalhamento elástico para o sistema ^{16}O + ^{60}Ni, na energia indicada. A linha cheia corresponde ao melhor ajuste ($\chi^2 = 9.7$) obtido com os cálculos de canais acoplados. As linhas tracejadas representam os ajustes provenientes da variação de V_0, considerando aumento de uma unidade em χ^2.

Para energias acima da barreira, tem sido observado para vários sistemas que o raio de absorção forte é praticamente independente da energia. Por exemplo, para o sistema $^{16}O + ^{60}Ni$ a variação é de apenas 0.3 *fm* numa ampla região de energia, que estende-se por aproximadamente 100 *MeV* [Fu85]. Na região de energia que estamos estudando, porém, o raio de sensibilidade apresenta forte dependência com a energia, de maneira similar ao ponto de retorno clássico. Nossas análises indicam uma variação de aproximadamente 0,7 *fm* em apenas 3 *MeV*, como ilustrado na figura IV.1b. Esse comportamento permite caracterizar a forma do potencial. Para o sistema $^{16}O + ^{60}Ni$, o potencial tem forma exponencial (linha cheia da figura IV.1b) com difusividade $a = (0{,}58 \pm 0{,}04)$ *fm*. Obtivemos resultados semelhantes para todos os sistemas (figuras IV.3 e IV.4). A tabela IV.2 fornece os respectivos valores de difusividade. Para cada conjunto de sistemas, os valores da difusividade são compatíveis com um valor médio: $\bar{a} = (0{,}59 \pm 0{,}02)$ *fm* e $\bar{a} = (0{,}64 \pm 0{,}02)$ *fm* para os sistemas $^{16}O + ^{58,60,62,64}Ni$ e $^{16}O + ^{88}Sr, ^{90,92}Zr, ^{92}Mo$, respectivamente. Como veremos adiante, esses valores concordam com as previsões dos potenciais *Folding*. Usando as difusividades médias, para cada sistema ajustamos todas as distribuições angulares com um potencial independente da energia. Para efeito de comparação, a tabela IV.2 fornece as intensidades dos potenciais no raio $\bar{R} = 10.7$ *fm*, que está aproximadamente no centro da região de sensibilidade para todos os sistemas estudados. As figuras IV.5 até IV.12 mostram os dados experimentais e os respectivos ajustes (os valores dos chi-quadrados reduzidos encontram-se na tabela IV.2).

Tabela IV.2 – Valores da difusividade e da intensidade (em $\overline{R} = 10.7\ fm$) da parte real dos potenciais de canais acoplados. Também estão indicados os valores do chi-quadrado reduzido, obtidos com o ajuste de todas as distribuições angulares, utilizando um potencial ótico independente da energia para cada sistema.

Núcleo Alvo	a (fm)	$V(\overline{R})\ (MeV)$	χ^2_{red}
^{58}Ni	0.57 ± 0.03	0.351 ± 0.009	1.2
^{60}Ni	0.58 ± 0.04	0.447 ± 0.008	1.2
^{62}Ni	0.60 ± 0.05	0.502 ± 0.019	1.0
^{64}Ni	0.67 ± 0.05	0.600 ± 0.010	1.2
^{88}Sr	0.71 ± 0.05	1.44 ± 0.05	2.3
^{90}Zr	0.63 ± 0.03	1.55 ± 0.03	2.1
^{92}Zr	0.61 ± 0.05	1.92 ± 0.06	2.8
^{92}Mo	0.63 ± 0.06	1.57 ± 0.03	2.2

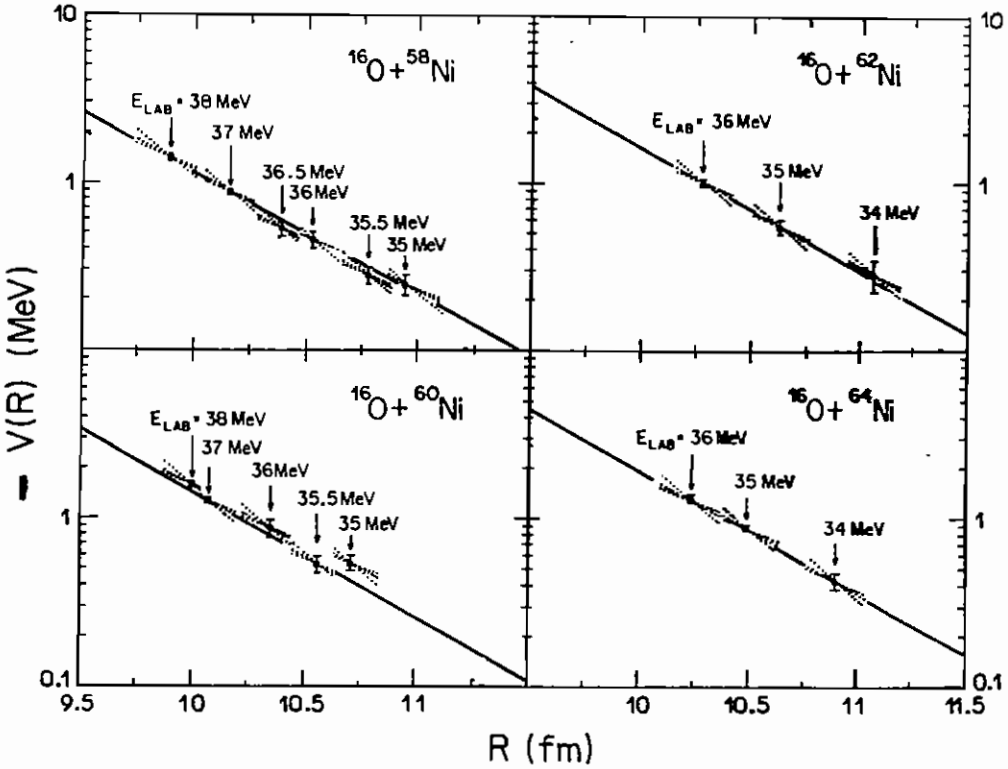

Figura IV.3 – A parte real do potencial ótico na região superficial para os sistemas $^{16}O + ^{58,60,62,64}Ni$, como obtido das análises de canais acoplados dos dados experimentais para diversas difusividades. As linhas cheias representam exponenciais com a difusividade média $\bar{a} = 0.59\ fm$.

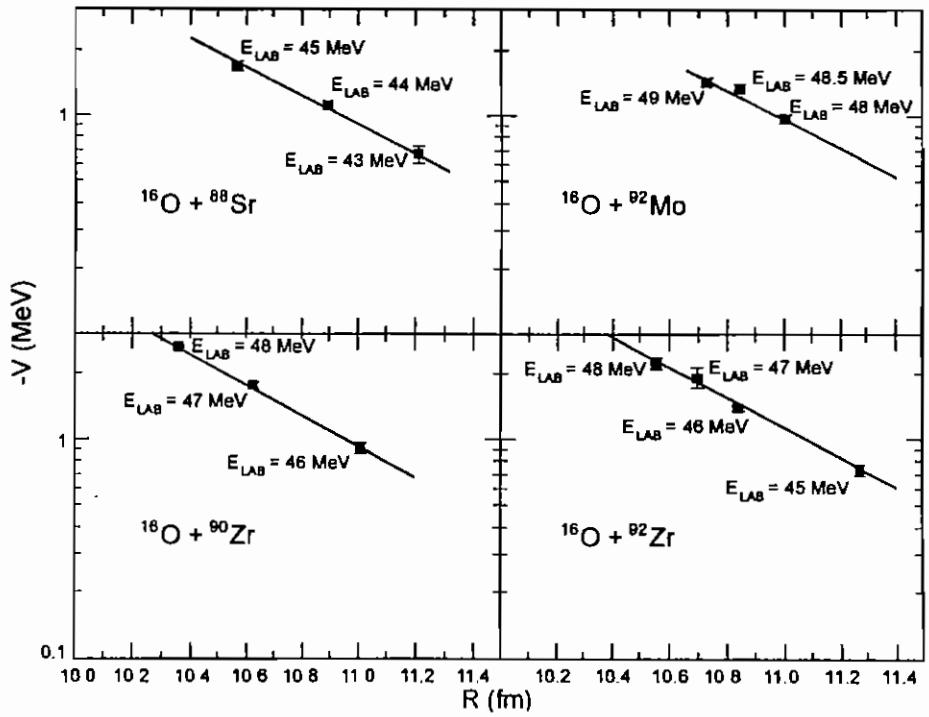

Figura IV.4 – A parte real do potencial ótico na região superficial para os sistemas $^{16}O + ^{88}Sr$, $^{90,\ 92}Zr$, ^{92}Mo, como obtido das análises de canais acoplados dos dados experimentais. As linhas representam exponenciais com a difusividade média $\bar{a} = 0.64\ fm$.

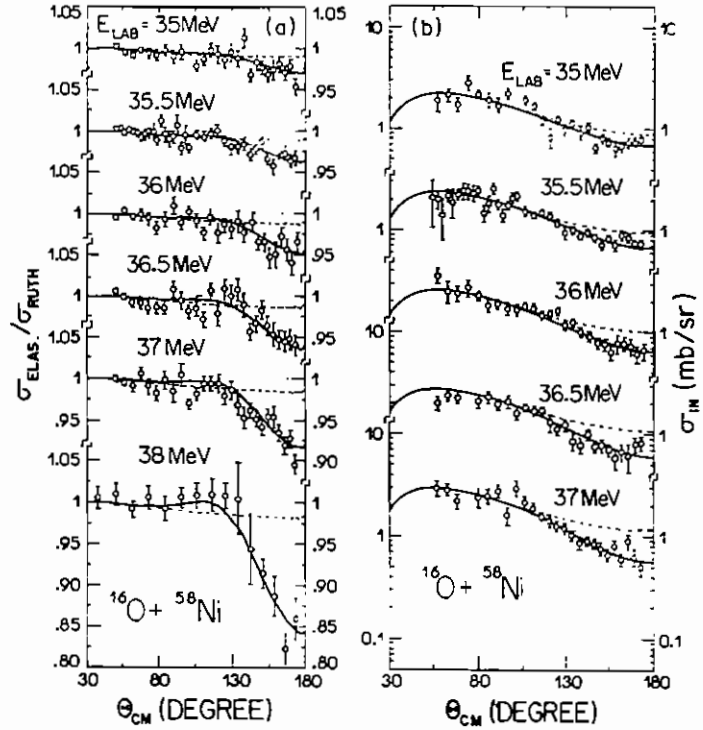

Figura IV.5 – Distribuições angulares de espalhamento elástico (a) e inelástico (b) para o sistema $^{16}O + ^{58}Ni$. As curvas correspondem a cálculos de canais acoplados considerando apenas a interação coulombiana (linha tracejada) e a coulombiana mais nuclear (linha cheia).

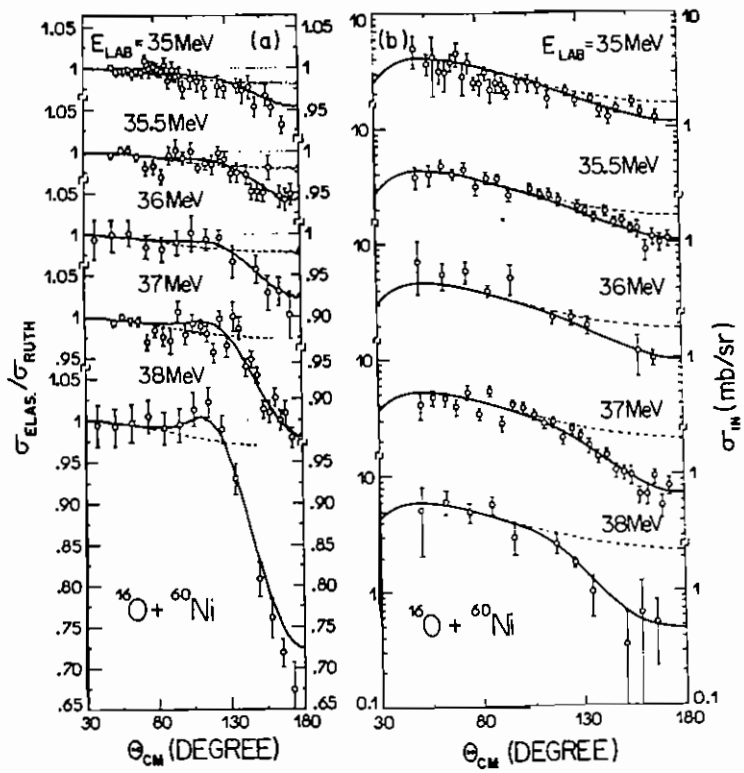

Figura IV.6 – O mesmo da figura IV.5, para o sistema $^{16}O + ^{60}Ni$.

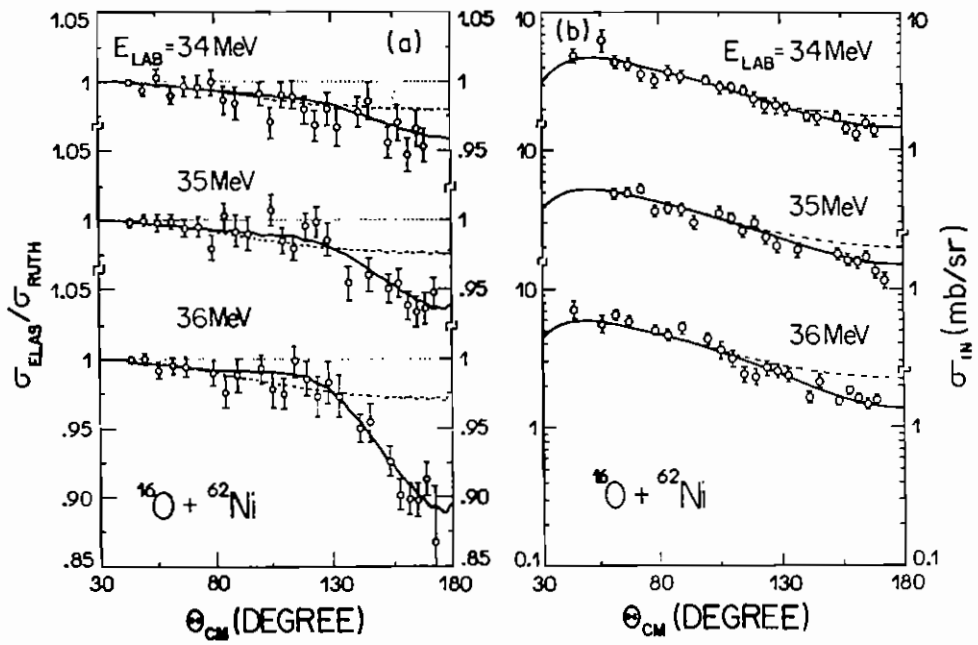

Figura IV.7 – O mesmo da figura IV.5, para o sistema $^{16}O + ^{62}Ni$.

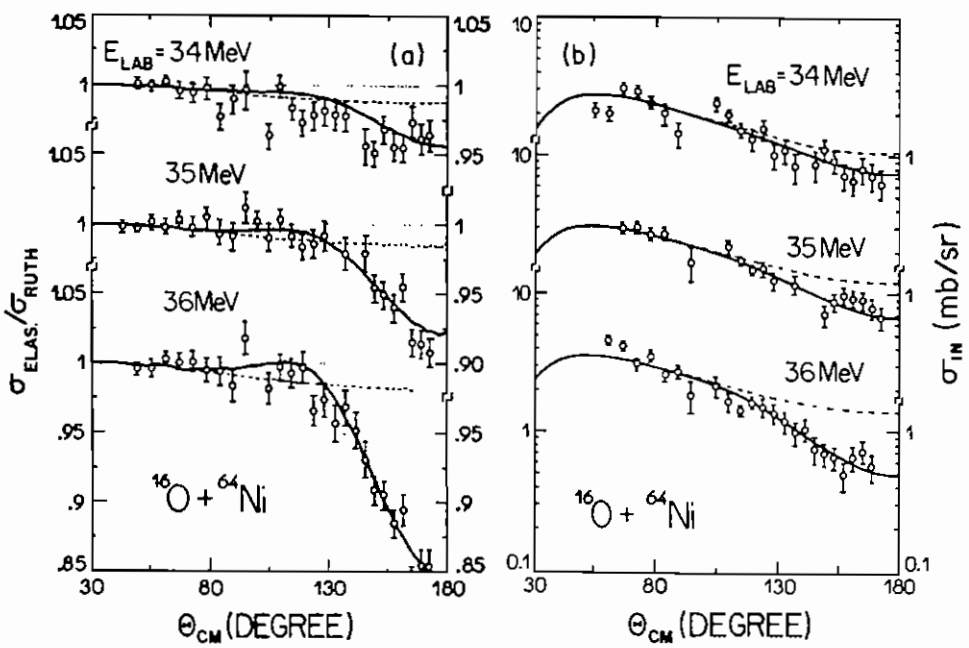

Figura IV.8 – O mesmo da figura IV.5, para o sistema $^{16}O + ^{64}Ni$.

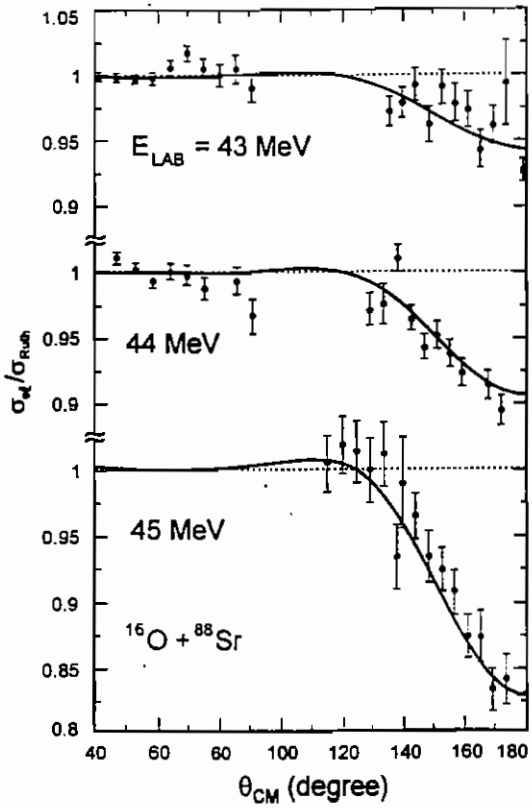

Figura IV.9 - Distribuições angulares de espalhamento elástico para o sistema $^{16}O + ^{88}Sr$. As linhas cheias correspondem a cálculos de canais acoplados.

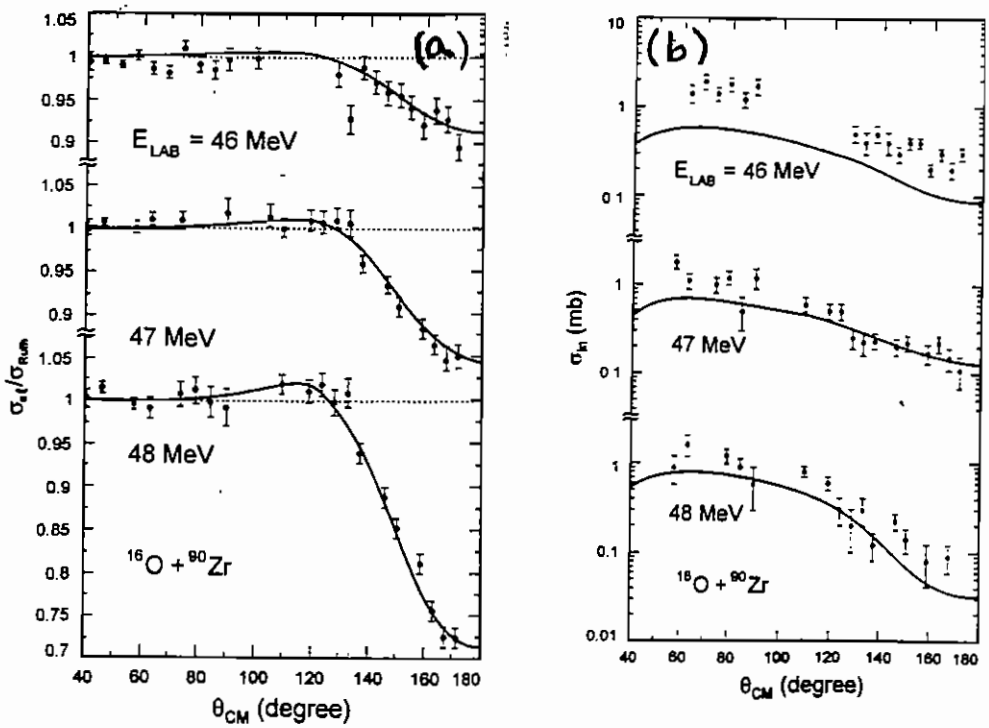

Figura IV.10 - Distribuições angulares de espalhamento elástico (a) e inelástico (b) para o sistema $^{16}O + ^{90}Zr$. As linhas cheias correspondem a cálculos de canais acoplados.

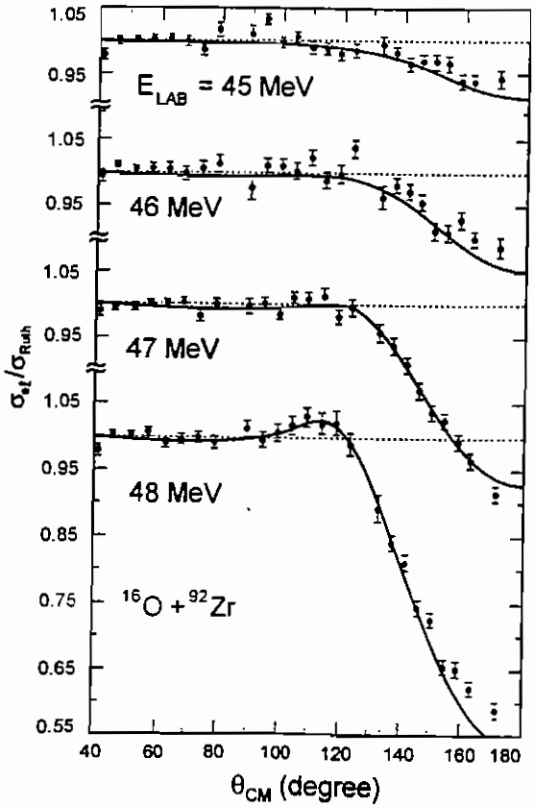

Figura IV.11 - Distribuições angulares de espalhamento elástico para o sistema $^{16}O + ^{92}Zr$. As curvas correspondem a cálculos de canais acoplados.

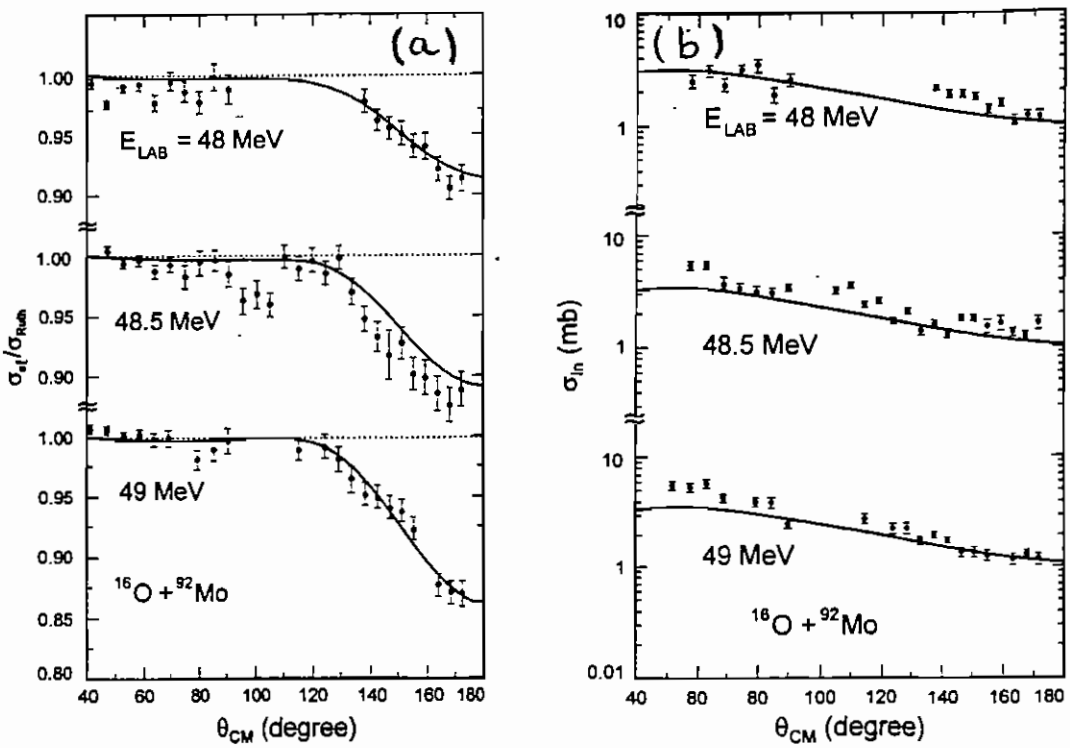

Figura IV.12 - Distribuições angulares de espalhamento elástico (a) e inelástico (b) para o sistema $^{16}O + ^{92}Mo$. As linhas cheias correspondem a cálculos de canais acoplados.

IV.4 – Comparação entre Potenciais "Experimentais" e "Teóricos"

No capítulo anterior foi enfatizado que, para energias em torno da barreira, o potencial local-equivalente NLM3Y é muito semelhante ao potencial *Double-Folding*. Assim, nesta seção iremos comparar os potenciais "experimentais" (isto é, extraídos da análise dos dados) com aqueles "teóricos" do tipo *Double-Folding*.

Em nossos cálculos, a densidade do estado fundamental do núcleo ^{16}O foi derivada de resultados experimentais de espalhamento de elétrons [DJ74], assumindo que as densidades de prótons e de nêutrons têm a mesma forma da densidade de carga. A densidade nuclear total é expressa por:

$$\rho_{Oxig.}(r) = \rho_0 \left[1 + \gamma \left(\frac{r}{c} \right)^2 \right] e^{-\left(\frac{r}{c}\right)^2}, \qquad \text{(IV.2)}$$

em que $\gamma = 1.554$, $c = 1.833\, fm$ (parâmetros de densidade de carga da referência DJ74) e $\rho_0 = 0{,}1407\, fm^{-3}$ para satisfazer a condição de normalização: $\int_0^\infty 4\pi\rho(r)\, r^2\, dr = N + Z = A$. (IV.3)

Para os núcleos alvos utilizamos densidades microscópicas oriundas de cálculos tipo *Shell-Model*. Tais cálculos predizem esquemas de níveis que concordam razoavelmente com resultados experimentais (figura IV.13). Com a finalidade de ilustrar certas características do potencial que discutiremos a seguir, escrevemos explicitamente a densidade nuclear total dos núcleos alvos (ρ_T) como uma soma da densidade de prótons (ρ_p) com a densidade de nêutrons (ρ_n).

$$\rho_T(r) = \rho_p(r) + \rho_n(r) \qquad \text{(IV.4)}$$

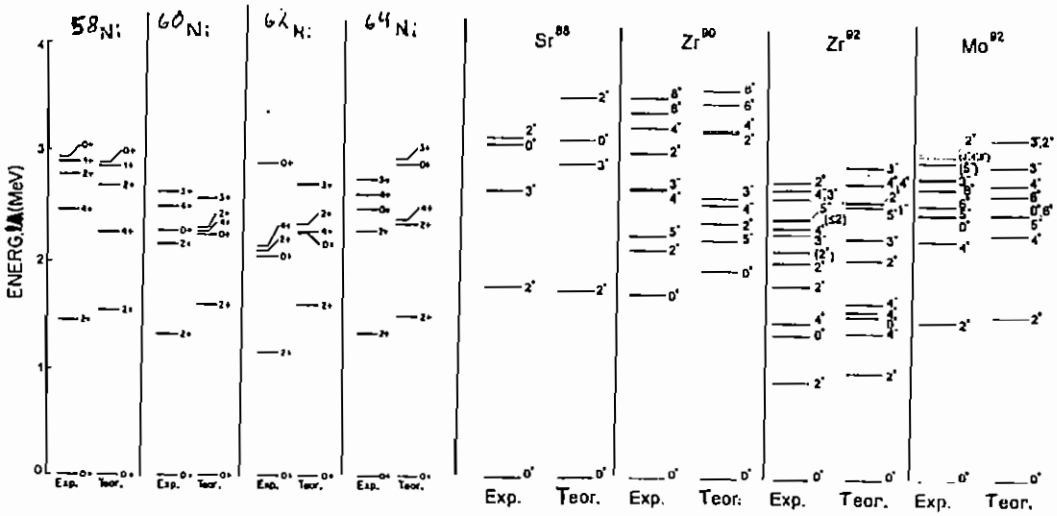

Figura IV.13 – Esquema de níveis de energia preditos por cálculos tipo *Shell-Model* em comparação com resultados experimentais.

Calculamos as contribuições das densidades de prótons e de nêutrons do alvo para o potencial *Folding* total, de acordo com as seguintes expressões:

$$V_p(R) = \iint \rho_{Oxig.}(r_1)\, v_0(\vec{R} - \vec{r}_1 + \vec{r}_2)\, \rho_p(r_2)\, d\vec{r}_1\, d\vec{r}_2\,, \qquad \text{(IV.5)}$$

$$V_n(R) = \iint \rho_{Oxig.}(r_1)\, v_0(\vec{R} - \vec{r}_1 + \vec{r}_2)\, \rho_n(r_2)\, d\vec{r}_1\, d\vec{r}_2\,, \qquad \text{(IV.6)}$$

$$V_{Fold}(R) = V_p(R) + V_n(R)\,. \qquad \text{(IV.7)}$$

A figura IV.14 mostra as densidades dos núcleos alvos (a) e os respectivos potenciais (b) para os sistemas ^{16}O + $^{58,\ 60,\ 62,\ 64}Ni$. Os isótopos de níquel (camada fechada $Z = 28$) têm densidades de prótons muito semelhantes e diferentes densidades de nêutrons. Assim, as diferenças observadas nos respectivos potenciais totais advém da contribuição dos nêutrons. Para os núcleos ^{88}Sr, $^{90,92}Zr$ e ^{92}Mo o número de nêutrons é significativamente maior que o número de prótons. Portanto, as densidades de nêutrons são um pouco mais externas que as correspondentes densidades de prótons (figura IV.15). Dessa maneira, a contribuição dos nêutrons para o potencial também é substancialmente maior que a dos prótons (figura IV.16). Os núcleos ^{88}Sr, ^{90}Zr

e ^{92}Mo (camada fechada $N = 50$) têm densidades de nêutrons muito semelhantes na região da superfície dos núcleos ($r \approx 6\ fm$), enquanto o núcleo ^{92}Zr (com 2 nêutrons extras) apresenta densidade de nêutrons aproximadamente 0,1 *fm* mais externa (figura IV.17). Dessa maneira, como veremos adiante, o potencial *Folding* para o sistema ^{16}O + ^{92}Zr apresenta intensidade maior que para os sistemas ^{16}O + ^{88}Sr, ^{90}Zr, ^{92}Mo.

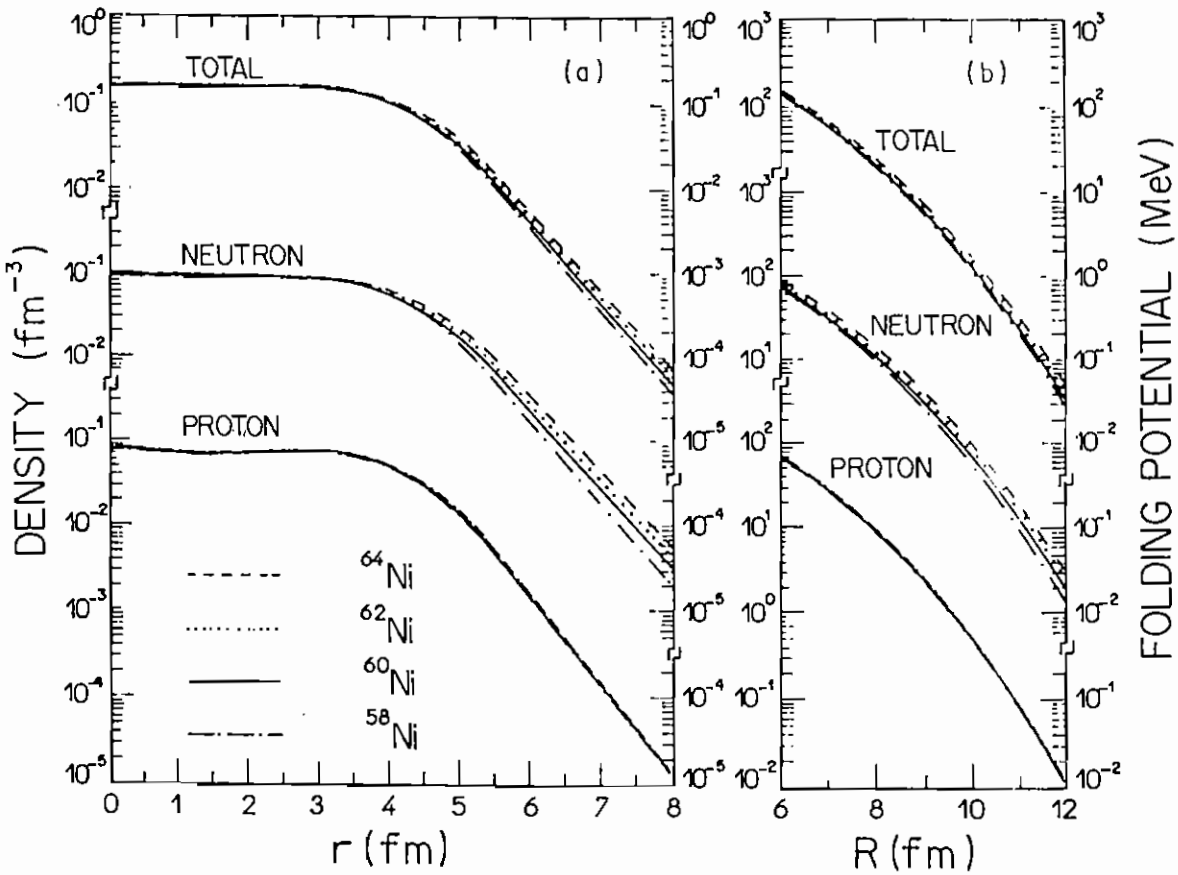

Figura IV.14 – a) As densidades total, de nêutrons e de prótons para os núcleos $^{58, 60, 62, 64}$Ni, derivadas de cálculos *Shell-Model*. b) Potenciais *Double-Folding* para os sistemas ^{16}O + $^{58, 60, 62, 64}$Ni, considerando separadamente as contribuições das densidades de nêutrons e de prótons dos isótopos de níquel.

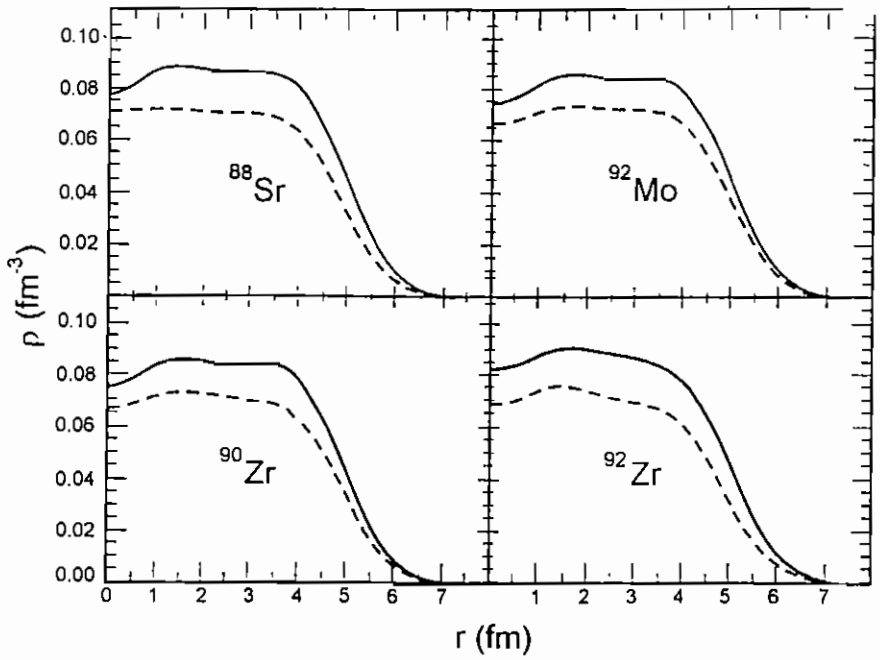

Figura IV.15 – As densidades de prótons (linhas tracejadas) e nêutrons (linhas cheias) derivadas de cálculos tipo *Shell-Model* para os núcleos ^{88}Sr, ^{90}Zr, ^{92}Zr e ^{92}Mo.

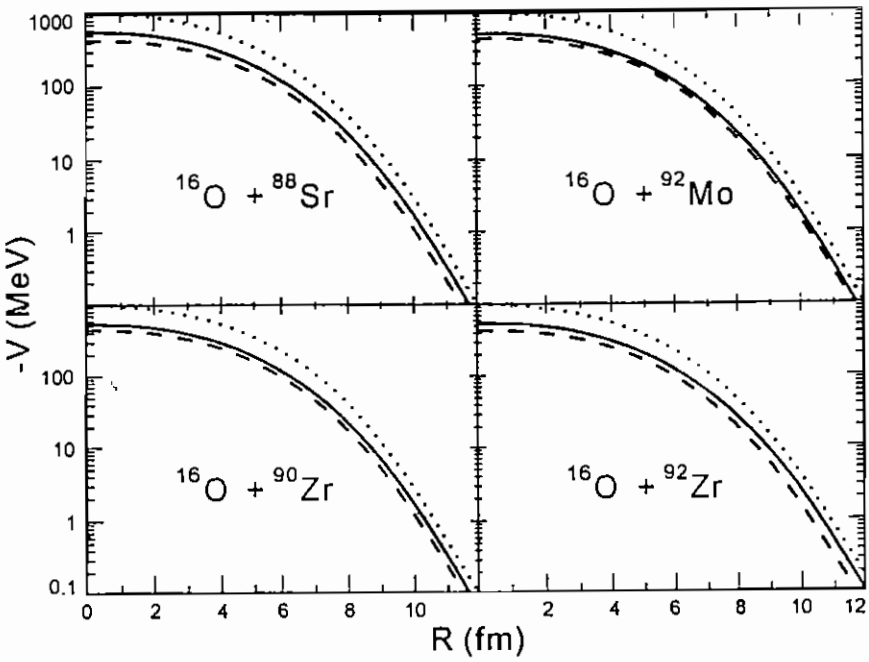

Figura IV.16 – Contribuições das densidades de prótons (linha tracejada) e de nêutrons (linhas cheias) para o potencial *Double-Folding* (linha pontilhada) dos sistemas ^{16}O + ^{88}Sr, ^{90,92}Zr, ^{92}Mo.

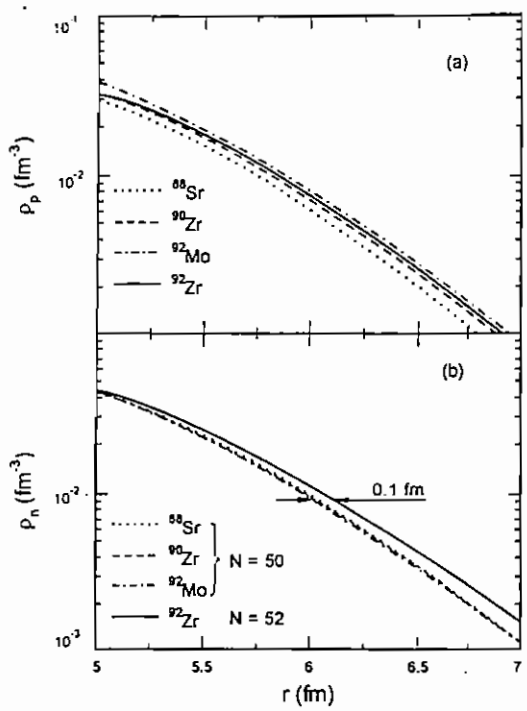

Figura IV.17 – Comparação entre as densidades de prótons (a) e nêutrons (b) na região da superfície dos núcleos ^{88}Sr, ^{90}Zr, ^{92}Zr e ^{92}Mo.

Na tabela IV.2 encontra-se os valores de difusividade dos potenciais *Folding*. Esses valores são próximos daqueles das difusividades médias dos potenciais de canais acoplados: $\bar{a} = (0{,}59 \pm 0{,}02)\, fm$ para os sistemas $^{16}O + ^{58,60,62,64}Ni$ e $\bar{a} = (0{,}64 \pm 0{,}02)\, fm$ para $^{16}O + ^{88}Sr, ^{90,92}Zr, ^{92}Mo$. Na realidade, é possível considerar que tanto as difusividades teóricas (*Folding*), como as experimentais (*canais acoplados*), têm valores muito próximos de $0{,}6\, fm$ para todos os sistemas estudados. Esses resultados indicam que os potenciais nucleares entre íons pesados têm uma forma (difusividade) quase independente do "tamanho do sistema". Como será discutido na seção IV.6, as características do potencial *Folding* na região de distâncias de interação superficial são dependentes, principalmente, das densidades nucleares na região da superfície dos núcleos. Como as experiências de espalhamento de elétrons têm demonstrado que os núcleos pesados têm difusividades de carga semelhantes [DJ74], é de esperar que também as difusividades dos potenciais nucleares sejam semelhantes para diferentes sistemas de íons pesados.

Tabela IV.2 – Valores da difusividade e da intensidade (em $\overline{R} = 10.7\ fm$) dos potenciais *Double-Folding*. Para efeito de comparação, estão incluídos os valores da intensidade dos potenciais de canais acoplados.

Sistema	$a\ (fm)$	$V_{Fold}(\overline{R})\ (MeV)$	$V_{CA}(\overline{R})\ (MeV)$	V_{CA}/V_{Fold}
$^{16}O + ^{58}Ni$	0.568	0.262	0.351 ± 0.009	1.34 ± 0.04
$^{16}O + ^{60}Ni$	0.576	0.306	0.447 ± 0.008	1.46 ± 0.03
$^{16}O + ^{62}Ni$	0.584	0.351	0.502 ± 0.019	1.43 ± 0.05
$^{16}O + ^{64}Ni$	0.592	0.399	0.600 ± 0.010	1.50 ± 0.03
$^{16}O + ^{88}Sr$	0.584	1.05	1.44 ± 0.05	1.37 ± 0.05
$^{16}O + ^{90}Zr$	0.586	1.13	1.55 ± 0.03	1.37 ± 0.03
$^{16}O + ^{92}Zr$	0.607	1.29	1.92 ± 0.06	1.49 ± 0.05
$^{16}O + ^{92}Mo$	0.587	1.19	1.57 ± 0.03	1.32 ± 0.03

As figuras IV.18 e IV.19 apresentam uma comparação entre os potenciais *Double-Folding* e os potenciais de canais acoplados. Na tabela IV.2 encontra-se a intensidade desses potenciais para $\overline{R} = 10.7\ fm$. Claramente, todas as expectativas que discutimos em relação à dependência dos potenciais *Folding* com as densidades são reproduzidas pelos potenciais de canais acoplados. Esse resultado fica caracterizado observando (tabela IV.2) que, dentro de uma precisão de aproximadamente 5%, a relação entre as intensidades dos potenciais "experimentais" e "teóricos" é independente do sistema e vale $\frac{V_{CA}}{V_{Fold}} \approx 1.4$. Uma peculiaridade interessante é o fato de que a intensidade do potencial para o sistema $^{16}O + ^{92}Zr$ é aproximadamente 15%

maior do que para $^{16}O + ^{92}Mo$, apesar do mesmo número de núcleons tanto no projétil como no alvo. Esse resultado está ligado à diferenças entre as respectivas densidades de nêutrons dos núcleos alvos.

Nas próximas seções, iremos discutir possíveis fontes para a diferença de 40% das intensidades dos potenciais de canais acoplados em relação aos correspondentes potenciais *Folding*. Na seção IV.5, investigamos que parcela dessa diferença está ligada com contribuições para a parte real do potencial de polarização, provenientes de acoplamentos de canais de reação com seção de choque desprezível, os quais não foram incluídos nas análises de canais acoplados. Na seção IV.6, são discutidos os efeitos sobre o potencial *Double-Folding* associados a diferentes modelos assumidos para as densidades dos núcleos envolvidos na colisão.

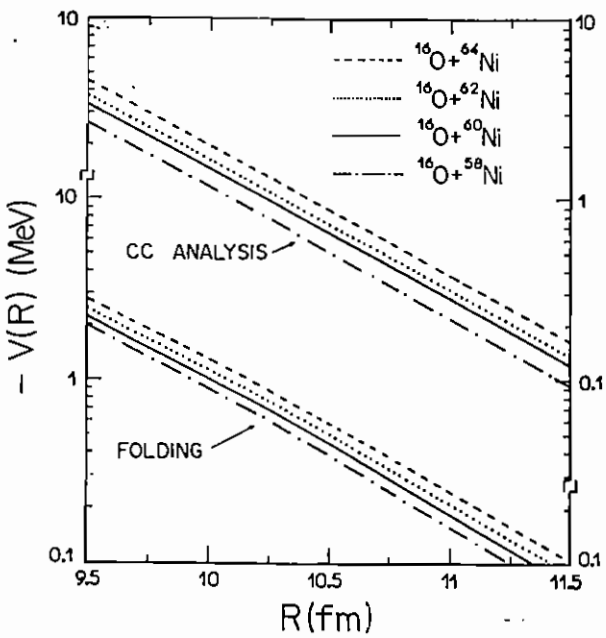

Figura IV.18 – Comparação entre potenciais de canais acoplados e *Double Folding* para os sistemas $^{16}O + ^{58, 60, 62, 64}Ni$. Observe a mudança de escala. Apesar de reproduzir a dependência isotópica dos potenciais "experimentais", os potenciais *Folding* apresentam intensidade aproximadamente 30% menor que os correspondentes potenciais de canais acoplados.

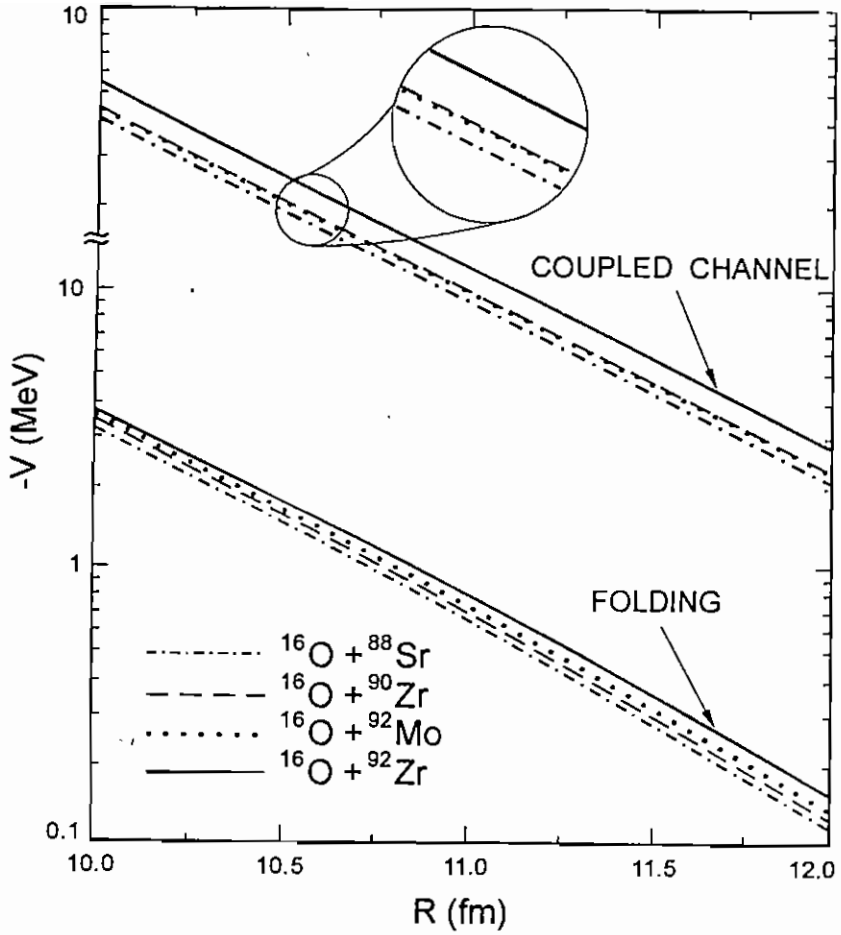

Figura IV.19 – Comparação entre potenciais de canais acoplados e *Double Folding* para os sistemas ^{16}O + ^{88}Sr, $^{90,\ 92}Zr$, ^{92}Mo. Observe a mudança de escala. Apesar de reproduzir a dependência isotônica (^{88}Sr, ^{90}Zr, ^{92}Mo – camada fechada $N = 50$) e isotópica (^{90}Zr, ^{92}Zr) dos potenciais "experimentais", os potenciais *Folding* apresentam intensidade aproximadamente 30% menor que os correspondentes potenciais de canais acoplados.

IV.5 – A Contribuição do Potencial de Polarização

Como discutido no capítulo II, a parte real do potencial ótico é composta pela soma do potencial nuclear com a parte real do potencial de polarização. Assim, a discrepância de aproximadamente 40% entre a parte real do potencial ótico de canais acoplados e o potencial *Double-Folding* (associado ao potencial nuclear) poderia estar relacionada ao potencial de polarização de canais de reação não incluídos nos cálculos.

Para os sistemas ^{16}O + $^{58,62}Ni$ em energias ao redor da barreira coulombiana, foi realizado por Keeley et al. [Ke96] um cálculo de canais acoplados bastante extenso e completo, em que foram incluídos acoplamentos de vários canais de reação inelásticos e, também, de processos de transferência (figura IV.20). Um potencial de polarização médio foi obtido através da solução das equações acopladas (figura IV.21). Vamos discutir alguns resultados desses cálculos, concentrando a atenção na região de baixas energias, $E_{CM} \leq 30\,MeV$ ($E_{LAB} \leq 38\,MeV$), que corresponde a região em que temos aplicado o método de determinação do potencial nuclear.

i) A intensidade da parte imaginária (absortiva) do potencial de polarização é muito pequena; resultado já esperado pois nessa região de energia a seção de choque dos canais de reação é desprezível em comparação com a seção de choque de espalhamento elástico.

ii) A contribuição do acoplamento para o estado 3_1^- do núcleo ^{16}O (o qual tem grande amplitude de acoplamento) corresponde a aproximadamente 50% de toda (considerando todos os acoplamentos) a intensidade da parte real do potencial de polarização.

iii) Para qualquer distância de interação na região superficial (não somente em $R = 10\,fm$ considerado na figura IV.21), a intensidade da parte real do potencial de polarização (com todos os acoplamentos) é uma fração aproximadamente constante da correspondente intensidade do potencial *Double-Folding*. Isto significa que a parte real do potencial ótico (nuclear + polarização) tem a mesma forma do potencial *Folding* (associado ao potencial nuclear). Esse resultado reforça a confiabilidade das difusividades obtidas com o nosso método para determinação do potencial nuclear.

iv) Finalmente, essa fração (V_{Pol} / V_{Fold}) é aproximadamente 17%.

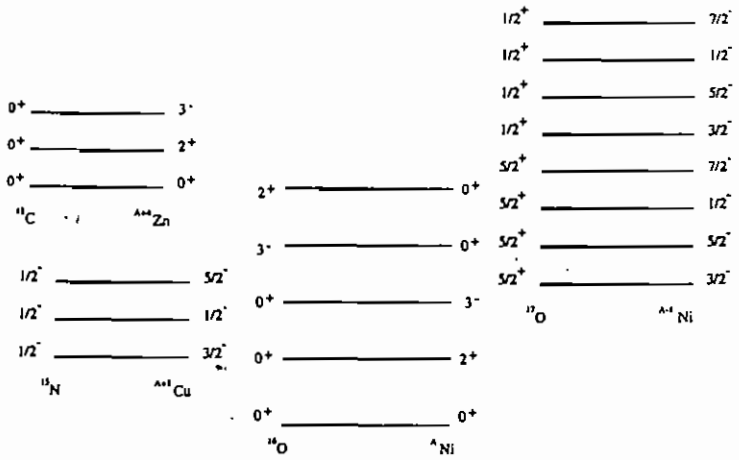

Figura IV.20 – O conjunto de canais de reação considerado por Keeley et al. [Ke96] nos cálculos de canais acoplados.

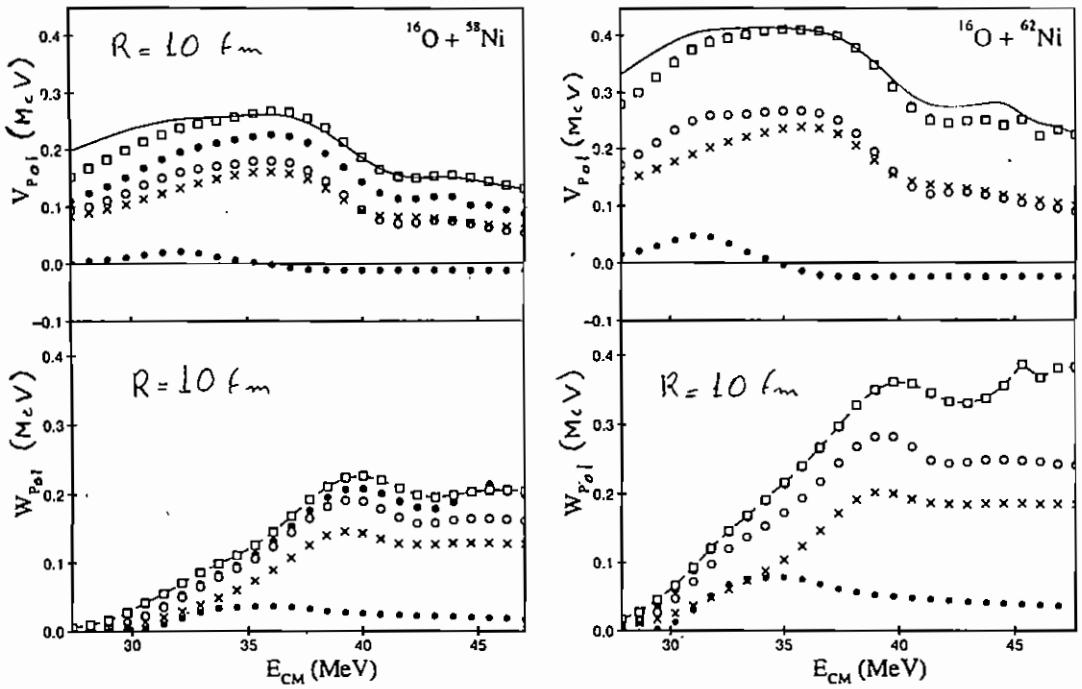

Figura IV.21 – Contribuições para o potencial de polarização médio na distância de interação $R = 10\ fm$, obtidas nos cálculos de canais acoplados realizados por Keeley et al. [Ke96]. Asteriscos representam somente acoplamentos inelásticos para os estados excitados do níquel. Cruzes: apenas acoplamento para o estado excitado 3_1^- do núcleo ^{16}O. Círculos vazios: todos os acoplamentos inelásticos. Círculos cheios: todos os inelásticos mais os canais de transferência de um único núcleon. Quadrados: o conjunto completo de acoplamentos (incluindo transferência de partículas alpha). As linhas cheias representam previsões para a parte real (V_{Pol}), obtidas utilizando a relação de dispersão e assumindo para a parte imaginária (W_{Pol}) a forma indicada pelas linhas tracejadas.

Em princípio, a inclusão no cálculo de ainda mais canais de reação poderia aumentar a intensidade do potencial de polarização. Entretanto, o já bastante completo cálculo de canais acoplados de Keeley et al., que acabamos de discutir, fornece previsões para a seção de choque de fusão que superestimam dados experimentais obtidos recentemente (figura IV.22) [Ke98]. A inclusão de mais canais de reação certamente tornaria piores essas previsões. Assim sendo, acreditamos que nas análises de Keeley et al., possivelmente as amplitudes dos acoplamentos foram superestimadas, e a intensidade do potencial de polarização é ainda menor do que 17% da intensidade do potencial *Folding*. Portanto, para os sistemas ^{16}O + Ni, a polarização deve contribuir com menos da metade da já comentada discrepância de 40% que obtivemos entre as intensidades dos potenciais *Folding* e "experimental".

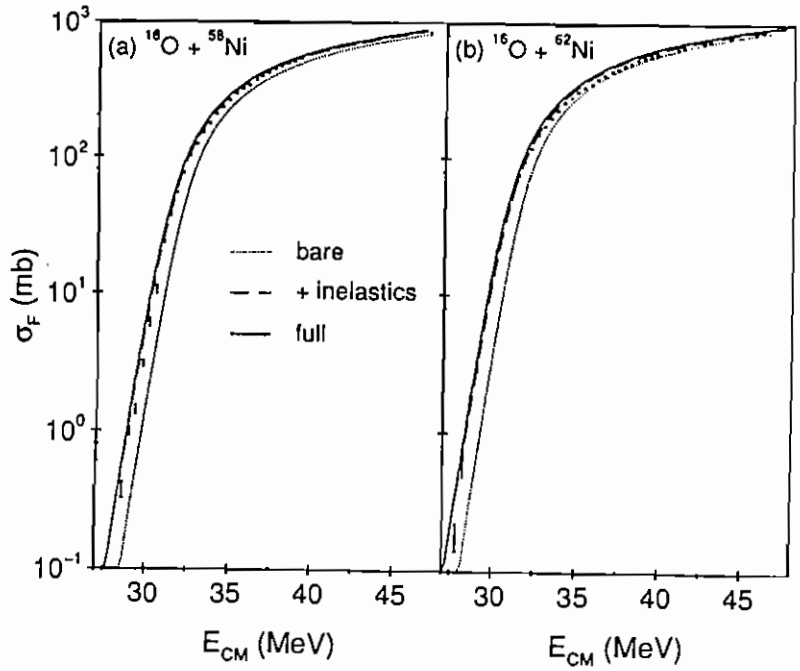

Figura IV.22 – Funções de excitação para seções de choque de fusão. As linhas cheias (todos os acoplamentos), tracejadas (apenas os inelásticos) e pontilhadas (nenhum acoplamento) são previsões do cálculo de canais acoplados de Keeley et al. [Ke96, Ke98].

Nós também realizamos cálculos de canais acoplados para o sistema $^{16}O + ^{90}Zr$ em que, além do estado 2_1^+ do ^{90}Zr, foram incluídos os estados 3_1^- dos núcleos ^{16}O e ^{90}Zr. Para a parte real do potencial ótico nós adotamos o potencial "experimental" de canais acoplados. A figura IV.23 mostra as previsões para seção de choque de espalhamento elástico na energia $E_{LAB} = 48\,MeV$, considerando: nenhum acoplamento (linha cheia); apenas o estado 2_1^+ (também linha cheia porque a diferença é desprezível); estados 2_1^+ e 3_1^- do ^{90}Zr (linha tracejada); estados 2_1^+ do ^{90}Zr e 3_1^- do ^{16}O (linha pontilhada). Os acoplamentos não afetam muito a seção de choque de espalhamento elástico. Para reajustar os dados considerando o acoplamento para o estado 3_1^- do ^{16}O, é necessário reduzir a intensidade do potencial "experimental" por aproximadamente 7%, sem modificar a difusividade. Esses resultados são muito semelhantes aos obtidos para os sistemas ^{16}O + Ni. Portanto, também para os sistemas $^{16}O + ^{88}Sr$, $^{90,92}Zr$, ^{92}Mo nós consideramos que o potencial de polarização está longe de explicar a diferença entre as intensidades dos potenciais *Folding* e "experimental".

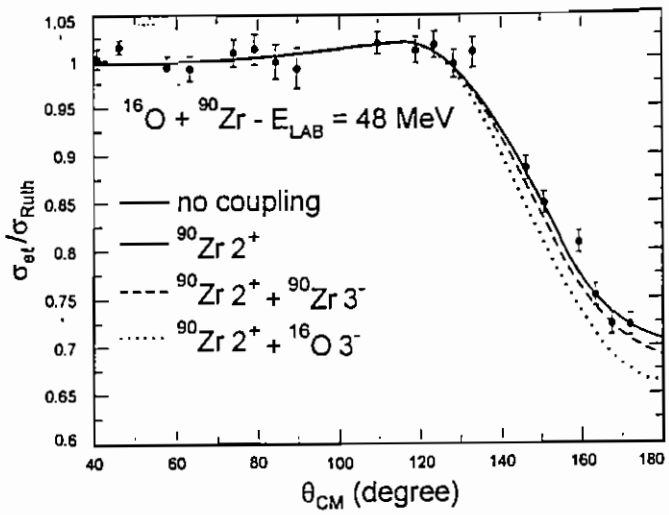

Figura IV.23 – Comparação entre dados experimentais de espalhamento elástico e cálculos de canais acoplados, considerando diferentes acoplamentos como indicado.

IV.6 – O Método como Teste para as Densidades Nucleares

Como discutido nas seções anteriores, os potenciais de canais acoplados extraídos das análises de dados em energias subcoulombianas são em torno de 40% mais intensos do que previsões teóricas do tipo *Double-Folding*, e o potencial de polarização proveniente de acoplamentos para canais de reação não incluídos nos cálculos é responsável por menos da metade dessa discrepância. Nós investigamos se essa diferença está relacionada com os modelos adotados para descrever as densidades nucleares. Como a diferença é muito aproximadamente independente do núcleo alvo, estudamos a densidade do projétil. Analisamos qual região da densidade do ^{16}O contribui significativamente para o potencial nuclear na região superficial de distâncias de interação. Para isso, tomamos o ^{90}Zr como núcleo alvo e incluímos uma perturbação de forma gaussiana na densidade do ^{16}O, conforme a expressão IV.8. Caracterizamos a região de sensibilidade para a densidade variando o centróide da perturbação (R_p) e calculando a diferença percentual, $100 \times \frac{V_{\text{PERTURBADA}} - V_{\text{SEM PERTURBAÇÃO}}}{V_{\text{SEM PERTURBAÇÃO}}}$, na intensidade do potencial *Folding* para a distância de interação $R = 11\,fm$ (região superficial). Os resultados estão apresentados na figura IV.24. A região de sensibilidade da densidade em baixas energias (RSBE) está ao redor de 4 *fm*, um valor aproximadamente 1.3 *fm* maior que o raio médio quadrático (RMQ) da distribuição de carga do ^{16}O [DJ74]. Nossas análises têm mostrado que um acréscimo de 30% na densidade do ^{16}O nessa região superficial (grosseiramente $3 \leq r \leq 5\,fm$), poderia explicar a previamente discutida discrepância entre potenciais teóricos e experimentais. É importante ressaltar que diferentes modelos fornecem

valores de densidade semelhantes na região próxima ao RQM e bastante diferentes na região superficial (RSBE) (figura IV.25).

$$\rho_{\text{PERTURBADA}}(r) = \rho_{\text{SEM PERTURBAÇÃO}}(r)\left[1 + 0.1\, e^{-\left(\frac{r-R_p}{0.5}\right)^2}\right] \qquad \text{(IV.8)}$$

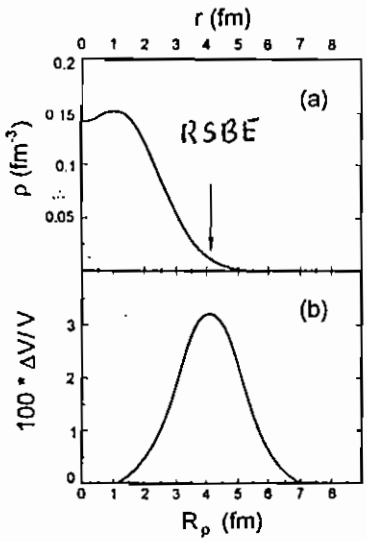

Figura IV.24 – a) A densidade não perturbada do núcleo ^{16}O. Está indicada a região de sensibilidade de baixas energias (RSBE). b) A diferença percentual $100 \times \frac{V_{\text{PERTURBADA}} - V_{\text{SEM PERTURBAÇÃO}}}{V_{\text{SEM PERTURBAÇÃO}}}$ na intensidade do potencial *Folding* em $R = 11\ fm$ para o sistema ^{16}O + ^{90}Zr.

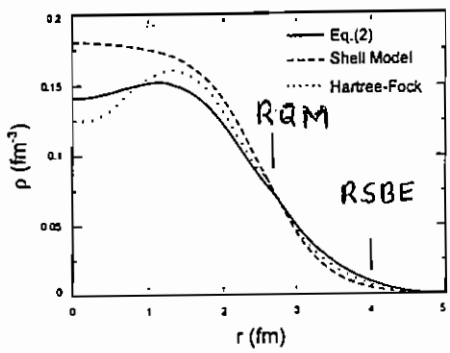

Figura IV.25 – Previsões para a densidade do núcleo ^{16}O considerando: a forma da distribuição de carga da equação IV.2, cálculos *Shell-Model* da referência Fa85 e cálculos *Hartree-Fock* da referência Ne70. Estão indicados o raio quadrático médio (RQM) e a região de sensibilidade de baixas energias (RSBE).

No capítulo III foi discutida a importância da não-localidade de Pauli na análise de dados de espalhamento elástico em energias intermediárias. Esse tipo de medidas foi realizado para o sistema ^{16}O + ^{90}Zr na energia $E_{LAB} = 1503\,MeV$ [Ro88]. Nesse caso, as seções de choque são sensíveis à uma região de distâncias de interação do potencial ao redor de $R \approx 8\,fm$ [Ro88] e nossas análises têm mostrado que a correspondente região de sensibilidade para a densidade está próxima do raio quadrático médio. A figura IV.26 mostra os dados experimentais comparados com previsões para seção de choque obtidas utilizando: o potencial *Double-Folding* (linha tracejada) e o potencial NLM3Y (linha cheia). Somente os parâmetros do potencial imaginário (Woods-Saxon) foram considerados livres para o ajuste dos dados experimentais. Tais previsões são muito similares considerando qualquer modelo da figura IV.25 para a densidade do núcleo ^{16}O (pois a seção de choque é sensível à região próxima do RQM). O potencial local-equivalente NLM3Y fornece boa previsão dos dados experimentais. Esse resultado precisa ser comparado com a requerida normalização de 40% no potencial *Folding* (equivalente ao NLM3Y em baixas energias) necessária para ajustar os dados experimentais na região subcoulombiana. Novamente enfatizamos que as regiões de densidade testadas em altas e baixas energias são muito diferentes. E ainda, diferentes modelos fornecem previsões de densidade semelhantes próximo ao RQM e diferentes na região superficial (RSBE). Portanto, nosso método experimental para a determinação do potencial nuclear através da análise de dados em energias subcoulombianas é uma poderosa ferramenta para testar diferentes modelos de densidade que fornecem ajustes de dados de alta energia semelhantes.

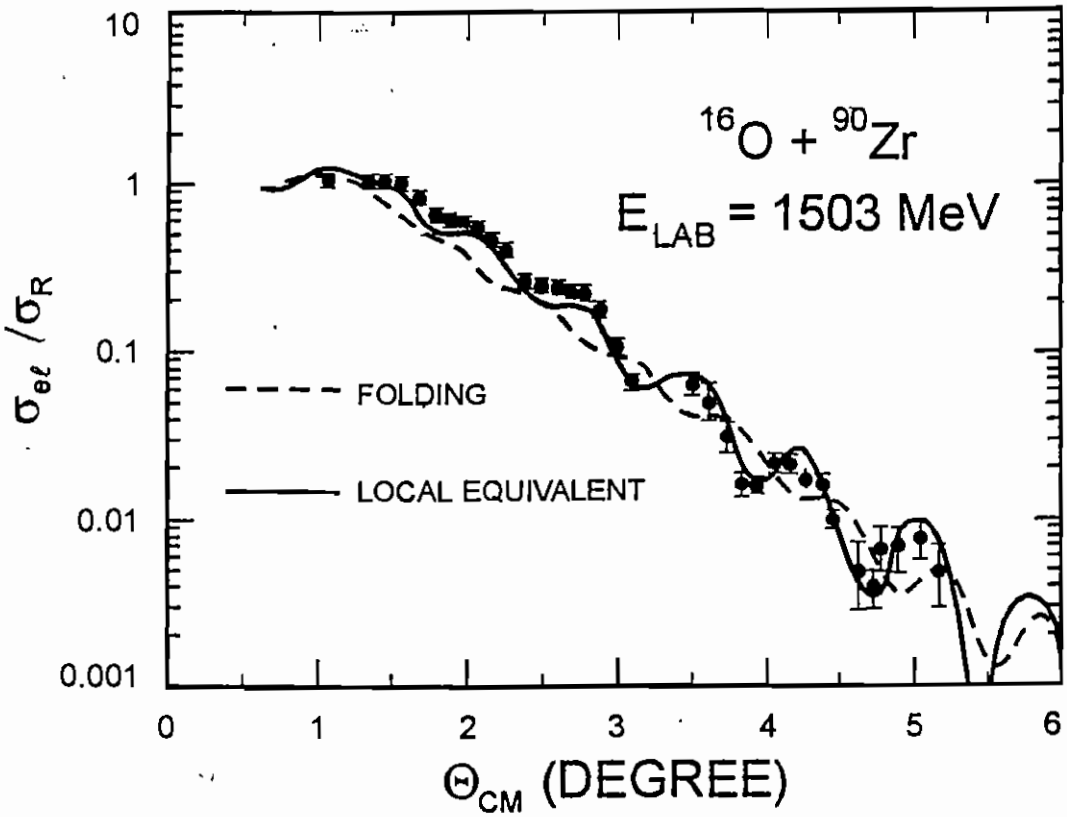

Figura IV.26 – Ajustes de modelo ótico de dados de espalhamento elástico utilizando: o potencial NLM3Y (linha cheia) e o potencial *Double Folding* (linha tracejada).

V - CONCLUSÃO

Neste trabalho, apresentamos um modelo teórico e um método experimental para a determinação do potencial nuclear em sistemas de íons pesados. A interação foi construída considerando os efeitos da não-localidade de Pauli, advinda do caráter de identidade dos núcleons que constituem a matéria nuclear. Esse modelo teórico é capaz de reproduzir, com boa precisão, dados experimentais de espalhamento elástico e inelástico de vários sistemas e em uma vasta região de energia. O potencial não-local que propomos é independente da energia, e uma generalização do já conhecido potencial *Double-Folding*. Apresentamos, também, uma aproximação para o potencial local-equivalente ao potencial não-local, denominada NLM3Y, a qual é independente do momento angular, mas dependente da energia. Em energias em torno da barreira coulombiana, o potencial NLM3Y é muito semelhante ao *Double-Folding*.

O método experimental para a determinação do potencial nuclear é baseado na análise de dados experimentais de espalhamento elástico em energias subcoulombianas. Nessa região de energia, o potencial pode ser extraído sem ambigüidade para distâncias de interação superficiais, devido a duas características:

i) como os canais de reação têm seção de choque desprezível, o potencial ótico não deve apresentar absorção na região de distâncias de interação superficial e isto permite fixar os parâmetros da correspondente parte imaginária;

ii) o raio de sensibilidade apresenta grande dependência com a energia, o que permite "mapear" a parte real do potencial ótico.

Esse método foi aplicado aos sistemas $^{16}O + {}^{58,60,62,64}Ni, {}^{88}Sr, {}^{90,92}Zr, {}^{92}Mo$. Os potenciais determinados experimentalmente apresentam a mesma forma dos respectivos potenciais *Double-Folding*. As difusividades extraídas das análises de dados são quase independentes do sistema e valem, aproximadamente, 0,6 *fm*. O potencial *Folding* também reproduz as dependências isotópica e isotônica dos potenciais obtidos experimentalmente. Entretanto, a intensidade dos potenciais "experimentais" são aproximadamente 40% maiores que as correspondentes intensidades dos potenciais *Folding*. Mostramos que o potencial de polarização dos canais de reação é responsável por menos da metade dessa discrepância. Nossas análises indicam que o restante da diferença deve estar ligada ao modelo adotado para a densidade do núcleo projétil, ^{16}O. Os dados de baixa energia são sensíveis à região superficial das densidades nucleares, enquanto os de alta energia à região próxima ao raio quadrático médio. Assim, o método para a determinação do potencial nuclear em energias subcoulombianas pode ser utilizado para testar diferentes modelos de densidade que produzem semelhantes ajustes de dados experimentais de alta energia.

REFERÊNCIAS

Al99 M. A. G.. Alvarez, L. C. Chamon, D. Pereira, E. S. Rossi Jr., C. P. Silva, L. R. Gasques, H. Dias, M. O. Roos, submetido à Nucl. Phys. A.

An73 N. Anantaraman, Phys. Rev. C8 (1973) 2245.

Ba79 A. J. Balts, N. K. Glendening, S. K. Kauffmann, K. Pruess, Nucl. Phys. A327 (1979) 221.

Be71 H. A. Bethe, Ann. Rev. Nucl. Sci. 21 (1971) 93.

Be77 G. Bertsch, J. Borysowics, H. McManus, W. G. Love, Nucl. Phys. A284 (1977) 399.

Be85 M. Beckerman, Phys. Rep. 129 (1985) 145.

Be93 M. Benjelloun, W. Galster, J. Vervier, Nucl. Phys. A560 (1993) 145.

Bl77 J. Blocki, J. Randrup, W. J. Swiatecki, C. F. Tsang, Ann. of Phys. 105 (1977) 427.

Bo82 H. G. Bohlen, M. R. Clover, G. Ingold, H. Lettau, W. von Oertzen, Z. Phys. A308 (1982) 121.

Bo92 A. M. Borges, C. P. Silva, D. Pereira, L. C. Chamon, E. S. Rossi Jr., C. E. Aguiar, Phys. Rev. C46 (1992) 2360.

Br97 M. E. Brandan, G. R. Satchler, Phys. Rep. 285 (1997) 143.

Bu63 B. Buck, A. P. Stamp, P. E. Hodgson, Phil. Mag. 8 (1963) 1805.

Bu84 M. Buenerd, A. Lounis, J. Chauvin, D. Lebrun, P. Martin, G. Duhamel, J. C. Gondrand, P. de Saintignon, Nucl. Phys. A424 (1984) 313.

Ch92 L. C. Chamon, D. Pereira, E. S. Rossi Jr., C. P. Silva, G. Ramirez, A. M. Borges, L. C. Gomes, O. Sala, Phys. Lett. 275B (1992) 29.

Ch95 L. C. Chamon, D. Pereira, E. S. Rossi Jr., C. P. Silva, R. Lichtentäler, L. C. Gomes, Nucl. Phys. A582 (1995) 305.

Ch96 L. C. Chamon, D. Pereira, E. S. Rossi Jr., C. P. Silva, H. Dias, L. Losano, C. A. P. Ceneviva, Nucl. Phys. A597 (1996) 253.

Ch97 L. C. Chamon, D. Pereira, M. S. Hussein, M. A. C. Ribeiro, D. Galleti, Phys. Rev. Lett. 79 (1997) 5218.

Ch98 L. C. Chamon, D. Pereira, M. S. Hussein, Phys. Rev. C58 (1998) 576.

De75 R. M. Devries, M. R. Glover, Nucl. Phys. A243 (1975) 528.

DJ74 C. M. De Jager, H. De Vries, C. De Vries, At. Data Nucl. Data Tables 14 (1974) 479.

Es89 H. Esbensen, F. Videbaek, Phys. Rev. C40 (1989) 126.

Fa85 M. E. Farid, G. R. Satchler, Nucl. Phys. A438 (1985) 525.

Fu85 B. R. Fulton, D. W. Banes, J. S. Lilley, M. A. Nagarajan, I. J. Thompson, Phys. Lett. 162B (1985) 55.

Fe58 H. Feshbach, Ann. of Phys., 5 (1958) 357.

Fe62 H. Feshbach, Ann. of Phys., 19 (1962) 287.

Fr57 W. E. Frahn, R. H. Lemmer, Nuovo Cimento 5 (1957) 1564.

Ga98 D. Galetti, S. S. Mizrahi, L. C. Chamon, D. Pereira, M. S. Hussein, M. A. C. Ribeiro, Phys. Rev. C58 (1998) 1627.

Gl70 R. J. Glauber, High-Energy Physics and Nuclear Structure (Plenum, New York, 1970) pág. 207.

Go74 D. A. Goldberg, S. M. Smith, G. F. Burdzik, Phys. Rev. C10 (1974) 1362.

Ho88 J. Y. Hostachy, M. Buenerd, J. Chauvin, D. Lebrun, P. Martin, J. C. Lugol, L. Papineau, P. Russel, N. Alamanos, J. Arviex, C. Cerruti, Nucl. Phys. A490 (1988) 441.

Ho89 S. W. Hong, T. Udagawa, T. Tamura, Nucl. Phys. A491 (1989) 492.

Hu91 M. S. Hussein, R. A. Rego, C. A. Bertulani, Phys. Rep. 201 (1991) 279.

Ja74 D. F. Jackson, R. C. Johnson, Phys. Lett. B49 (1974) 249.

Je77 J. P. Jeukenne, A. Lejeune, C. Mahaux, Phys. Rev. C16 (1977) 80.

Ke96 N. Keeley, J. S. Lilley, J. A. Christley, Nucl. Phys. A603 (1996) 97.

Ke98 N. Keeley, J. S. Lilley, J. X. Wei, M. Dasgupta, D. J. Hinde, J. R. Leigh, J. C. Mein, C. R. Morton, H. Timmers, N. Rowley, Nucl. Phys. A628 (1998) 1.

Kh93 D. T. Khoa, W. von Oertzen, Phys. Lett. B304 (1993) 8.

Kh94 D. T. Khoa, W. von Oertzen, H. G. Bohlen, Phys. Rev. C49 (1994) 1652.

Kh95a D. T. Khoa, W. von Oertzen, Phys. Lett. B342 (1995) 6.

Kh95b D. T. Khoa, W. von Oertzen, H. G. Bohlen, G. Bartnitzky, H. Clement, Y. Sugiyama, B. Gabauer, A. N. Ostrowski, T. Wilpert, M. Wilpert, C. Langner, Phys. Rev. Lett. 74 (1995) 34.

Ko82 A. M. Kobos, B. A. Brown, P. E. Hodgson, G. R. Satchler, A. Budzanowski, Nucl. Phys. A384 (1982) 65.

Ko84 A. M. Kobos, B. A. Brown, R. Lindsay, G. R. Satchler, Nucl. Phys. A425 (1984) 205.

Ko92 J. J. Kolata et al., Phys. Rev. Lett. 69 (1992) 2631.

Ko98 J. J. Kolata, comunicação privada.

Lo77 W. G. Love, T. Terasawa, G. R. Satchler, Nucl. Phys. A291 (1977) 183.

Lu95 B. J. Lund, N. P. T. Bateman, S. Utku, D. J. Horen, G. R. Satchler, Phys. Rev. C51 (1995) 635.

Ma77 N. V. Mau, Phys. Lett. B71 (1977) 5.

Ma82 C. Mahaux, H. Ngô, Nucl. Phys. A378 (1982) 205.

Ma85 C. Mahaux, P. F. Bortgnon, R. A. Broglia, C. H. Dasso, Phys. Rep. 120 (1985) 1.

Ne70 J. W. Negele, Phys. Rev. C4 (1970) 1260.

Pe62 F. G. Perey, B. Buck, Nucl. Phys. A32 (1962) 353.

Pe80 R. Peierls, N. V. Mau, Nucl. Phys. A343 (1980) 1.

Ra87 S. Raman C. H. Malarkey, W. T. Milner, C. W. Nestor Jr., P. H. Stelson, At. Data Nuclear Data Tables 36 (1987) 1.

Ri97 M. A. C. Ribeiro, L. C. Chamon, D. Pereira, M. S. Hussein, D. Galetti, Phys. Rev. Lett. 78 (1997) 253.

Ro88 P. Roussel-Chomaz, N. Alamanos, F. Auder, J. Barrete, B. Berthier, B. Fernandez, L. Papineau, Nucl. Phys. A477 (1988) 345.

Ro97 E. S. Rossi Jr., L. C. Chamon, D. Pereira, C. P. Silva, G. Ramirez, Journal of Physics G23 (1997) 1473.

Sa74 G. R. Satchler, Proc. of the Internacional Conference on Reactions between Complex Nuclei, vol. 2, Amsterdam (1974) 171.

Sa79 G. R. Satchler, W. G. Love, Phys. Rep. 55 (1979) 183.

Sa86 C. C. Sahm et al., Phys. Rev. C34 (1986) 2165.

Sa91 G. R. Satchler, Phys. Rep. 199 (1991) 147.

Si97 C. P. Silva, D. Pereira, L. C. Chamon, E. S. Rossi Jr., G. Ramirez, A. M. Borges, C. E. Aguiar, Phys. Rev. C55 (1997) 3155.

Sm73 S. M. Smith, G. Tebell, A. A. Cowley, D. A. Goldberg, H. G. Pugh, W. Reichart, N. S. Wall, Nucl. Phys. A207 (1973) 273.

St79 R. G. Stokstad et al., Phys. Rev. C20 (1979) 655.

Ta65 T. Tamura, Rev. Mod. Phys. 37 (1965) 679.

Th85 I. J. Thompson, M. A. Nagarajan, J. S. Lilley, B. R. Fulton, Phys. Lett. 157B (1985) 250.

Th88 I. J. Thompson, Computer Physics Reports 7 (1988) 167.

Th89 I. J. Thompson, M. A. Nagarajan, J. S. Lilley, M. J. Smithson, Nucl. Phys. A505 (1989) 84.

Tr80 W. Treu, H. Frohlich, W. Galster, P. Duck, H. Voit, Phys. Rev. C22 (1980) 2462.

Ud89 T. Udagawa, T. Tamura, B. T. Kim, Phys. Rev. C39 (1989) 1840.

Va81 L. C. Vaz, J. M. Alexander, Phys. Rep. 69 (1981) 373.

Wo73 C. Y. Wong, Phys. Rev. Lett. 31 (1973) 766.

Wy60 P. J. Wyatt, J. G. Wills, A. E. S. Green, Phys. Rev. 119 (1960) 1031.

Yo99 D. H. Yongblood, H. L. Clark, Y. W. Lui, Phys. Rev. Lett. 82 (1999) 691.

Experimental determination of the ion-ion potential in the N=50 target region: a tool to probe ground-state nuclear densities.

M. A. G. Alvarez, L. C. Chamon, D. Pereira, E. S. Rossi Jr. , C. P. Silva and L. R. Gasques

Laboratório Pelletron, Instituto de Física da Universidade de São Paulo, Caixa Postal 66318, 05315-970, São Paulo, SP, Brasil.

H. Dias

Grupo de Física Nuclear Teórica e Fenomenologia de Particulas Elementares, Instituto de Física da Universidade de São Paulo, Caixa Postal 66318, 05315-970, São Paulo, SP, Brasil.

M. O. Roos

Departamento de Física, Universidade Federal de Mato Grosso, Av. Fernando Corrêa, 78060-900, Cuiaba, MT, Brasil.

March 16, 1999

Abstract

Precise elastic and inelastic differential cross sections have been measured for the ^{16}O + ^{88}Sr,$^{90,92}Zr$,^{92}Mo systems at sub-barrier energies. From a coupled channel data analysis, the corresponding "experimental" bare potentials have been determined. The comparison of these potentials with those derived from double-folding theoretical calculations and the high energy (96 MeV/nucleon) elastic scattering data analysis indicate that the method is a very sensitive probe of the ground-state nuclear densities in the surface region.

NUCLEAR REACTIONS: $^{88}Sr(^{16}O,^{16}O)^{88}Sr$, $^{90,92}Zr(^{16}O,^{16}O)^{90,92}Zr$, $^{92}Mo(^{16}O,^{16}O)^{92}Mo$, measured elastic and inelastic (2^+) cross sections at $43 \leq E_{LAB} \leq 49\ MeV$. Deduced optical potentials. Shell model and double-folding calculations.

I. Introduction

In this work, we present precise elastic and inelastic (2_1^+) differential cross sections for the ^{16}O + ^{88}Sr,$^{90,92}Zr$,^{92}Mo systems at sub-barrier energies, $43 \leq E_{LAB} \leq 49\ MeV$. The main purpose of the experiment was to determine the bare ion-ion potentials for these systems through coupled channel (CC) elastic and inelastic data analyses. Recently, this method has been successfully applied in a study of the ^{16}O + $^{58,60,62,64}Ni$ systems [1, 2]. As discussed in these previous works, it was possible to study the isotopic dependence of the ion-ion potential for the proton closed shell nuclei (Z=28). because the coupled channel data analyses at sub-barrier energies are very reliable due to the small number of open reaction channels. In the present work, we investigate the isotonic (Z) dependence of the potential for the neutron closed shell targets (N=50) ^{88}Sr, ^{90}Zr and ^{92}Mo, and the influence on the potential due to the two extra neutrons in the ^{92}Zr nucleus.

In the data analysis, the best fits have been achieved with reasonable Coulomb and nuclear phonon amplitudes, and the slopes and strengths of the ion-ion potentials have been determined within 5% accuracy. Through the comparison of the "experimental" (i.e. extracted from data analyses) potentials with those derived from M3Y double-folding calculations, it was possible to probe the ground-state nuclear densities in the surface region ($\rho \simeq 0.01\ fm^{-3}$). The consistency of these studies has been tested, for the ^{16}O + ^{90}Zr system, through the comparison of the sub-barrier elastic data analysis with that at much higher energy ($E_{LAB} = 1503\ MeV$), in which an inner region of the nuclear density is probed. In the optical model high energy data analysis, the non-local exchange effects were taken into account.

The paper is organized as follows: section 2 gives the experimental details and results. The CC data analysis is presented in section 3. In section 4. we study the influence on the potentials due to the increasing number of protons in the ^{16}O + ^{88}Sr,^{90}Zr,^{92}Mo systems, and also the influence of the two extra neutrons in the ^{16}O + ^{92}Zr system. In section 5, we discuss the role played by the reaction channels with negligible cross sections in the polarization potential. In section 6, the sensitivity of our method as a probe of the nuclear densities is discussed. Section 7 contains a brief summary and the main conclusions.

II. Experimental Details and Results

The measurements were made using the ^{16}O beam from the São Paulo SUD Pelletron Accelerator. The detecting system has been already described in ref. [1]; it consisted of a set of nine surface barrier detectors spaced 5° apart. The thickness of the carbon (10 $\mu g/cm^2$) backed ^{88}Sr, ^{90}Zr,^{92}Zr,^{92}Mo targets were about 40 $\mu g/cm^2$, with a layer of gold (50 $\mu g/cm^2$) for the purpose of data normalization. We have estimated the Coulomb barrier for the ^{16}O + ^{88}Sr, $^{90,92}Zr$,^{92}Mo systems as $V_B^{Lab} \simeq 51$, 53, 53 and 55 MeV, respectively. Data were taken in the bombarding energy range $43 \leq E_{LAB} \leq 49$ MeV, which corresponds to 5 to 8 MeV below the Coulomb barrier for these systems. Due to the high precision required for the experimental data, the following procedures were taken into account in the data aquisition and reduction: i) the use of two monitor detectors ($\theta_{LAB} = \pm 35^o$) to be sure that no target deterioration occurred during bombardment; ii) high energy resolution to allow (see Fig. 1) a complete separation among the elastic, inelastic (2_1^+) and also the contaminant associated peaks; iii) corrections in the counting rate related to the elastic and inelastic processes due to the small background near those peaks.

Figs. 2 to 7 exhibit the elastic and inelastic (target - 2_1^+) differential cross sections for the ^{16}O + ^{88}Sr,$^{90,92}Zr$,^{92}Mo systems. Due to the very small counts in the peaks related to the inelastic process, the corresponding cross sections are somewhat "contaminated" due to the background subtraction, and it was not possible to obtain inelastic cross sections for the ^{16}O + ^{88}Sr,^{92}Zr systems. No evidence was found in the energy spectra for population of other excited target or projectile states with cross sections near those for the 2_1^+ state. The integrated inelastic cross sections vary between 5 to 50 mb in the energy range investigated. These values are one or two orders of magnitude larger than those associated to other reaction channels, such as the sub-barrier few nucleon transfer [3] and fusion [4] processes.

III. Data Analysis

In the coupled channel calculations, we have adopted a procedure similar to that described in the analysis of the sub-barrier elastic and inelastic data

for the $^{16}O + ^{58,60,62,64}Ni$ systems [1, 2]. The target nuclei have been assumed spherically symmetric but susceptible to vibrations around their spherical shapes [5]. For these nuclei, we have considered the contribution of the 2_1^+ state. We have used phonon amplitudes according to Refs. [6, 7, 8]. The value $r_c = 1.06\ fm$, obtained from electron scattering experiments [9], have been assumed for the Coulomb radius. For the real nuclear potential we have assumed a Woods-Saxon shape with a radius parameter equal to the Coulomb radius ($r_0 = r_c = 1.06\ fm$). We have used in the CC calculations an inner imaginary potential [1, 2], which takes into account the small internal absorption from barrier penetration. No sensitivity in the CC cross section predictions has been detected related to strength variations of this absorptive potential. The depth, V_0, and the diffuseness, a, of the real nuclear potential were searched for the best data fits. In a similar way as reported for the $^{16}O + ^{58,60,62,64}Ni$ systems [1, 2], for each system and bombarding energy we have found a family of real potentials, with different diffuseness parameters, which give equivalent data fits, as illustrated in Fig. 8 for the $^{16}O + ^{90}Zr$ system at the energies of 46 and 48 MeV. These potentials cross (see Fig. 8) at a particular radius, R_S, which is usually referred as the strong absorption radius in the case of higher energy elastic scattering data analysis. At sub-barrier energies, this radius is related to the classical turning point, and is energy dependent. Due to the small absorption involved in this case, in this work we refer to R_S as the sensitivity radius.

We have used the energy dependence of R_S (see Fig. 9) to characterize the shape of the real nuclear potential in the surface region. The uncertainties of the nuclear potential strengths at the sensitivity radius were obtained as already discussed in Refs. [1, 2]. The shape of the nuclear potential is quite close to an exponential, represented by solid lines in Fig. 9. Table 1 gives the diffuseness values obtained for the $^{16}O + ^{88}Sr, ^{90,92}Zr, ^{92}Mo$ systems. Within the uncertainties, the diffuseness parameters are compatible with the average value $\overline{a} = 0.64 \pm 0.02\ fm$. This diffuseness value is in good agreement with theoretical double-folding calculations, as will be discussed in the next section. Using the value $a = 0.64\ fm$ for the $^{16}O + ^{88}Sr, ^{90,92}Zr, ^{92}Mo$ systems, we were able to fit all the angular distributions (see Figs. 2 to 7) with an energy-independent bare potential for each system. Table 1 gives the CC potential strengths for all the systems investigated in this work at the interaction radius $R = 11\ fm$, which is near the center of the sensitivity region.

IV. Double-Folding Calculations

In this section, we present the theoretical calculations with the aim of evaluating the nuclear ion-ion potential by using the double-folding method [10] with shell model densities. In such analyses, we have used the well known nucleon-nucleon M3Y interaction in its standard form [10].

$$v_o(r) = \left[7999\frac{e^{-4r}}{4r} - 2134\frac{e^{-2.5r}}{2.5r}\right] + 262\ \delta(\vec{r})\ \ MeV \tag{1}$$

In our calculations, the ground-state density of the ^{16}O nucleus was derived from electron scattering experimental results [9], with the assumption that the neutron (ρ_n) and proton (ρ_p) densities have the same shape as the charge density (ρ_c). The total nuclear density is expressed by:

$$\rho(r) = \rho_n(r) + \rho_p(r) = \rho_0\left[1 + \gamma\left(\frac{r}{c}\right)^2\right] e^{-\left(\frac{r}{c}\right)^2}, \tag{2}$$

where $\gamma = 1.544$, $c = 1.833\ fm$ (charge density parameters of Ref. [9]), and $\rho_0 = 0.1407$ to satisfy the normalization condition:

$$\int_0^\infty 4\pi\rho(r)r^2dr = N + Z = A. \tag{3}$$

For the target nuclei we have used densities from shell model calculations. assuming, for the ^{88}Sr,^{90}Zr and ^{92}Mo nuclei, the $N = 50$ neutron closed shell and the $(2p_{3/2},\ 1f_{7/2},\ 2p_{1/2},\ 1g_{9/2})^{Z-28}$ proton orbital configuration. For the ^{92}Zr nucleus, we have considered the $(1f_{7/2},\ 1f_{5/2},\ 2p_{3/2})^{18}\ (2p_{1/2},\ 1g_{9/2})^2$ proton and the $(1g_{9/2})^{10}\ (1g_{7/2},\ 2d_{5/2},\ 2d_{3/2},\ 3s_{1/2})^2$ neutron orbital configurations. The shell model calculations predict level schemes for these nuclei which are in reasonable agreement with those derived from experiments up to excitation energies of about 3 MeV (see Fig. 10).

Fig. 11 presents the proton (dashed lines) and neutron (solid lines) densities for the ^{88}Sr,$^{90,92}Zr$ and ^{92}Mo nuclei. For these nuclei, the number of protons is significantly smaller than the number of neutrons, thus the proton densities are somewhat more internal as compared to the corresponding

neutron ones. We have calculated the folding potential contributions of the proton and neutron target densities according to the following expressions:

$$V_p(R) = \int \rho_o\left(\vec{r_1}\right) v_o\left(\left|\vec{R} - \vec{r_1} + \vec{r_2}\right|\right) \rho_p(\vec{r_2})\, d\vec{r_1}\, d\vec{r_2}, \tag{4}$$

$$V_n(R) = \int \rho_o\left(\vec{r_1}\right) v_o\left(\left|\vec{R} - \vec{r_1} + \vec{r_2}\right|\right) \rho_n(\vec{r_2})\, d\vec{r_1}\, d\vec{r_2}, \tag{5}$$

$$V_T(R) = V_p(R) + V_n(R) = \int \rho_o\left(\vec{r_1}\right) v_o\left(\left|\vec{R} - \vec{r_1} + \vec{r_2}\right|\right) \rho_T(\vec{r_2})\, d\vec{r_1}\, d\vec{r_2}, \tag{6}$$

where ρ_o is the total ^{16}O density; ρ_p, ρ_n and ρ_T are the proton, neutron and total target densities, respectively; and V_p, V_n and V_T are the corresponding proton, neutron and total folding potentials. These folding potentials are shown in Fig. 12. As expected, due to the neutron and proton density features (see Fig. 11), the neutron potential contribution in the surface interaction region is significantly more important in comparison to the corresponding proton one.

Since the neutron densities for the ($N = 50$ closed shell) ^{88}Sr, ^{90}Zr and ^{92}Mo nuclei are quite similar in the surface density region (see Fig. 13), the corresponding ^{16}O + ^{88}Sr,^{90}Zr,^{92}Mo systems present, as expected, similar double-folding potentials for large interaction distances (see Fig. 14 bottom). The neutron density for the two extra neutron ^{92}Zr nucleus, as indicated in Fig. 13, is shifted by about 0.1 fm in the surface region in relation to the other target nuclei. Since this value is of the same order of magnitude of the potential diffuseness ($a \simeq 0.6\ fm$), the double-folding theoretical calculations predict for the ^{16}O + ^{92}Zr system a bare potential which is about 20% greater in the surface region as compared to those for the ^{16}O + ^{88}Sr,^{90}Zr,^{92}Mo systems (see Fig. 14). We point out that the ^{16}O + ^{92}Zr,^{92}Mo systems present different surface folding potentials in spite of the same nucleon number in the target and projectile. The comparison of the potentials extracted from CC data analyses (Fig. 14 top) and those from double-folding calculations (Fig. 14 bottom) indicates clearly that all our expectations about the isotopic and isotonic dependence of these potentials are reasonably met. A similar result was obtained for the isotopic dependence of the nuclear potential for the ^{16}O + ^{58,60,62,64}Ni systems, as reported earlier [2]. Nevertheless, the strengths of the "experimental" potentials are

about 40% greater than the folding predictions (see Table 1). Again a similar result was found for the $^{16}O + {}^{58,60,62,64}Ni$ systems. Possible sources of such discrepancy will be discussed in the next sections.

Table 1 gives the "diffuseness parameters" (α) obtained from the slopes of the folding potentials, calculated in the surface region by Eq. (7). The folding diffuseness values are similar for all systems and close to the average "experimental" one (0.64 fm). A similar result has been obtained for the $^{16}O + {}^{58,60,62,64}Ni$ systems, and an average value of 0.59 fm has been found [1, 2]. These results indicate that the heavy-ion system potentials have a "universal" shape in the surface region rather independent of the "size of the system". As we will discuss in section 6, the features of the folding potential in the surface interaction region are dependent on the nuclear densities in the nucleus surface region. Since the electron scattering experiments [9] have shown that the heavy nuclei have similar charge diffuseness values, one should expect the potential diffuseness to be similar for different heavy-ion systems.

$$\alpha = \left| \frac{V(R)}{dV/dR} \right| \tag{7}$$

V. Contributions to the Polarization Potential

As discussed in the previous section, a difference of about 40% between the folding potential strengths in the surface interaction region and the corresponding "experimental" values from CC data analysis was found for the $^{16}O + {}^{88}Sr, {}^{90,92}Zr, {}^{92}Mo$ systems (present work), and also for the $^{16}O + {}^{58,60,62,64}Ni$ systems (Refs. [1, 2]). We have performed the following studies in order to explain this discrepancy: i) in this section, we intend to investigate how much of such difference is connected to contributions to the polarization potential arising from couplings of reaction channels with negligible cross sections, which were not included in our CC calculations at low energies; ii) in the next section, we will discuss the effects on the folding potential associated with different models assumed for the nuclear matter densities.

Referring back to the ^{16}O + Ni studies, an extensive and rather com-

plete coupled channel calculation, that included both inelastic excitation and transfer processes, was performed by Keeley et al. [11] for the $^{16}O + ^{58,62}Ni$ systems, and an "average" polarization potential was extracted through the solution of the coupled equations. Table 2 contains some results extracted from that work for the $^{16}O + ^{58}Ni$ system at $E_{CM} = 28\ MeV$, since this energy is in the energy range in which we have extracted the "experimental" nuclear potential for that system [2]. We point out the following features of the CC calculations: i) the contribution of the coupling for the $^{16}O\ 3^-$ state (which has a large phonon amplitude) is about 50% of the full polarization potential (which corresponds to all coupled channels); ii) the polarization potential due to this 3^- state is about 8% of the folding potential independent of the interaction distance considered. These results indicate that the polarization potential should not change significantly the shape (diffuseness) of the total (folding + polarization) potential in comparison to the folding potential. Another important point is that the strength of the full polarization potential is only about 17% in comparison to the folding potential. This result indicates that the polarization potential should be responsible for less than half of the observed discrepancy (40%) between the "experimental" and the folding potential strengths found in our previous work [2]. In principle, as discussed by Keeley et al. [11], the source of that discrepancy could be other possible couplings such as that for the $^{16}O\ 3_1^-$ state. Nevertheless, recent comparison [12] between the predicted fusion cross sections of this full CC analysis and precise fusion data for the $^{16}O + ^{58,62}Ni$ systems indicate that such CC calculations overpredict the data at energies below the fusion barrier (see Fig. 3 of Ref. [12]). The inclusion of other reaction channels in the CC calculations certainly would worsen the fusion cross section predictions. Thus, we believe that the strengths of the couplings are not so strong as considered in such calculations and the polarization potential strength should be even less significant in comparison to the bare potential.

We have also performed coupled channel calculations for the $^{16}O + ^{90}Zr$ system including the $^{16}O\ 3_1^-$ and $^{90}Zr\ 3_1^-$ states, besides that for the $^{90}Zr\ 2_1^+$ state. For the nuclear potential, we have adopted the "experimental" CC potential according to Table 1. Fig. 15 shows the predicted elastic cross sections for $E_{LAB} = 48\ MeV$, considering: no couplings (solid line), only the $^{90}Zr\ 2_1^+$ coupling (also solid line because the difference is negligible), both couplings $^{90}Zr\ 2_1^+ + ^{90}Zr\ 3_1^-$ states (dashed line) and $^{90}Zr\ 2_1^+ + ^{16}O\ 3_1^-$ states (dotted line). The couplings do not have much effect on the elastic scattering

cross sections. In order to fit the data considering the coupling for the ^{16}O 3_1^- state, it is necessary to reduce the "experimental" potential strength by about 7% and the diffuseness parameter persists changeless. These results are very similar to those found for the ^{16}O + Ni systems. Therefore, we consider that also for the systems studied in the present work, ^{16}O + ^{88}Sr,$^{90,92}Zr$,^{92}Mo, the polarization potential is far from being capable of accounting for the detected difference between the folding and the "experimental" potential strengths.

VI. The Missing Potential Strength: Probing the Nuclear Density

As discussed in the previous sections, the ion-ion potentials extracted from low energy CC data analyses are about 40% greater than the theoretical double-folding predictions for the ^{16}O + $^{58,60,62,64}Ni$,^{88}Sr,$^{90,92}Zr$,^{92}Mo systems, and the polarization potential that arises from couplings to reaction channels with negligible cross sections can only account for part of this difference. We have investigated if the source of such discrepancy is related to the models adopted to describe the ground-state nuclear densities. Since this discrepancy is approximately target independent, we have investigated the projectile density. We have studied which region of the ^{16}O density contributes significantly to the nuclear potential in the surface region. In order to perform such a study, we have taken the ^{90}Zr as the target nucleus and we have included a spline with gaussian shape, according to Eq. (8), on the nuclear density of the ^{16}O nucleus. We have characterized the sensitivity region of the density by varying the position of the perturbation (R_p), and calculating the percentage difference ($100 \times \frac{\Delta V}{V_{unperturbed}}$) in the strength of the folding potential at the interaction distance $R = 11\ fm$ ($\Delta V = V_{perturbed} - V_{unperturbed}$). The results of such calculations are shown in Fig. 16. The low energy sensitivity region (LESR) for the ^{16}O density lies at radius around 4 fm, a value about 1.3 fm greater the root-mean-square (RMS) radius of the ^{16}O charge distribution [9]. Double-folding calculations show that an increase of about 30% in the ^{16}O density in this surface region (roughly $3 \leq r \leq 5\ fm$) could explain the theoretical-experimental potential strength discrepancy previously discussed. We point out that nuclear density calculations for the ^{16}O nucleus based on different models give similar density values in the region near the RMS radius, and predict quite different results

in the surface region, which differ from each other by about 30% (see Fig. 17). On the other hand, we have not observed such behavior for the targets studied in this work, as illustrated in Fig. 18.

$$\rho_{perturbed}(r) = \rho_{unperturbed}(r) \left[1 + 0.1e^{-\left(\frac{r-R_p}{0.5}\right)^2}\right] \tag{8}$$

The low energy data analysis for the ^{16}O + ^{88}Sr,$^{90,92}Zr$,^{92}Mo systems have shown that the elastic scattering cross sections are sensitive to an interaction distance region around 11 fm, which corresponds to a region of sensitivity for the nuclear densities about 1.5 fm larger than the RMS radius. For much higher energies, inner distances are probed by elastic scattering cross section data analysis. Such measurements have been performed for the ^{16}O + ^{90}Zr system at $E_{LAB} = 1503$ MeV [15]. In this case, the elastic scattering cross sections are sensitive to the nuclear potential in an interaction distance region around 8 fm [15], and our analysis indicate that the corresponding density sensitivity region is near the RMS radius. At such high energies and such internal interaction distance region, as discussed in Refs. [16, 17], the polarization potential from reaction channel couplings (Feshbach nonlocality) contributes mainly to the imaginary part of the optical potential, while the effects of nucleon exchange (Pauli nonlocality) are important to the real part of the nuclear interaction. Recently, a model [16]-[18] that takes into account the Pauli non-local nature of the nuclear interaction was developed with the aim to describe the nucleus-nucleus collision at low and high energies. The model is based on the Perey and Buck prescription [19], with the non-local parameter range (b) given by the Jackson and Johnson theoretical prediction [20]; $b = b_0\frac{\mu_0}{\mu}$ ($b_0 = 0.85$ fm, μ_0 is the nucleon mass and μ is the reduced mass of the system). In the model, the parameter free non-local real nucleus-nucleus interaction is expressed by

$$V(\vec{R}, \vec{R}') = V_{folding}\left(\frac{R+R'}{2}\right)\frac{1}{\pi^{3/2}b^3}e^{-\left(\frac{\vec{R}-\vec{R}'}{b}\right)^2}, \tag{9}$$

and the corresponding energy-dependent local equivalent potential is expressed approximately by

$$V_{LE}(R,E) \simeq \frac{1-\sqrt{1-4\gamma V_{folding}(R)e^{-\gamma[E-V_C(R)]}}}{2\gamma}, \qquad (10)$$

where $\gamma = \mu b^2/2\hbar^2$.

For an interaction radius near the barrier radius and energies close to the Coulomb barrier, the local equivalent potential is quite close to the folding one, $V_{LE}(R \simeq R_B, E \simeq V_B) \simeq V_{folding}(R)$, and the effect of the nonlocality is negligible. Fig. 19 shows the folding potential (dashed line) and the local equivalent potential at $E_{LAB} = 1503\ MeV$ (solid line) for the $^{16}O + {}^{90}Zr$ system. In Fig. 20, the elastic cross section data [15] for the same system and energy are shown. Also the corresponding optical model predictions, either considering the folding potential (dashed line) or the local equivalent potential (solid line), are shown in the same figure. In the data fit procedure, as reported in Ref. [17], only the Woods-Saxon imaginary potential parameters were allowed to vary. The elastic scattering cross section predictions are quite similar considering any density model of Fig. 17 for the ^{16}O nucleus. The parameter free local equivalent real potential provides a good data prediction (see Fig. 20) without any normalization of the folding potential included in Eq. (10). This result should be compared to the required normalization of 40% in elastic scattering data fits at sub-barrier energies. We again point out that the density sensitivity regions probed at low and high energies are rather different. We stress that different models usually give similar density results in the region close to the RMS radius, and very different density values in the surface region (LESR). Therefore, the low energy elastic scattering data provide a test for different density models which give similar high energy data fits.

VII. Summary and Conclusions

In summary, we have performed coupled channel analysis of elastic and inelastic angular distributions for the $^{16}O + {}^{88}Sr, {}^{90,92}Zr, {}^{92}Mo$ systems at the sub-barrier energies $43 \leq E_{LAB} \leq 49\ MeV$. The data are well reproduced with energy-independent nuclear bare potentials, which are real and have an exponential shape in the surface region. These CC potentials have the same diffuseness parameter, $\overline{a} = 0.64\ fm$, defined within an accuracy of 5% for all systems. The slope of the resulting CC potentials is well reproduced by the

M3Y double-folding calculations using shell model densities for the targets. The isotonic and isotopic dependence of the CC potentials are also reasonably described by the double-folding potential. Very similar results had already been obtained for the $^{16}O + {}^{58,60,62,64}Ni$ systems. All these results are closely related to the nuclear density features of the collision partners.

Nevertheless, for both sets of systems the strengths of the sub-barrier CC bare potentials are about 40% greater than the corresponding values from M3Y folding potential calculations. Based on a previous extensive and rather complete coupled channel analysis for the $^{16}O + {}^{58,62}Ni$ systems, we have concluded that the contributions to the polarization potential associated to other reaction channel couplings only account for part of such discrepancy. Our studies indicate that the discrepancy is connected mainly to the ^{16}O nuclear density model adopted in the folding calculations. The predictions of the low energy elastic scattering cross section are very sensitive to the nuclear matter densities in the surface region. In the high energy case, in which the effects on the nuclear interaction due to the non-local nucleon exchange are very important, the sensitivity region for the densities is somewhat more internal than the corresponding region for the sub-barrier case. Thus, a consistent low and high energy elastic scattering data analysis has been demonstrated to be a powerful tool to probe ground-state nuclear densities.

This work was partially supported by Financiadora de Estudos e Projetos (FINEP), Fundação de Amparo à Pesquisa do Estado de São Paulo (FAPESP), Conselho Nacional de Desenvolvimento Científico e Tecnológico (CNPq), and Programa PICD/CAPES da Universidade Federal de Mato Grosso.

We thank Prof. B. A. Brown from Michigan State University, for providing us the computer shell-model codes.

References

[1] L.C. Chamon, D. Pereira, E.S. Rossi Jr., C.P. Silva, R. Lichtenthaler Filho and L. C. Gomes, Nucl. Phys. **A582** (1995) 305.

[2] L.C. Chamon, D. Pereira, E.S. Rossi Jr., C.P. Silva, H. Dias, L. Losano and C. A. P. Ceneviva, Nucl. Phys. **A597** (1996) 253.

[3] N. Anantaraman, Phys. Rev. **C8** (1973) 2245.

[4] M. Benjelloun, W. Galster and J. Vervier, Nucl. Phys. **A560** (1993) 145.

[5] T. Tamura, Rev. Mod. Phys. **37** (1965) 679.

[6] S. Raman, C. H. Malarkey, W. T. Milner, C. W. Nestor Jr. and P. H. Stelson, At. Data Nucl. Data Tables **36** (1987) 1.

[7] H. Esbensen and F. Videbaek, Phys. Rev. **C40** (1989) 126.

[8] B. J. Lund, N. P. T. Bateman, S. Utku, D. J. Horen and G. R. Satchler, Phys. Rev. **C51** (1995) 635.

[9] C. M. De Jager, H. De Vries and C. De Vries, At. Data Nucl. Data Tables **14** (1974) 479.

[10] G. R. Satchler and W. G. Love, Phys. Rep. **55** (1979) 183.

[11] N. Keeley, J. S. Lilley and J. A. Christley, Nucl. Phys. **A603** (1996) 97.

[12] N. Keeley, J. S. Lilley, J. X. Wei, M. Dasgupta, D. J. Hinde, J. R. Leigh, J. C. Mein, C. R. Morton, H. Timmers and N. Rowley, Nucl. Phys. **A628** (1998) 1.

[13] G. R. Satchler, Nucl. Phys. **A329** (1979) 233.

[14] M. El-Azab Farid and G. R. Satchler, Nucl. Phys. **A438** (1985) 525.

[15] P. Roussel-Chomaz, N. Alamanos, F. Auder, J. Barrete, B. Berthier, B. Fernandez and L. Papineau, Nucl. Phys. **A477** (1988) 345.

[16] M. A. C. Ribeiro, L. C. Chamon, D. Pereira, M. S. Hussein and D. Galetti, Phys. Rev. Lett. **78** (1997) 3270.

[17] L. C. Chamon, D. Pereira, M. S. Hussein, M. A. C. Ribeiro and D. Galetti, Phys. Rev. Lett. **79** (1997) 5218.

[18] L. C. Chamon, D. Pereira and M. S. Hussein, Phys. Rev. **C58** (1998) 576.

[19] F. Perey and B. Buck, Nucl. Phys. **32** (1962) 253.

[20] D. F. Jackson and R. C. Johnson, Phys. Lett. **B49** (1974) 249.

[21] J. W. Negele, Phys. Rev. **C4** (1970) 1260.

FIGURE CAPTIONS

Figure 1. Energy spectrum for the $^{16}O + ^{92}Mo$ system at $E_{Lab} = 49\ MeV$ and $\theta_{Lab} = 160^o$. The molybdenum isotopes ^{94}Mo, ^{95}Mo, ^{96}Mo, ^{97}Mo and ^{100}Mo are the main contaminants in the ^{92}Mo target.

Figure 2. Elastic scattering angular distributions for the $^{16}O + ^{88}Sr$ system at the bombarding energies $E_{Lab} = 43$, 44 and 45 MeV. The solid lines correspond to coupled channel calculations (see details in the text).

Figure 3. The same as in Fig. 2, for the $^{16}O + ^{90}Zr$ system at $E_{Lab} =$ 46, 47 and 48 MeV.

Figure 4. The same as in Fig. 2, for the $^{16}O + ^{92}Zr$ system at $E_{Lab} =$ 45, 46, 47 and 48 MeV.

Figure 5. The same as in Fig. 2, for the $^{16}O + ^{92}Mo$ system at $E_{Lab} =$ 48, 48.5 and 49 MeV.

Figure 6. The inelastic (2_1^+ target state) angular distributions for the $^{16}O + ^{90}Zr$ system at $E_{Lab} = 46$, 47 and 48 MeV. The solid lines in the figure correspond to coupled channel calculations (see text for details).

Figure 7. The same as in Fig. 6, for the $^{16}O + ^{92}Mo$ system at $E_{Lab} =$ 48, 48.5 and 49 MeV.

Figure 8. Determination of the nuclear real bare potential at the sensitivity radius (R_S) for the $^{16}O + ^{90}Zr$, as obtained from CC analysis of the experimental data ($E_{Lab} = 46$ and 48 MeV) considering different values of diffuseness and potential depth parameters.

Figure 9. The nuclear real bare potential as a function of the sensitivity radius for the $^{16}O + ^{88}Sr, ^{90,92}Zr$ and ^{92}Mo systems. The solid lines in the figure represent the CC potentials with the same diffuseness value ($\overline{a} = 0.64\ fm$) for all the systems.

Figure 10. Energy level scheme predictions from shell model calculations for the $^{88}Sr, ^{90,92}Zr$ and ^{92}Mo nuclei. For comparison purpose, the corresponding experimental schemes were included in the figure.

Figure 11. The ground-state proton (dashed lines) and neutron (solid

lines) densities derived from shell model calculations for the ^{88}Sr, ^{90}Zr, ^{92}Zr and ^{92}Mo nuclei.

Figure 12. Proton (dashed line), neutron (solid line), and total (dotted line) double-folding potentials for the ^{16}O + ^{88}Sr,^{90,92}Zr and ^{92}Mo systems, using shell model densities for the target nuclei and charge distribution shape density (Eq. 2) for the projectile (see text for details).

Figure 13. Comparison between ground-state proton (a) and neutron (b) densities in the surface region, for the ^{88}Sr, ^{90}Zr, ^{92}Zr and ^{92}Mo nuclei.

Figure 14. Comparison between the bare potentials from CC data analyses (top) and double-folding calculations (bottom), for the ^{16}O + ^{88}Sr,^{90,92}Zr and ^{92}Mo systems (see text for details).

Figure 15. Comparison between the experimental elastic scattering angular distribution for the ^{16}O + ^{90}Zr system ($E_{Lab} = 48\ MeV$) and different CC calculations which include: a) no reaction channel (solid line), b) only the ^{90}Zr 2_1^+ state (also solid line), c) the 2_1^+ and 3_1^- states of the ^{90}Zr nucleus (dashed line), and d) the 2_1^+ and 3_1^- states of the ^{90}Zr and ^{16}O nuclei, respectively (dotted line).

Figure 16. a) The charge distribution shape nuclear density for the ^{16}O nucleus (Eq. 2), indicating the "low energy sensitivity region (LESR)" in the determination of the bare potential through sub-barrier elastic data analysis. b) The percentage difference ($100 \times \frac{\Delta V}{V_{unperturbed}}$) in the strength of the folding potential at $R = 11\ fm$ for the ^{16}O + ^{90}Zr system (see text for details).

Figure 17. Different ^{16}O nuclear density predictions considering: a) the charge distribution shape of Eq. 2 (solid line), b) shell model calculations from Ref. [14] (dashed line), and c) Hartree-Fock calculations from Ref. [21] (dotted line). In the figure are indicated the root-mean-square radius (RMS), and the "low energy sensitivity region" in the determination of the CC potential (LESR).

Figure 18. Comparison between proton and neutron densities for the ^{90}Zr nucleus considering shell model (this work) and Hartree-Fock (Ref. [21]) calculations. In the figure are indicated the root-mean-square radius (RMS) and the "low energy sensitivity region" in the determination of the CC potential

(LESR).

Figure 19. The local equivalent potential (solid line) for the $^{16}O + ^{90}Zr$ system at the bombarding energy $E_{Lab} = 1503\ MeV$. The dashed line represents the corresponding double-folding potential (Eq. 1).

Figure 20. Optical model elastic scattering data fits for the $^{16}O + ^{90}Zr$ system at the bombarding energy $E_{Lab} = 1503\ MeV$, considering for the nuclear interaction: a) the double-folding potential (dashed line), and b) the local equivalent potential (solid line). In the data fits only the Woods-Saxon imaginary potential parameters were allowed to vary.

TABLES

Table 1: The diffuseness values from CC (a) and double-folding (α) calculations, and also the strengths of the CC (V_{CC}) and double-folding (V_{fold}) potentials at the interaction distance $R = 11\ fm$.

nucleus	$a\ (fm)$	$\alpha\ (fm)$	$V_{CC}\ (MeV)$	$V_{fold}\ (MeV)$	V_{CC}/V_{fold}
^{88}Sr	0.71 ± 0.05	0.584	0.90 ± 0.03	0.628	1.43 ± 0.05
^{90}Zr	0.63 ± 0.03	0.586	0.97 ± 0.02	0.675	1.44 ± 0.03
^{92}Zr	0.61 ± 0.05	0.607	1.20 ± 0.04	0.787	1.52 ± 0.05
^{92}Mo	0.63 ± 0.06	0.587	0.98 ± 0.02	0.716	1.37 ± 0.03

Table 2: Double-folding potential (V_{fold}) and polarization potential contribution corresponding to the coupling for the ^{16}O 3_1^- state only ($V_{pol}^{3^-}$) and also to all reaction channels included in the CC calculations (V_{pol}^{full}), for the ^{16}O + ^{58}Ni system at $E_{CM} = 28\ MeV$. These values were extracted from Refs. [15, 2] at three different surface interaction radii.

$R\ (fm)$	$V_{pol}^{3^-}\ (MeV)$	$V_{pol}^{full}\ (MeV)$	$V_{fold}\ (MeV)$
10.0	0.08	0.16	0.91
10.5	0.03	—	0.37
11.0	0.006	—	0.064

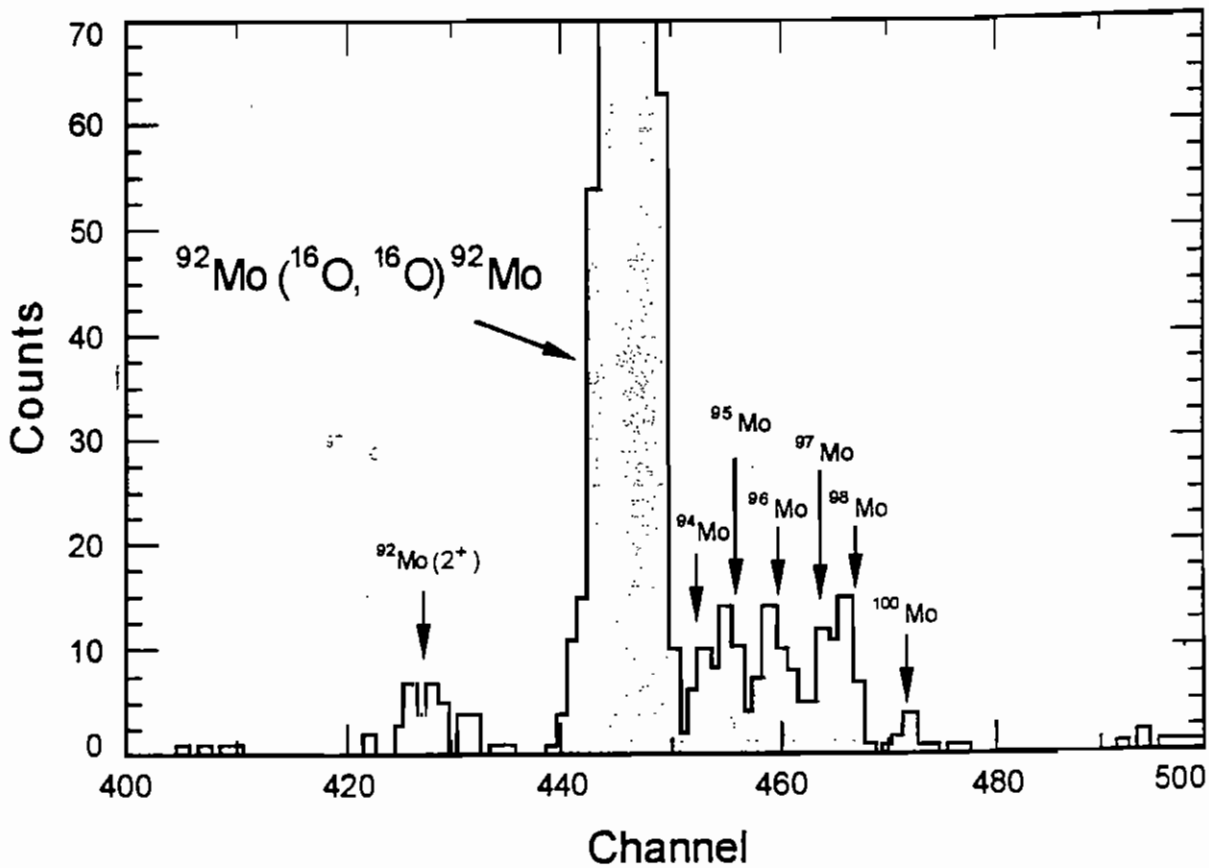
Counts
Channel
^{92}Mo (^{16}O, ^{16}O) ^{92}Mo
^{92}Mo (2^{+})
^{94}Mo
^{95}Mo
^{96}Mo
^{97}Mo
^{98}Mo
^{100}Mo
0
10
20
30
40
50
60
70
400
420
440
460
480
500

Fig. 1

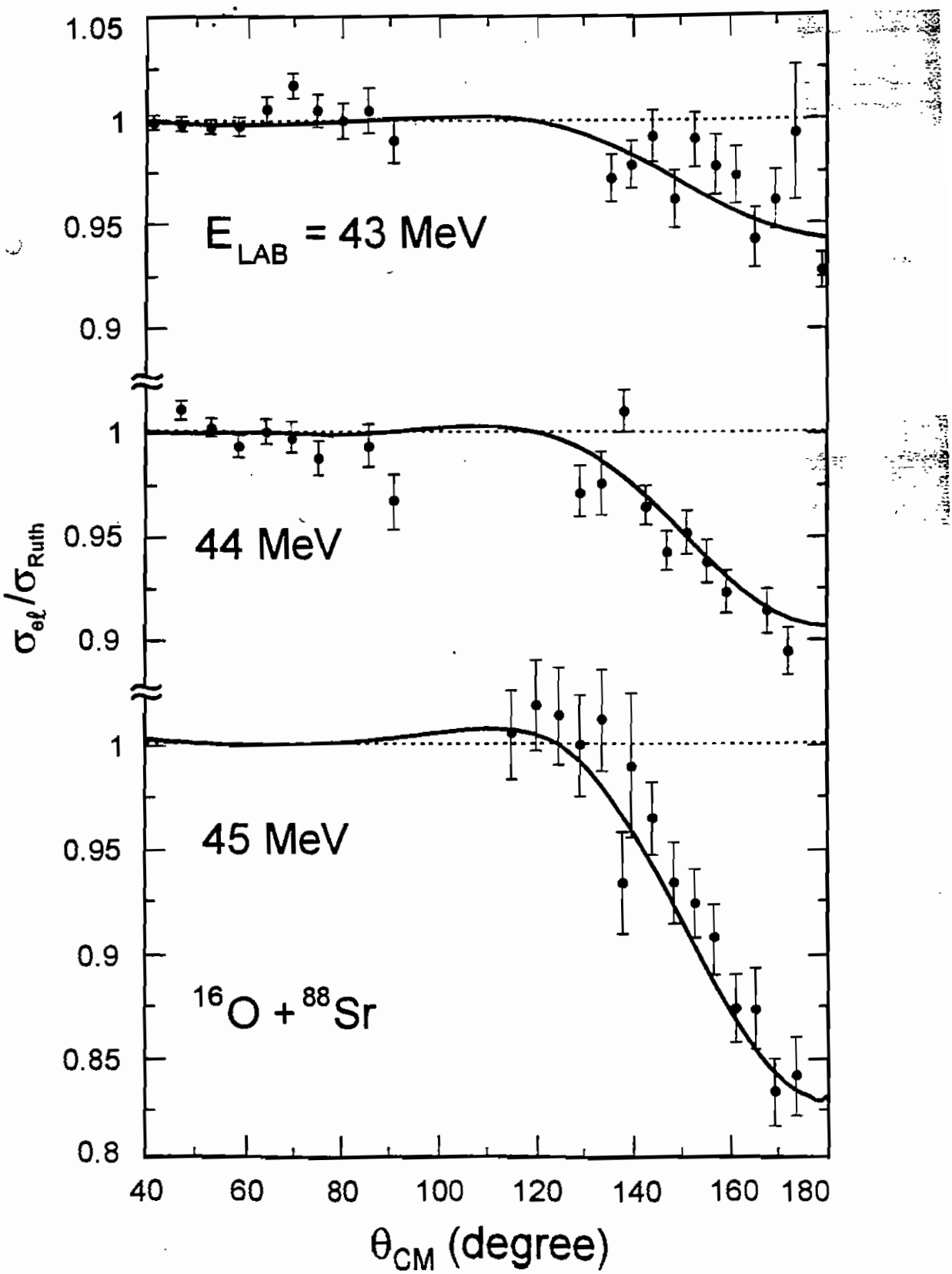
1.05
1
0.95
0.9
E_{LAB} = 43 MeV
1
0.95
0.9
44 MeV
1
0.95
0.9
0.85
0.8
45 MeV
$^{16}O + ^{88}Sr$
$\sigma_{el}/\sigma_{Ruth}$
40
60
80
100
120
140
160
180
θ_{CM} (degree)

Figure 2

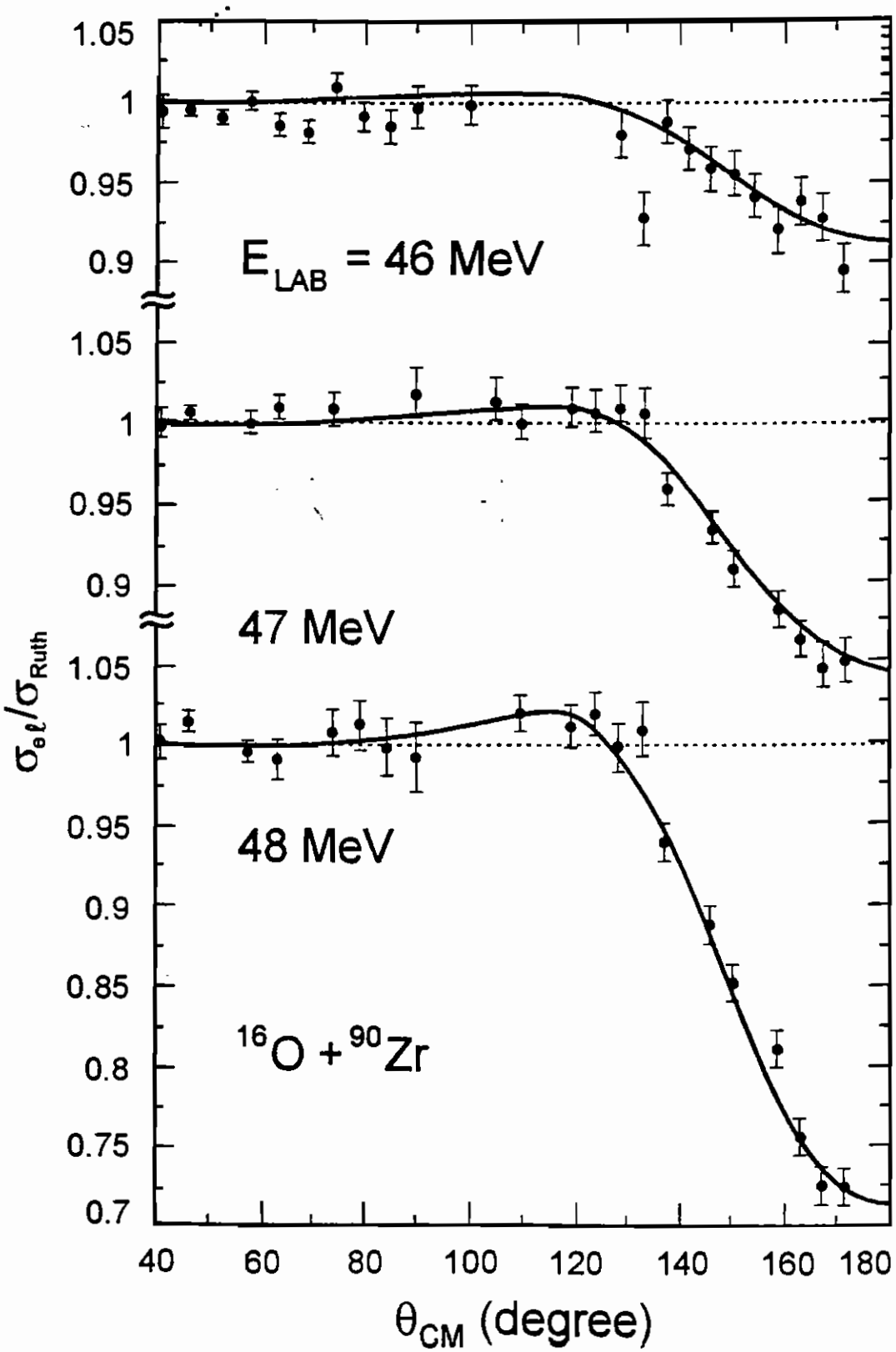
1.05
1
0.95
0.9
E_{LAB} = 46 MeV
1.05
1
0.95
0.9
47 MeV
1.05
1
0.95
0.9
0.85
0.8
0.75
0.7
48 MeV
$^{16}O + ^{90}Zr$
$\sigma_{el}/\sigma_{Ruth}$
40
60
80
100
120
140
160
180
θ_{CM} (degree)

Fig. 3

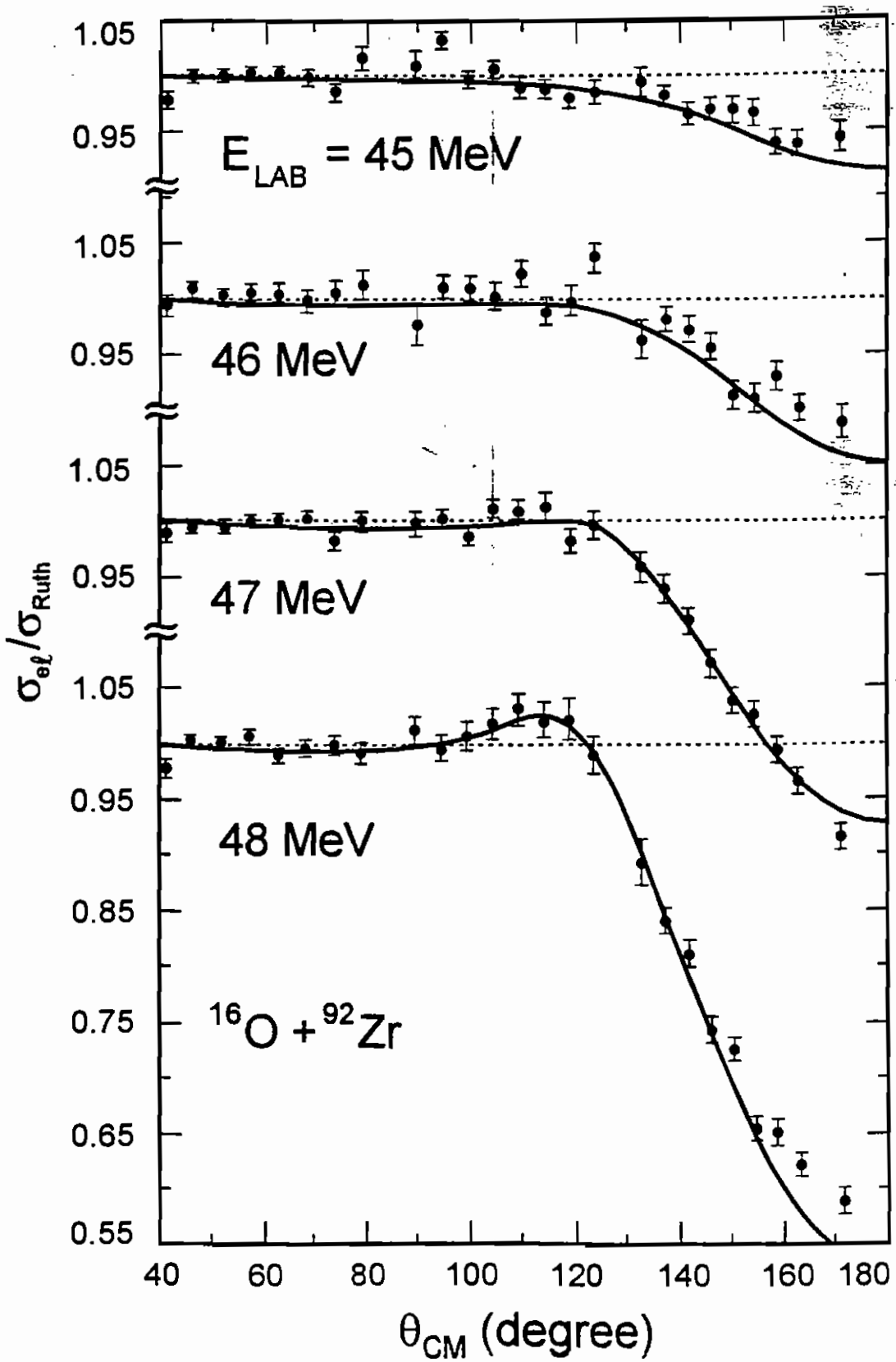
1.05
0.95
E_{LAB} = 45 MeV
46 MeV
47 MeV
48 MeV
$^{16}O + ^{92}Zr$
$\sigma_{el}/\sigma_{Ruth}$
0.85
0.75
0.65
0.55
40
60
80
100
120
140
160
180
θ_{CM} (degree)

Fig. 4

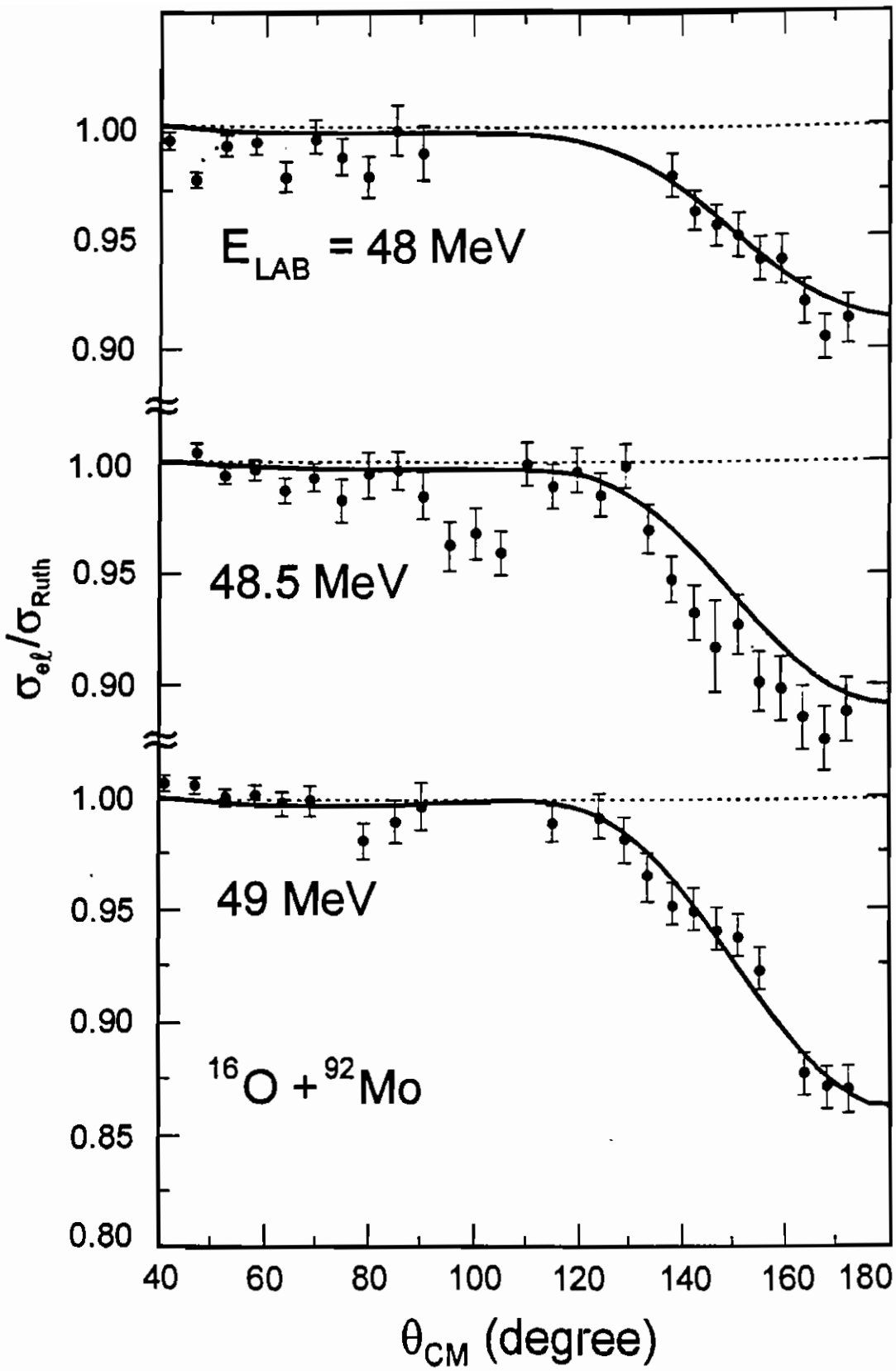
1.00
0.95
0.90
E_{LAB} = 48 MeV
1.00
0.95
0.90
48.5 MeV
1.00
0.95
0.90
0.85
0.80
49 MeV
$^{16}O + ^{92}Mo$
$\sigma_{el}/\sigma_{Ruth}$
40
60
80
100
120
140
160
180
θ_{CM} (degree)

Fig. 5

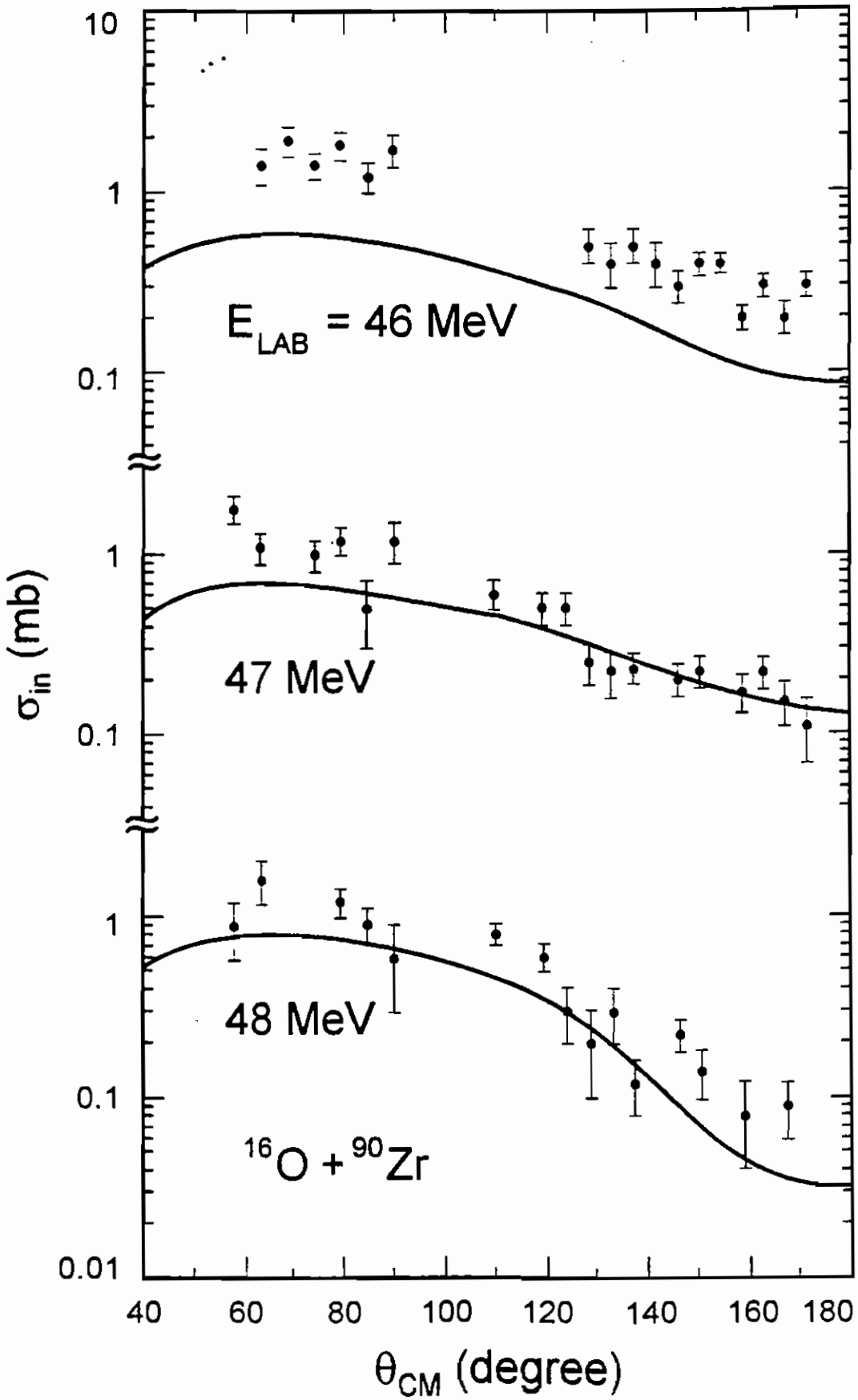
10
1
0.1
1
0.1
1
0.1
0.01
E_{LAB} = 46 MeV
47 MeV
48 MeV
$^{16}O + ^{90}Zr$
σ_{in} (mb)
40
60
80
100
120
140
160
180
θ_{CM} (degree)

Fig. 6

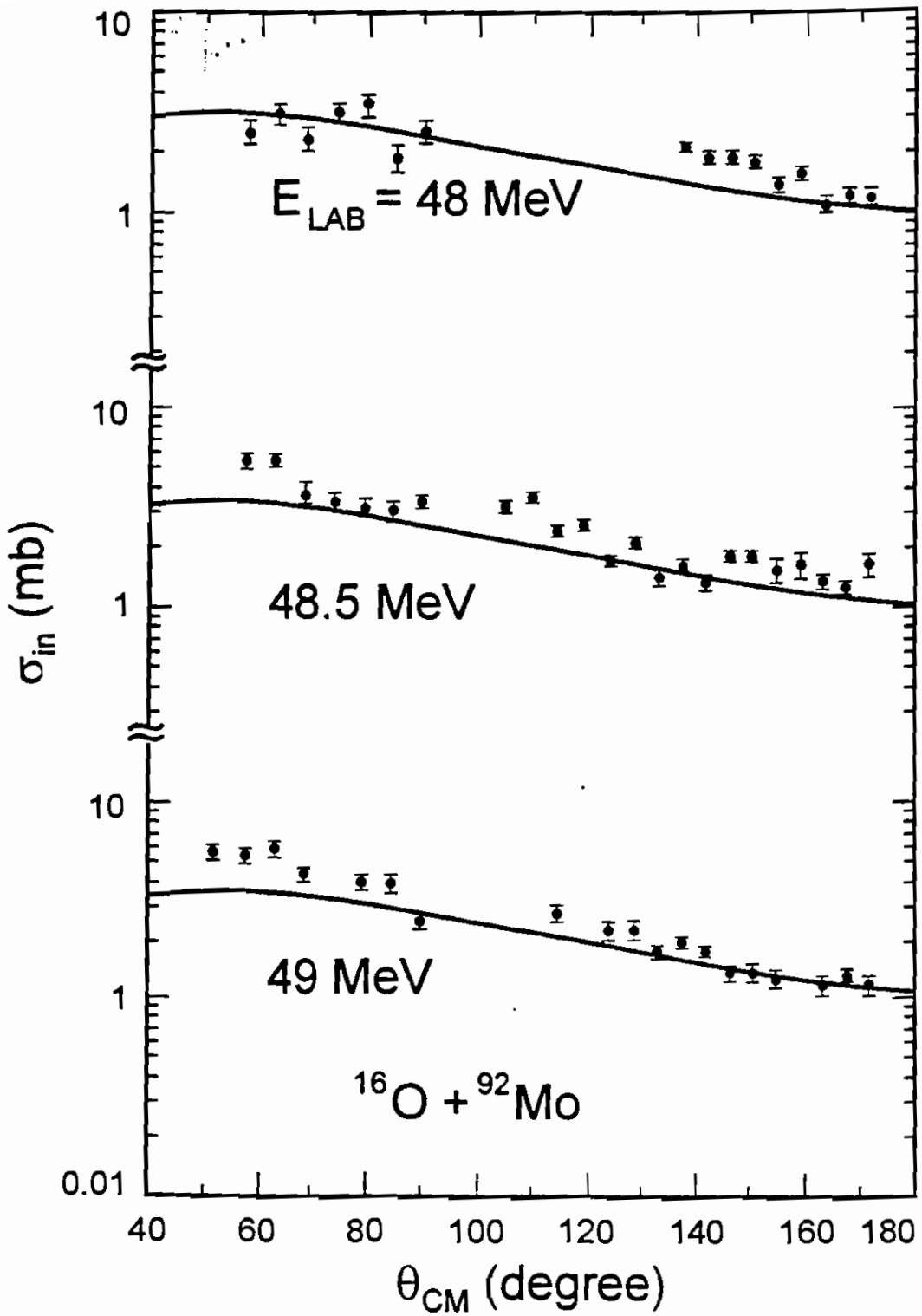
10
1
10
1
10
1
0.01
E_{LAB} = 48 MeV
48.5 MeV
49 MeV
$^{16}O + ^{92}Mo$
σ_{in} (mb)
40
60
80
100
120
140
160
180
θ_{CM} (degree)

Fig. 7

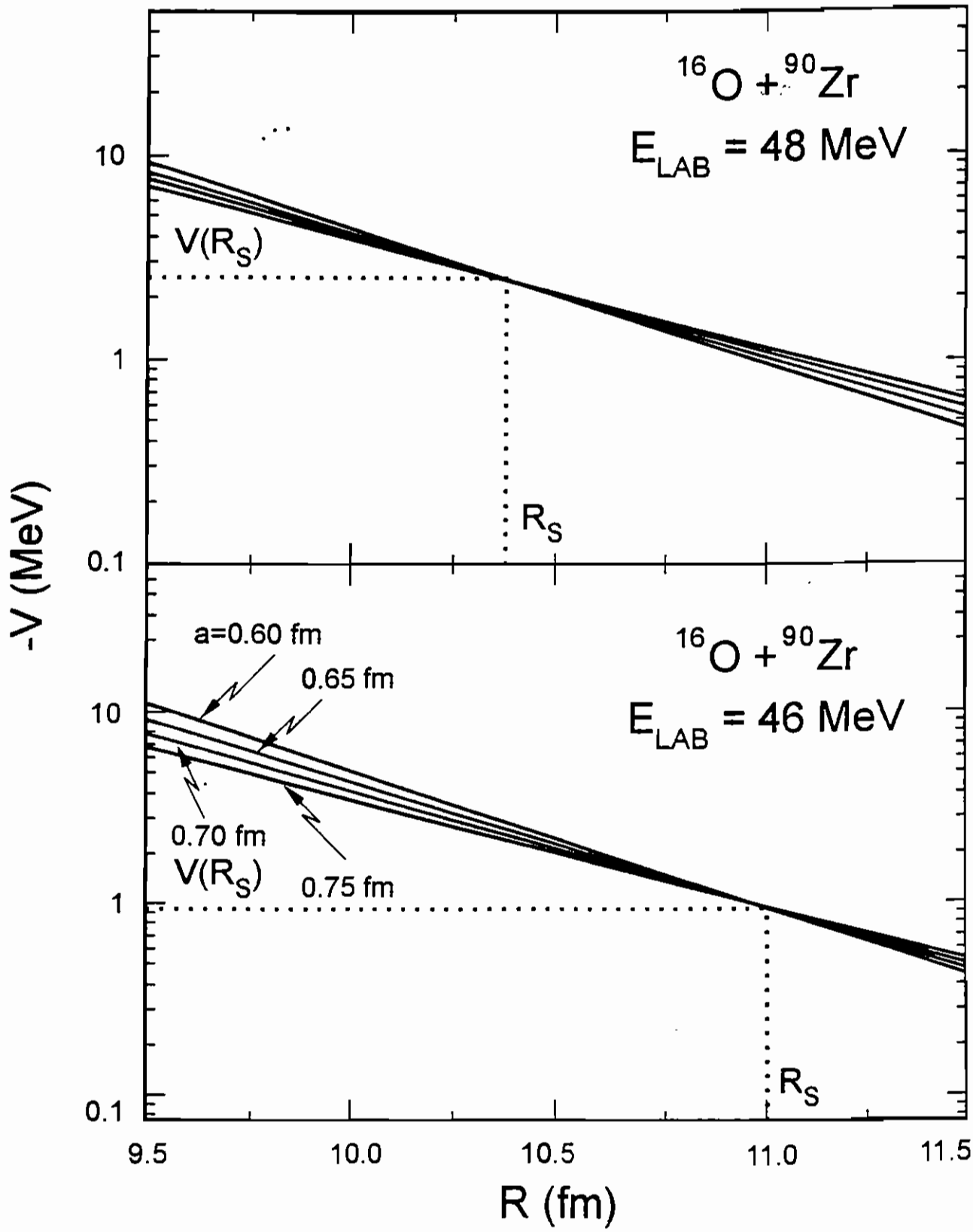
$^{16}O + ^{90}Zr$
E_{LAB} = 48 MeV
$V(R_S)$
R_S
$^{16}O + ^{90}Zr$
E_{LAB} = 46 MeV
a=0.60 fm
0.65 fm
0.70 fm
0.75 fm
$V(R_S)$
R_S
-V (MeV)
R (fm)
10
1
0.1
9.5
10.0
10.5
11.0
11.5

Fig. 8

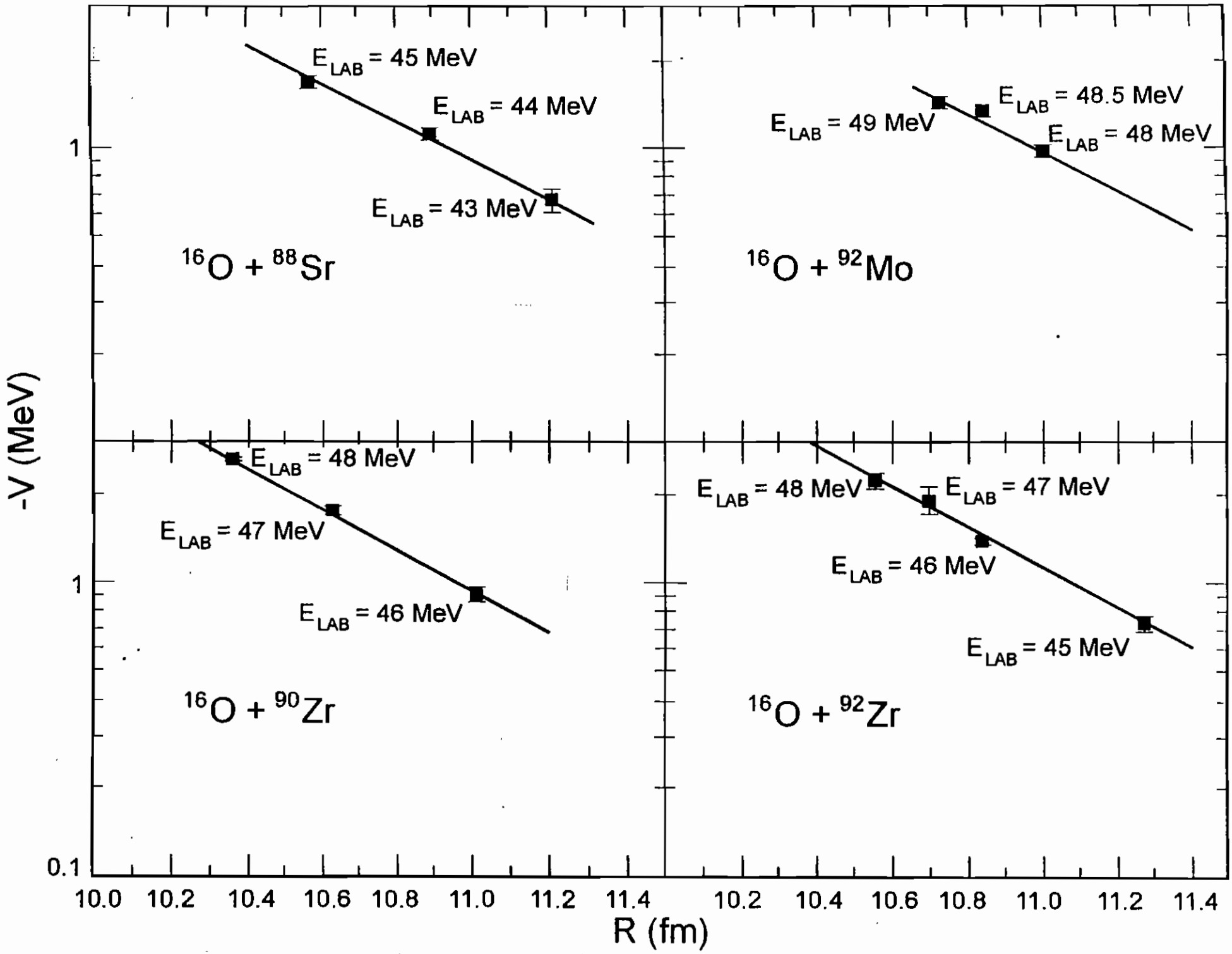
E_LAB = 45 MeV
E_LAB = 44 MeV
E_LAB = 43 MeV
16O + 88Sr
E_LAB = 49 MeV
E_LAB = 48.5 MeV
E_LAB = 48 MeV
16O + 92Mo
E_LAB = 48 MeV
E_LAB = 47 MeV
E_LAB = 46 MeV
16O + 90Zr
E_LAB = 48 MeV
E_LAB = 47 MeV
E_LAB = 46 MeV
E_LAB = 45 MeV
16O + 92Zr
-V (MeV)
1
1
0.1
10.0
10.2
10.4
10.6
10.8
11.0
11.2
11.4
R (fm)

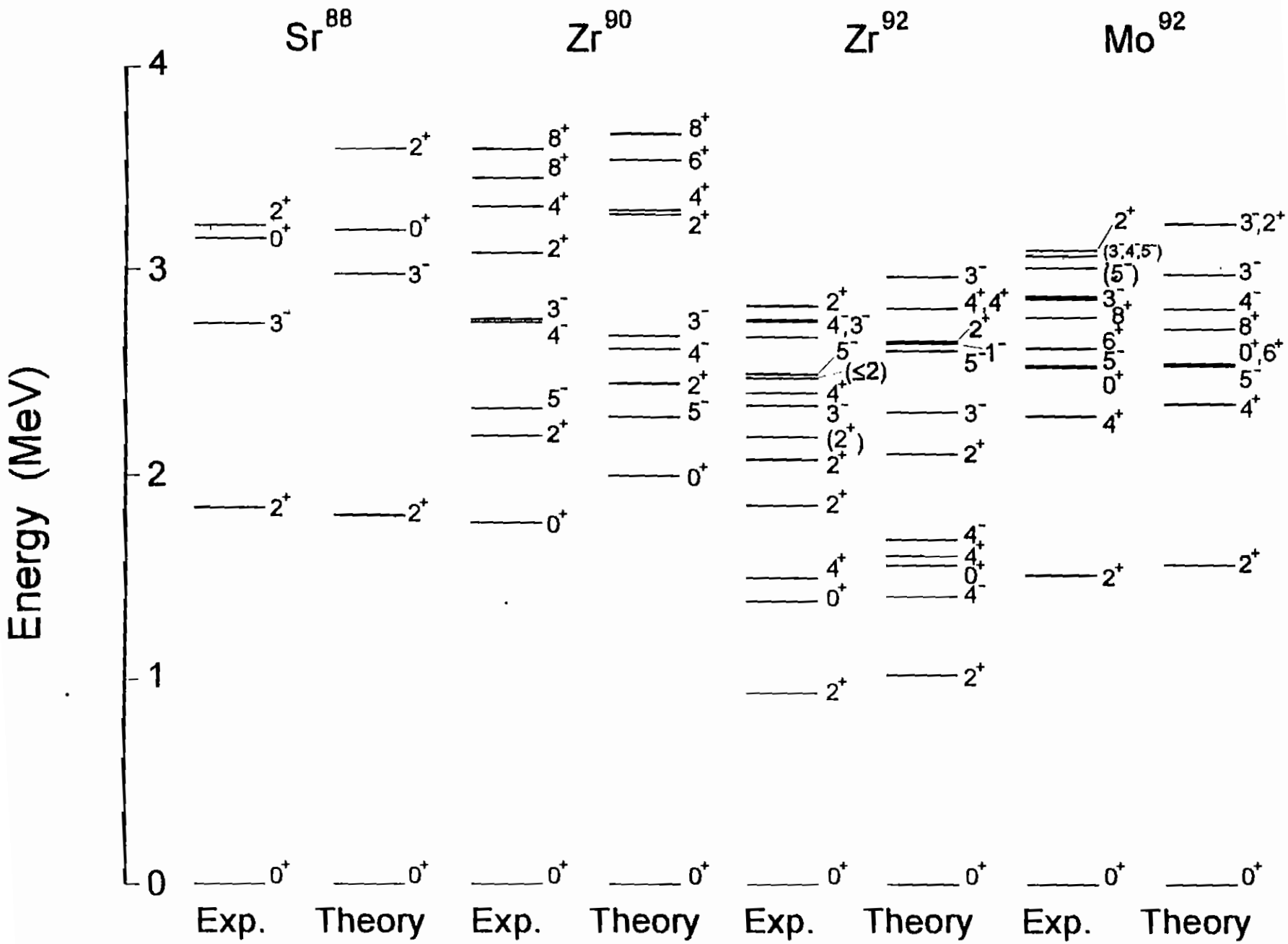
Sr88
Zr90
Zr92
Mo92
Energy (MeV)
0
1
2
3
4
Exp.
Theory
Exp.
Theory
Exp.
Theory
Exp.
Theory

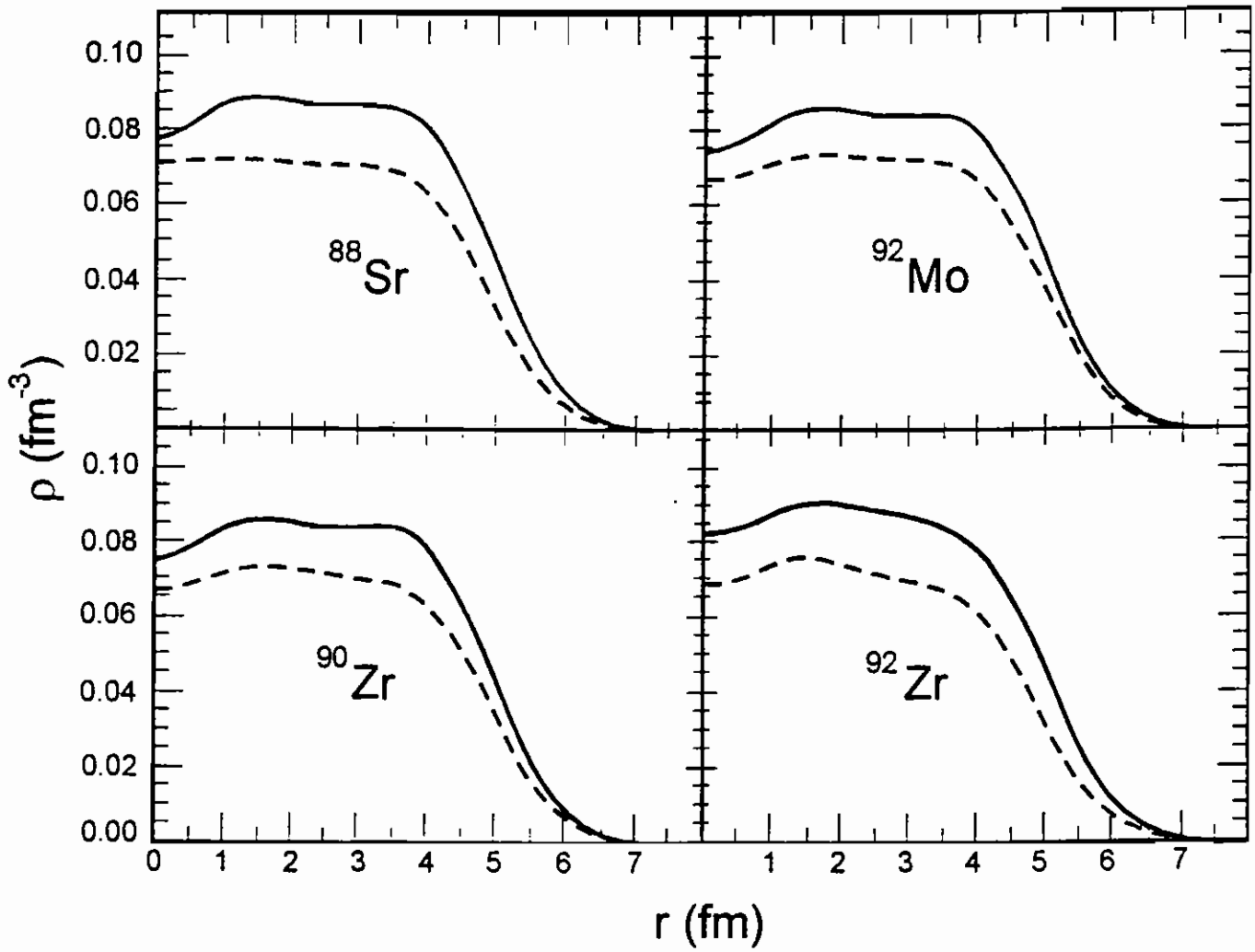
0.10
0.08
0.06
0.04
0.02
0.00
ρ (fm^{-3})
^{88}Sr
^{92}Mo
^{90}Zr
^{92}Zr
0 1 2 3 4 5 6 7
1 2 3 4 5 6 7
r (fm)

Fig. 11

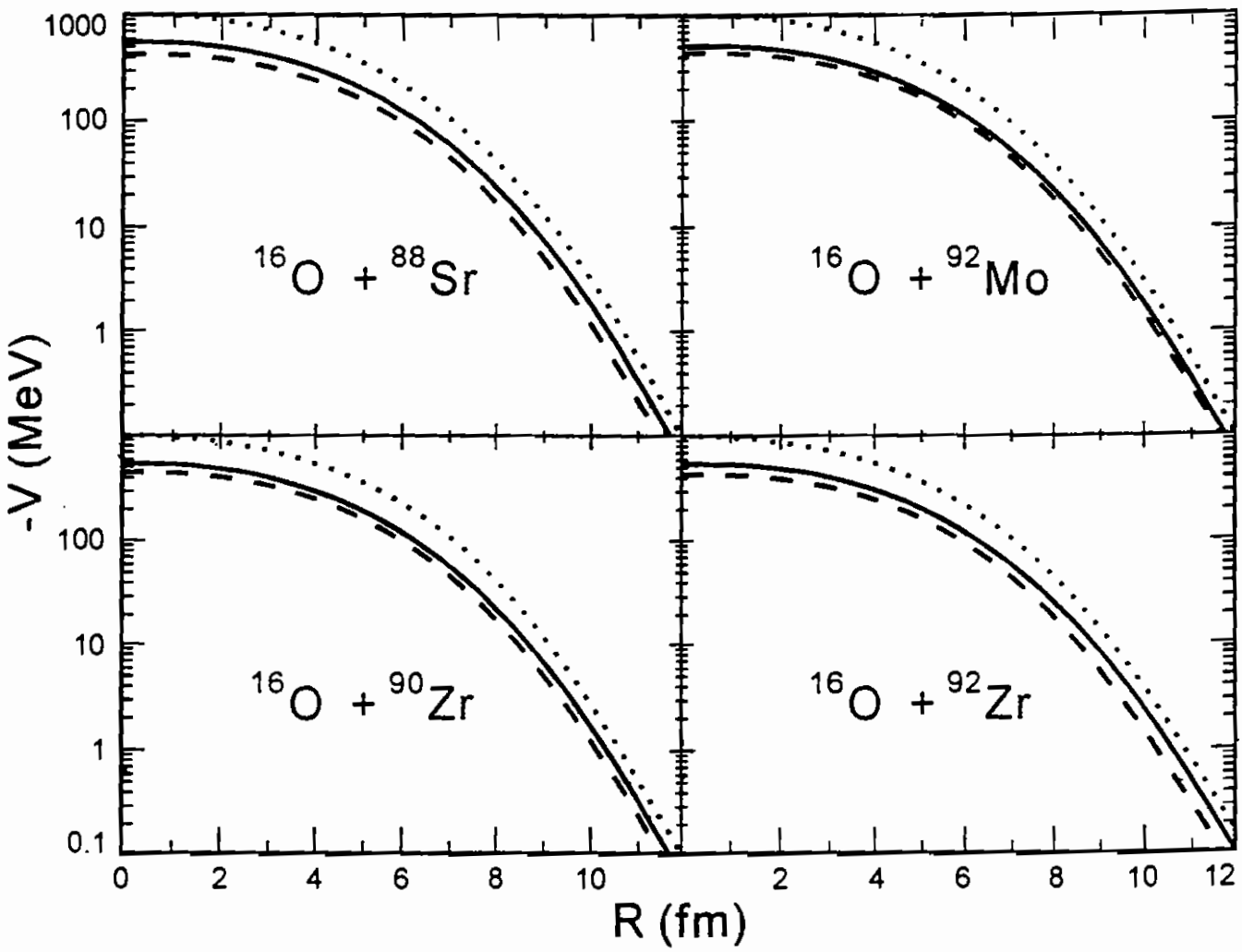
1000
100
10
1
100
10
1
0.1
-V (MeV)
$^{16}O + ^{88}Sr$
$^{16}O + ^{92}Mo$
$^{16}O + ^{90}Zr$
$^{16}O + ^{92}Zr$
0
2
4
6
8
10
2
4
6
8
10
12
R (fm)

Fig. 12

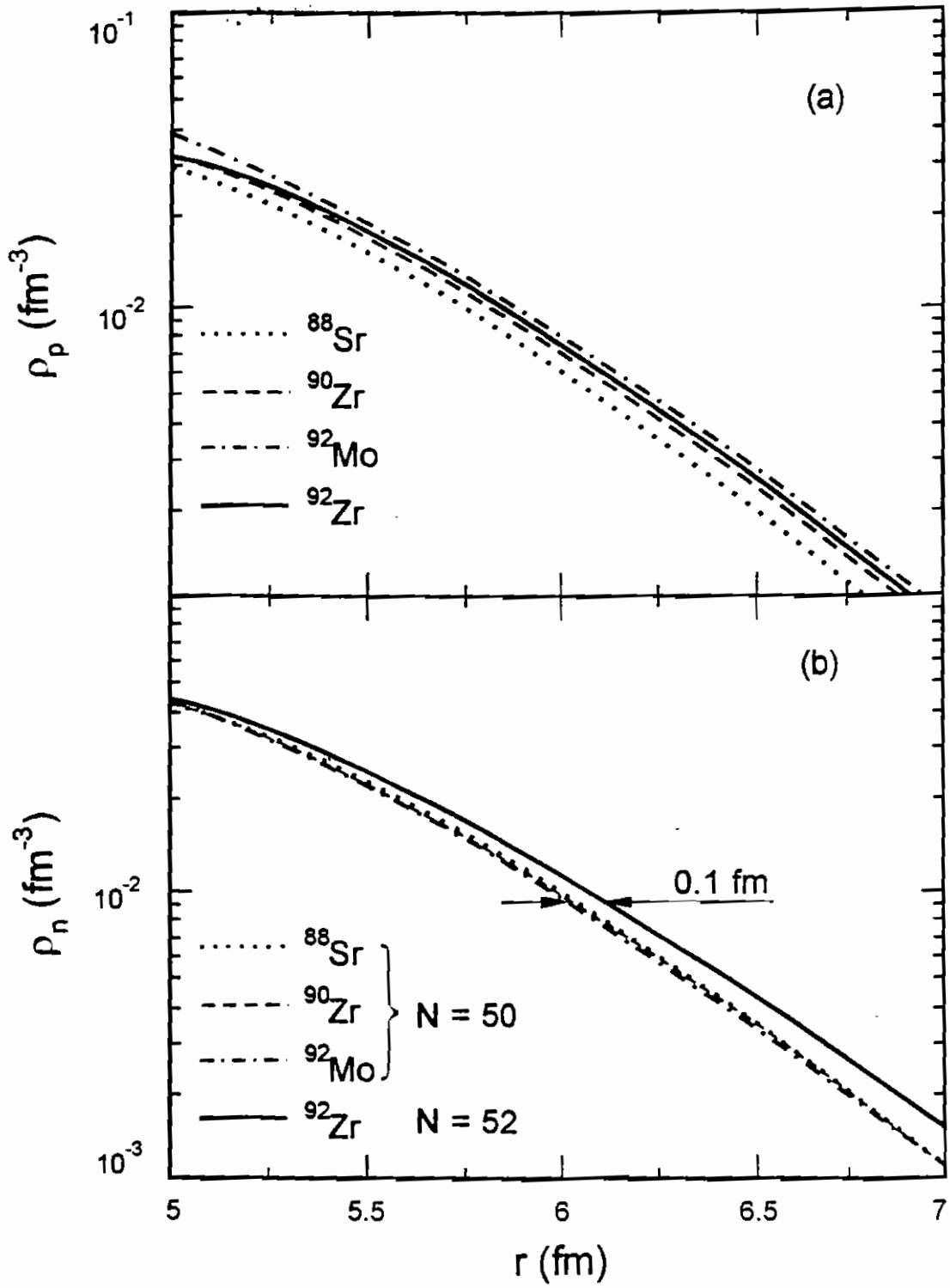
(a)
(b)
ρ_p (fm^{-3})
ρ_n (fm^{-3})
10^{-1}
10^{-2}
10^{-3}
^{88}Sr
^{90}Zr
^{92}Mo
^{92}Zr
N = 50
N = 52
0.1 fm
5
5.5
6
6.5
7
r (fm)

Fig. 13

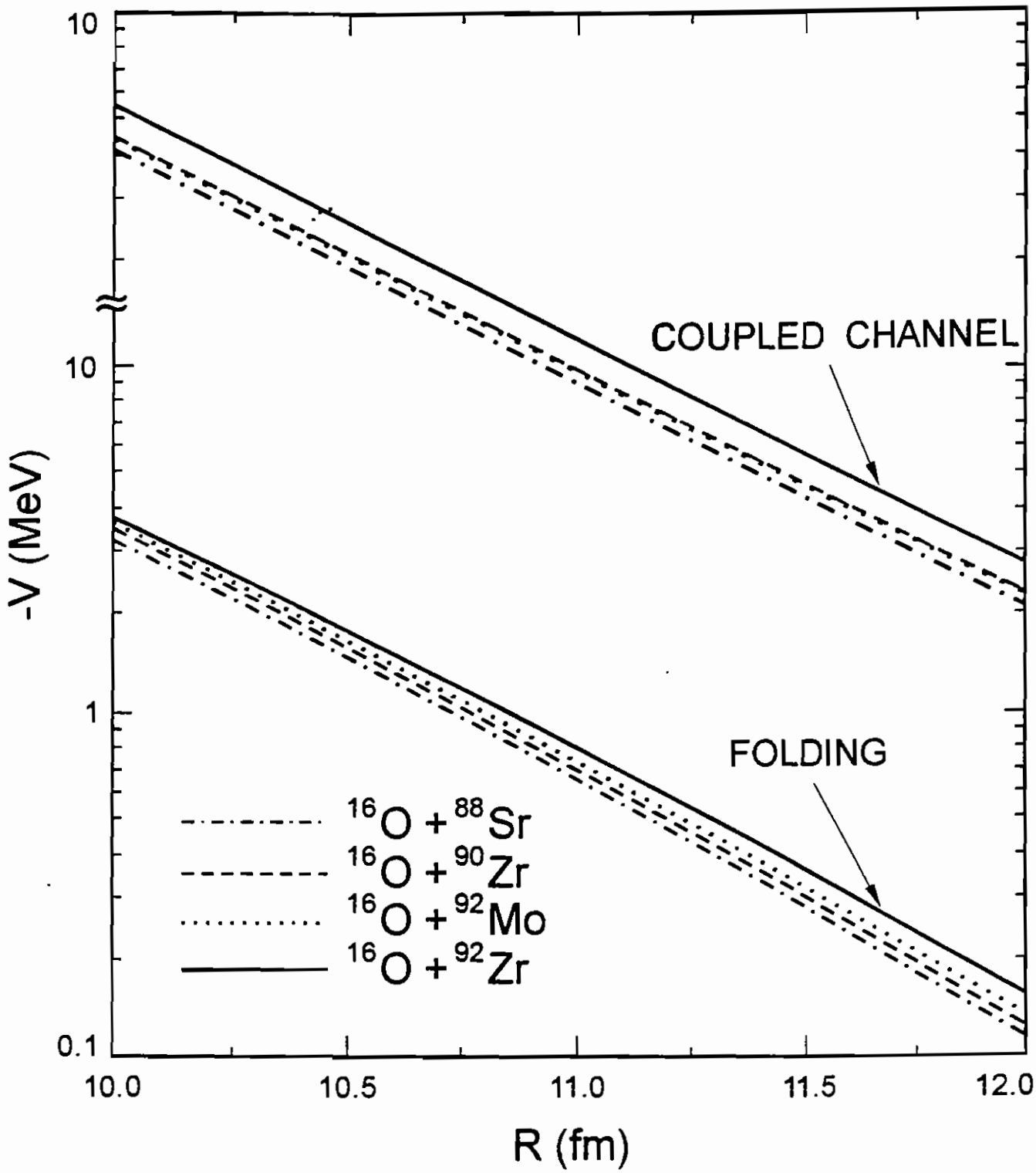
10
10
1
0.1
-V (MeV)
10.0
10.5
11.0
11.5
12.0
R (fm)
COUPLED CHANNEL
FOLDING
$^{16}O + ^{88}Sr$
$^{16}O + ^{90}Zr$
$^{16}O + ^{92}Mo$
$^{16}O + ^{92}Zr$

Fig. 14

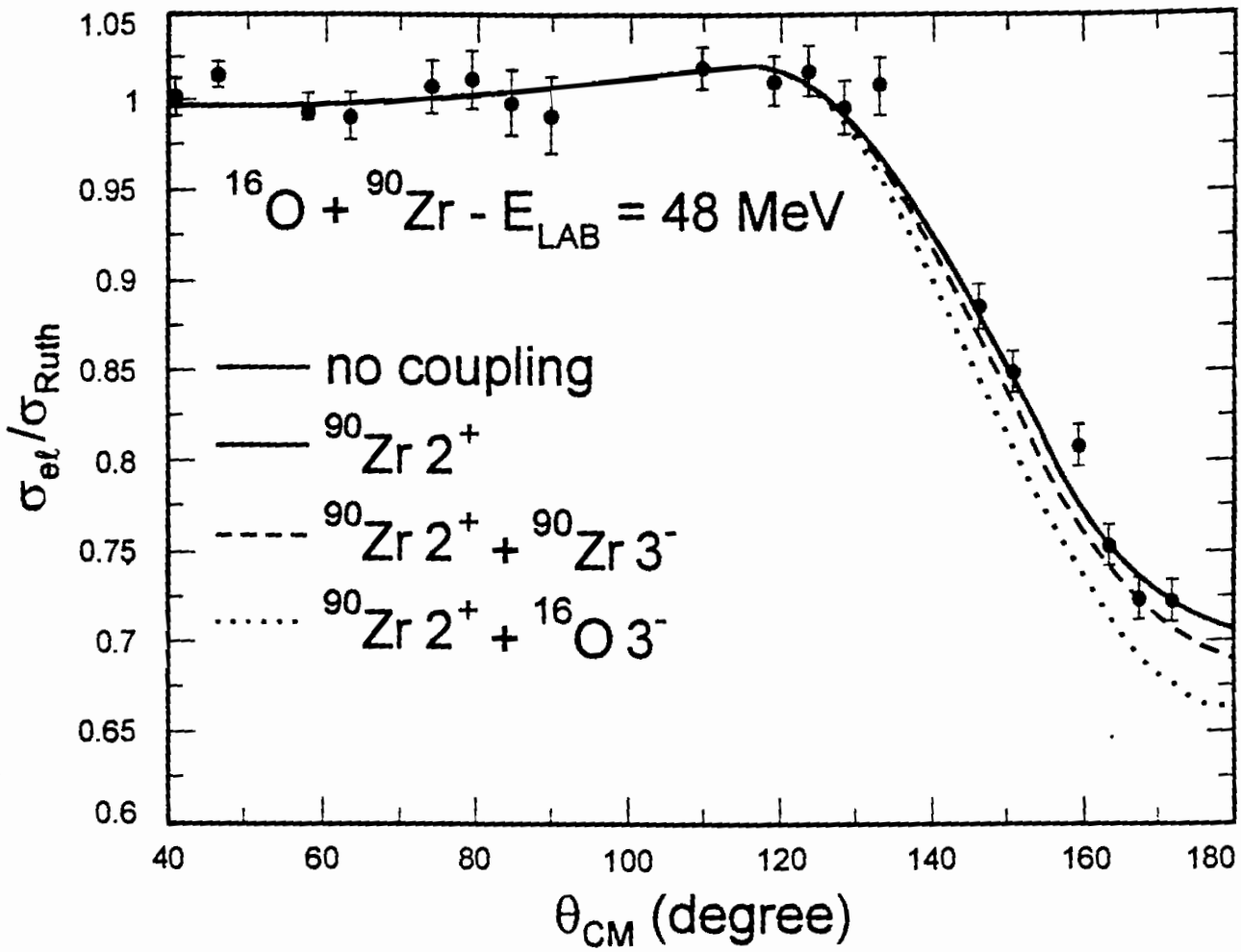
$^{16}O + ^{90}Zr$ - E_{LAB} = 48 MeV
no coupling
$^{90}Zr\ 2^+$
$^{90}Zr\ 2^+ + ^{90}Zr\ 3^-$
$^{90}Zr\ 2^+ + ^{16}O\ 3^-$
$\sigma_{el}/\sigma_{Ruth}$
θ_{CM} (degree)
1.05
1
0.95
0.9
0.85
0.8
0.75
0.7
0.65
0.6
40
60
80
100
120
140
160
180

Fig. 15

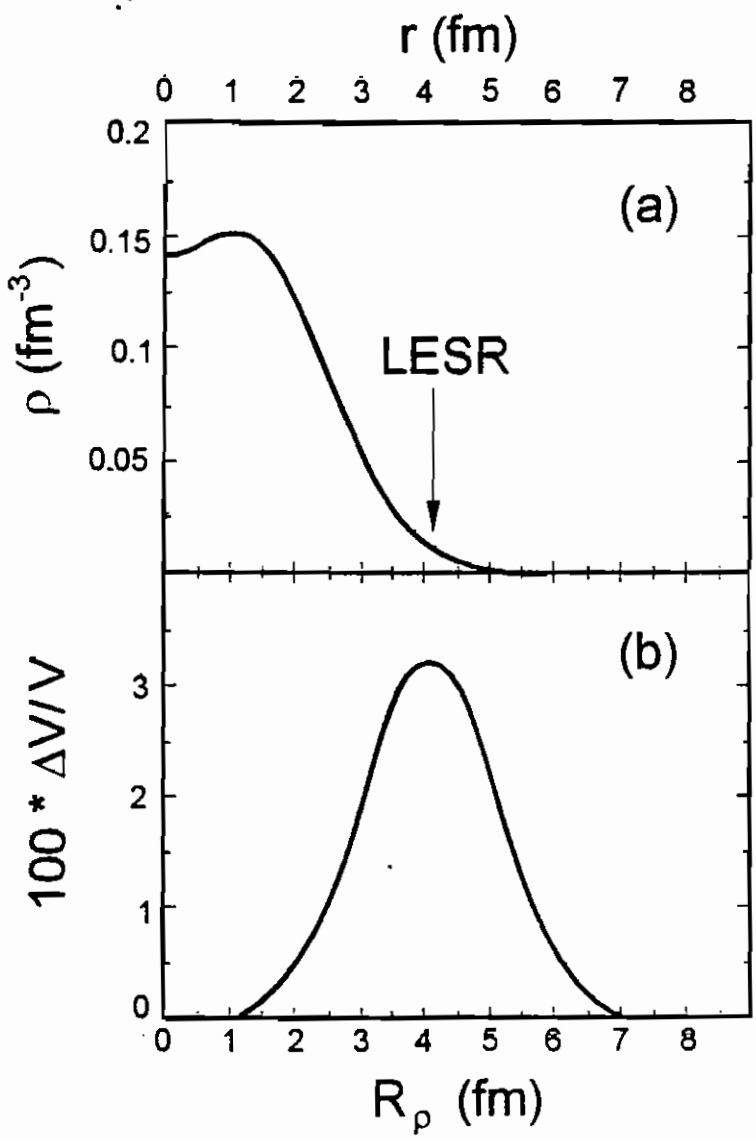
r (fm)
0 1 2 3 4 5 6 7 8
0.2
0.15
0.1
0.05
ρ (fm^{-3})
(a)
LESR
(b)
100 * ΔV/V
3
2
1
0
0 1 2 3 4 5 6 7 8
R_ρ (fm)

Fig. 16

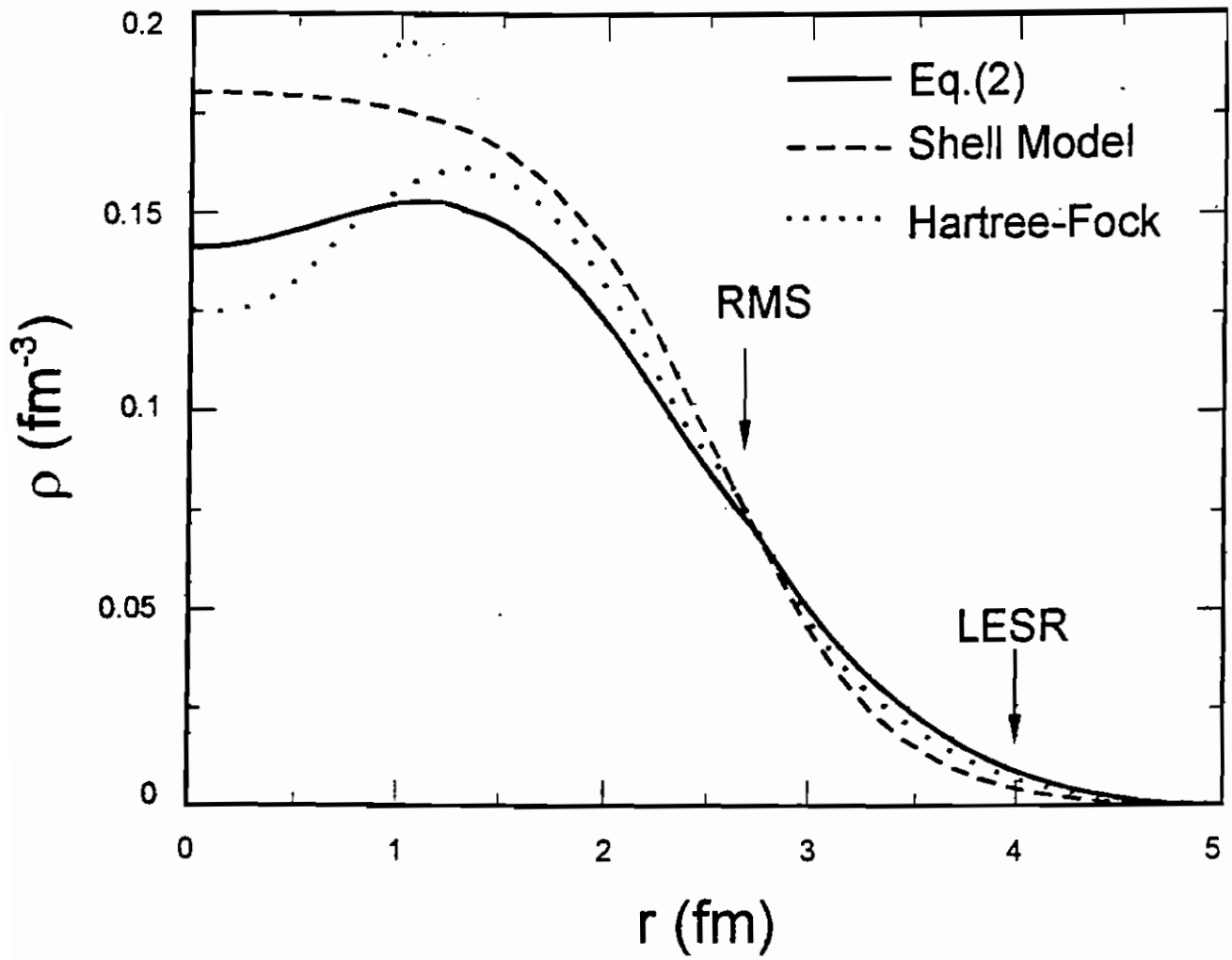
0.2
0.15
0.1
0.05
0
ρ (fm^{-3})
0
1
2
3
4
5
r (fm)
Eq.(2)
Shell Model
Hartree-Fock
RMS
LESR

Fig. 17

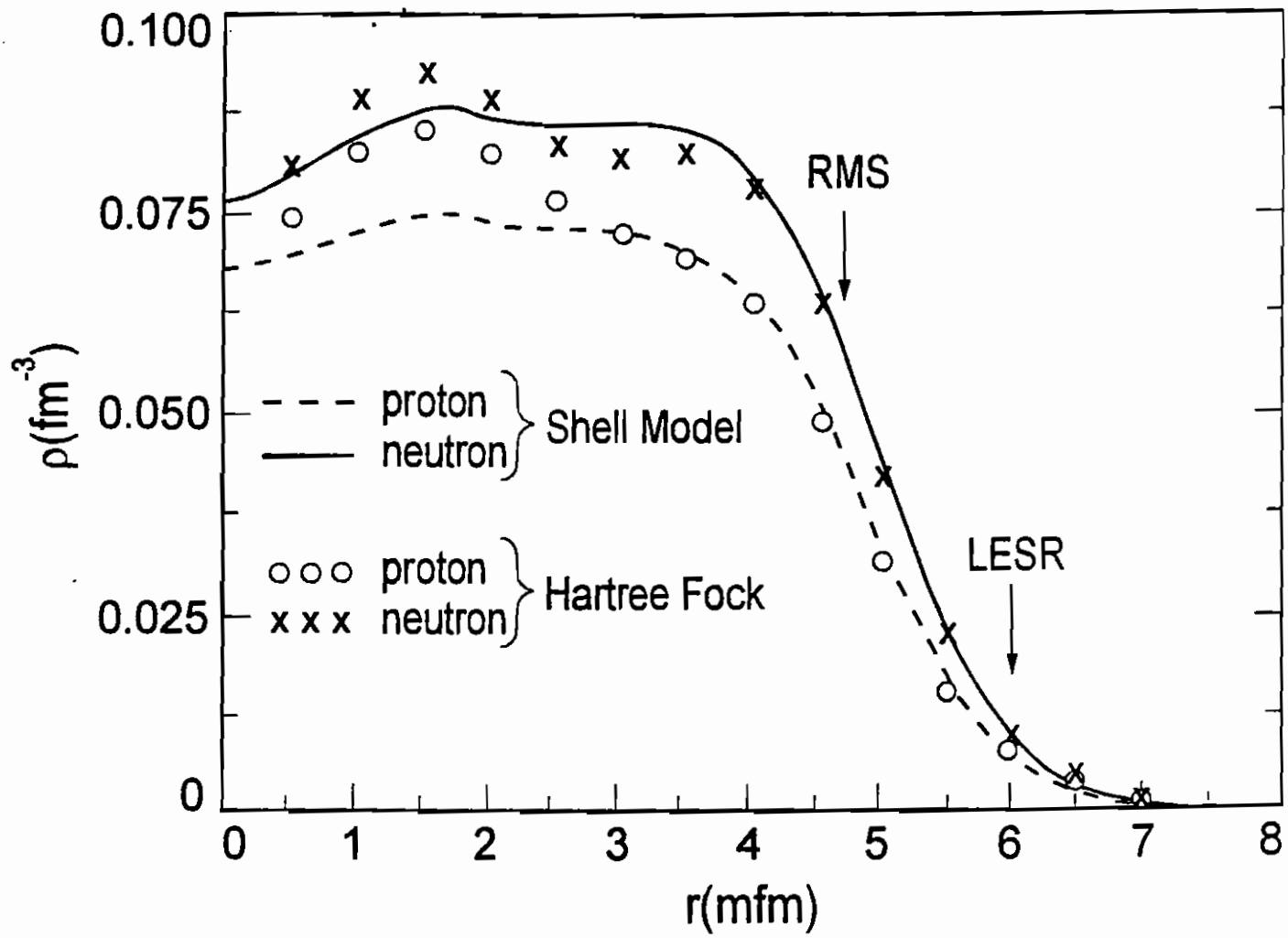
0.100
0.075
0.050
0.025
0
ρ(fm⁻³)
0
1
2
3
4
5
6
7
8
r(mfm)
RMS
LESR
proton
neutron
Shell Model
proton
neutron
Hartree Fock

Fig. 18

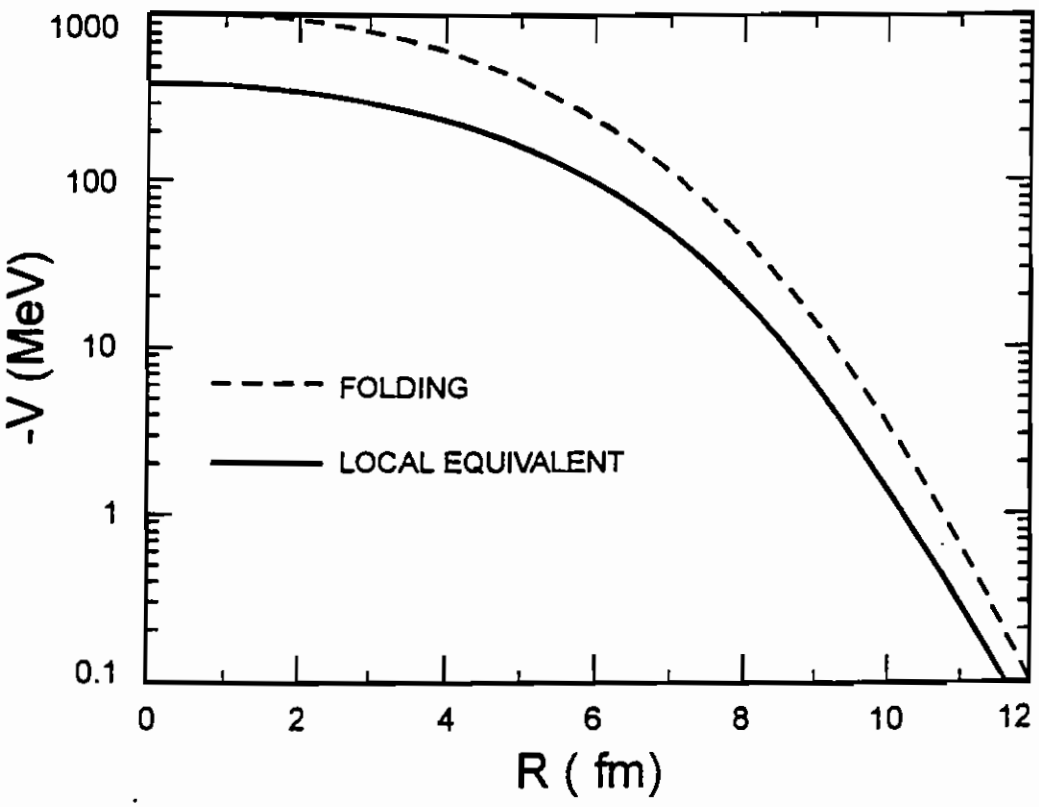
1000
100
10
1
0.1
-V (MeV)
FOLDING
LOCAL EQUIVALENT
0
2
4
6
8
10
12
R (fm)

Fig. 19

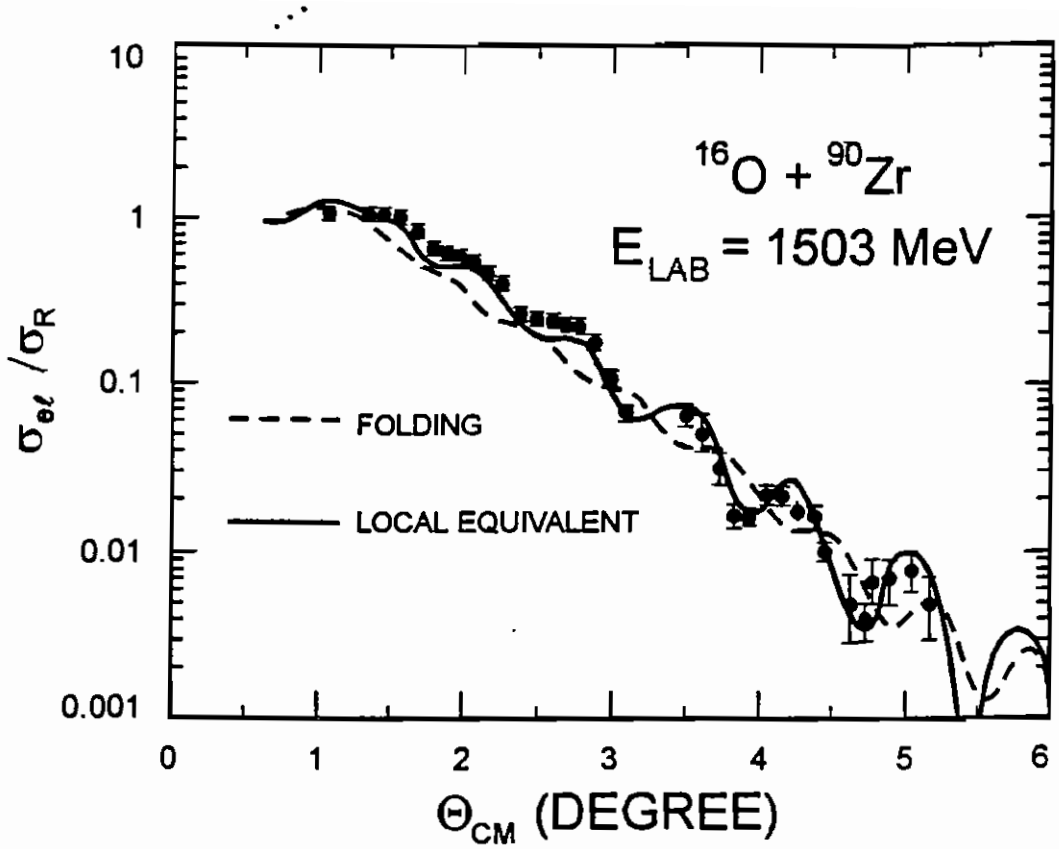
$^{16}O + ^{90}Zr$
E_{LAB} = 1503 MeV
FOLDING
LOCAL EQUIVALENT
σ_{el}/σ_R
Θ_{CM} (DEGREE)
10
1
0.1
0.01
0.001
0
1
2
3
4
5
6

Fig. 20

Ref. Ch 95

ELSEVIER

Nuclear Physics A 582 (1995) 305–313

NUCLEAR PHYSICS A

Experimental investigation of the ion–ion potential for the $^{16}O + ^{60}Ni$ system at large interaction distances *

L.C. Chamon, D. Pereira, E.S. Rossi Jr., C.P. Silva [1], R. Lichtenthäler Filho, L.C. Gomes

Laboratório Pelletron, Instituto de Física da Universidade de São Paulo, Caixa Postal 20516, 01452-990 São Paulo, SP, Brazil

Received 15 March 1994; revised 3 October 1994

Abstract

Precise measurements of the elastic and inelastic scattering cross sections for the $^{16}O + ^{60}Ni$ system at the sub-barrier energies were made. Coupled channel analysis of the only two open channels were performed. The behaviour of the ion–ion potential at large distances is discussed.

Keywords: NUCLEAR REACTIONS: $^{16}O + ^{60}Ni$ and $^{16}O + ^{60}Ni^*(2^+)$, measured $\sigma(\theta)$ at $E_{lab} = 35.0$, 35.5 and 37.0 MeV. Deduced optical potential. Coupled channel calculations.

1. Introduction

We present the recently measured elastic and inelastic cross sections for the $^{16}O + ^{60}Ni$ system at the sub-barrier energies $E_{lab} = 35.0$, 35.5 and 37.0 MeV. The differential cross sections were measured from $\theta_{CM} = 40°$ to 175°, with a precision in the elastic data of 1%. With this accuracy, we were able to investigate the importance of the nuclear interaction at these low energies. We have also included in our analysis the data for $E_{lab} = 36.0$ and 38.0 MeV from Refs. [1,2]. The only reaction channel with relevant cross section at $35 \leqslant E_{lab} \leqslant 38$ MeV, 4.5 to 7.5 MeV below the fusion barrier [3], is the inelastic collision for the first $^{60}Ni(2^+, 1.33\ MeV)$ excited state. Due to the fact

* Partially supported by FINEP and CNPq.

[1] Post-graduate fellowship from FAPESP.

SSDI 0375-9474(94)00491-9

that only two channels are important, the coupled channel (CC) calculations by the ECIS code [4] were very reliable. Our main conclusions based on the coupled channel analysis of the experimental data are: (i) the only important reaction channel within the accuracy of the data is the 2^+ (1.33 MeV) target excitation; (ii) the small deviations from the Rutherford scattering of the elastic data for $\theta_{CM} \leqslant 130°$ are explained mainly by the long range Coulomb absorption; therefore, the nuclear interaction contribution is restricted to the backward angles; (iii) it is possible to explain the data using a nuclear potential which is real in the surface region and independent of the bombarding energy. The consistency between this nuclear potential and the M3Y double folding potential is discussed.

This paper is organized as follows: Section 2 gives the experimental details and results, Section 3 describes the coupled channel analysis and Section 4 contains our conclusions.

2. Experimental details and results

Our measurements were made using the ^{16}O beam from the São Paulo 8UD Pelletron Accelerator. The detection system was a set of nine surface barrier detectors spaced 5° apart. In front of each detector there was a set of three collimators to avoid slit-scattered particles from reaching the detectors. The solid angle and the angular aperture for each detector and the target were 4.0×10^{-4} sr and 0.6° respectively. The thickness of the enriched (99.9%) nickel target was about 30 $\mu g/cm^2$ evaporated onto a carbon foil (5 $\mu g/cm^2$). A layer of gold was evaporated onto the target for data normalization. We used a monitor detector at $\theta_{lab} = 30°$ to be sure that no target deterioration occurred during bombardment. The energy resolution was about 200 keV that allowed a complete separation between the elastic and the inelastic (2^+, 1.33 MeV) scattering peaks. A typical energy spectrum is shown in Fig. 1. Due to the background near the elastic scattering peak (see Fig. 1b), a very small correction was necessary in the counts related to the elastic and inelastic scattering processes. Figs. 2 and 3 exhibit the elastic and the inelastic scattering cross sections for the $^{16}O + ^{60}Ni$ system at $35 \leqslant E_{lab} \leqslant 38$ MeV. The differential cross sections for the inelastic target excitation (2^+, 1.33 MeV) are about 1% of the corresponding elastic scattering cross sections, and the integrated (2^-) inelastic scattering cross sections have values between 30 and 50 mb. No evidence was found in the energy spectra for population of other target or projectile excited states (see Fig. 1b). We used the time of flight technique [5] for the detection of the few nucleon transfer processes. The cross sections for these processes do not have values anywhere near those of the 2^+ target excitation; for example, at the bombarding energy of 38 MeV our measurements give a cross section of the order of 10^2 μb for the reaction $^{60}Ni(^{16}O,^{12}C)$; for lower energies no evidence of a transfer process was detected.

We assumed that the fusion cross section is negligible at these energies. This conclusion results from the analysis that Udagawa et al. [6] made of our previous fusion data for the $^{16}O+^{60}Ni$ system [3,7] in the bombarding energy range $40 \leqslant E_{lab} \leqslant 64$ MeV. In

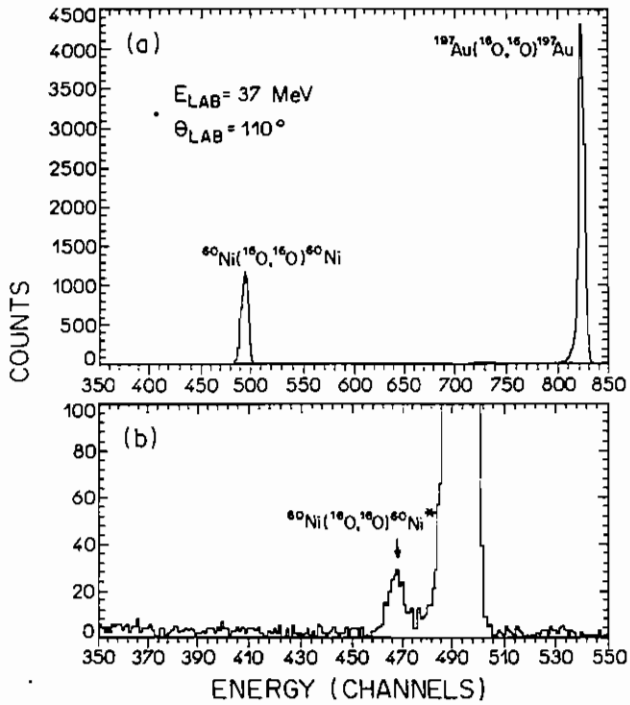

Fig. 1. (a) Energy spectrum at E_{lab} = 37 MeV and θ_{lab} = 110°. The peaks correspond to the elastic scattering processes for the systems as indicated. (b) Expansion of both axes of Fig. 1a in the region of the elastic scattering peak for the $^{16}O+^{60}Ni$ system. The arrow indicates the peak corresponding to the inelastic excitation for the 2^+ (1.33 MeV) target state.

their studies in the sub and near fusion barrier region, they obtained a threshold energy T_{CM} = 29.3 MeV that is 4.5 MeV below the fusion barrier (V^B_{CM} = 33.8 MeV). From Stelson's systematics [8] we estimated fusion cross sections of the order of 10^2 μb for energies near T_{CM}. Therefore, we can consider the inelastic collision for the first 2^+ target excitation as the only reaction channel with relevant cross section for $E_{lab} \leqslant 38.0$ MeV.

3. Coupled channel analysis and discussion

The value r_c = 1.06 fm, obtained from electron scattering experiments [9], was assumed for the Coulomb radius in the CC analysis. The parameter β_c was obtained by fitting the inelastic scattering data for E_{lab} = 35.0, 35.5 and 36.0 MeV and considering only $\theta_{CM} \leqslant 100°$. The best fit value for β_c was 0.265 ± 0.010, which is in agreement with values obtained from other experiments [2,10]. In Figs. 2 and 3 we show the results of the CC calculations considering only the Coulomb interaction (dotted lines) and including both Coulomb and nuclear interaction (solid lines). We would like to emphasize that the nuclear interaction is only important for backward angles, $\theta_{CM} \geqslant$ 130°.

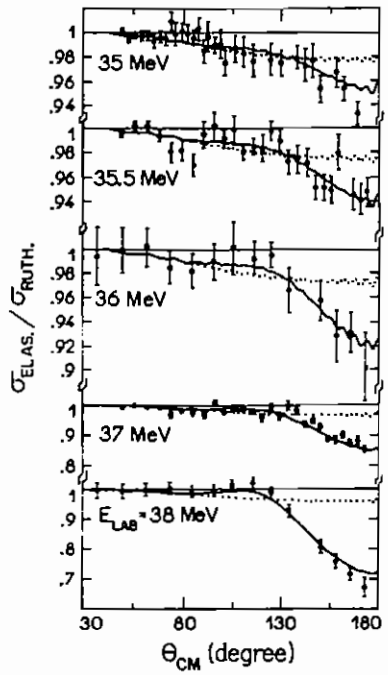

Fig. 2. Elastic differential angular distributions for the $^{16}O + ^{60}Ni$ system at E_{lab} = 35.0, 35.5 and 37.0 MeV (this work) and E_{lab} = 36.0 and 38.0 MeV (Ref. [1]). Note the change of scale for the E_{lab} = 37.0 and 38.0 MeV data. The curves correspond to the coupled channel calculations considering only the Coulomb interaction (dotted curves) and Coulomb plus the nuclear interaction (solid curves).

Similarly to Tamura in the CC analysis of the proton plus nickel systems [11], we assumed ^{60}Ni spherically symmetric but susceptible to vibration around the spherical shape. The one phonon 2_1^+(1.33 MeV) was considered by us in the CC calculations. We used a matching radius of 30 fm, 50 partial waves in the integration of the coupled equations, Coulomb corrections [12] up to 250 partial waves and integration stepsize of 0.05 fm. With these settings we observed no problem of numerical convergence in the CC computation. As it is commonly used in CC calculations [13], we also considered an imaginary potential of the Woods–Saxon shape, with depth W_0 = 30 MeV, diffuseness a_I = 0.2 fm and radius parameter r_I = 0.8 fm. In the surface region this potential is very small ($W(r) < 10^{-7}$ MeV for $r > 9$ fm) and represents a small internal absorption of the system. It is important to mention that the results of the calculations are rather insensitive to the variations of W_0.

The real potential had a Woods–Saxon shape with a fixed radius equal to the Coulomb radius of 1.06 fm. The depth V_0, the diffuseness a and the nuclear phonon amplitude β_N were searched for the best fit. For each energy we found a family of potentials that gave equivalent fits to the data; the χ^2 values for these fits are shown in Table 1. In Fig. 4a several of these potentials are exhibited and we observe that for each energy they cross at a well-defined radius, usually referred to as the strong absorption radius, where

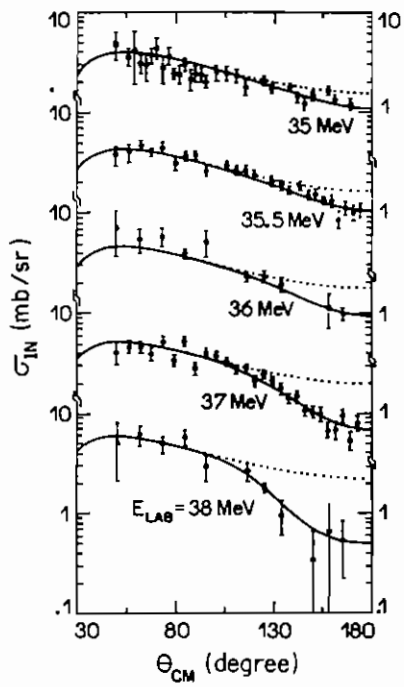

Fig. 3. The same as in Fig. 2 but for the inelastic scattering cross sections. The vertical scale represents the cross sections in millibarns. The data of 36.0 and 38.0 MeV are from Ref. [2].

the value of the potential has the least ambiguity. Contrary to what happens at higher energies [14], this "strong absorption radius" is very sensitive to the bombarding energy. In Fig. 4b we plotted these potential values for the five energies under consideration with the error bars estimated from the variation of χ^2 by unity. Fig. 5 illustrates how the fits, indicated by dashed lines, deviate from the elastic data (E_{lab} = 36 MeV) for such a change in χ^2. It is important to mention that the results for estimation of the error bar for the strength of the potential are rather insensitive to the diffuseness parameter a.

The solid line in Fig. 4b exhibits a fit to the potential values at the strong absorption radius which shows that the resulting real nuclear potential has a simple exponential shape in the surface region. The best fit diffuseness for this potential was found to be

Table 1
Values of χ^2 obtained for the elastic and inelastic angular distributions in the bombarding energy range $35.0 \leqslant E_{lab} \leqslant 38.0$ MeV. N_E and N_I are the number of elastic and inelastic scattering data points

E_{lab} (MeV)	N_E	N_I	χ^2
35.0	31	29	73.5
35.5	26	25	55.3
36.0	14	10	9.7
37.0	27	27	94.4
38.0	14	11	7.6

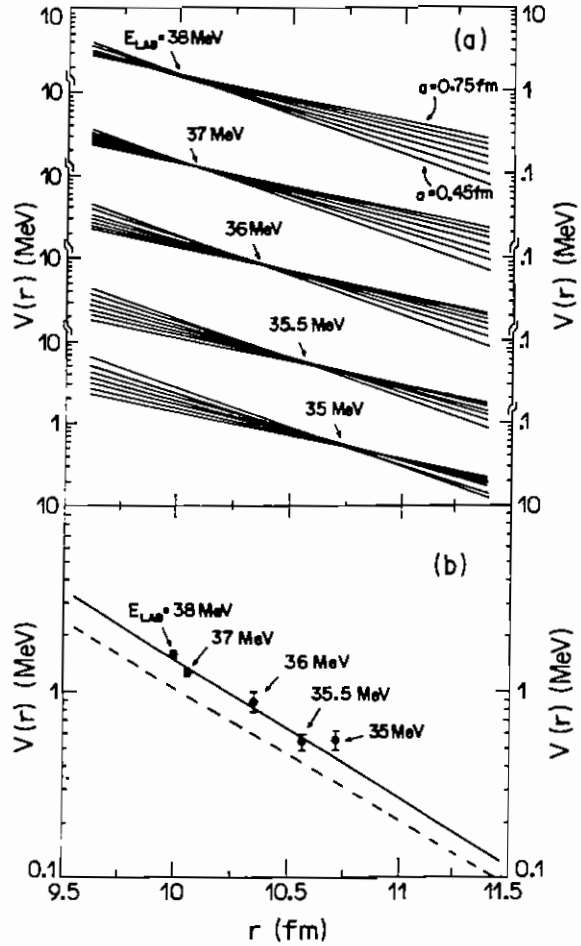

Fig. 4. (a) The nuclear real potential in the surface region as obtained by the coupled channel analysis for several values of the diffuseness and depth parameters. (b) Comparison among different potentials. The solid points represent the nuclear potential at the strong absorption radius as obtained from our CC analysis. The solid curve is an exponential potential with diffuseness of 0.58 fm. The dashed line is the M3Y double folding potential with unit normalization.

$a = 0.58 \pm 0.04$ fm. One should mention that, using a non-energy dependent nuclear potential in the CC calculations, it was also possible to fit simultaneously all the elastic and inelastic scattering data in the energy range $35 \leqslant E_{\rm lab} \leqslant 38$ MeV, with a reduced chi-square $\chi^2_{\rm red} = 1.19$. As an important result from these calculations a nuclear potential was obtained also with a best fit diffuseness value $a = 0.58$ fm. The solid lines in Figs. 2 and 3 represent the results of the CC calculations using this energy independent potential. For the corresponding $\beta_{\rm N}$ parameter we obtained the value 0.26 ± 0.03 that is equal, within the uncertainties, to that found for $\beta_{\rm c} = 0.265 \pm 0.010$.

We realized other CC calculations to investigate the contribution to the elastic and inelastic (2^+_1) scattering cross sections of couplings associated to other reaction channels

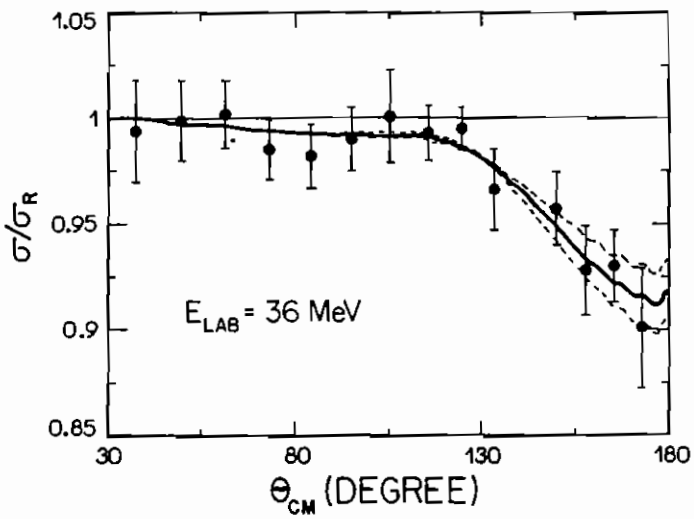

Fig. 5. Elastic scattering angular distribution at E_{lab} = 36.0 MeV. The solid curve corresponds to the best fit using coupled channel calculations with χ^2 = 9.7. The dashed curves correspond to fits considering the χ^2 increasing by unity.

which, due to their very small cross section values, have been not detected in our experiments. For inelastic channel couplings we considered the contribution of the lowest excitation energy two phonons states of ^{60}Ni, 2_2^+ (2.16 MeV), O_2^+ (2.28 MeV) and 4_2^+ (2.51 MeV); and also the 3^- (6.13 MeV) state of ^{16}O due to its large phonon amplitude [15]. The calculations showed that, in the energy range considered (4.5 to 7.5 MeV below the fusion barrier), the contributions of those couplings to the elastic and inelastic (2_1^+) cross sections are small compared with the data accuracy. We also evaluated the contribution of the 3^- state for energies just 1 to 2 MeV below to the fusion barrier. The results show much larger effects in the elastic cross sections compared to the lower energy cases, and the calculations predict an important contribution of this coupling to the fusion cross section, defined as the loss of flux in the CC space. A similar result was reported [15] for the system ^{16}O +^{208} Pb at E_{lab} = 80 MeV, a bombarding energy around 1 MeV below the corresponding fusion barrier. We also estimated the contribution of couplings associated to the one neutron, one proton and alpha stripping transfer processes. Since we used the code ECIS in the zero range approximation, as reported early [16] the calculations serve only as an indication of the importance of these couplings. Even in this case the calculations show small effects in the elastic cross sections compared to the uncertainties of the experimental data. It is important to mention that, to simulate peripherical absorption, we did other CC calculations including a surface imaginary potential, centered at 10 fm, with a strength which corresponds to a cross section of 1 mb at E_{lab} = 38 MeV. These calculations showed negligible contributions to the elastic and inelastic scattering cross sections. We remark that, due to the increase of the number of couplings, to avoid convergence problems we used an integration stepsize equal to 0.02 fm, 20 to 50 partial waves in the integration of the

coupled equations and we kept Coulomb corrections up to 250 partial waves.

Also exhibited in Fig. 4b is the double folding potential (dashed line) with the M3Y effective nucleon–nucleon interaction with unit normalization [17]. As reported by Satchler and Love [17], for the $^{16}O + ^{60}Ni$ system the tail of the folded potential may be represented by:

$$V(r) \approx s^n \exp(-s/\beta) , \tag{1}$$

where $s = r - R$, $R = 6.8$ fm, $n \approx 1$ and $\beta \approx 0.534$ fm.

A measure of the slope of the potential in the surface region is given by the logarithmic derivative,

$$\alpha = -V(r)/(dV(r)/dr) . \tag{2}$$

In the range $9.5 \leqslant r \leqslant 11.5$ fm, for the folded potential α assumes values in the interval $0.60 \leqslant \alpha_{\text{fold}} \leqslant 0.67$ fm. For the exponential potential obtained from the CC analysis we got $\alpha_{\text{exp}} = a = 0.58 \pm 0.04$ fm, which, considering the uncertainty, is close to the values defined for α_{fold}. In this sense, the shapes of the double folding and the exponential potential are quite similar in the surface region. Nevertheless, the strength of the exponential potential is about 40% greater than that for the folded potential with unit normalization.

It is interesting to compare the results obtained from the CC analysis with those obtained by Fulton et al. [14] from conventional optical model (OM) analysis of the elastic data for the $^{16}O + ^{60}Ni$ system in the energy range $36.0 \leqslant E_{\text{lab}} \leqslant 141.7$ MeV. The OM analysis was realized using the double folding potential as the real part of the optical potential and large double folding potential renormalizations in the barrier region was reported. There are two important features about the comparison between the OM and the CC analysis. (i) In both analyses, for energies $E_{\text{lab}} \leqslant 38.0$ MeV the resulting strengths of the potentials in the surface region are about 40% greater than those for the folded potential with unit normalization (see Fig. 4b). (ii) In the energy range $35 \leqslant E_{\text{lab}} \leqslant 38$ MeV, there is a potential, that is real and has a simple exponential shape in the surface region, which is a solution of the CC calculations for the elastic and inelastic data.

4. Conclusions

In summary, the experimental study of the $^{16}O + ^{60}Ni$ system at bombarding energies 4.5–7.5 MeV below the fusion barrier, is reduced to only one reaction channel (2_1^+ excitation) and the elastic process. In this situation, it was possible to do a reliable CC analysis of the data. In this paper we demonstrated the importance of the long range Coulomb absorption. The data are explained by using, besides the Coulomb absorption, a real nuclear potential, without energy dependence, with an exponential shape in the surface region which has a slope close to the M3Y double folding potential.

Acknowledgements

We would like to thank Prof. Neil R. Fletcher for providing, in the form of tables, the elastic and inelastic scattering data for the 36 and 38 MeV energies.

References

[1] L. West Jr., K.W. Kemper and N.R. Fletcher, Phys. Rev. C 11 (1975) 859.
[2] L. West Jr. and N.R. Fletcher, Phys. Rev. C 15 (1977) 2052.
[3] A.M. Borges, C.P. Silva, D. Pereira, L.C. Chamon, E.S. Rossi Jr. and C. Aguiar, Phys. Rev. C 46 (1992) 2360.
[4] J. Raynal, Computer Code ECIS.
[5] D. Pereira, G. Ramirez, O. Sala, L.C. Chamon, C.A. Rocha, J.C. Acquadro and C. Tenreiro, Phys. Lett. B 220 (1989) 347.
[6] T. Udagawa, M. Naito and B.T. Kim, Phys. Rev. C 45 (1992) 876.
[7] D. Pereira, L.C. Chamon, C.P. Silva, E.S. Rossi Jr., G. Ramirez, A.M. Borges, L.C. Gomes and O. Sala, Proc. Workshop on Heavy ion collisions at energies near the Coulomb barrier, Daresbury Laboratory, ed. M.A. Nagarajan (UK, July 1990) p. 77.
[8] P.H. Stelson, Proc. Workshop on Heavy ion collisions at energies near the Coulomb barrier, Daresbury Laboratory, ed. M.A. Nagarajan (UK, July 1990) p. 191.
[9] Nucl. Data Tables 14 (1974) 485.
[10] M.E. Cage, A.J. Cole and G.J. Pyle, Nucl. Phys. A 210 (1973) 418.
[11] T. Tamura, Rev. Mod. Phys. 37 (1965) 679.
[12] J. Raynal, Phys. Rev. C 23 (1981) 2571.
[13] G.R. Satchler, M.A. Nagarajan, J.S. Lilley and I.J. Thompson, Ann. Phys. (N.Y.) 178 (1987) 110.
[14] B.R. Fulton, D.W. Banes, J.S. Lilley, M.A. Nagarajan and I.J. Thompson, Phys. Lett. B 162 (1985) 55.
[15] I.J. Thompson, M.A. Nagarajan, J.S. Lilley and B.R. Fulton, Phys. Lett. B 157 (1985) 250.
[16] J. Dias, J.L. Ferrero and J.A. Ruiz, Nucl. Phys. A 494 (1989) 311.
[17] G.R. Satchler and W.G. Love, Phys. Rep. 55 (1979) 183.

Ref. Ch 96

ELSEVIER

Nuclear Physics A 597 (1996) 253–268

NUCLEAR PHYSICS A

Isotopic dependence of the ion–ion potential in the systems $^{16}O+^{58,60,62,64}Ni$ ★

L.C. Chamon [a], D. Pereira [a], E.S. Rossi Jr. [a,1], C.P. Silva [a,2], H. Dias [b], L. Losano [b,3], C.A.P. Ceneviva [b]

[a] *Laboratório Pelletron, Instituto de Física da Universidade de São Paulo, Caixa Postal 66318, 05389-970 São Paulo, SP, Brazil*

[b] *Grupo de Física Nuclear Teórica e Fenomenologia de Partículas Elementares, Instituto de Física da Universidade de São Paulo, Caixa Postal 66318, 05389-970 São Paulo, SP, Brazil*

Received 31 July 1995; revised 8 November 1995

Abstract

Precise measurements of the elastic and inelastic scattering cross sections for the systems $^{16}O+^{58,60,62,64}Ni$ at the sub-barrier energies were made. Coupled-channel analysis were performed. The isotopic dependence of the resulting ion–ion potentials is compared with theoretical calculations using the double-folding method with the M3Y as the nucleon–nucleon interaction and shell-model densities.

Keywords: NUCLEAR REACTIONS: $^{58,60,62,64}Ni(^{16}O,^{16}O),(^{16}O,^{16}O')$, $E = 34$–37 MeV; measured $\sigma(\theta)$, deduced optical potential, $^{58,60,62,64}Ni$ levels deduced $B(E2)$, deformation lengths. Shell-model, double-folding calculations, coupled-channel analysis.

1. Introduction

In a recent paper [1], we presented the precise measurements and the coupled-channel (CC) analysis of the elastic and inelastic scattering cross sections, in the energy range $35 \leqslant E_{LAB} \leqslant 38$ MeV, for the $^{16}O+^{60}Ni$ system. In this low-energy region, due to the small number of relevant channels (0_1^+, 2_1^+), the coupled-channel calculations by

★ Partially supported by FINEP, CNPq and FAPESP.

[1] Post-graduate fellowship from CAPES.

[2] Post-graduate fellowship from FAPESP.

[3] Permanent address: Depto. de Física da Universidade Federal da Paraíba, Brazil.

SSDI 0375-9474(95)00467-X

the ECIS code [2] are very reliable and it is possible to explain the data using an energy-independent nuclear potential, which is real and has an exponential shape in the surface region ($9.5 \leqslant R \leqslant 11.5$ fm). In this paper, as an extension of that work, we present the experimental investigation of the isotopic dependence of the ion–ion potential for the systems $^{16}O+^{58,60,62,64}Ni$, by measuring the elastic and inelastic (2_1^+) scattering cross sections at sub-barrier energies ($34 \leqslant E_{LAB} \leqslant 37$ MeV). The main features of the data [1] are the following: (i) the small deviations from the Rutherford scattering of the elastic data at forward angles ($\theta_{CM} \leqslant 130°$) are due to the long-range Coulomb absorption, the nuclear contribution is restricted to the backward angles; (ii) the 2_1^+ target excitation is the only reaction channel with relevant cross section at those energies. In these conditions, it was possible to fit the experimental data with reasonable Coulomb and nuclear phonon amplitudes and to determine, with 3% accuracy, the slopes and the strengths of the CC ion–ion potentials in the surface region. We have also investigated the consistence between the obtained nuclear CC potentials and those from the M3Y double-folding calculations using (f-p) shell-model nuclear densities. This paper is organized as follows: Section 2 gives the experimental details and results; in Section 3 is described the CC analysis of the experimental data; in Section 4 we discuss the isotopic dependence of the resulting CC potentials and the comparison with the M3Y double-folding calculations; Section 5 contains a brief summary and our main conclusions.

2. Experimental details and results

Our measurements were made using the ^{16}O beam from the São Paulo 8UD Pelletron accelerator. The detecting system was the same as described in Ref. [1] and consisted of a set of nine surface barrier detectors spaced 5° apart. The thickness of the nickel targets was about 30 $\mu g/cm^2$, with a thin layer of gold with the aim of data normalization. The $^{58,60,62,64}Ni$ targets were about 99.9, 99.9, 98.4 and 96.7% enriched, respectively. The typical energy spectra at backward angles are shown in Fig. 1. Due to the high precision required for the experimental data [1], the following cares were taken into account in the data acquisition and reduction:

(i) The use of a monitor detector ($\theta_{LAB} = 30°$) to be sure that no target deterioration occurred during the bombardment.

(ii) High-energy resolution (a) to allow a complete separation between the elastic and inelastic (2_1^+) peaks (see Fig. 1a) and (b) to separate the elastic and inelastic peaks from the other elastic peaks associated with the contaminants in the targets. This is illustrated in Fig. 1b for the $^{16}O+^{62}Ni$ system where the main contaminants in the ^{62}Ni target are the nickel isotopes $^{58,60,64}Ni$. At backward scattering angles it was possible to separate the elastic peaks of the contaminants from those associated with the elastic and inelastic scattering of the $^{16}O+^{62}Ni$ system. With this information it was possible to eliminate the effect of the contaminants in the measured cross sections at forward angles.

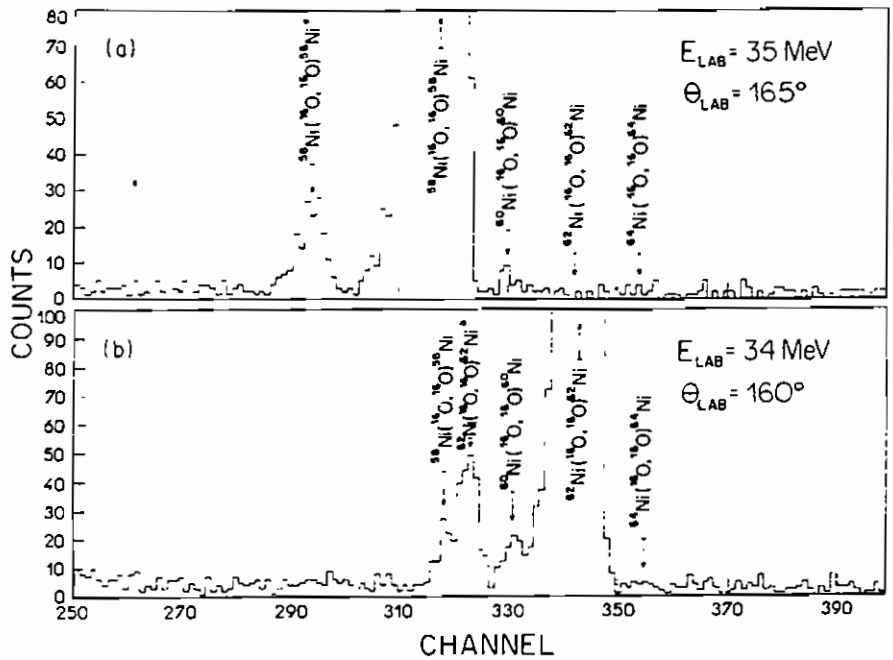

Fig. 1. Energy spectra for: (a) E_{LAB} = 35 MeV and θ_{LAB} = 165° for a highly enriched (99.9%) ^{58}Ni target and (b) E_{LAB} = 34 MeV and θ_{LAB} = 160° for a 98.4% enriched ^{62}Ni target. The ^{58,60,64}Ni are the main contaminants in the ^{62}Ni target.

(iii) Small corrections in the counting rate related to the elastic and inelastic scattering processes due to the small background near the elastic and inelastic peaks (see Fig. 1).

Figs. 2–5 exhibit the elastic and inelastic (2_1^+) cross sections for the systems ^{16}O $+^{58,60,62,64}$Ni. The integrated inelastic cross sections vary between 20 and 50 mb. No evidence was found in the energy spectra for population of other excited states of the target or projectile with cross sections anywhere near those for the 2_1^+ state. We used the time of flight technique [3] to evaluate the importance of the few nucleon transfer and the fusion processes at these low bombarding energies for the ^{16}O+^{58,64}Ni systems. The results indicate very small cross sections for the nucleon transfer processes compared to the 2_1^+ excitation, as already has been reported for the ^{16}O+^{60}Ni system [1]. The analysis of the measured [4–7] fusion cross sections for the systems ^{16}O+^{58,60,64}Ni ($39 \leqslant E_{LAB} \leqslant 64$ MeV), using the same method described by Udagawa et al. [8], results in values of $T_{CM} \approx 29$ MeV for the fusion threshold energies. These threshold energies are 4.0 to 4.5 MeV below the corresponding fusion barriers ($V_B \approx 33.5$ MeV). From Stelson's systematic [9], the fusion cross section at energies below the threshold energy is of order of 0.1 mb. With all these results we can consider, at bombarding energies $E_{LAB} \leqslant 38$ MeV, that the 2_1^+ target excitation is the reaction channel with dominant cross sections, which are one or two orders of magnitude larger compared to those associated to other reaction channels.

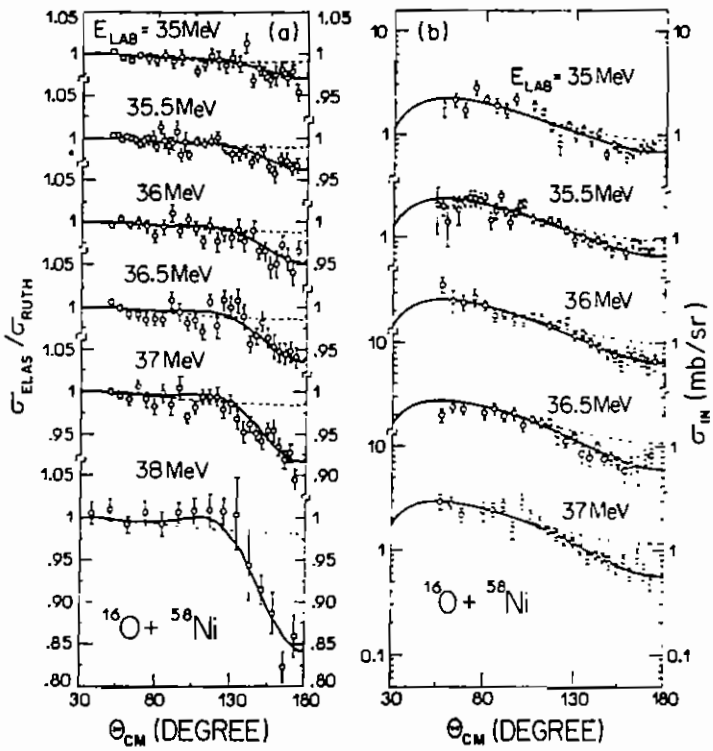

Fig. 2. (a) Elastic and (b) inelastic angular distributions for the $^{16}O+^{58}Ni$ system at E_{LAB} = 35.0, 35.5, 36.0, 36.5 and 37.0 MeV (this work) and E_{LAB} = 38.0 MeV (from Ref. [28]). The curves correspond to coupled-channel calculations considering only the Coulomb (dashed lines) and the Coulomb plus the nuclear interactions (solid lines).

Table 1
The Coulomb (β_c) and nuclear (β_n) phonon amplitudes and the corresponding deformation lengths (δ_c and δ_n) for the $^{58,60,62,64}Ni$ nuclei, as obtained from the CC analysis of the experimental data. In the table are shown the corresponding $B(E2)\uparrow$ values in e^2fm^2 units

Nucleus	β_c	$B(E2)$	δ_c (fm)	β_n	δ_n (fm)
^{58}Ni	0.233 ± 0.006	688 ± 34	0.96 ± 0.03	0.22 ± 0.03	0.90 ± 0.12
^{60}Ni	0.265 ± 0.010	931 ± 70	1.10 ± 0.04	0.26 ± 0.03	1.08 ± 0.12
^{62}Ni	0.247 ± 0.010	845 ± 68	1.04 ± 0.04	0.17 ± 0.03	0.71 ± 0.13
^{64}Ni	0.218 ± 0.008	686 ± 50	0.87 ± 0.03	0.19 ± 0.03	0.76 ± 0.12

3. Coupled-channel analysis

In the coupled-channel calculations we adopted a similar procedure described in the analysis of the sub-barrier elastic and inelastic data for the $^{16}O+^{60}Ni$ system [1]. We used a matching radius of 30 fm, integration step size of 0.05 fm, 60 partial waves in the integration of the coupled equations and Coulomb corrections [10] up to 300 partial waves. The $^{58,60,62,64}Ni$ nuclei were assumed spherically symmetric and susceptible

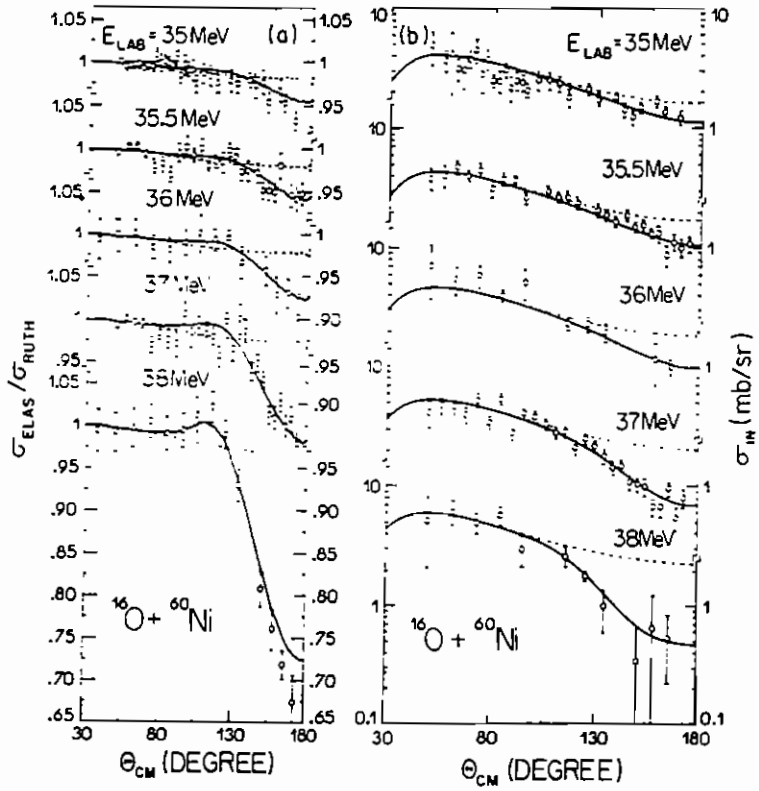

Fig. 3. The same as in the Fig. 2 for the $^{16}O+^{60}Ni$ system at E_{LAB} = 35.0, 35.5 and 37.0 MeV (this work) and E_{LAB} = 36.0 and 38.0 MeV (from Refs. [20,28]).

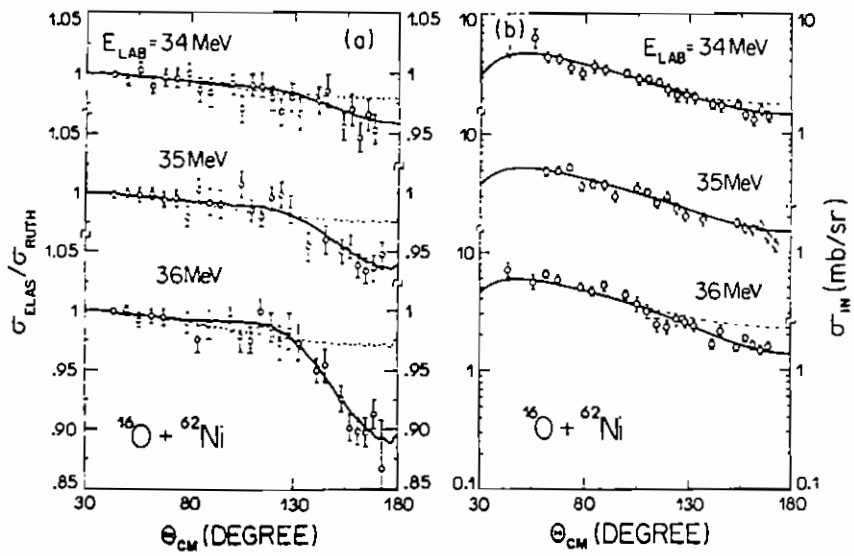

Fig. 4. The same as in the Fig. 2 for the $^{16}O+^{62}Ni$ system at E_{LAB} = 34.0, 35.0 and 36.0 MeV (this work).

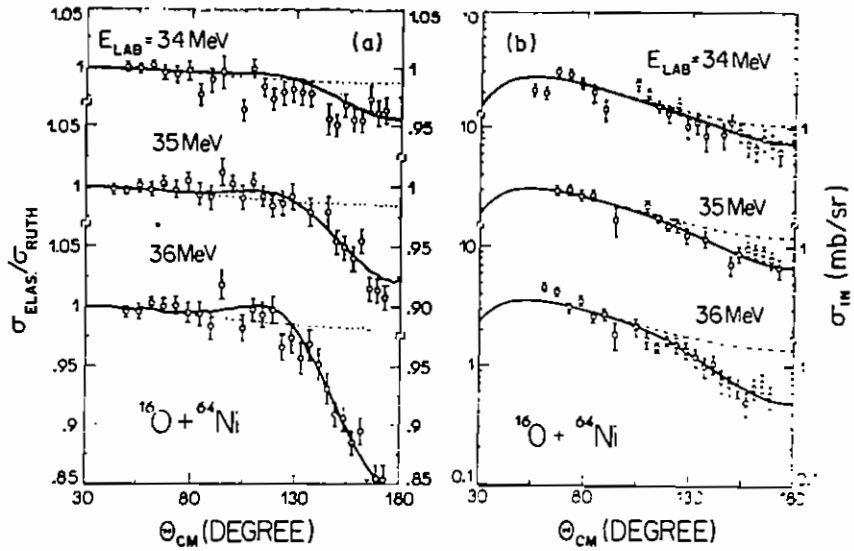

Fig. 5. The same as in the Fig. 2 for the $^{16}O+^{64}Ni$ system at E_{LAB} = 34.0, 35.0 and 36.0 MeV (this work).

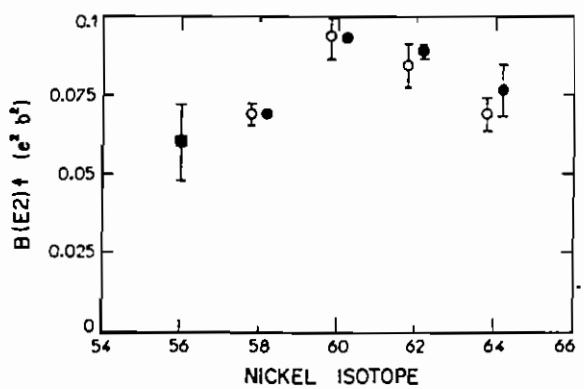

Fig. 6. The $B(E2)\uparrow$ values for the $^{58,60,62,64}Ni$ nuclei obtained from the CC analysis of the experimental data in this work (open circles) and the values from Ref. [15] (closed circles). Also included in the figure the recently reported [16] $B(E2)\uparrow$ value for the double magic ^{56}Ni.

to vibration around their spherical shapes [11]. We considered for the nickel nuclei the contributions of one-phonon (2_1^+) states: ^{58}Ni (1.454 MeV), ^{60}Ni (1.332 MeV), ^{62}Ni (1.173 MeV) and ^{64}Ni (1.344 MeV). Using the same procedure described in Ref. [1] for the $^{16}O+^{60}Ni$ system, we investigated also, in other nickel target systems, the importance of couplings associated with other reaction channels which, due to their very small cross section values, have not been detected in our experiments. The corresponding CC calculations, using the ECIS code, showed that the target two-phonon states (0_2^+, 2_2^+, 4_2^+), the (3^-, 6.13 MeV) state of the ^{16}O and the couplings associated with the few nucleon transfer resulted in smaller contributions to the elastic and inelastic (2_1^+) cross sections as compared to the data accuracy. Thus, within the energy range

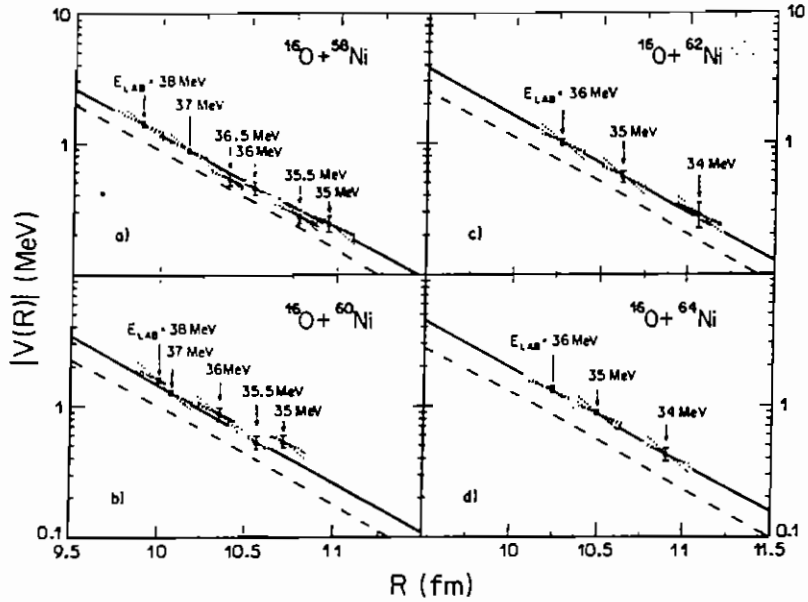

Fig. 7. The nuclear real potential in the surface region for (a) ^{16}O+^{58}Ni, (b) ^{16}O+^{60}Ni, (c) ^{16}O+^{62}Ni and (d) ^{16}O+^{64}Ni systems, as obtained from the CC analysis of the experimental data for several values of diffuseness and depth parameters. The solid lines in the figure are the CC solutions with the same diffuseness parameter (a = 0.59 fm) for all the systems. The dashed lines are the predictions of the M3Y double-folding calculations using shell-model densities for the nickel isotopes.

Table 2
The best-fit diffuseness parameters of the real nuclear potentials and the corresponding reduced χ^2_{red} values as obtained from the CC analysis ($34 \leqslant E_{LAB} \leqslant 38$ MeV) considering: (i) each system separately and (ii) all the systems investigated in this work. NE and NI are the number of the experimental elastic and inelastic data points

System	NE	NI	a (fm)	χ^2_{red}
^{16}O+^{58}Ni	158	136	0.57 ± 0.03	1.22
^{16}O+^{60}Ni	112	102	0.58 ± 0.04	1.19
^{16}O+^{62}Ni	72	65	0.60 ± 0.05	0.99
^{16}O+^{64}Ni	77	64	0.67 ± 0.05	1.37
^{16}O+^{58,60,62,64}Ni	419	367	0.59 ± 0.02	1.20

and the data precision of this work, we consider the inelastic collision for the 2^+_1 target excitation as the only relevant reaction channel in the CC calculations. The value r_c = 1.06 fm, obtained from electron scattering experiments [12], was assumed for the Coulomb radius. We obtained the values of the Coulomb phonon amplitudes, β_c, by fitting the inelastic data for $\theta_{CM} \leqslant 100°$ at energies $E_{LAB} \leqslant 36$ MeV. The dashed lines in Figs. 2–5 represent the CC calculations considering only the Coulomb interaction on the elastic and inelastic data. The best-fit values for the parameter β_c and the corresponding deduced [13,14] B(E2) ↑ values are shown in Table 1. Fig. 6 exhibits a comparison between our B(E2) ↑ values and those reported in Ref. [15],

resulting from a large compilation over other experimental values which were obtained using different techniques. We point out the excellent agreement between both sets of data. Just for comparison purposes, the recently reported [16] experimental value for the double magic ^{56}Ni nucleus is included in the same figure. We observe a bell shape behavior of the $B(E2)\uparrow$ values as a function of the mass number with a maximum for the ^{60}Ni nucleus.

For the real nuclear potential we assumed a Woods–Saxon shape with a radius equal to the Coulomb radius $r_0 = r_c = 1.06$ fm. As it is commonly used in the CC calculations, we have considered an inner imaginary potential [1] which has very small values in the surface region ($W(R) \leqslant 10^{-7}$ MeV, for $R \geqslant 9$ fm) and represents a small internal barrier absorption. The CC calculations are rather insensitive to variations of the strength of this imaginary potential. It is important to mention that we have also investigated the effect of a surface absorption to simulate the peripherical processes which were not considered in the CC calculations. As discussed in Ref. [1], the adopted small surface imaginary potential generates a loss of flux compatible with the very small cross sections of our measurements associated with these processes. Taking into account the above conditions, the inclusion of this surface imaginary potential in the CC calculations has shown a completely negligible contribution to the elastic and inelastic (2_1^+) cross sections. In the data analysis, the nuclear depth potential, V_0, the diffuseness, a, and the nuclear phonon amplitude, β_n, were searched for the best fit. For each system and bombarding energy we found a family of potentials (in the diffuseness range of $0.45 \leqslant a \leqslant 0.85$ fm) that gave equivalent fits to the data. These potentials cross at a strong absorption radius (R_{SA}) as shown in Fig. 7 and also in Fig. 2 of Ref. [1]. Taking into account that there is no correlation between the potential strength at R_{SA} and the diffuseness parameter, we estimated the potential error bars at the above radius by considering a unitary variation of the χ^2. At backward angles ($\theta_{CM} \geqslant 140°$), where the nuclear potential contribution is relevant, such variation generates other elastic data fits which deviate from the corresponding best fits by about 1%, a value which is close to the elastic data uncertainties. The results of these calculations, which are illustrated in Fig. 5 of our previous work [1], are rather insensitive to the diffuseness parameter.

As shown in the Fig. 7, at these low energies the strong absorption radius is rather energy sensitive; we have used this dependence to characterize the shape of the real nuclear potential, which is quite close to an exponential, in the surface region ($9.5 \leqslant R \leqslant 11.5$ fm). As a second step of the CC analysis, for each system we have considered the diffuseness and the potential depth as energy-independent parameters. In Table 2 are shown the corresponding best-fit diffuseness parameters and the reduced χ^2_{red} values. We note that, within the uncertainties, the diffuseness parameters have compatible values for all the systems; a fit assuming a constant value results in an average diffuseness equal to 0.593 fm with a reduced chi-square of 1.03. We point out that this result is consistent with the M3Y folding calculations using shell-model densities. As discussed on Subsection 4.2, these theoretical calculations predict, for the ^{16}O+^{58,60,62,64}Ni systems, nuclear potentials with shapes quite close to an exponential in the surface region and slopes which differ by less than 4%. Then, we have considered in the CC analysis of

the data the same diffuseness for all the systems and bombarding energies investigated in this work. A best-fit value for the diffuseness parameter, $a = 0.59 \pm 0.02$ fm, was obtained from these calculations with a corresponding $\chi^2_{red} = 1.20$. The results of these last CC calculations for the elastic and inelastic cross sections are indicated by solid lines in the Figs. 2–5. The corresponding nuclear potentials are indicated by solid lines in the Fig. 7.

It should be noted that the present CC analysis allows us to obtain the surface ion–ion potentials in a reliable form assuming an energy-independent potential of fixed shape in the energy range $34 \leqslant E_{LAB} \leqslant 38$ MeV. In a recent paper [17], the optical model (OM) analysis of elastic data for the systems $^{16}O+^{58,60,62,64}Ni$, in a much larger energy range ($40 \leqslant E_{LAB} \leqslant 120$ MeV), showed that the resulting nuclear potentials present an energy dependence which is described by a dispersion relation. We point out that there are no inconsistencies between the OM and the present CC analysis. In the small energy range investigated in this work ($\Delta E_{LAB} \leqslant 3$ MeV), the OM analysis indicate (Fig. 2 of Ref. [17]) that the surface imaginary potential is very small and the renormalization of the real nuclear potential varies only by about 3%. Since in the present CC calculations we have taken into account the most important reaction channel, in principle this weak energy dependence should be smaller. Thus, the assumption which considers the CC nuclear potential as an energy-independent term is a very good approach within the energy range and data precision of this work. Our CC data analysis also gives a better understanding of the ambiguities, reported in the same Ref. [17], which are responsible for the rather undefined real optical potential at $E_{LAB} \leqslant 38$ MeV. These ambiguities arise from the OM analysis of the elastic scattering data, using a Woods–Saxon shape imaginary potential to simulate the total reaction channel absorption. For each energy, the procedure adopted in the OM elastic data analysis was a search for the best-fit parameters of a short-range imaginary potential and of a folded real potential. However, our measurements showed that at these low energies the absorption is strongly dominated by the long-range Coulomb excitation for the 2_1^+ nickel state. This absorption is defined by only two energy-independent parameters (β_c and β_n), which are well determined by the CC analysis of the inelastic data. As discussed in Refs. [18,19], the corrections in the optical potential taking into account the Coulomb absorption cannot be simulated by the usual short-range Woods–Saxon imaginary potential.

The best-fit values for the nuclear and Coulomb deformation lengths ($\delta_n = \beta_n R_0$ and $\delta_c = \beta_c R_c$ [4]) are shown in Table 1. For the systems $^{16}O+^{58,60,64}Ni$ the δ_n and δ_c parameters are compatible within the uncertainties, while for the system $^{16}O+^{62}Ni$ we found δ_n around 30% lower compared to the corresponding δ_c. Our results for the deformations lengths are in a reasonable agreement with the values from DWBA inelastic (2_1^+) data analysis at higher (42 and 48 MeV) energies [20]. It is important to mention that the nuclear potential in the surface region, the nuclear deformation length and the $B(E2)\uparrow$ parameter, are rather independent of the adopted Coulomb and nuclear radii (r_c and r_0). This was demonstrated by other CC calculations assuming different

[4] $R_0 = r_0 A^{1/3}_{TARGET}$ and $R_c = r_c A^{1/3}_{TARGET}$.

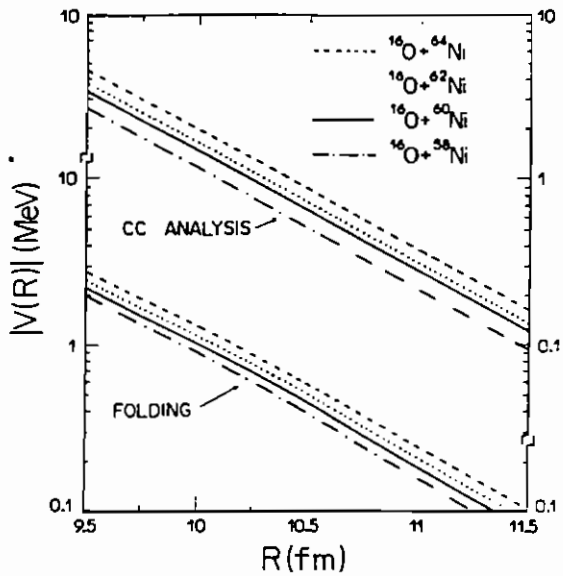

Fig. 8. The nuclear potentials for the systems ^{16}O+^{58,60,62,64}Ni as obtained from the CC analysis of the data (top) and the double-folding method (bottom).

Table 3
Nuclear potential values for the ^{16}O+^{58,60,62,64}Ni systems at the interacting radius R = 10.5 fm as obtained from (i) the CC analysis of the experimental data (V_{cc}) and (ii) the M3Y double-folding calculations (V_{fold}). In the table are shown also the ratios of the CC potential values in relation to those from the folding calculations and the slope (α) of the folded potential at R = 10.5 fm

System	V_{cc} (MeV)	V_{fold} (MeV)	V_{cc}/V_{fold}	α (fm)
^{16}O+^{58}Ni	0.493 ± 0.013	0.373	1.32 ± 0.03	0.568
^{16}O+^{60}Ni	0.627 ± 0.011	0.433	1.45 ± 0.03	0.576
^{16}O+^{62}Ni	0.705 ± 0.026	0.494	1.43 ± 0.05	0.584
^{16}O+^{64}Ni	0.842 ± 0.014	0.560	1.50 ± 0.03	0.592

values for the parameters r_c and r_0, which resulted in equivalent data fits and the same surface nuclear potential, δ_n and B(E2) ↑ values.

4. Discussion of the results

4.1. The isotopic dependence of the ion–ion potential

From the CC analysis described in the last section, the resulting ion–ion potentials for the systems ^{16}O+^{58,60,62,64}Ni, in the surface region, have a simple exponential shape and the same diffuseness parameter defined with a precision of about 3% ($a = 0.59 \pm 0.02$ fm). These results are in agreement with theoretical models [21,22] which consider that the shape of the nuclear potential varies slowly as a function of the size of the

Table 4
The root-mean-square (RMS) radii, in fm units, for the ^{58,60,62,64}Ni nuclei of the neutron, proton, total and charge densities, as obtained from the shell-model calculations (see Subsection 4.2)

Nucleus	Neutron	Proton	Total	Charge
^{58}Ni	3.665	3.674	3.669	3.769
^{60}Ni	3.730	3.698	3.715	3.792
^{62}Ni	3.792	3.724	3.762	3.818
^{64}Ni	3.851	3.751	3.807	3.845

system. As shown in Fig. 8 (top), the strength of the ion–ion potential for the systems ^{16}O+^{58,60,62,64}Ni is an increasing function of the nickel mass number. Table 3 gives the nuclear potential values at the interacting radius R = 10.5 fm. The ratios of these potential values for the systems ^{16}O+^{60,62,64}Ni in relation to that of the ^{16}O+^{58}Ni system are 1.27, 1.43 and 1.71, respectively. We note that only a small fraction of these ratios is connected to the usual potential dependence with the size of the system. In the present studies this trivial dependence is easily evaluated by the quantity $e^{\Delta R_{Ni}/a}$, where ΔR_{Ni} is the nuclear radius difference between two different nickel isotopes. Assuming for the nickel radius the half-way radius density dependence $R_{Ni} = 1.06A_{Ni}^{1/3}$ fm, the ratio between the potential strengths for the ^{16}O+^{64}Ni and the ^{16}O+^{58}Ni systems should be only 1.26; a value that should be compared to 1.71 from the CC analysis.

As discussed in Ref. [14], the connection between the central, $V(R)$, and the deformed, $H_\ell(R)$, nuclear components of the ion–ion potential, is expressed through the relation:

$$H_\ell(R) = -\delta_{n,\ell}\frac{dV}{dR}, \tag{1}$$

where ℓ is the transferred angular momentum in the collision. Thus, since the ^{16}O +^{58,60,62,64}Ni systems have the same exponential shape for the potential $V(R)$ and close δ_n values (see Table 1), we can say that these systems have similar ratios for the nuclear potential parts $H_{\ell=2}(R)$ and $V(R)$.

4.2. Double-folding potential calculations

In this section we present the theoretical calculations with the aim of evaluating the nuclear ion–ion potential, using the double-folding method with an effective nucleon–nucleon interaction and shell-model densities. In the calculations we have used the well-known nucleon–nucleon M3Y interaction in its standard form [23]:

$$v_0(r) = \left[7999\frac{e^{-4r}}{4r} - 2134\frac{e^{-2.5r}}{2.5r}\right] + 262\delta(r)\ \text{MeV}. \tag{2}$$

The nuclear ion–ion potential was calculated through the relation [24]:

$$V(R) = \int \rho_1(r_1)v_0(|R - r_1 + r_2|)\rho_2(r_2)\,dr_1\,dr_2, \tag{3}$$

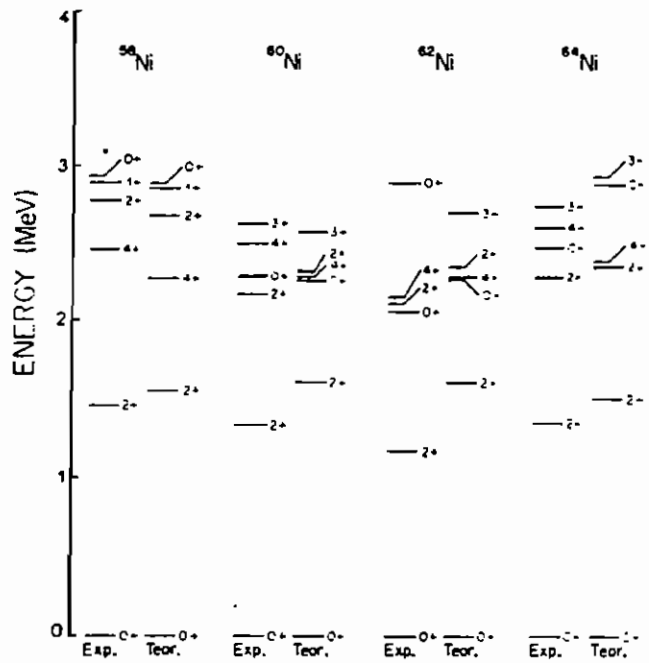

Fig. 9. Energy level scheme predictions from shell-model calculations for the ^{58,60,62,64}Ni nuclei. For comparison purposes, the corresponding experimental schemes were included in the figure.

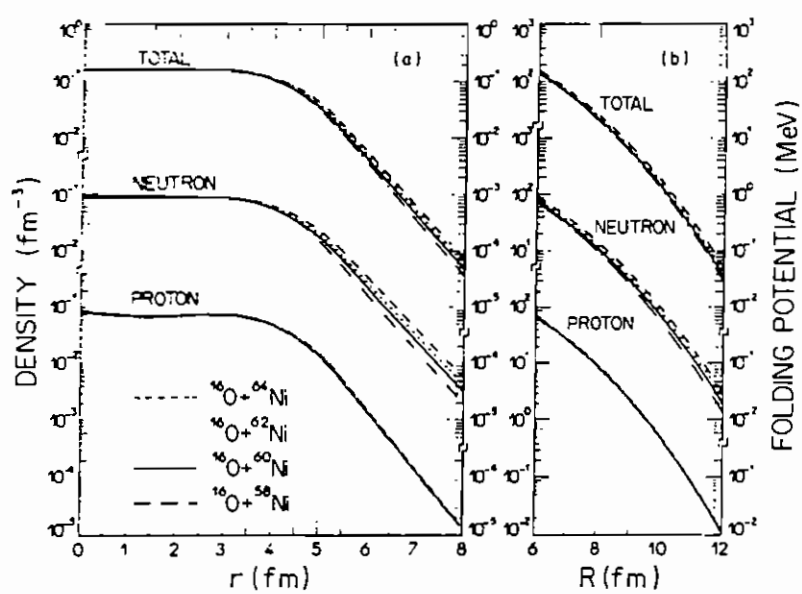

Fig. 10. (a) The ground-state neutron, proton and total nuclear densities derived from the shell-model calculations for the ^{58,60,62,64}Ni nuclei (see Subsection 4.2). (b) M3Y double-folding potentials for the ^{16}O+^{58,60,62,64}Ni systems using the shell-model densities and considering the contribution of the neutrons and protons of the nickel isotopes separately.

where $\rho_1(r_1)$ and $\rho_2(r_2)$ are the nuclear densities of the collision partners.

The spin-scalar, isoscalar density of a nucleus is expressed by the matrix element [24]:

$$\rho(r) = \langle A'| \sum_i \delta(r - r_i) |A\rangle, \tag{4}$$

where A denotes the wave function of an A-nucleon system. The situations $A' = A$ and $A' \neq A$ yield the ground-state and the transition densities, respectively. The use of the ground-state or transition densities in the expression (3) leads to the central or transition potential for a transferred angular momentum ℓ.

In our calculations the ground-state density of the ^{16}O nucleus was derived from the electron scattering experimental results [12], with the assumption that the neutron (ρ_n) and proton (ρ_p) densities have the same form of the charge density (ρ_c). The total nuclear density (ρ) was expressed by:

$$\rho(r) = \rho_n(r) + \rho_p(r) = \rho_0 \left[1 + \gamma \left(\frac{r}{b}\right)^2\right] e^{-(r/b)^2}, \tag{5}$$

where $\gamma = 1.544$, $b = 1.883$ fm (charge density parameters of Ref. [12]) and $\rho_0 = 0.1407$ to satisfy the normalization conditions:

$$\int_0^\infty 4\pi\rho_p(r) r^2 \, dr = Z,$$

$$\int_0^\infty 4\pi\rho_n(r) r^2 \, dr = N,$$

$$\int_0^\infty 4\pi\rho(r) r^2 \, dr = A. \tag{6}$$

As pointed out by Satchler and Love [24], theoretical calculations assuming $\rho_n \neq \rho_p$ for the ^{16}O nucleus result in a neutron distribution with the root-mean-square (RMS) radius smaller than that for protons by only 1 to 2%. On the other hand, the hypothesis $\rho_n = \frac{N}{Z}\rho_p$ for the nickel isotopes is inadequate to the present studies, since the intensity of the corresponding folded potentials becomes proportional to the nickel mass number. This means a difference of only 10% between the potential strengths for the ^{16}O+^{64}Ni and the ^{16}O+^{58}Ni systems: a value that should be compared to 70% as obtained from the CC analysis of the experimental data (see Table 3). Thus, for the nickel isotopes the neutron and the proton densities were derived from shell-model calculations considering the four orbital configuration $(1f_{7/2})^{16}$ $(1f_{5/2}\text{-}2p_{3/2}\text{-}2p_{1/2})^{A-56}$ and an effective interaction obtained recently for the lower part of the 1f-2p shell [25]. The same kind of shell-model calculations were realized earlier [16] with the aim of calculating the $B(E2)\uparrow$ values for the ^{56,58,60,62,64}Ni. We note that the average effective neutron charge, necessary to reproduce our experimental $B(E2)$ values with the shell-model calculations performed by us, is quite close to 0.9, the value that has been used by Kraus et al. [16].

In Fig. 9 is shown a comparison among the level schemes predicted by the shell-model calculations and those obtained experimentally. We note the reasonable agreement between the two energy level schemes for energy levels up to the lowest two-phonon states (0_2^+, 2_2^+, 4_2^+). The ground-state neutron, proton and total densities from the shell-model calculations for the ^{58,60,62,64}Ni nuclei, with the normalization conditions given by expressions (6), are exhibited in Fig. 10a. As expected for the ^{58,60,62,64}Ni ($Z = 28$ closed shell), the proton densities are quite similar; a behavior not observed for the corresponding neutron densities which, in the surface region ($r \geqslant 4$ fm), are increasing functions of the neutron number. In Table 4 are shown the nickel isotope charge, neutron, proton and total RMS radii from the shell-model calculations. We point out that the theoretical charge distribution RMS radii are in a very good agreement with those from electron scattering experiments [12]. In order to investigate how the theoretical densities depend on the orbital configuration, we performed other shell-model calculations where we considered only the valence neutron orbitals ($1f_{5/2}$-$2p_{3/2}$-$2p_{1/2}$). These calculations resulted in quite similar densities, differing by only about 0.1% in the surface region from those obtained by inclusion of the ($1f_{7/2}$) orbital. The two sets of shell-model calculations predict also similar energy level schemes.

In Fig. 10b are shown the corresponding folded potentials for the ^{16}O+^{58,60,62,64}Ni systems in the surface region. We have calculated separately, as indicated in the figure, the contribution of the neutrons and protons of the target to the total ion–ion potential. We did other calculations, with similar procedure as described in Ref. [26], which indicate that the region $3.0 \leqslant r \leqslant 7.0$ fm of the nuclear target density is the one which contributes significantly to the total ion–ion potential in the surface interacting region. Since the proton density distributions are very similar for the different nickel isotopes (Fig. 10a), the proton contribution to the ion–ion potential is also practically independent of the nickel mass number (Fig. 10b). Therefore, the differences among the total surface ion–ion potentials for the different nickel isotopes are connected to the corresponding neutron densities. In Figs. 7 and 8 are shown the comparisons among the calculated folded potential and those from the CC analysis of the experimental data for the different systems. We can observe in these figures that the shapes of the folding potentials are quite close to the exponential form. An important conclusion of these comparison is that the slopes α of the folded potentials (Table 3), calculated in the surface region by Eq. (7), are very weakly dependent of the system (the greatest difference is only about 4%) and differ from the diffuseness of the CC potentials ($a = 0.59 \pm 0.02$ fm) by less than 3%.

$$\alpha = \left| \frac{V(R)}{\mathrm{d}V/\mathrm{d}R} \right| . \tag{7}$$

Table 3 contains a comparison between the intensities of the folded and the CC potentials at $R = 10.5$ fm. The isotopic dependence of the potential strengths obtained by the CC analysis of the experimental data is reasonably reproduced by the theoretical folding calculations; for instance, the calculated ratio of the folded potential values for the ^{16}O+^{64}Ni and ^{16}O+^{58}Ni systems is 1.50; a value that approaches 1.71, which is

the value from the CC calculations. On the other hand, for each system the strength of the corresponding CC potential is about 40% greater compared to that associated to the folded potential. The lowest discrepancy (32%) has been detected for the $^{16}O+^{58}Ni$ system. As discussed by Satchler and Love [24], the intensity of the folding potential in the surface region is rather sensitive to the nuclear densities of the collision partners. For instance, in order to eliminate the discrepancy cited above it would be necessary [24] to modify the sum of the RMS radii of the ^{16}O and the nickel isotope by only about 0.16 fm ($\approx$ 3.5%). Nevertheless, apparently we have used quite reasonable densities in the calculations, since the resulting folding potentials are in a good agreement with other M3Y folded potentials, which were derived from elastic scattering data fits [17,27] at high energies where the normalization is believed to be reliable. Finally, we point out that the discrepancy ($\approx$ 40%) between the high- and low-energy potential strengths reported [17,27] from the optical model analysis of the elastic data for the same systems of this work, was not removed in the present CC calculations at low energies, even taking into account the most relevant reaction channel (2_1^+).

5. Summary and conclusions

In summary, we have performed coupled-channel (0_1^+, 2_1^+) analysis of the 33 elastic and inelastic angular distributions (786 experimental points) for the systems $^{16}O+^{58,60,62,64}Ni$ at the sub-barrier energies $34 \leqslant E_{LAB} \leqslant 38$ MeV. The data are well reproduced (χ^2_{red} = 1.20) with reasonable Coulomb and nuclear phonon amplitudes and energy-independent nuclear potentials, which are real and have an exponential shape in the surface region. These CC potentials have the same diffuseness parameter (a = 0.59 fm), defined with an accuracy of 3%, for all the systems investigated in this work. The slope of the resulting CC potentials is well reproduced, also with a precision of 3%, by the M3Y double-folding calculations using (f-p) shell-model densities for the nickel isotopes. These theoretical results are also in reasonable agreement with the obtained isotopic CC potential strength dependence which cannot be explained by considering only the usual variation of the potential with the size of the system. Nevertheless, for each system the strength of the CC potential is about 40% greater than the corresponding calculated M3Y folded potential. Such discrepancy has been already reported [1] for the low-energy coupled-channel potential of the $^{16}O+^{60}Ni$ system, in relation to the M3Y folded potential with unit normalization, obtained from elastic scattering data analysis at higher energies. These results indicate that still remain important corrections to be made in the coupled-channel calculations and (or) in the folding method, in order to describe the low- and high-energy heavy-ion collisions in a coherent form.

Acknowledgements

We would like to thank Prof. D. Galleti for many useful discussions and Prof. Neil R. Fletcher for providing the tabulated elastic and inelastic data of 38 MeV for the

$^{16}O+^{58}Ni$ system and of 36 and 38 MeV for the $^{16}O+^{60}Ni$ system. We thank also Prof. B.A. Brown for providing us the computer shell-model codes.

References

[1] L.C. Chamon, D. Pereira, E.S. Rossi Jr., C.P. Silva, R. Lichtenthaler Filho and L.C. Gomes, Nucl. Phys. A 582 (1995) 305.
[2] J. Raynal, computer code ECIS.
[3] D. Pereira, G. Ramirez, O. Sala, L.C. Chamon, C.A. Rocha, J.C. Acquadro and C. Tenreiro, Phys. Lett. B 220 (1989) 347.
[4] D. Pereira, L.C. Chamon, C.P. Silva, E.S. Rossi Jr., G. Ramirez, A.M. Borges, L.C. Gomes and O. Sala, Proc. Workshop on Heavy Ion Collisions at Energies Near the Coulomb Barrier, Daresbury Laboratory, UK (July 1990) p. 77.
[5] A.M. Borges, C.P. Silva, D. Pereira, L.C. Chamon, E.S. Rossi Jr. and C. Aguiar, Phys. Rev. C 46 (1992) 2360.
[6] C.P. Silva, D. Pereira, L.C. Chamon, E.S. Rossi Jr., A.M. Borges, G.R. Razeto and C.E. Aguiar, Proc. Workshop Heavy-Ion Fusion: Exploring the Variety of Nuclear Properties, Padova, Italy (May 1994) p. 325.
[7] C.P. Silva, D. Pereira, L.C. Chamon, E.S. Rossi Jr., G.R. Razeto, A.M. Borges and C.E. Aguiar, to be published.
[8] T. Udagawa, M. Naito and B.T. Kim, Phys. Rev. C 45 (1992) 876.
[9] P.H. Stelson, Proc. Workshop on Heavy Ion Collisions at Energies Near the Coulomb Barrier, Daresbury Laboratory, UK (July 1990) p. 191.
[10] J. Raynal, Phys. Rev. C 23 (1981) 2571.
[11] T. Tamura, Rev. Mod. Phys. 37 (1965) 679.
[12] C.M. De Jager, H. De Vries and C. De Vries, At. Data Nucl. Data Tables 14 (1974) 479.
[13] F. Videbaek, P.R. Christensen, O. Hansen and K. Ulbak, Nucl. Phys. A 256 (1976) 301.
[14] B.J. Lund, N.P.T. Bateman, S. Utku, D.J. Horen and G.R. Satchler, Phys. Rev. C 51 (1995) 635.
[15] S. Raman, C.H. Malarkey, W.T. Milner, C.W. Nestor Jr. and P.H. Stelson, At. Data Nucl. Data Tables 36 (1987) 1.
[16] G. Kraus, P. Egelhof, C. Fischer, H. Geissel, A. Himmler, F. Nickel, G. Munzenberg, W. Schwab and A. Weiss, Phys. Rev. Lett. 73 (1994) 1773.
[17] N. Keeley, J.A. Christley, N.M. Clarke, B.R. Fulton, J.S. Lilley, M.A. Nagarajan and I.J. Thompson, Nucl. Phys. A 582 (1995) 314.
[18] A.J. Baltz, N.K. Glendening, S.K. Kauffmann and K. Pruess, Nucl. Phys. A 327 (1979) 221.
[19] W.G. Love, T. Terasawa and G.R. Satchler, Nucl. Phys. A 291 (1977) 183.
[20] L. West Jr. and N.R. Fletcher, Phys. Rev. C 15 (1977) 859.
[21] C. Ngô, B. Tamain, M. Beiner, R.J. Lombard, D. Mas and H.H. Deubler, Nucl. Phys. A 252 (1975) 237.
[22] J. Blocki, J. Randrup, W.J. Swiatecki and C.F. Tsang, Ann. of Phys. 105 (1977) 427.
[23] G. Bertsch, J. Borysowics and W.G. Love, Nucl. Phys. A 284 (1977) 399.
[24] G.R. Satchler and W.G. Love, Phys. Rep. 55 (1979) 183.
[25] W.A. Richter, M.G. van der Merwe, R.E. Julies and B.A. Brown, Nucl. Phys. A 523 (1991) 325.
[26] J.G. Cramer and R.M. De Vries, Phys. Rev. C 22 (1980) 91.
[27] B.R. Fulton, D.W. Banes, J.S. Lilley, M.A. Nagarajan and I.J. Thompson, Phys. Lett. B 162 (1985) 250.
[28] L. West Jr., K.W. Kemper and N.R. Fletcher, Phys. Rev. C 11 (1975) 859.

Nonlocal Description of the Nucleus-Nucleus Interaction

L. C. Chamon, D. Pereira, and M. S. Hussein
Instituto de Física, Universidade de São Paulo, C.P. 66318, 05315-970 São Paulo, SP, Brazil

M. A. Cândido Ribeiro
Department of Physics, University of Wisconsin, 1150 University Avenue, Madison, Wisconsin 53706

D. Galetti
Instituto de Física Teórica, Universidade Estadual Paulista, Rua Pamplona 145, 01405-900 São Paulo, SP, Brazil
(Received 2 July 1997)

A parameter-free nonlocal double-folding-inspired interaction is proposed for the nucleus-nucleus systems. Excellent reproductions of elastic scattering differential cross section data were obtained for several systems over a wide range of bombarding energies. Our results should be of value in the description of the scattering of other many-body systems. [S0000-0000(97)00002-8]

PACS numbers: 21.30.Fe, 21.60.−n, 24.10.−i, 25.70.Bc

The mean field interaction between complex quantum many-body systems (nucleus-nucleus, cluster-cluster, etc.) is still an open question in current physics research. The study of this matter is a fundamental step in the understanding of many-body dynamics. In the nucleus-nucleus case, significant progress has been achieved concerning this question during the last decade [1], as a consequence of the measurement of accurate and extensive elastic scattering data at intermediate energies. Nuclear rainbow scattering, first observed in α systems [2–4] and later in light heavy ions [5–7], probes the nucleus-nucleus potential not only at the surface region but also at smaller distances, and ambiguities in the real part of the potentials have been removed. The resulting phenomenological interactions have significant dependence upon the bombarding energies. Some theoretical models have been developed to account for this energy dependence through realistic mean field potentials. Nowadays, the most successful models seem to be those based on the DDM3Y interaction [8–10] which is an improvement of the originally energy-independent double-folding potential [11]. But, in order to fit the data, the density- and energy-dependent DDM3Y potential needs a renormalization factor which besides being system dependent [1,12] is still slightly energy dependent [1].

In this Letter we show, by an extensive description of elastic scattering data using an optical integro-differential equation, that the dependence on the bombarding energy of the real bare potential is mostly due to the intrinsically nonlocal nature of the effective one-body interaction. The real bare potential (by bare we mean the average, mean field, interaction with no coupled channels effects) is constructed using the folding model. It contains no adjustable parameters and is energy independent. The absorptive part is taken to be a three parameters Woods-Saxon interaction. We also supply a simple approach to obtain the local-equivalent energy-dependent potential. Before we set the stage for the analysis of elastic scattering data, we first describe our theoretical model.

When dealing with nonlocal interactions, one is required to solve the integro-differential equation

$$-\frac{\hbar^2}{2\mu}\nabla^2\Psi(\vec{R}) + \int U(\vec{R},\vec{R}')\Psi(\vec{R}')\,d\vec{R}' = E\Psi(\vec{R}), \tag{1}$$

where, on physical grounds [13], the kernel function is taken to be symmetric: $U(\vec{R},\vec{R}') = U(\vec{R}',\vec{R})$. We take for $U(\vec{R},\vec{R}')$ the following form motivated by the physics problem at hand

$$U(\vec{R},\vec{R}') = V(\vec{R},\vec{R}') + i\delta(\vec{R}-\vec{R}')W(R,E) + \delta(\vec{R}-\vec{R}')V_C(R). \tag{2}$$

In our analysis, the Coulomb interaction, $V_C(R)$, was obtained using an expression for the double sharp cutoff folded potential [14] and the local energy-dependent imaginary potential, $W(R,E)$, was taken to have a Woods-Saxon form with three adjustable parameters.

Guided by the microscopic treatment of neutron-nucleus scattering [15], we have assumed for the real nuclear interaction the Perey-Buck or Frahn-Lemmer ansatz [16,17]

$$V(\vec{R},\vec{R}') = V_{NL}\left(\frac{R+R'}{2}\right)\frac{1}{\pi^{3/2}b^3} \times \exp\left[-\left(\frac{|\vec{R}-\vec{R}'|}{b}\right)^2\right], \tag{3}$$

where b is the range of the Pauli nonlocality of the ion-ion interaction. Therefore, the nonlocality introduced in this way is a correction to the local model and in the $b \to 0$ limit Eq. (1) reduces to the usual Schrödinger differential equation. We should mention, at this point, that the use of the simple Gaussian shape to represent nonlocality in the nucleus-nucleus interaction has been justified, within the single-folding model, by Jackson and Johnson [18].

 0031-9007/97/79(26)/5218(4)$10.00

In a recent publication [19], we have shown that the values of b can be obtained for light heavy-ion systems from the energy dependence of phenomenological potentials extracted from elastic scattering data analyses. These b values were found to be in accord with the Jackson and Johnson [18] theoretical prediction: $b = b_0 m_0/\mu$, where b_0 is the nucleon-nucleus nonlocality parameter, m_0 is the nucleon mass, and μ is the reduced mass of the system. The value $b_0 = 0.85$ fm was well established by an extensive nucleon-nucleus elastic data analysis [16]. We have used the above system-dependent expression for b in the interaction, Eq. (3).

We propose that $V_{NL}(\frac{R+R'}{2})$ is of the following folding-inspired form:

$$V_{NL}(\xi) = V_{\text{fold}}(R = \xi), \tag{4}$$

$$V_{\text{fold}}(R) = \int \rho_1(r_1) v(\vec{R} - \vec{r}_1 + \vec{r}_2) \rho_2(r_2)\, d\vec{r}_1\, d\vec{r}_2, \tag{5}$$

where $\rho_1(r_1)$ and $\rho_2(r_2)$ are the nuclear densities of the colliding partners and $v(r)$ is the effective nucleon-nucleon interaction. We point out that $V_{\text{fold}}(R)$ is assumed to have the local standard form of the double-folding potential [11]. We have used the well-known nucleon-nucleon M3Y interaction

$$v(r) = \left[7999\,\frac{e^{-4r}}{4r} - 2134\,\frac{e^{-2.5r}}{2.5r}\right] - 262\delta(\vec{r})\ \text{MeV}. \tag{6}$$

The pseudopotential, $-262\delta(\vec{r})$ MeV, describes the knock-on exchange collision at 10 MeV/nucleon [12]. The two other Yukawa terms are responsible for the direct component of the interaction. We stress that $V(\vec{R}, \vec{R}')$ is a nonlocal exchange potential, since we have considered the exchange as the main source of the nonlocality. In our approach, we have not considered the intrinsic energy dependence in the effective nucleon-nucleon interaction since we associate all the observed energy dependence of the local equivalent potential to the parameter b. As has been discussed earlier within a microscopic treatment [15], such a hypothesis should be valid at energies up to 200 MeV/nucleon. Therefore, the present data analysis is a further test to check our recent findings [19], which associate most of the observed energy dependence of the phenomenological local real potential to finite range exchange effects.

We turn next to the data analyses. After projecting over partial waves, we have solved numerically Eq. (1) by an iterative method. In order to test how general is our model, we have analyzed elastic scattering angular distributions for the $^{12}C + {}^{12}C$, ^{208}Pb and $\alpha + {}^{12}C$, ^{58}Ni systems. These systems correspond to quite different nonlocality range parameters: $b = 0.075$ fm ($^{12}C + {}^{208}Pb$), $b = 0.14$ fm ($^{12}C + {}^{12}C$), $b = 0.23$ fm ($\alpha + {}^{58}Ni$), and $b = 0.28$ fm ($\alpha + {}^{12}C$). For the first two systems, the data are available at a wide energy range ($1 \le E_{\text{lab}}/A_{\text{proj}} \le 200$ MeV/nucleon), whereas the last two systems represent typical cases of refractive scattering that have been studied in details in the early 1970s [2–4]. In the present analyses, we have used realistic microscopic nuclear densities as reported in the literature [11,12,20]. The only parameters that were allowed to vary were those of the absorptive Woods-Saxon imaginary potential. In Figs. 1 and 2 we show the angular distributions for the systems above at the following bombarding energies: $E_{\text{lab}} =$ 16, 112, 300, 1016, 1449, and 2400 MeV ($^{12}C + {}^{12}C$), $E_{\text{lab}} = 420$, 1449, and 2400 MeV ($^{12}C + {}^{208}Pb$), and $E_{\text{lab}} = 139$ MeV ($\alpha + {}^{12}C$, ^{58}Ni). The agreement between the theoretical calculations (solid lines) and the experimental data (from Refs. [4,5,21–26]) is impressive. The quality of the fits are at least as good as that of any other analyses using realistic potentials.

The resulting reaction cross section values are very similar to the already reported ones (Refs. [1,4,5,21–26]). The geometry of the imaginary potential $W(R)$ and the corresponding volume integral $J_W(E)$ behave as a function of E quite smoothly. More specifically for the $^{12}C + {}^{12}C$ system, the behavior of $J_W(E)$ as a function of the bombarding energy is just like the one shown in Fig. (6.8) of Ref. [1]. To our knowledge, the results reported here correspond to a first attempt to reproduce light- and heavy-ion elastic angular distributions for such a variety of systems and such a wide energy range with completely parameter-free real interaction. Furthermore, the usual renormalization factor of the DDM3Y interaction is absent in our analyses. Thus, one reaches the conclusion that the widely used

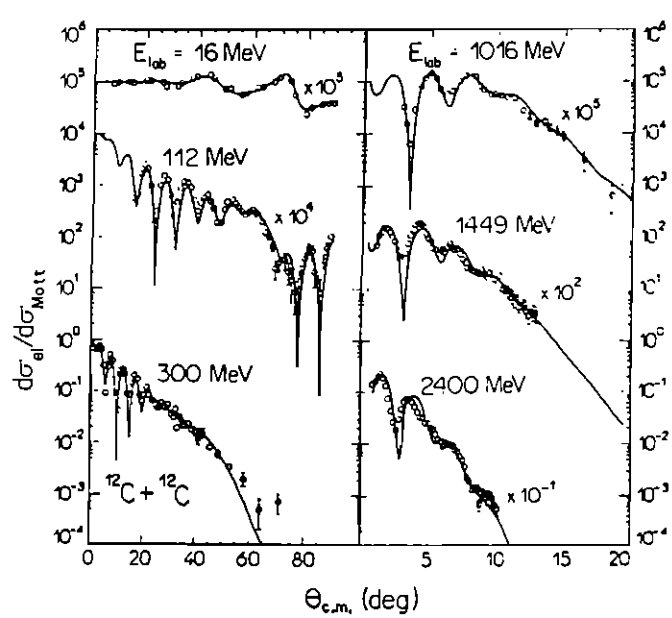

FIG. 1. Elastic scattering angular distributions for the $^{12}C + {}^{12}C$ system at several bombarding energies as indicated. The data are from Refs. [5,21–24]. The solid lines correspond to nonlocal optical model calculations using an energy-independent and parameter-free real potential (see text). Note the change in the scattering angle scale.

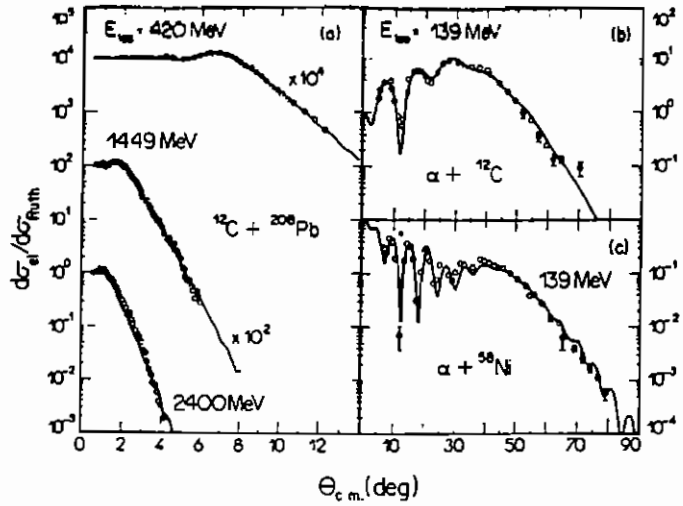

FIG. 2. The same as Fig. 1 for the systems $^{12}C + {}^{208}Pb$ and $\alpha + {}^{12}C, {}^{58}Ni$. The data are from Refs. [4,24–26]. Note the changes in the scales of both axes.

energy-dependent potential hides to some extent the underlying nonlocal interaction. We should mention, however, that there is room to have some density dependence in our model if a more optimized fit is undertaken. From the result we obtain, it is clear that this dependence is bound to be weak.

Because of the high values of orbital angular momentum involved in the calculations, the numerical solution of the integro-differential equation (1) is a very hard task for heavy-ion systems. Thus, it is desirable to develop a method to obtain the local equivalent potential (LEP) in order to calculate cross sections solving the usual Schrödinger equation. In the early 1960s, Perey and Buck [16] showed that the LEP is only weakly ℓ dependent and supplied an approximate relation to obtain that potential for neutron-nucleus systems. We have generalized [19] that expression to the nucleus-nucleus case, namely,

$$V_{LE}(R;E)\exp[-\gamma V_{LE}(R;E)] \approx V_{fold}(R)\exp\{-\gamma[E - V_C(R) - iW(R,E)]\}, \quad (7)$$

with $\gamma = \mu b^2/2\hbar^2$. The above equation can be solved for $V_{LE}(R;E)$ by the iterative method. Since for heavy-ion systems the value of γ is very small (for $^{12}C + {}^{12}C$, $\gamma = 0.0014\ \mathrm{MeV}^{-1}$) we can appropriately expand (7) to obtain

$$V_{LE}(R;E) \approx V_{fold}(R)[1 - \gamma E] = V_{fold}(R)\left(1 - \beta\frac{E_{lab}}{A_{proj}}\right), \quad (8)$$

where $\beta = m_0 b_0^2/2\hbar^2$ is a system-independent constant equal to $0.0086\ \mathrm{MeV}^{-1}$. This linear behavior of the potential with the energy has been particularly observed in α nucleus scattering [18] and the experimentally extracted slope is in agreement with the theoretical β value.

A better approximation, valid over a greater energ range, is obtained by neglecting the imaginary part of th potential and expanding the left hand side of Eq. (7) : lowest order in γ. The resulting quadratic equation ma be solved to obtain

$$V_{LE}(R;E) \approx \frac{1 - \sqrt{1 - 4\gamma V_{fold}(R)\exp\{-\gamma[E - V_C(R)]\}}}{2\gamma}. \quad (9$$

We point out that in the limit $b \to 0$ we find for bo Eqs. (8) and (9) $V_{LE}(R,E) = V_{fold}(R)$, which contair the exchange effects in the zero-range approximatic as should be the case. We have calculated the loc equivalent potential using Eq. (9) for the system ^{12}C - ^{12}C at three bombarding energies. The results are show as solid lines in Fig. 3. For comparison, the foldir potential, $V_{fold}(R)$, is also shown (dashed line). W can observe that the LEP have slightly different shape than that of $V_{fold}(R)$. At high energies, we observe th $V_{LE}(R,E)$ becomes factorized as $V_{LE}(R)f(E)$ with $f(E$ being roughly exponential.

We have also calculated the real part of the exa local equivalent potential through Eq. (1). The resul convinced us that, as expected [16], the ℓ dependence c the LEP is very weak. The potential values arising fror the exact calculation agree with those from Eq. (9) withi about 3%. We have also calculated elastic scatterin angular distributions by solving the local Schrödinge differential equation using the approximate LEP fror Eq. (9). The results are quite similar to those generate from the solution of the full integro-differential equatio (1). It is important to mention that the parameters c the imaginary Woods-Saxon potential, $W(R,E)$, used i the exact calculations are somewhat different from thos

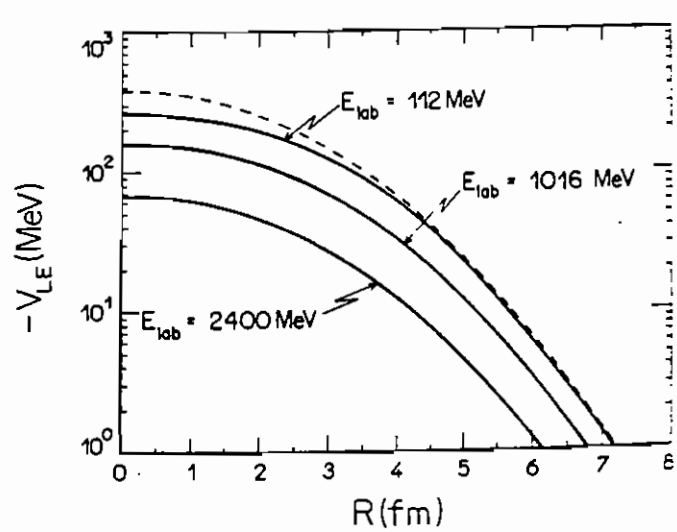

FIG. 3. The local equivalent potential (solid lines) for th $^{12}C + {}^{12}C$ system at three different bombarding energies The dashed line corresponds to the double-folding energy independent potential.

used in the approximate ones, owing to the absence of $\mathrm{Im}[V_{\mathrm{LE}}(R,E)]$ in Eq. (9).

In conclusion, we have presented in this Letter a new model for the nucleus-nucleus interaction. The corresponding real potential is nonlocal and completely parameter-free. The local equivalent version of this interaction is angular-momentum independent and with a very simple energy dependence. Such potential reproduces the experimental elastic differential cross sections for a variety of systems and over a wide range of bombarding energies. Thus, the explicit consideration of the intrinsically quantum, finite range exchange nonlocality is of fundamental importance in the description of the nucleus-nucleus collision. Our results could be potentially important for the description of the scattering of other many-body systems.

A more detailed account of our work which will include an extensive comparison with the quasielastic scattering data of several other heavy ion systems will be published shortly.

M. A. C. R. is supported by FAPESP (Contract No. 96/3240-5) and all other authors are partly supported by CNPq. We thank G. R. Satchler for comments and suggestions.

[1] M. E. Brandan and G. R. Satchler, Phys. Rep. **285**, 143 (1997).
[2] D. A. Goldberg and S. M. Smith, Phys. Rev. Lett. **29**, 500 (1972).
[3] D. A. Goldberg and S. M. Smith, Phys. Rev. Lett. **33**, 715 (1974).
[4] D. A. Goldberg, S. M. Smith, and G. F. Burdzik, Phys. Rev. C **10**, 1362 (1974).
[5] H. G. Bohlen, M. R. Clover, G. Ingold, H. Lettau, and W. von Oertzen, Z. Phys. A **308**, 121 (1982).
[6] H. G. Bohlen, X. S. Chen, J. G. Cramer, P. Frobrich, B. Gebauer, H. Lettau, A. Miezaika, W. von Oertzen, R. Ulrich, and Th. Wilpert, Z. Phys. A **322**, 241 (1985).
[7] E. Stiliaris, H. G. Bohlen, P. Frobrich, B. Gebauer, D. Kolbert, W. von Oertzen, M. Wilpert, and Th. Wilpert, Phys. Lett. B **223**, 291 (1982).
[8] A. M. Kobos, B. A. Brown, P. E. Hodgson, G. R. Satchler, and A. Budzanowski, Nucl. Phys. **A384**, 65 (1982).
[9] A. M. Kobos, B. A. Brown, R. Lindsay, and G. R. Satchler, Nucl. Phys. **A425**, 205 (1984).
[10] D. T. Khoa, W. von Oertzen, and A. A. Ogloblin, Nucl. Phys. **A602**, 98 (1996).
[11] G. R. Satchler and W. G. Love, Phys. Rep. **55**, 183 (1979).
[12] M. El-Azab Farid and G. R. Satchler, Nucl. Phys. **A438**, 525 (1985).
[13] R. Peierls and N. Vinh Mau, Nucl. Phys. **A343**, 1 (1980).
[14] R. M. Devries and M. R. Clover, Nucl. Phys. **A243**, 528 (1975).
[15] W. Bauhoff, H. V. von Geramb, and G. Palla, Phys. Rev. C **27**, 2466 (1983).
[16] F. Perey and B. Buck, Nucl. Phys. **32**, 253 (1962).
[17] W. E. Frahn and R. H. Lemmer, Nuovo Cimento **5**, 1564 (1957).
[18] D. F. Jackson and R. C. Johnson, Phys. Lett. **49B**, 249 (1974).
[19] M. A. Cândido Ribeiro, L. C. Chamon, D. Pereira, M. S. Hussein, and D. Galetti, Phys. Rev. Lett. **78**, 3270 (1997).
[20] L. C. Chamon, D. Pereira, E. S. Rossi, Jr., C. P. Silva, H. Dias, L. Losano, and C. A. P. Ceneviva, Nucl. Phys. **A597**, 253 (1996).
[21] W. Treu, H. Frohlich, W. Galster, P. Duck, and H. Voit, Phys. Rev. C **22**, 2462 (1980).
[22] R. G. Stokstad, R. M. Wieland, G. R. Satchler, C. B. Fulmer, D. C. Hensley, S. Raman, L. D. Rickersten, A. H. Snell, and P. H. Stelson, Phys. Rev. C **20**, 655 (1979).
[23] M. Buenerd, A. Lounis, J. Chauvin, D. Lebrun, P. Martin, G. Duhamel, J. C. Gondrand, and P. de Saintignon, Nucl. Phys. **A424**, 313 (1984).
[24] J. Y. Hostachy, M. Buenerd, J. Chauvin, D. Lebrun, Ph. Martin, J. C. Lugol, L. Papineau, P. Roussel, N. Alamanos, J. Arviex, and C. Cerruti, Nucl. Phys. **A490**, 441 (1988).
[25] C. C. Sahm, T. Murakami, J. G. Cramer, A. J. Lazzarini, D. D. Leach, D. R. Tieger, R. A. Loveman, W. G. Lynch, M. B. Tsang, and J. Van der Plicht, Phys. Rev. C **34**, 2165 (1986).
[26] S. M. Smith, G. Tebell, A. A. Cowley, D. A. Goldberg, H. G. Pugh, W. Reichart, and N. S. Wall, Nucl. Phys. **A207**, 273 (1973).

Rel. Ch98

Parameterfree account of quasielastic scattering of stable and radioactive nuclei

L. C. Chamon, D. Pereira, and M. S. Hussein
Instituto de Física, Universidade de São Paulo, Caixa Postal 66318, 05315-970 São Paulo, SP, Brazil
(Received 13 March 1998)

Elastic and inelastic scattering cross sections of the system $^{12}C+^{12}C$ at several bombarding energies are calculated within a parameterfree model using the recently developed nonlocal energy-independent bare potential. Comparison with the data indicates that such a calculation gives accurately the average values of the cross sections. The system $^{12}C+^{11}Li$ is also discussed. [S0556-2813(98)01407-1]

PACS number(s): 25.70−z, 24.10.−i

Recently, we have proposed an energy and density independent real bare interaction for the description of heavy ion scattering [1,2]. In Ref. [2], we subjected our potential (coined the NLM3Y potential) to a stringent test by confronting it with elastic scattering data of a wide range of systems and energies. The imaginary part of the potential was taken to be a Woods-Saxon one with three adjustable parameters (in fact the diffuseness was taken to be fixed with respect to energy). The good agreement with the data, especially in the refractive region, convinced us that the NLM3Y interaction captures the essentials of the physics. The purpose of this work is to develop a parameterfree model by using for the absorptive part a $t\rho_1\rho_2$-inspired form. The energy dependence of such an interaction is then completely determined by that of the effective nucleon-nucleon total cross section [3]. We calculate both the elastic and inelastic cross sections for the $^{12}C+^{12}C$ at several energies where data are available. We also compare our theory with the elastic scattering of the halo nucleus ^{11}Li off ^{12}C. There are no free parameters in our calculation. The NLM3Y interaction is given by

$$V(\vec{r},\vec{r}')=V_{DF}\left(\frac{r+r'}{2}\right)\frac{1}{\pi^{3/2}b^3}\exp\left[-\frac{|\vec{r}+\vec{r}'|^2}{b^2}\right], \quad (1)$$

where $V_{DF}(r)$ is the local energy- and density-independent (aside from the folding of the two densities) double folding potential and $b=0.85/\mu$ fm with μ being the reduced mass of the two colliding nuclei.

We have shown in Ref. [2] that the energy-dependent local equivalent potential of Eq. (1) is, to a very good approximation, given by

$$V_{LE}(r;E)=\frac{1-\sqrt{1-4\gamma V_{DF}(r)\exp\{-\gamma[E-V_c(r)]\}}}{2\gamma}, \quad (2)$$

where $\gamma=\mu b^2/2\hbar^2$ and $V_c(r)$ is the double folding Coulomb interaction. As for the imaginary part we employ here the Lax interaction

$$W(r,E)=-\frac{E}{k_N}\sigma_T^{NN}(E)\int dr'\rho_A(|\vec{r}-\vec{r}'|)\rho_B(|\vec{r}'|), \quad (3)$$

where $\rho_T^{NN}(E)$ is the average nucleon-nucleon total cross section with Pauli blocking [3].

We have solved the optical differential equation using Eq. (2) as the bare real interaction and W of Eq. (3) as the energy-dependent imaginary potential. The model and the method of solution are fully discussed in Ref. [2]. The systems we chose to discuss the model are $^{12}C+^{12}C$ at several bombarding energies and $^{11}Li+^{12}C$ at $E_{lab}=637$ MeV. The value of $\sigma_T^{NN}(E)$ were taken from Ref. [4] and realistic densities were used in the double folding calculation. In the evaluation of the cross section for the inelastic transition $^{12}C+^{12}C\rightarrow^{12}C(E_{2+}=4.4\text{ MeV})+^{12}C$ we used the distorted wave Born approximation (DWBA) with an appropriate collective form factor having the form

$$F(r)=\delta\left(\frac{dU}{dr}+i\frac{dW}{dr}\right), \quad (4)$$

with $\delta=\beta R_0$, $R_0=1.2A^{1/3}$, and $\beta=0.6$ [4].

The potentials U and W are the same as those of Eqs. (2) and (3). We ignore Coulomb excitation since the system is light and the bombarding energy is high. In Fig. 1 we show our result both for the elastic [Fig. 1(a)] and inelastic [Fig. 1(b)] cross sections for the $^{12}C+^{12}C$ system. The data points were taken from Ref. [4].

Although the calculated cross section shows stronger oscillatory behavior, the magnitude, however, is in good agreement with the data. We consider this a very positive aspect of our parameterfree model. Clearly, space is available for improvement since what is at stake is not so much the energy dependence, which we believe to be well accounted for, but the geometry of the imaginary part.

In Table I we present a comparison of the calculated total reaction cross sections and the ones obtained directly or indirectly from the data. The agreement is excellent.

We consider next the scattering of a typical halo nucleus ^{11}Li. A measurement of the differential, inclusive, quasielastic cross section for $^{11}Li+^{12}C$ at $E_{lab}=637$ MeV has already been reported [5]. Several attempts to account for the data were made [6,7]. Here our aim is not so much to get a better fit to the data, but rather to test the parameterfree NLM3Y interaction.

In the case of the scattering of ^{11}Li we have learned in the last few years that two competing effects come into play due to the extended size of the system: the enhanced probability for the breakup into $^9Li+2n$ (due to the very small separation energy of the $2n$) and the longer tail in the attractive bare potential due to the halo. The first effect brings in a

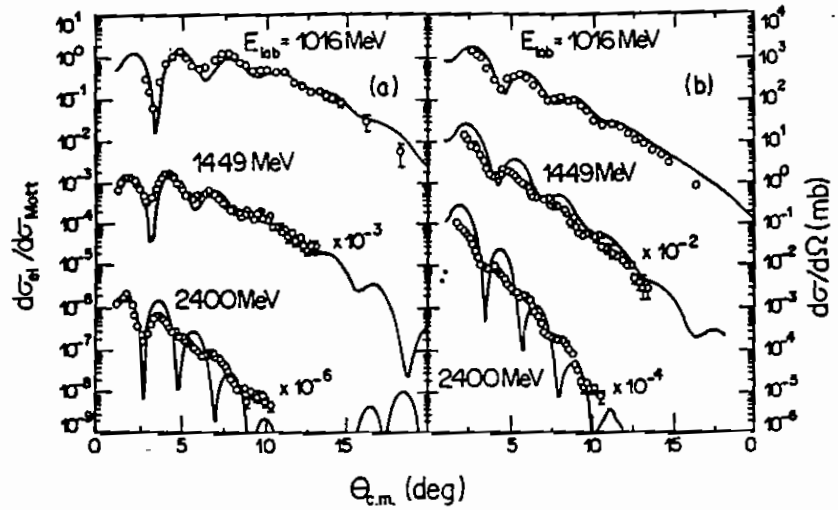

FIG. 1. Elastic (a) and inelastic (b) differential cross sections for the $^{12}C+^{12}C$ system. The data points are from Ref. [4] and also from Ref. [11].

long-range absorption to be added to W while the second adds to refraction. There is a third effect which is inherent in our NLM3Y interaction and that is the nonlocality range b.

On general ground and from the arguments given in Ref. [8], a slightly different (smaller) value of b is expected for the halo nucleus-stable nucleus NLM3Y interaction. To be precise, the value of b adapted for our analysis of the stable projectile-stable target NLM3Y interaction, namely, $b=0.85/\mu$ fm, is in fact obtained by Jackson and Johnson in the limit of an infinite size projectile or target (zero binding energy). This is not so bad an approximation, since relaxing this approximation by using Gaussian form for the density of the projectile or target, gives rise to a reduction in b by [8]

$$b \rightarrow \bar{b} = b\left[1+\left(\frac{0.85}{2R}\right)^2\right]^{-1/2}. \tag{5}$$

Thus the larger R is, the closer b would be to the value used above, $0.85/\mu$ fm.

Another, potentially important, consequence of the finite size of the nucleus is a reduction factor that multiplies the double folding potential, viz.

$$U_{DF} \rightarrow \bar{U}_{DF} = \left(\frac{\bar{b}}{b}\right)^3 U_{DF} = \left[1+\left(\frac{0.85}{2R}\right)^2\right]^{-3/2} U_{DF}. \tag{6}$$

The effects represented by Eqs. (5) and (6), are appreciable in the case of tightly bound (small) nuclei such as α particles. Thus, at most, the smaller value of $\bar{b}$ and the reduced strength of the double folding potential for halo nuclei result in few percent effects. This, coupled with the need to take into account the breakup channel, suggests the use of a model for elastic scattering following the line of Ref. [9], which uses the adiabatic approximation and takes into account the breakup effects to all orders, viz.,

$$\frac{d\sigma}{d\Omega} = |F(Q)|^2 \frac{d\sigma_{core}}{d\Omega}, \tag{7}$$

where $d\sigma_{core}/d\Omega$ is the core (^{9}Li) $+^{11}$C elastic scattering differential cross section, while $F(Q)$ is the form factor related to the ground state wave function of ^{11}Li. This form factor has a value of unity at $Q=0$ and drops gradually with increasing Q, thus simulating the effect of breakup coupling. At the small angles (Q) involved in the measurement of Ref. [5] we set for the time being $F(Q)=1$. With this we are approximating the combined effect of smaller $\bar{b}$ and breakup damping by considering the ^{11}Li$+^{12}$C cross section, to be roughly the ^{9}Li$+^{12}$C cross section. In the following we give a description of our calculation for the system ^{11}Li$+^{12}$C.

Although a slightly different W from Eq. (3) should be used, owing to the loosely bound two neutrons halo, we have simply employed Eq. (3) for the imaginary part. We calculated the elastic and inelastic cross section for the 2^+ and 3^- states in ^{12}C. The result of the calculation is shown in Fig. 2, together with the data of Kolata *et al.* [5]. The summed cross section comes a bit short of accounting for the data in the

TABLE I. Calculated and experimental reaction cross sections of the $^{12}C+^{12}C$ system.

E_{lab} (MeV)	σ_{theory} (mb)	$\sigma_{experimental}$ (mb)	$\sigma_{inelastic}$ (mb)
1016	958	960±25 [a]	29
1449	886	907±50 [b]	24
2400	825	860±50 [a]	15

[a]Data taken from Refs. [12,13].
[b]Data taken from Ref. [4].

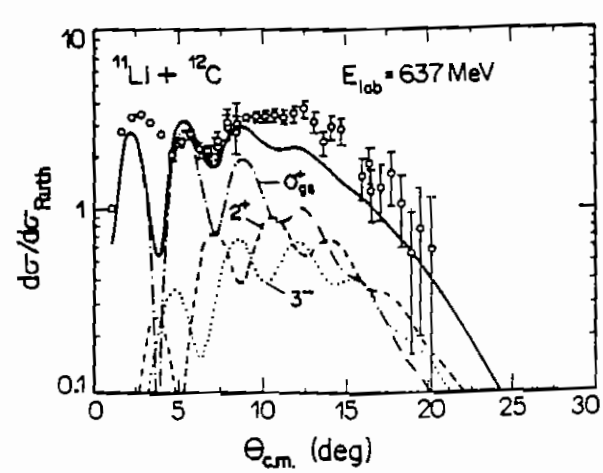

FIG. 2. The calculated summed quasielastic cross section for ^{11}Li$+^{12}$C at $E_{lab}=637$ MeV (see text for details). The data points are from Ref. [5].

angular region $10° < \theta < 15°$ and also in the region around $\theta = 4°$. This latter region is also missed by most other calculations reported in the literature [6]. The total reaction cross section comes out to be $\sigma_R = 1.41$ b, in good agreement with the deduced one [5]. This result is very similar to the one obtained by Khoa, Satchler, and von Oertzen [6] where a three-parameter Woods-Saxon imaginary potential was employed. We stress here that we do not have in our model any adjustable parameter. We consider our result reasonable and certainly there is room for improvement such as considering higher-order terms in the multiple scattering theory-inspired form for W. It is also quite possible that other inelastic cross-sections may have to be added, such as the transition to the "3α" 0^+ state at $E^* = 7.68$ MeV [10].

[1] M.A. Cândido Ribeiro, L.C. Chamon, D. Pereira, M.S. Hussein, and D. Galetti, Phys. Rev. Lett. **78**, 3270 (1997).

[2] L.C. Chamon, D. Pereira, M.S. Hussein, M.A. Cândido Ribeiro, and D. Galetti, Phys. Rev. Lett. **79**, 5218 (1997).

[3] See, e.g., M.S. Hussein, R.A. Rego, and C.A. Bertulani, Phys. Rep. **201**, 279 (1991).

[4] J.Y. Hostachi *et al.*, Nucl. Phys. **A490**, 441 (1988).

[5] J.J. Kolata *et al.*, Phys. Rev. Lett. **69**, 2631 (1992).

[6] See, e.g., D.T. Khoa, G.R. Satchler, and W. von Oertzen, Phys. Lett. B **358**, 14 (1995), and references therein.

[7] C.A. Bertulani, L.F. Canto, and M.S. Hussein, Phys. Rep. **227**, 281 (1993).

[8] D. Jackson and R.C. Johnson, Phys. Lett. **49B**, 249 (1974).

[9] R.C. Johnson, J.S. al-Khalili, and J.A. Tostevin, Phys. Rev. Lett. **79**, 2771 (1997).

[10] J. J. Kolata, private communication.

[11] M. Buenerd *et al.*, Nucl. Phys. **A424**, 313 (1984).

[12] S. Kox *et al.*, Phys. Rev. C **35**, 1678 (1987).

[13] C. Perrin *et al.*, Phys. Rev. Lett. **49**, 1905 (1982).

Nonlocal effects in the ^{8}Be breakup

Ref. Ga 98

D. Galetti
Instituto de Física Teórica, Universidade Estadual Paulista, Rua Pamplona 145, 01405-900 - São Paulo, SP – Brazil

Salomon S. Mizrahi
Departamento de Física, Universidade Federal de São Carlos, Rodovia Washington Luiz, km 235, São Carlos, SP – Brazil

L. C. Chamon, D. Pereira, and M. S. Hussein
Instituto de Física, Universidade de São Paulo, C.P. 66318, 05315-970 - São Paulo, SP – Brazil

M. A. Cândido Ribeiro
Department of Physics, University of Wisconsin, 1150 University Ave., Madison, Wisconsin 53706
(Received 2 April 1998)

A collective Hamiltonian for a two alpha particles aggregate, which describes the ^{8}Be nucleus, encompassing a collective potential and an inertia function of that system, is obtained and analyzed through the use of a technique — derived from an approach of the generator coordinate method (GCM) — which allows for the extraction of collective information. The nucleon-nucleon interaction considered here is the one proposed by Volkov plus the Coulomb repulsion. It is shown that nonlocal effects appear in those collective functions describing the spontaneously occurring breakup process. Furthermore, the result for the inertia function stands for a microscopically generated evidence supporting a double-folding-based model of the real part of the nucleus-nucleus nonlocal interaction recently proposed. [S0556-2813(98)03509-2]

PACS number(s): 24.10.−i, 25.90.+k

I. INTRODUCTION

The description of the interaction between two colliding heavy nuclei has long been the subject of study in nuclear physics and the determination of its features a major goal to be attained. In the past years systematic accurate and extensive measurements involving elastic scattering at intermediate energies gave rise to a great improvement in the understanding of the nucleus-nucleus interaction [1]. As a consequence of the analysis of the nuclear rainbow scattering that occurs in those cases the real part of that interaction can be nowadays unambiguously described and its determination, not only at the surface, but also at smaller distances, can be accomplished [2,3]. The resulting phenomenological interactions present significant dependence upon the bombarding energies. To account for this dependence some theoretical models have been developed which make explicit use of density dependent interactions [4–6]. On the other hand, it has been recently shown in a description of elastic scattering, using an integrodifferential equation, that the real mean field (with no coupled channels effects) potential dependence on the bombarding energy comes mostly from nonlocal exchange effects [7,8]. That mean field potential has been proposed to be constructed using the usual double folding model with an energy-independent nonlocal exchange interaction. The results have shown that the obtained nucleus-nucleus interaction can be written in such a form so as to embody the nonlocal exchange effects through a simple form. The nonlocal real part of that potential can be rewritten as a local equivalent one which clearly displays the energy dependence preconized by the phenomenological approach. Furthermore, the double folding inspired inertia function that comes in the treatment reveals the fundamental character of the nonlocal effects in the scattering processes, much in the same spirit as has been previously seen in nuclear fusion processes [9,10].

The aim of the present paper is twofold. First, we intend to show that the exchange nonlocal effects, being primarily of quantum mechanical origin, thus pervading general many-body phenomena, manifest themselves also in still another type of nuclear process, namely the nuclear breakup. Second, we intend to show that the microscopic extraction of the nonloeal effects presented here for that particular type of process do in fact stand for a microscopic support for the ansatz previously proposed for the real part of the nucleus-nucleus interaction, as mentioned above [7,8].

As the ^{8}Be is known to be a spontaneous fissionable nucleus, it constitutes a convenient testing ground for studying the nonlocal effects appearing in this particular process. This convenience comes from the fact that this nucleus is light enough, thus leading to calculations much less involved than those necessary for heavier nuclei where spontaneous fission also occurs, and also because the nonlocal effects are more manifest in this case due to the value of the corresponding nonlocality range that is greater than for heavier systems. Since it is known from the experience that the ^{8}Be nucleus decays into two alpha particles, it seems natural to describe it within the generator coordinate method (GCM) [11–14] by a model consisting of a deformed two alpha particles structure. In fact, the resonating group approach [15] could be used as well, but here we will follow the GCM scheme. Thus, we see that we can describe the ^{8}Be nucleus through a model consisting of a preformed structure of two alpha clusters that can be accomplished by considering two harmonic oscillator (HO) potentials symmetrically located about the origin of a coordinate system, each one describing a single cluster [16–19]. Therefore, because we are inter-

ested in studying the breakup of the ^{8}Be, *after it is formed*, in the present treatment it is natural to choose the half distance between the centers of the two HO potentials only along the breakup axis, say the z-axis, as the *generator coordinate* (GC). The same is not true if one wants to study the general alpha-alpha scattering problem within the GCM [17], where the generator coordinate is then **r**, the spatial separation between the centers of the alpha clusters. The full 8×8 Slater determinant wave function of the ^{8}Be nucleus is constructed with the $1s$ single particle wave function of these two HO's thus yielding the parametrized generating function of the method. The microscopic nuclear potential acting between the nucleons that we consider here is the one proposed by Volkov [20], since it is simple enough to handle and suitable to light nuclei calculations. Furthermore, it has also been shown within the GCM that this kind of interaction gives good results for the partial waves $l=0,2,4,6$ phase shifts of an alpha-alpha scattering [17]. As we concern ourselves with the breakup process, we expect both, this simple Volkov potential and the Coulomb repulsive force, to be sufficient to give origin to that particular resonance level which will characterize the ^{8}Be nucleus. The GCM energy kernel we propose is then composed of two parts, namely, the nuclear Volkov-generated contribution and a full microscopic Coulomb term. In the present treatment of the ^{8}Be nucleus we have not carried ahead the calculation of the projected ground state energy within the GCM, in order to compare it with the experimental value.

In this description, the nonlocal effects come mostly from two sources, namely from the nonorthogonality of the GCM states and from the full 8×8 determinantal character of the associated GCM kernels. In fact, using the Volkov nucleon-nucleon interaction plus the Coulomb repulsion we were able to explicitly obtain the GCM kernels which are manifestly nonlocal.

It has been shown in the past that it is possible to extract collective information from the GCM kernels [21–26]. However, these procedures lack some quantum information because they handle directly with the GC, which is a parameter. Although the GC itself is not a dynamical variable, a pair of genuine collective coordinate-momentum variables can be constructed out of the original GC, and, in fact, it has been shown in the past that a collective Hamiltonian can be written which encompasses a collective potential and an inertia function as the GCM kernels are given. In the present case, the main feature of this new collective Hamiltonian is that it embodies the nonlocal effects present in the initial GCM microscopic description of the breakup process. Therefore, in order to extract the collective potential and the inertia function, which are the constituents of the Hamiltonian, out of the GCM kernels, we took advantage of a procedure based on the GCM and on the Weyl formalism [27] presented many years ago [28]. Using a numerical technique derived from this approach [29], it is possible to extract the collective potential (inertia function) as the discretized version of a zeroth-moment (second moment) of a discretized transformed GCM energy kernel. With these numerical results for those functions we were able to discuss the microscopically generated nonlocal effects present in the breakup process.

This paper is organized as follows. In Sec. II we present the calculations of the GCM kernels. In Sec. III we briefly present the numerical technique and results, while in Sec. IV we discuss the nonlocal effects in our particular breakup process. Finally Sec. V is devoted to the conclusions and final remarks.

II. THE GCM KERNELS

An alpha cluster model, based on the GCM has been developed by Brink [18] many years ago to study the structure of light nuclei. We will follow here that method of Brink in order to calculate the overlap and energy kernels that enters the Griffin-Wheeler (GW) equation,

$$\int [\langle\alpha|H|\alpha'\rangle - E\langle\alpha|\alpha'\rangle] f(\alpha')d\alpha' = 0 \tag{1}$$

for the ^{8}Be nucleus, since they constitute the essential quantities for the derivation of the collective potential, inertia function and energy spectrum, as already discussed [29].

We will choose a coordinate system whose z-axis coincides with the path along which the alpha particles motion occurs, each alpha cluster being described by a HO potential whose center is located at a distance z_0 about the origin. The spatial part of the single particle wave function is written as

$$\varphi(x,y,z) = \frac{1}{\pi^{3/4} b^{3/2}} \exp[-(x^2+y^2)/2b^2] \times \exp[-(z\pm z_0)^2/2b^2], \tag{2}$$

where the sign $\pm$ in front of z_0 is introduced in order to specify to which cluster a particular nucleon belongs. The parameter z_0, the half distance between the fragments, will constitute our generator coordinate and b is the HO parameter whose value allows us to fix the α radius.

Once we have constructed the 8×8 Slater determinant of the ^{8}Be nucleus, $|\Psi(z_0)\rangle$, it is immediate to calculate the normalized overlap kernel

$$N(z_0,z_0') = \langle\Psi(z_0')|\Psi(z_0)\rangle = \frac{[\det\langle\varphi_i(z_0')|\varphi_j(z_0)\rangle]^4}{[\det\langle\varphi_i(z_0')|\varphi_j(z_0')\rangle\det\langle\varphi_i(z_0)|\varphi_j(z_0)\rangle]^2}$$

$$= \frac{\{\exp[-(z_0-z_0')^2/2b^2] - \exp[-(z_0+z_0')^2/2b^2]\}^4}{[1-\exp(-2z_0'^2/b^2)]^2[1-\exp(-2z_0^2/b^2)]^2}. \tag{3}$$

where φ_i corresponds to the occupied orbital states and $\det\langle\varphi_i|\varphi_j\rangle$ stands for the determinant whose elements are the overlap of the single particle wave functions.

In the same fashion we calculate the contribution of the kinetic energy term to the GCM energy kernel,

$$T(z_0,z_0')=\langle\Psi(z_0')|\hat{T}|\Psi(z_0)\rangle$$
$$=4N(z_0,z_0')\sum_{i,j}\langle\varphi_i(z_0')|\hat{t}|\varphi_j(z_0)\rangle(B^{-1})_{ij}, \quad (4)$$

where the factor 4 stands for the spin-isospin degeneracy. B is the matrix whose elements are

$$B_{ij}=\langle\varphi_i(z_0')|\varphi_j(z_0)\rangle. \quad (5)$$

and $\hat{t}$ is the one-body kinetic energy operator. The analytic expression of $T(z_0,z_0')$ is

$$T(z_0,z_0')=4N(z_0,z_0')\left(\frac{\hbar^2}{mb^2}\right)\left\{\frac{3}{2}-\frac{[(z_0-z_0'/2b)]^2\exp[-(z_0-z_0')^2/2b^2]-[(z_0+z_0'/2b)]^2\exp[-(z_0+z_0')^2/2b^2]}{\exp[-(z_0-z_0')^2/2b^2]-\exp[-(z_0+z_0')^2/2b^2]}\right\}, \quad (6)$$

where m is the nucleon mass. The value of the diagonal expression $T(z_0,z_0)$, in the limit $z_0\to\infty$, gives $6\hbar^2/mb^2$, which is exactly the kinetic energy value of a system of two *free* alpha particles, each being described by $1s$ HO orbital states. In the other limit, $z_0\to 0$, $T(z_0,z_0)$ goes to $8\hbar^2/mb^2$, which is exactly the kinetic energy of a system of eight nucleons occupying the $1s$ and $1p$ orbital states. Expression (6) contains the spurious center-of-mass motion effect, however this can be corrected by subtracting the contribution of the center-of-mass term.

$$\frac{\hat{P}^2}{2mA}=\frac{1}{A}\sum_i\frac{\hat{p}_i^2}{2m}+\sum_{i\neq j}\frac{\hat{p}_i\cdot\hat{p}_j}{mA}, \quad (7)$$

which gives

$$\left\langle\Psi(z_0')\left|\frac{\hat{P}^2}{2mA}\right|\Psi(z_0)\right\rangle=\frac{T(z_0,z_0')}{A}+\frac{\hbar^2}{2mAb^2}\frac{N(z_0,z_0')}{\exp[-(z_0-z_0')^2/2b^2]-\exp[-(z_0+z_0')^2/2b^2]}$$
$$\times\left(\frac{(z_0-z_0')^2}{b^2}\left\{\exp\left[-\frac{(z_0-z_0')^2}{2b^2}\right]-\exp\left[-\frac{(z_0-z_0')^2+(z_0+z_0')^2}{2b^2}\right]\right\}\right.$$
$$\left.+\frac{(z_0+z_0')^2}{b^2}\left\{\exp\left[-\frac{(z_0+z_0')^2}{2b^2}\right]-\exp\left[-\frac{(z_0-z_0')^2+(z_0+z_0')^2}{2b^2}\right]\right\}\right). \quad (8)$$

where A is the total number of nucleons. As $z_0\to\infty$, the diagonal part of the second term in Eq. (8) vanishes, while for $z_0\to 0$ it goes to $-\hbar^2/mAb^2$.

The nuclear two-body potential of Volkov [20], together with the Coulomb repulsion, constitute the full interaction between the nucleons.

$$\hat{V}(|\vec{r}_1-\vec{r}_2|)=(1-M+M\hat{P}_x)\{V_{0a}\exp[-\alpha_a|\vec{r}_1-\vec{r}_2|^2]$$
$$+V_{0r}\exp[-\alpha_r|\vec{r}_1-\vec{r}_2|^2]\}+\frac{e^2}{|\vec{r}_1-\vec{r}_2|}. \quad (9)$$

where $\hat{P}_x$ is the coordinate exchange operator and the values of the constants are: $V_{0a}=-76.69$ MeV, $V_{0r}=408.27$ MeV, $\alpha_a=0.444$ fm^{-2}, $\alpha_r=4.94$ fm^{-2}, $M=0.60$, $e^2=1.44$ MeV·fm, and $b=1.27$ fm is the value of the oscillator parameter: this value for b fixes the alpha radius as $R_\alpha=1.56$ fm.

For a potential of the form

$$\hat{V}(|\vec{r}_1-\vec{r}_2|)=u(|\vec{r}_1-\vec{r}_2|)[(1-M)+M\hat{P}_x], \quad (10)$$

the corresponding GCM energy kernel is [18]

$$\langle\Psi(z_0')|\hat{V}|\Psi(z_0)\rangle$$
$$=N(z_0,z_0')\sum_{ijkl}\langle\varphi_i(z_0')\varphi_j(z_0')|u|\varphi_k(z_0)\varphi_l(z_0)\rangle$$
$$\times[X_d(B^{-1})_{ki}(B^{-1})_{lj}+X_e(B^{-1})_{kj}(B^{-1})_{li}], \quad (11)$$

where $X_d=8-10M$, $X_e=10M-2$ and the matrix B is that already introduced in Eq. (5). In this way, for the Coulomb forces, we have $X_d^C=8$ and $X_e^C=-2$.

Finally, the analytic expression of the energy kernel of the full two-body potential is constituted of the following terms, namely: Gaussian terms

$$K_G(z_0,z_0')=\frac{2V_0}{(1+2\alpha_i b^2)^{3/2}}\frac{N(z_0,z_0')}{\{\exp[-(z_0-z_0')^2/2b^2]-\exp[-(z_0+z_0')^2/2b^2]\}^2}$$
$$\times\Bigg\{(X_d+X_e)\left\{\exp\left[-\frac{(z_0-z_0')^2}{2b^2}\right]+\exp\left[-\frac{(z_0+z_0')^2}{2b^2}\right]\right\}-2(X_d+X_e)\exp\left[-\frac{(z_0-z_0')^2}{4b^2}-\frac{(z_0+z_0')^2}{4b^2}\right]$$
$$\times\exp\left\{\left[-\frac{1}{4}\left(1+\frac{b^2\alpha_i}{1+2b^2\alpha_i}\right)\right]\left[\frac{(z_0-z_0')^2}{b^2}+\frac{(z_0+z_0')^2}{b^2}\right]\right\}\left\{\exp\left[\frac{b^2\alpha_i}{2(1+2b^2\alpha_i)}\left(\frac{z_0-z_0'}{b}\right)\left(\frac{z_0+z_0'}{b}\right)\right]\right.$$
$$\left.+\exp\left[-\frac{b^2\alpha_i}{2(1+2b^2\alpha_i)}\left(\frac{z_0-z_0'}{b}\right)\left(\frac{z_0+z_0'}{b}\right)\right]\right\}+\exp\left[-\frac{b^2\alpha_i}{1+2b^2\alpha_i}\left(\frac{z_0+z_0'}{b}\right)^2\right]\left\{X_d\exp\left[-\frac{(z_0-z_0')^2}{b^2}\right]\right.$$
$$\left.+X_e\exp\left[\frac{(z_0+z_0')^2}{2b^2}-\frac{(z_0-z_0')^2}{2b^2}\right]\right\}+\exp\left[-\frac{b^2\alpha_i}{1+2b^2\alpha_i}\left(\frac{z_0-z_0'}{b}\right)^2\right]\left\{X_d\exp\left[-\frac{(z_0+z_0')^2}{b^2}\right]\right.$$
$$\left.\left.+X_e\exp\left[\frac{(z_0+z_0')^2}{2b^2}-\frac{(z_0-z_0')^2}{2b^2}\right]\right\}\Bigg\},\tag{12}$$

and the Coulomb term

$$K_C(z_0,z_0')=\frac{4e^2}{b(2\pi)^{1/2}}\frac{N(z_0,z_0')}{\{\exp[-(z_0-z_0')^2/2b^2]-\exp[-(z_0+z_0')^2/2b^2]\}^2}\Bigg(\exp\left[-\frac{(z_0-z_0')^2}{b^2}\right]+\exp\left[-\frac{(z_0+z_0')^2}{b^2}\right]$$
$$+\frac{\pi^{1/2}}{2}\frac{\Phi(z_0+z_0'/\sqrt{2}b)}{z_0+z_0'/\sqrt{2}b}\left\{2\exp\left[-\frac{(z_0-z_0')^2}{b^2}\right]-\exp\left[-\frac{(z_0-z_0')^2+(z_0+z_0')^2}{2b^2}\right]\right\}$$
$$+\frac{\pi^{1/2}}{2}\frac{\Phi(z_0-z_0'/\sqrt{2}b)}{z_0-z_0'/\sqrt{2}b}\left\{2\exp\left[-\frac{(z_0+z_0')^2}{b^2}\right]-\exp\left[-\frac{(z_0-z_0')^2+(z_0+z_0')^2}{2b^2}\right]\right\}$$
$$-\pi^{1/2}\exp\left[-\frac{(z_0-z_0')^2+(z_0+z_0')^2}{2b^2}\right]\left[\frac{\Phi(z_0/\sqrt{2}b)}{z_0/\sqrt{2}b}+\frac{\Phi(z_0'/\sqrt{2}b)}{z_0'/\sqrt{2}b}\right]\Bigg),\tag{13}$$

respectively, where $\Phi(x)$ is the probability integral [30]. The complete GCM energy kernel can now be immediately written out of these contributions. It is worth mentioning that these expressions were specifically calculated for the breakup process, where the generator coordinate is z, and must not be directly compared with other energy kernels aiming at scattering problems. Besides, differently from approximated versions of the Coulomb term, as has been proposed [17], our expression for this contribution is fully microscopic.

III. NUMERICAL CALCULATIONS

In order to extract numerically the nuclear collective potential and inertia function for the ^{8}Be, we will follow the procedure presented in [29]. The first step consists in the diagonalization of the overlap kernel (3). However, by simple inspection of that expression we note that the overlap is not translationally invariant (it does not depend only on the difference z_0-z_0') around the origin, but for $z_0,z_0'\gtrsim b$ it goes as $\exp[-2(z_0-z_0')^2/b^2]$, thus exhibiting a narrower width than that around the origin. In what refers to the numerical results, the adoption of the asymptotic expression for the overlap kernel, for all values of z_0 and z_0', induces a small distortion in the exact description of the collective potential and inertia function near the origin [28,29]. Besides, for the exact overlap the numerical techniques used to extract the nuclear collective potential and inertia functions become extremely complicated and the results at present are not reliable. But, in fact, it has been verified in a 50 points mesh calculation that the lowest energy levels of the spectrum, obtained with the exact overlap, do not differ significantly from those calculated with the translationally invariant kernel. So, in spite of the approximated character of the description, we adopt here the asymptotic translationally invariant kernel, instead of the exact one, since the calculations can be performed with a high density of points in the interval of interest, which allows more reliable results. The introduction of that approximation leads to a collective potential and an inertia function that will present a slightly modified behavior near the origin (as compared to the expected exact results), where the exact overlap and the adopted one differ; however, this fact does not constitute a drastic drawback since the physically interesting region $z_0,z_0'\gtrsim b$ will be correctly described.

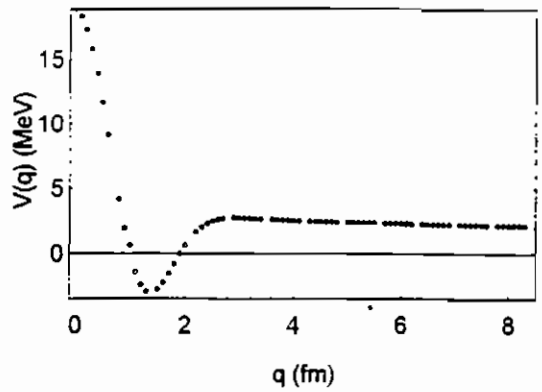

FIG. 1. Collective potential for the ^{8}Be breakup. The constant asymptotic nuclear behavior has been subtracted. The calculations were performed with a 70×70 mesh in the interval $-25\leq z_0\leq 25$ and a step of $\Delta z_0=0.7$.

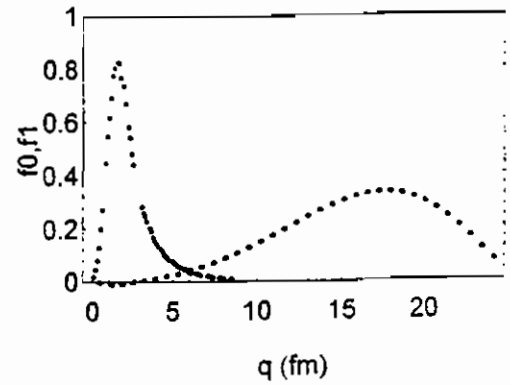

FIG. 2. The intrinsic first and second GCM calculated dimensionless wave functions for the two alpha system. The calculations were performed with a 70×70 mesh in the interval $-25\leq z_0\leq 25$ and a step of $\Delta z_0=0.7$.

After the GCM kernels have been calculated, the sums of the generator coordinates $(z_0+z_0')/2$ are transformed into a genuine collective coordinate and the differences z_0-z_0' into the canonically conjugated momentum through a Weyl-Wigner mapping [28]. In this way, we end up with an expression for the collective Hamiltonian which has the half-distance between the centers of the densities of the two alpha system as the quantum collective coordinate. Keeping the lowest order terms in its expansion in terms of anticommutators the collective Hamiltonian reads

$$H(q,p)=H^{(0)}(q)-\frac{1}{4\hbar^2}\{p,\{p,H^{(2)}(q)\}\}$$
$$+\text{higher order terms}, \qquad (14)$$

where we identify $H^{(0)}(q)\equiv V(q)$ as the collective potential for the ^{8}Be breakup and $B(q)\equiv\hbar^2/2H^{(2)}(q)$ as the inertia function [29]. The higher order terms will be neglected since they are smaller than the first two. In the numerical scheme, $H^{(2)}(q)$ is the second moment of the matrix representing the transformed mesh associated to the GCM energy kernel and the collective coordinate, q, is now, naturally, the half-distance between the alpha clusters. The numerical calculations have been made with the GC taken in the interval ranging from -25.0 fm to 25.0 fm, with a step of 0.7 fm, corresponding to matrices of order $N=70$. This particular choice of the interval permits a numerically reliable set of points to be calculated in its central part, namely, up to 15 fm. The collective potential is presented in Fig. 1 (where we have subtracted -43.05 MeV, the constant asymptotic pure nuclear contribution of the potential), while the first two intrinsic wave functions, obtained from a numerical diagonalization of the transformed GW equation as indicated in [28], are depicted in Fig. 2.

Only two energy levels lie below the top of the barrier, namely at 1.14 MeV and 2.12 MeV, respectively, whereas all others occur above. The discretization process and the finiteness of the interval of variation of the GC constitute a constraint in this procedure, leading, obviously, to a discrete spectrum, while the actual one has a continuum.

IV. NONLOCAL EFFECTS

The calculated breakup potential for the ^{8}Be can be seen to be different from the diagonal part of the GCM energy kernel, which corresponds to the variational potential approach for the problem. The difference, which comes from the off-diagonal terms of the GCM energy kernel matrix, reflects the *nonlocal effects* embodied in the formalism and, at the same time, clearly displays a strong repulsion in the inner region. This feature of the potential *is not only due to Coulomb repulsion*; in fact it is strongly marked by the blocking effects of pure kinematical nature. As is well known, the short life of the ^{8}Be nucleus ($\sim10^{-16}$ s) is basically due to these effects. Thus, at short range, the nuclear part of the nucleon-nucleon interaction and the blocking effects dominate, whereas, asymptotically, the breakup potential tends to the two alphas Coulomb interaction, where no nonlocal effects are expected.

The calculated ratio between the inertia function and the reduced mass of the two alpha system is depicted in Fig. 3 (we remind the reader that the GC adopted is half the distance between the centers of the HO's potentials so that the reduced mass of the system corresponds to eight nucleon masses). The asymptotic behavior of the inertia function goes to the reduced mass of the two alpha system, as expected, since, there, only the direct part of the nucleon-nucleon interaction effects show up, whereas in the alphas'

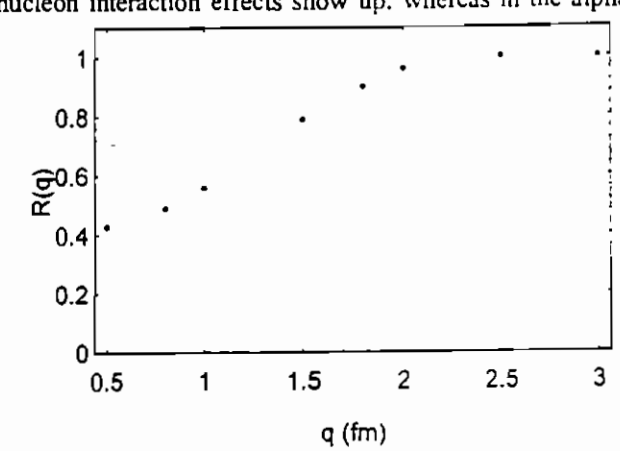

FIG. 3. The microscopically calculated dimensionless ratio $R(q)=\mu^*(q)/\mu$ for the ^{8}Be breakup. The calculations were performed with a 70×70 mesh in the interval $-25\leq z_0\leq 25$ and a step of $\Delta z_0=0.7$.

overlapping region, by assuming a peculiar form, the inertia function clearly reveals the nonlocal effects occurring at short distances, due to the exchange effects. At the same time that this result reveals important nonlocal contributions to the breakup process, therefore strongly suggesting the presence of the same characteristics already found in the nuclear fusion processes [9,10], its behavior also confirms a recent proposal for the description of nucleus-nucleus elastic scattering [7,8]. There, it was proposed that the real part of the nucleus-nucleus interaction is described by a nonlocal potential which amounts to having an inertia function that should be given by the expression [31]

$$\mu^*(q)=\frac{\mu}{1+\mu\beta^2/2\hbar^2|V(q)|}, \tag{15}$$

where β is the nonlocality range of the nucleus-nucleus system, μ is its asymptotic reduced mass and $V(q)$ is a double folding potential

$$V_f(q)=\int \rho_1(r_1)v(\vec{q}-\vec{r}_1+\vec{r}_2)\rho_2(r_2)d\vec{r}_1 d\vec{r}_2. \tag{16}$$

Here $v(r)$ is the effective nucleon-nucleon interaction and $\rho_1(r_1)$ and $\rho_2(r_2)$ are the nuclear densities of the colliding partners, respectively. We can directly compare that expression for the inertia function involving the folding potential, used to describe the nuclear scattering, with our previous microscopically derived quantum numerical result, obtained for the breakup using, by its turn, the completely antisymmetrized GCM wave function. For this purpose, we calculate expression (15) using the Wigner part of the Volkov interaction as $v(r)$. This can be analytically accomplished if we use the HO wave functions for the calculations of the alpha densities (as we have done also for the GCM calculations) thus giving

$$V_f(q)=6.4\left[V_{0a}\left(\frac{\alpha_a^2}{\alpha_a^2+2b^2}\right)^{3/2}\exp\left(\frac{-4q^2}{\alpha_a^2+2b^2}\right)+V_{0r}\left(\frac{\alpha_r^2}{\alpha_r^2+2b^2}\right)^{3/2}\exp\left(\frac{-4q^2}{\alpha_r^2+2b^2}\right)\right]. \tag{17}$$

Now, in order to compare the two results for the inertia function, we must first introduce the Jackson and Johnson expression for the nonlocality range [32], namely $\beta=\beta_0 m/\mu$, where μ is the reduced mass of the system, m is the nucleon mass and β_0 is the nucleon-nucleus nonlocality as given by Perey and Buck [33]. The comparison between the microscopically based calculated inertia function and the one calculated from the Volkov double folding potential using expression (17) is shown in Fig. 4. We verify that there is a substantial agreement between the two results in the region $z_0, z_0' \gtrsim b$, which corresponds to the exact description of the overlap kernel, while for $z_0, z_0' \lesssim b$ there appears a slight deviation, since the overlap kernel was approximated in that region. Besides, in the numerical results there are other quantum exchange effects which are not present in Eq. (17). Thus, we can see from the figure that the inertia function for the breakup under study has the same form as that proposed

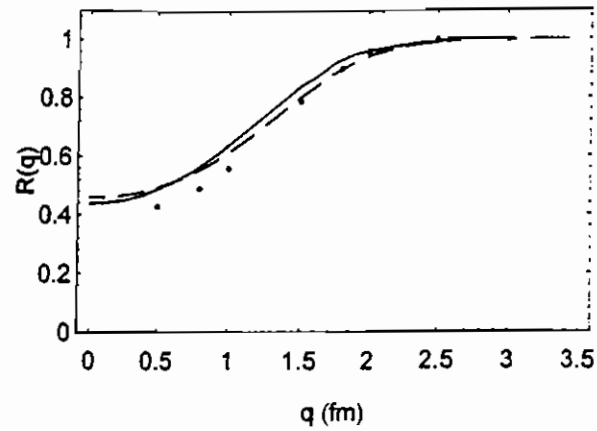

FIG. 4. Comparison between the microscopically calculated dimensionless ratio (points) and the phenomenological one using the folding ansatz, the Volkov interaction, and the Jackson and Johnson nonlocality range (dashed line). Also shown is the same ratio calculated from the nucleon-nucleon M3Y interaction with the parameters given in the text (continuous line).

for the description of nucleus-nucleus scattering—this means that it can be quite well described by expression (15)—and, therefore, it is direct to see that it depends on the double folding potential, but not on that describing the breakup, namely the one presented in Fig. 1. In this form, besides being consistent with what is expected for the process, this result also gives full microscopic support for the the ansatz proposed in the nuclear reactions context [7,8].

For the sake of completeness, we have also calculated the inertia function from the double folding potential using the nucleon-nucleon M3Y interaction [34]:

$$v(r)=7999\frac{e^{-4r}}{4r}-2134\frac{e^{-2.5r}}{2.5r}-262\delta(\vec{r}), \tag{18}$$

and HO wave functions for the alpha densities. The pseudopotential, $-262\delta(\vec{r})$ MeV, describes the knock-on exchange collision at 10 MeV/nucleon [35]. The result practically coincides with those of the previous calculation, as can be seen also in Fig. 4.

V. CONCLUSIONS

Recently, we have presented arguments that emphasized the importance of the nonlocal effects arising from the quantum exchange which are present in many-body systems and in particular in nuclear ones. Specifically we have proposed a way to incorporate these effects in the description of the real part of a nucleus-nucleus potential and we have also shown how these nonlocal effects can explain the energy dependence present in the local-equivalent real part of the phenomenological nucleus-nucleus potentials at intermediate energies [7,8]. At the same time, that proposal serves as a test for the nonlocality range for composed nuclear systems as obtained in a simple folding model. In the present paper we have shown that the same nonlocal effects also show up in nuclear breakup processes. Here, we have adopted a full microscopic starting point, namely the generator coordinate method, GCM, for the description of the ^{8}Be nucleus that is known to undergo spontaneous fission into two alpha particles. The nucleons degrees of freedom are washed out in the calculations so that one ends up with the GCM kernels

which are then functions only of the parameter associated to the half distance between the clusters. By an appropriate transformation, the GCM energy kernel is converted into a collective Hamiltonian which is written in terms of a collective potential and an inertia function. Therefore, all the underlying nonlocal effects of microscopic origin in the ^{8}Be nucleus are taken into account now in these new functions. The collective potential clearly reveals a shallow pocket that does not allow for a bound state and a strong repulsion at short distances, mainly due to Pauli blocking. In fact, the solution of the GCM equation admits two levels below the top of the barrier but above the asymptotic Coulomb tail; the lowest level is the candidate for representing the ^{8}Be resonance although its energy eigenvalue is above the 100 keV expected for this case. The inertia function, by its turn, bears the hallmark of the presence of nonlocal effects in a marked way. Being a function of the half-distance degree of freedom, the ratio of the effective reduced mass to the reduced mass for the breakup process has a form that clearly resembles the ones already found in other nuclear processes and also that of a nucleon in a self-consistent potential [36]. Furthermore, we have compared the numerical result for that ratio with the one analytically obtained from a double folding inspired expression and the Volkov interaction. The results almost entirely match. We can therefore see that the present microscopic-based treatment of the ^{8}Be exhibits the importance of nonlocal exchange effects in the breakup, which can be of great importance for more accurate descriptions of astrophysical processes, such as the capture of an α particle by a breaking up ^{8}Be in the process that populates the 7.6 MeV Hoyle 0^+ resonance in ^{12}C.

ACKNOWLEDGMENTS

M.A.C.R. was supported by FAPESP (Contract No. 96/3240-5) and all other authors were partly supported by CNPq. D.G. wants to thank B.M. Pimentel for a valuable suggestion.

[1] M. E. Brandan and R. Satchler, Phys. Rep. **285**, 143 (1997).
[2] D. A. Goldberg and S. M. Smith, Phys. Rev. Lett. **33**, 715 (1974).
[3] E. Stiliaris, H. G. Bohlen, P. Frobrich, B. Gebauer, D. Kolbert, W. von Oertzen, M. Wilpert, and Th. Wilpert, Phys. Lett. B **223**, 291 (1982).
[4] A. M. Kobos, B. A. Brown, P. E. Hodgson, G. R. Satchler, and A. Budzanowski, Nucl. Phys. **A384**, 65 (1982).
[5] A. M. Kobos, B. A. Brown, R. Lindsay, and G. R. Satchler, Nucl. Phys. **A425**, 205 (1984).
[6] D. T. Khoa, W. von Oertzen, and A. A. Ogloblin, Nucl. Phys. **A602**, 98 (1996).
[7] M. A. Cândido Ribeiro, L. C. Chamon, D. Pereira, M. S. Hussein, and D. Galetti, Phys. Rev. Lett. **78**, 3270 (1997).
[8] L. C. Chamon, D. Pereira, M. S. Hussein, M. A. Cândido Ribeiro, and D. Galetti, Phys. Rev. Lett. **79**, 5218 (1997).
[9] D. Galetti and M. A. Cândido Ribeiro, Phys. Scr. **45**, 417 (1992).
[10] D. Galetti and M. A. Cândido Ribeiro, Phys. Rev. C **50**, 2136 (1994).
[11] D. L. Hill and J. A. Wheeler, Phys. Rev. **89**, 112 (1953).
[12] J. J. Griffin and J. A. Wheeler, Phys. Rev. **108**, 311 (1957).
[13] C. W. Wong, Phys. Rep., Phys. Lett. **15C**, 283 (1975).
[14] P. Ring and P. Schuck, *The Nuclear Many-Body Problem* (Springer Verlag, New York 1980).
[15] K. Wildermuth and W. McClure, *Cluster Representation of Nuclei*, Springer Tracts in Modern Physics, Vol. 41 (1966).
[16] M. Harvey and A. Jensen, Nucl. Phys. **A179**, 33 (1972).
[17] A. Lumbroso, Phys. Rev. C **10**, 1271 (1974).
[18] D. Brink, in *Proceedings of the International School of Physics Enrico Fermi*, course 36, Varenna, 1965, edited by C. Bloch (Academic Press, New York, 1966).
[19] S. Saito, Prog. Theor. Phys. Suppl. **62**, 11 (1977).
[20] A. B. Volkov, Nucl. Phys. **74**, 33 (1965).
[21] H. Flocard and D. Vautherin, Phys. Lett. **52B**, 399 (1974).
[22] W. Bauhoff, Ann. Phys. (N.Y.) **130**, 307 (1980).
[23] L. S. Ferreira and M. H. Caldeira, Nucl. Phys. **A189**, 250 (1972).
[24] B. Banerjee and D. M. Brink, Z. Phys. **258**, 46 (1973).
[25] G. Holzwarth, Nucl. Phys. **A207**, 545 (1973).
[26] B. Giraud and B. Grammaticos, Nucl. Phys. **A255**, 141 (1975).
[27] H. Weyl, *Group Theory and Quantum Mechanics* (Dover, New York, 1950).
[28] D. Galetti and A. F. R. de Toledo Piza, Phys. Rev. C **17**, 774 (1978).
[29] D. Galetti and S. S. Mizrahi, Phys. Rev. C **25**, 2795 (1982).
[30] I. S. Gradshtein and I. M. Rhyzik, *Table of Integrals, Series and Products* (Academic Press, New York, 1965), Sec. 8.25.
[31] W. E. Frahn and R. H. Lemmer, Nuovo Cimento 5, 1564 (1957).
[32] D. F. Jackson and R. C. Johnson, Phys. Lett. **49B**, 249 (1974).
[33] F. Perey and B. Buck, Nucl. Phys. **32**, 253 (1962).
[34] G. R. Satchler and W. G. Love, Phys. Rep. **55**, 183 (1979).
[35] M. El-Azab Farid and G. R. Satchler, Nucl. Phys. **A438**, 525 (1985).
[36] D. Vautherin and D. M. Brink, Phys. Rev. C **5**, 626 (1972).

Ref. Rc SP

Pauli Nonlocality in Heavy-Ion Rainbow Scattering: A Further Test of the Folding Model

M. A. Cândido Ribeiro,[1] L. C. Chamon,[1] D. Pereira,[1] M. S. Hussein,[1] and D. Galetti[2]
[1]*Instituto de Física, Universidade de São Paulo, C.P. 66318, CEP 05315-970 São Paulo SP, Brazil*
[2]*Instituto de Física Teórica, Universidade Estadual Paulista, Rua Pamplona 145, CEP 01405-900 São Paulo SP, Brazil*
(Received 7 November 1996)

Nonlocal interactions are an intrinsically quantum phenomenon. In this work we point out that, in the context of heavy ions, such interactions can be studied through the refractive elastic scattering of these systems at intermediate energies. We show that most of the observed energy dependence of the local equivalent bare potential arises from the exchange nonlocality. The nonlocality parameter extracted from the data was found to be very close to the one obtained from folding models. The effective mass of the colliding, heavy-ion, system was found to be close to the nucleon effective mass in nuclear matter. [S0031-9007(97)02958-X]

PACS numbers: 25.70.Bc, 21.30.Fe, 21.65.+f, 24.10.–i

Of fundamental importance in nuclear physics are the effects arising from the Fermi nature of the nucleons. When calculating interaction potentials between nuclei, these effects translate into a nonlocality. This Pauli nonlocality has been discussed in the context of the nucleon-nucleus scattering [1,2]. A fully microscopic calculation of the nucleus-nucleus interaction is quite complicated and one relies here on procedures such as the resonating-group method [3]. Other methods rely on relating the nucleus-nucleus nonlocality to that of the nucleon-nucleus one using folding procedure [4]. However, the prediction of Jackson and Johnson [4], namely, the nonlocality range in the nucleus-nucleus systems, is smaller than that in the nucleon-nucleus one by about the inverse of the reduced mass in the former, was never really subjected to tests. In this Letter we supply such a test through a careful analysis of the elastic scattering of the systems $^{12}C + {}^{12}C$ and $^{16}O + {}^{12}C$ at intermediate energies.

Before we set the stage for our analysis of exchange effects in the ion-ion interaction, we first say a few words about this interaction. The effective, one-body interaction that determines the elastic scattering between two nuclei can be written in a schematic way as

$$V(\vec{r},\vec{r}') = V_{\text{bare}}(\vec{r},\vec{r}') + \sum_i V_i(\vec{r}) G_i^{(+)}(\vec{r},\vec{r}';E) V_i(\vec{r}') . \tag{1}$$

The first term, $V_{\text{bare}}(\vec{r},\vec{r}')$, is usually called the bare interaction. It represents the ground state expectation value of the interaction operator, which contains as basic input the average effective nucleon-nucleon force (G matrix). The nonlocality here is solely due to the Pauli exclusion principle and in what follows we refer to it as the Pauli nonlocality. The second term contains the contribution arising from virtual transitions to intermediate states i (inelastic channels, transfer channels, etc). The corresponding nonlocality arises almost entirely from the polarizations that ensue in the heavy-ion system owing to the propagation in the intermediate channels. This is exemplified by the channel Green's function $G_i^{(+)}(\vec{r},\vec{r}';E)$, which contains an explicit energy dependence. This latter contribution is called the Feshbach term and thus we refer to its nonlocality as the Feshbach nonlocality.

When confronting theory with experiment one usually relies on a one-body optical model with a local potential. This brings into light immediately the issue of extracting from Eq. (1) a local equivalent potential. This potential is thus defined through the equation

$$\int V(\vec{r},\vec{r}')\psi_E^{(+)}(\vec{r}')\,d\vec{r}' \equiv V(\vec{r},E)\psi_E^{(+)}(\vec{r}) , \tag{2}$$

where $\psi_E^{(+)}(\vec{r})$ is the exact wave function that describes the elastic scattering of the nucleus-nucleus system.

Clearly, from the structure of Eq. (1) for $V(\vec{r},\vec{r}')$, the energy-dependent local equivalent potential is

$$V(\vec{r},E) = V_{\text{PAULI}}(\vec{r},E) + V_{\text{FESHBACH}}(\vec{r},E) , \tag{3}$$

where V_{PAULI} is the local equivalent of V_{bare} and V_{FESHBACH} is the corresponding one for the second term on the right-hand side of Eq. (1). Here V_{FESHBACH} is manifestly complex, whereas V_{PAULI} is taken to be predominantly real. A small imaginary component in V_{PAULI} may be present due to the complex nature of the underlying effective nucleon-nucleon interaction (G matrix) and as a consequence of Eq. (2) through the wave function. The energy dependence of V_{PAULI} would have two origins: the nucleon-nucleon G matrix and, more importantly, the Pauli nonlocality.

Notwithstanding the fact that the major part of the nonlocality in the potential is related to channel couplings (Feshbach nonlocality), we take the view that the effect of these couplings is embedded in the energy-dependent imaginary potential. Further energy dependence may be expected in the real part of the potential that comes from the dispersion relation. However, the part of the ion-ion interaction which contains this Feshbach nonlocality-related energy dependence is concentrated in the surface. Therefore, in the inner region the ion-ion potential is expected to have its energy dependence arising predominantly from the Pauli nonlocality alluded to above. The

 0031-9007/97/78(17)/3270(4)$10.00

probe of the inner region is made possible through the elastic scattering at intermediate energies [5].

In a recent review article [5] the phenomenon of rainbow scattering seen in several heavy-ion elastic scattering data was discussed. It was emphasized that by measuring the angular distribution of systems such as $^{12}C + ^{12}C$, $^{16}O + ^{16}O$, etc., in the energy region where the far-side amplitude dominates, one is able to extract unambiguously the depth of the real part of the ion-ion potential. This has been shown in detail in [6–9]. Further, by tracing the nucleus-nucleus interaction to its underlying, density-dependent, effective nucleon-nucleon interaction, one is eventually able to extract the compressibility of nuclear matter,

$$K = 9\rho_0^2 \frac{\partial^2}{\partial \rho^2}\left(\frac{E}{A}\right)_{\rho=\rho_0}, \tag{4}$$

where ρ is the density and E/A is the average binding energy per nucleon of the cold system. The extracted value of K from the $^{16}O + ^{16}O$ system [9] at several center of mass energies was found to be roughly 220 MeV, indicative of a soft equation of state. What other physics may one extract from these angular distributions? The question which we raise here is certainly asked by many other heavy-ion physicists. We shall give sufficient evidence in the affirmative to the above question. In particular, we show below that the same data that were analyzed by Khoa *et al.* [7–9] for the purpose of the extraction of K can be used to extract the nonlocality parameter b which measures the nonlocal spread in configuration space where the ion-ion force is operative. The extracted value of b is very close to the one predicted 22 years ago by Jackson and Johnson [4], who showed within the single folding model that $b \approx b_0 m/\mu$, where b_0 is the nucleon-nucleus nonlocality parameter, m is the nucleon mass, and μ is the reduced mass of the nucleus-nucleus system. Theoretically, it was estimated [10,11] that $b_0 \sim 1$ fm. By an extensive fit of nucleon-nucleus elastic scattering data, Perey and Buck [1] have found $b_0 = 0.85$ fm.

As stressed in the introduction, we assume that the bare nucleus-nucleus real potential is nonlocal and we adopt the following form for it:

$$V_{\rm bare}(\vec{r},\vec{r}\,') = V_{\rm NL}\left(\frac{|\vec{r}+\vec{r}\,'|}{2}\right)\exp\left[-\frac{(\vec{r}-\vec{r}\,')^2}{b^2}\right], \tag{5}$$

where the nonlocal potential $V_{\rm NL}(|\vec{r}+\vec{r}\,'|/2)$ is of a density-density folding inspired form. Using the Perey prescription [1], based on Eq. (2), for finding a local equivalent potential, we obtain

$$V_{\rm LE}(r,E) = V_{\rm NL}(r)\exp\left\{-\frac{\mu\, b^2}{2\,\hbar^2}\left[E_{\rm c.m.} - V_{\rm LE}(r,E) - V_{\rm C}(r)\right]\right\}, \tag{6}$$

where we use the notation $V_{\rm LE}$ to designate $V_{\rm PAULI}$. Here $V_{\rm C}(r)$ is the Coulomb interaction given as usual by

$$V_{\rm C}(r) = \begin{cases} (3R_{\rm C}^2 - r^2)Z_1Z_2e^2/2R_{\rm C}^3 & r < R_{\rm C} \\ Z_1Z_2e^2/r & r \geq R_{\rm C} \end{cases}, \tag{7}$$

where $R_{\rm C}$ is the Coulomb radius. Thus a plot of $\ln V_{\rm LE}(r,E)$ against $E_{\rm c.m.} - V_{\rm LE}(r,E)$ should yield a straight line whose slope is just $-\mu b^2/2\hbar^2$.

As said above, ample proof has been accumulated over the last several years, which indicates that the real part of the ion-ion interaction, at very short distances, can be unambiguously extracted from the refractive scattering of heavy ions at intermediate energies. Elastic scattering angular distributions for the system $^{12}C + ^{12}C$ at intermediate energies were analyzed in Ref. [12]. It was shown that the region of radial sensitivity, where the optical potential is probed, is $r \simeq 4$ fm. Those angular distributions are dominated by the far side component in the region of momentum transfer $q \geq 400$ MeV/c. Theoretically, using the semiclassical approach, it is possible to demonstrate [13] that for this value of momentum transfer the real part of the potential is probed at interacting distances around 4 fm.

Having spelled out the possible limitations of our model, we turn now to the extraction of the nonlocality range parameter b, using Eq. (6) and the potential values in the probed radial region, which were unambiguously determined from the elastic data analyses of Refs. [7,12,14–16]. In Fig. 1(a) is shown $\ln V_{\rm LE}(r)$ versus $E_{\rm c.m.} - V_{\rm LE}(r)$ for the system $^{12}C + ^{12}C$ at $r = 4$ fm (circles). The extracted value of b is 0.14 fm to be compared to 0.15 fm expected from single folding result of Ref. [4], $b \approx b_0 m/\mu$, where b_0 is about 0.9 fm. Also shown in the inset in Fig. 1(a) is the energy dependence of $V_{\rm LE}(r = 4\ {\rm fm})$. Similar analysis was made on the system $^{16}O + ^{12}C$. This is shown in Fig. 1(b) (circles). Here b was found to be 0.11 fm, whereas $b_0 m/\mu$ is 0.13 fm. We point out that within about 10% accuracy, as shown in Fig. 1, the energy dependence of $V_{\rm LE}$ extracted from data analyses is described by Eq. (6). There is also an excellent agreement for the extracted b values and those predicted by the folding model. These findings are consistent with our hypothesis that associates the main energy dependence of the local equivalent potential to exchange nonlocal effects.

We should mention that the region of radial sensitivity, where the potential is unambiguously extracted from refrative elastic data, is rather system dependent. For example, nucleon, deuteron, and alpha-nucleus systems present radial sensitivity near $r \simeq 0$ fm [17] while, as discussed above, for systems like $^{12}C + ^{12}C$ this region is around 4 fm. Thus, with the aim to extend our analyses to other systems, we have considered the potential values at $r = 0$ fm. The potential extrapolation from the

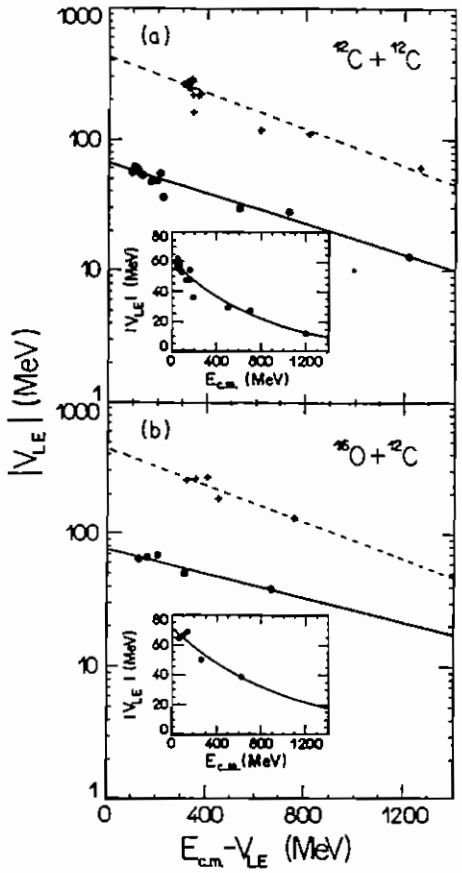

FIG. 1. The energy dependence of the local equivalent potential, V_{LE} at $r = 4$ fm (circles) and $r = 0$ fm (crosses), in the energy range $10 \leq E_{lab}/A \leq 200$ MeV/nucleon for (a) $^{12}C + ^{12}C$ and (b) $^{16}O + ^{12}C$. The solid and dashed lines represent the Perey prescription at $r = 4$ fm and $r = 0$ fm, respectively (see text for details).

sensitivity region to $r = 0$ is shape dependent. Therefore, in our analyses we have considered only realistic shapes, such as those provided by the DDM3Y folding calculations. Using this extrapolation for the ^{12}C, $^{16}O + ^{12}C$ systems, the energy dependence of $V_{LE}(r = 0)$ (crosses in Fig. 1) is well described by Eq. (6) and the corresponding b values are also very close to those obtained through the potential values at $r = 4$ fm.

We have used expression (6) and the data analysis from Refs. [1,7–9,12,14,16–18] to extract $V_{NL}(0)$ as a function of μ. For the systems which the data energy range was not sufficiently extensive, we have used the b values from Ref. [4]. As is shown in Fig. 2, $V_{NL}(0)$ increases linearly with μ.

A further test of the consistency of our analysis method is supplied by a look at the effective reduced mass μ^* of the combined system. Back in 1956, Frahn established the following simple relation [19]:

$$\frac{\mu^*(r)}{\mu} = \frac{1}{1 + \frac{\mu b^2}{2\hbar^2} \mid V_{NL}(r) \mid}. \tag{8}$$

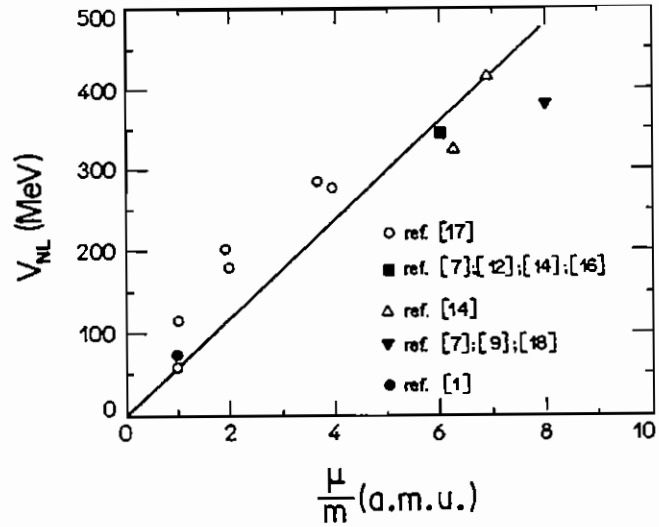

FIG. 2. The resulting nonlocal potential $V_{NL}(r = 0)$. using the Perey prescription [1] and the elastic data analyses as a function of the reduced mass of the system. The data point [•] is the result of the Perey and Buck analyses of several nucleon-nucleus systems. The solid line in the figure serves only as a guide to the eye.

We stress at the outset that the concept of effective mass is intimately related to the nonlocal nature of the interaction [19]. We further stress that since the nucleon effective mass determined from the mean free path in the nuclear matter [20,21] is $m^*/m \cong 0.7$, one should find $\mu^*(0)/\mu \approx 0.7$. In Fig. 3 we show the extracted $\mu^*(0)/\mu$, using Eqs. (6) and (8) and the experimentally determined $V_{LE}(0)$. Clearly, our expectations are reasonably met.

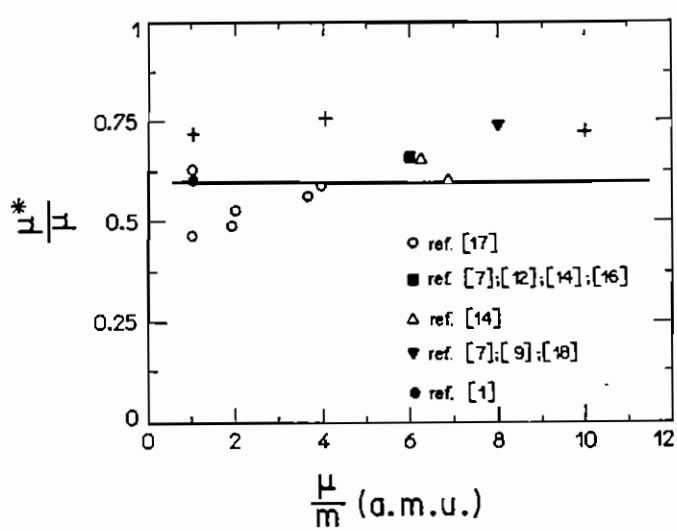

FIG. 3. The dimensionless effective reduced mass μ^*/μ as a function of the reduced mass of the colliding system. The solid line in the figure represents the average value from several systems. The data point [•] is the result of the Perey and Buck analyses of several nucleon-nucleus systems. The [+] points represent the theoretical predictions using the generator coordinate method (see text for details).

It is worth mentioning that the same conclusion can also be attained through theoretical considerations. In fact, in a procedure based on a fully microscopic generator coordinate method, using a Skyrme interaction, aiming at the extraction of the collective potential and effective mass for the giant dipole resonance for light double magic nuclei [22], the proposed behavior was completely verified. The results from these theoretical calculations are represented by crosses in Fig. 3.

It is further worth mentioning that Perey and Buck have analyzed [1] a large set of elastic scattering data for several nucleon-nucleus systems. They have taken into account the effects of exchange nonlocality using a Schrödinger-like integrodifferential equation. It is impressive that the results of those analyses, included in Figs. 2 and 3 as the full circles, are very similar to the results for the heavier systems that we have analyzed.

We turn now to the case of exotic, radioactive, nuclei. Recently, measurements of elastic scattering of ^{11}Li with ^{12}C [23] and ^{28}Si [24] targets, at only one energy, were reported. The phenomenological optical potential in conjunction with coupled channels was employed in the analysis [25–27]. The simple cluster model for the ground state of ^{11}Li implies a structure where the core nucleus ^{9}Li is weakly bound to a dineutron. The folding procedure of Ref. [4] would then lead to a larger b. This in turn will translate into a stronger energy dependence of the bare halo nucleus-ion potential. An extension of the measurement to other energies is urgently called for testing these proposals.

In conclusion, we have considered the exchange nonlocal effects of the nucleus-nucleus interaction arising from the Fermi nature of the nucleons. We have demonstrated in this paper that most of the observed energy dependence of the local equivalent potential, extracted from the refractive elastic scattering data analysis of nucleus-nucleus systems at intermediate energies, arises from nonlocal exchange effects. The obtained values of the parameter b, which measures the range of this Pauli nonlocality, agrees with predictions using the single folding model. The effective mass of the system $\mu^*(0)/\mu$ is found to be very close to the nucleon effective mass of 0.7. The relevance of these findings to the scattering of radioactive, halolike, nuclei is briefly discussed.

We thank G. R. Satchler and M. E. Brandan for useful correspondence. M. A. C. R. is supported by FAPESP (Contract No. 94/3191-9) and all other authors are partly supported by CNPq.

[1] F. Perey and B. Buck, Nucl. Phys. **32**, 253 (1962).
[2] W. Bauhoff, H. V. von Geramb, and G. Palia, Phys. Rev. C **27**, 2466 (1983).
[3] See, e.g., H. Horiuchi and K. Ikeda, *Cluster Model of the Nucleus*, International Review of Nuclear Physics Vol. 4 (World Scientific, Singapore, 1986).
[4] D. F. Jackson and R. C. Johnson, Phys. Lett. B **49**, 249 (1974).
[5] M. E. Brandan, M. S. Hussein, K. W. McVoy, and G. R. Satchler, Commun. Part. Nucl. Phys. **22**, 77 (1996); M. E. Brandan and G. R. Satchler (to be published).
[6] D. A. Goldberg, S. M. Smith, and G. F. Burdzik, Phys. Rev. C **10**, 1362 (1974).
[7] D. T. Khoa, W. von Oertzen, and H. G. Bohlen, Phys. Rev. C **49**, 1652 (1994).
[8] D. T. Khoa and W. von Oertzen, Phys. Lett. B **342**, 6 (1995).
[9] D. T. Khoa *et al.*, Phys. Rev. Lett. **74**, 34 (1995).
[10] T. H. R. Skyrme, Philos. Mag. **1**, 1043 (1956).
[11] G. Ripka, Nucl. Phys. **42**, 75 (1963).
[12] J. Y. Hostachi *et al.*, Nucl. Phys. **A490**, 441 (1988).
[13] M. S. Hussein and M. P. Pato, Phys. Rev. C **51**, 2681 (1995).
[14] M. E. Brandan and G. R. Satchler, Nucl. Phys. **A487**, 477 (1988).
[15] M. E. Brandan, M. Rodrigues-Villafuerte, and A. Ayala, Phys. Rev. C **41**, 1520 (1990).
[16] H. G. Bohlen, M. R. Clover, G. Ingold, H. Lettau, and W. von Oertzen, Z. Phys. A **308**, 121 (1982).
[17] M. Ermer *et al.*, Phys. Lett. B **224**, 40 (1989).
[18] D. T. Khoa and W. von Oertzen, Phys. Lett. B **304**, 8 (1993).
[19] W. E. Frahn, Nuovo Cimento **4**, 313 (1956).
[20] J. W. Negele and K. Yazaki, Phys. Rev. Lett. **47**, 71 (1981).
[21] S. Fantoni, B. L. Friman, and V. R. Pandharipande, Phys. Lett. B **104**, 89 (1981).
[22] D. Galetti, J. Phys. G **11**, 711 (1985).
[23] J. J. Kolata *et al.*, Phys. Rev. Lett. **69**, 2631 (1992).
[24] M. Lewitowicz *et al.*, Nucl. Phys. **A562**, 301 (1993).
[25] I. J. Thompson, J. S. Al-Khalili, J. A. Tostevin, and J. M. Bang, Phys. Rev. C **47**, R1364 (1993).
[26] M. S. Hussein and G. R. Satchler, Nucl. Phys. **A567**, 165 (1994).
[27] D. T. Khoa, G. R. Satchler, and W. von Oertzen, Phys. Lett. B **358**, 14 (1996).